
Chemo-mechanical Modeling of Lithium-Ion Batteries

Chemomechanische Modellierung von Lithium-Ionen-Batterien

Zur Erlangung des Grades eines Doktors der Naturwissenschaften (Dr. rer. nat.)

genehmigte Dissertation von Yang Bai, M. Sc. aus Chongqing, China

Tag der Einreichung: 26.08.2020, Tag der Prüfung: 20.11.2020

1. Gutachten: Prof. Dr. Bai-Xiang Xu, TU Darmstadt

2. Gutachten: Prof. Dr.-Ing. Marc Kamlah, Karlsruhe Institute of Technology



TECHNISCHE
UNIVERSITÄT
DARMSTADT

Fachbereich
Material- und
Geowissenschaften
MFM-Mechanik
Funktionaler Materialien

Chemo-mechanical Modeling of Lithium-Ion Batteries
Chemomechanische Modellierung von Lithium-Ionen-Batterien

Doctoral thesis by Yang Bai, M. Sc.

1. Review: Prof. Dr. Bai-Xiang Xu, TU Darmstadt
2. Review: Prof. Dr.-Ing. Marc Kamlah, Karlsruhe Institute of Technology

Date of submission: 26.08.2020

Date of thesis defense: 20.11.2020

Bitte zitieren Sie dieses Dokument als:

URN: [urn:nbn:de:tuda-tuprints-175426](https://nbn-resolving.org/urn:nbn:de:tuda-tuprints-175426)

URL: <http://tuprints.ulb.tu-darmstadt.de/17542>

Dieses Dokument wird bereitgestellt von tuprints,
E-Publishing-Service der TU Darmstadt
<http://tuprints.ulb.tu-darmstadt.de>
tuprints@ulb.tu-darmstadt.de

Published under CC BY-SA 4.0 International

<https://creativecommons.org/licenses/by-sa/4.0/>

Erklärungen laut Promotionsordnung

§8 Abs. 1 lit. c PromO

Ich versichere hiermit, dass die elektronische Version meiner Dissertation mit der schriftlichen Version übereinstimmt.

§8 Abs. 1 lit. d PromO

Ich versichere hiermit, dass zu einem vorherigen Zeitpunkt noch keine Promotion versucht wurde. In diesem Fall sind nähere Angaben über Zeitpunkt, Hochschule, Dissertationsthema und Ergebnis dieses Versuchs mitzuteilen.

§9 Abs. 1 PromO

Ich versichere hiermit, dass die vorliegende Dissertation selbstständig und nur unter Verwendung der angegebenen Quellen verfasst wurde.

§9 Abs. 2 PromO

Die Arbeit hat bisher noch nicht zu Prüfungszwecken gedient.

Darmstadt, 26.08.2020

Yang Bai

Y. Bai

*A time will come to ride the wind and cleave the waves, I'll set my cloudlike
sail to cross the sea which raves.*

Bai Li

直 乘
掛 風
雲 破
帆 浪
濟 會
滄 有
海 時

Acknowledgement

First and foremost, my advisor Prof. Dr. Bai-Xiang Xu is sincerely appreciated for her kind supervision. She provided me with comprehensive instructions, lightened my scientific path with her fruitful knowledge, and corrected my manuscript patiently. I have benefited and learned a great deal from her knowledge and intelligence. It will be my precious memory in all my life.

Simultaneously, I am fairly thankful to all the members of my host group (Mechanics of Functional Materials) for their kind support and the fantastic working atmosphere. I am particularly grateful to Dr. Peter Stein, Binbin Lin, Ziqi Zhou, and Yao Liu, due to their friendly aid.

Also, I thank Prof. Marc Kamlah in Karlsruhe Institute of Technology sincerely for sacrificing his valuable time acting as the co-referee. I had many excellent discussions with him, learned plenty of useful knowledge in this process.

I dedicate this work to my lovely girlfriend Yunxia Li, and my parents. They are always my backbone to kicking out the stumbling block in front of me so that I am unafraid.

The funding of "Adolf Messer-Prize" is gratefully acknowledged for supporting me to pursue my Ph.D. degree. Computer Center of High-Performance Computing in Hesse is appreciated for the calculation resources, which provided reliable facilities to carry out my research.

Finally, I wish to respectfully thank the Evaluators and the Examiners of this work, Prof. Dr. Marc Kamlah, Prof. Dr. Dietmar Gross, and Prof. Dr. Karsten Durst for their time, fruitful discussions of the results and the insight into improvements.

Abstract

Due to the high energy and power density, Lithium-ion batteries (LIBs) have been widely employed in portable electronics and electric vehicles, and have become a promising solution for the storage of renewable energy. Besides the electrochemistry, it has been widely recognized that mechanics plays a critical role in the performance and the lifetime of LIBs. In particular, electrode materials with a high theoretical capacity suffer from irreversible mechanical degradation already after few cycles due to high internal stress, which is the well-known dilemma between capacity and cyclability of LIBs. It has motivated a number of chemo-mechanical studies on both the active particle level and the cell level in the last two decades.

This thesis presents first a thermodynamically consistent framework to derive a fully coupled electro-chemo-mechanical model for LIB electrode materials. In particular, it regards not only the chemo-mechanical bulk behavior in large deformation regions with phase separation but also the chemo-mechanical interface model, which addresses both the damage-dependent across grain boundary (GB) transport and a chemo-mechanically coupled cohesive zone law for mechanical failure. Although the unique mechanical and transport features of grain boundaries or interfaces in polycrystalline ion conductors have been recognized, the understanding of the chemo-mechanical interplay at the interface and its impact is insufficient. Based on the derived model, 3D finite element simulations for $\text{LiNi}_x\text{Mn}_y\text{Co}_z\text{O}_2$ meatball particles have been carried out. Results demonstrate that the enhanced intergranular chemical inhomogeneity can weaken the interface mechanical strength and can lead to the GB cracking. In contrast, the interface damage can, in turn, influence or even block the across-GB transport, thus enhance further the chemical inhomogeneity. This positive feedback explains the simulated results of chemical hot spots and surface layer delamination, which have been observed experimentally but go beyond the start-of-the-art simulation work.

In order to investigate the impact of chemo-mechanical particle behavior and damage on the cell performance, a particle-cell two-level finite element model is further developed in this thesis. The widely used Pseudo-Two-Dimensional (P2D) cell model for LIBs is generally based on a simplified lithium diffusion model of active particles with simple geometry. This thesis presents a two-level framework, which extends the P2D cell

model and incorporates a chemo-mechanically coupled 3D particle model as mentioned above. The two-level model allows a more detailed diffusion study of particles with general geometry and can include the full coupling among mechanics, phase separation, interface transport and damage. To improve the computational efficiency, we manage to reduce one degree of freedom at the cell level by treating the ion flux between the electrolyte and active particle as a dependent quantity. The two-level framework is validated against the original one and applied to study the impact of particle's geometry, elastic properties, and phase separation on the cell performance. For instance, results show that the oblate particle has better cell performance than other spheroidal particles. It is attributed to the mechanical drifting at the higher curvature.

The combination of the proposed chemo-mechanical particle model and the extended particle-cell two-level model lay a good foundation for chemo-mechanical simulations of LIBs and other related ion batteries. A series of parameter studies can be carried out, which are helpful to reveal both the mechanism and degradation of the particle and the related cell performance change, and can thus serve as powerful tools for multiphysics battery designs and optimization.

Zusammenfassung

Aufgrund hoher Energie und Leistungsdichte wurden Lithium Ionen Batterien (LIBs) in großem Umfang im Bereich mobiler Elektronik und elektrisch betriebener Fahrzeuge eingesetzt und sind zu einer vielversprechenden Lösung für das Problem der Speicherung von erneuerbaren Energien geworden. Es ist allgemein anerkannt, dass neben der Elektrochemie die Mechanik eine entscheidende Rolle für die Leistung und Lebensdauer von LIBs spielt. Insbesondere leiden Elektrodenmaterialien mit einer hohen theoretischen Kapazität bereits nach wenigen Zyklen unter einer irreversiblen mechanischen Verschlechterung aufgrund hoher innerer Spannungen, was das bekannte Dilemma zwischen Kapazität und Zyklisierbarkeit von LIBs ist. Es hat in den letzten zwei Jahrzehnten eine Reihe chemomechanischer Studien sowohl auf der Ebene der aktiven Partikel als auch auf der Ebene der Zelle motiviert.

Die vorliegende Arbeit präsentiert zunächst ein thermodynamisch konsistentes Framework, um ein vollständig gekoppeltes elektrochemisch-mechanisches Modell für LIB-Elektrodenmaterialien abzuleiten. Insbesondere geht es nicht nur um das chemomechanische Volumenverhalten in großen Verformungsbereichen mit Phasentrennung, sondern auch um das chemomechanische Interface Modell, das sowohl den schadensabhängigen Transport über Korngrenzen als auch ein chemomechanisch gekoppeltes Kohäsionszonenengesetz für das mechanische Versagen betont. Obwohl die einzigartigen mechanischen Merkmale und Transportmerkmale von Korngrenzen oder Interfaces in polykristallinen Ionenleitern erkannt wurden, ist das Verständnis für das chemomechanische Zusammenspiel am Interface und dessen Auswirkungen unzureichend. Das abgeleitete Modell dient genau diesem Zweck. Basierend auf diesem Modell wurden 3D-Finite-Elemente-Simulationen für $\text{LiNi}_x\text{Mn}_y\text{Co}_z\text{O}_2$ Fleischbällchen Partikeln durchgeführt. Die Ergebnisse zeigen, dass die verstärkte intergranulare chemische Inhomogenität die mechanische Stabilität vom Interface abschwächen und so zu GB-Rissen führen kann. Im Gegensatz dazu kann der Interfaceschaden wiederum den Transport über GB beeinflussen oder sogar blockieren, wodurch die chemische Inhomogenität weiter verstärkt wird. Dieses positive Feedback erklärt die simulierten Ergebnisse chemischer Hotspots und Oberflächendelamination, die experimentell beobachtet wurden, aber über die hochmodernen Simulationsarbeiten hinausgehen.

Um den Einfluss des chemomechanischen Partikelverhaltens und der Schädigung auf die Zelleistung zu untersuchen, wird in dieser Arbeit ein Partikel-Zell Zwei Level Finite-Elemente-Modell weiter entwickelt. Das weit verbreitete Pseudo-Two-Dimensional (P2D) -Zellmodell für LIBs basiert im Allgemeinen auf einem vereinfachten Lithiumdiffusionsmodell von aktiven Partikeln mit einfacher Geometrie. Diese Arbeit präsentiert ein Zwei Level Framework, welches das P2D-Zellmodell erweitert und ein oben erwähntes chemomechanisch gekoppeltes 3D-Partikelmodell enthält. Das Zwei Level Modell ermöglicht eine detailliertere Diffusionsstudie in Partikeln allgemeiner Geometrie und kann die vollständige Kopplung zwischen Mechanik, Phasentrennung sowie Interface Transport und -beschädigung umfassen. Um die Recheneffizienz zu verbessern, haben wir einen Freiheitsgrad auf der Zell Ebene reduziert, indem wir den Ionenfluss zwischen Elektrolyt und aktiver Partikel als abhängige Größe behandelten. Das Zwei Level Framework wird gegen das ursprüngliche validiert und angewendet, um den Einfluss der Partikelgeometrie, der elastischen Eigenschaften und der Phasentrennung auf die Zelleistung zu untersuchen. Zum Beispiel zeigen die Ergebnisse, dass die abgeflachte Partikel eine bessere Zelleistung aufweist als andere kugelförmige Partikeln. Dies wird auf das mechanische Driften bei der höheren Krümmung zurückgeführt.

Die Kombination des vorgeschlagenen chemomechanischen Partikelmodells und des erweiterten Partikel-Zell Zwei Level Modells bildet eine gute Grundlage für chemo-mechanische Simulationen von LIBs und anderen verwandten Ionenbatterien. Eine Reihe von Parameterstudien kann durchgeführt werden, die hilfreich ist um sowohl den Mechanismus und den Abbau der Partikel als auch die damit verbundene Änderung der Zelleistung aufzudecken, und kann somit als leistungsstarkes Werkzeug für das Design und die Optimierung von Multiphysik-Batterien dienen.

Contents

Acknowledgement	v
1 Introduction	1
1.1 Lithium-ion battery	3
1.2 Chemo-mechanics in LIBs	5
1.3 Goal and outline	8
2 Chemo-Mechanical Model for Particles with Interface	11
2.1 Kinematics	11
2.1.1 The motion of grains	12
2.1.2 The motion of grain boundaries (GBs)	16
2.2 Governing equations	16
2.2.1 Mass conservation	16
2.2.2 Mechanical equilibrium equation	18
2.3 Thermodynamics	18
2.4 Constitutive laws and ion transport equations	24
2.5 Free energies	27
2.5.1 Helmholtz free energy for the grains	27
2.5.2 Helmholtz free energy for interfaces	30
3 Two-level Modeling of Particle and Cell	39
3.1 Concentrated solution	39
3.2 Porous electrode theory	43
3.3 Electrochemical reaction	44
3.4 Bridging of the cell level and the particle level	46
4 Finite Element Implementation	49
4.1 Basics of the finite element method	49
4.2 Finite element implementation for the cell model	51
4.3 Finite element implementation for the chemo-mechanical particle model	53



4.4	Data transfer between two levels	55
5	Results and Publications	59
5.1	Considered Problems	59
5.2	Author's contribution to the publications	61
5.3	Publication A	62
5.4	Publication B	68
5.5	Publication C	81
6	Summary and outlook	107
6.1	Summary	107
6.2	Outlook	109
	Bibliography	109
	Publications and Presentations	122

List of Figures

1.1	Comparison between different battery technologies in terms of volumetric and gravimetric energy densities (taken with permission from [2]). . . .	2
1.2	Schematics of (a) the structure of LIB as well as the mechanistic and mechanical degradation mechanisms (b) chemo-mechanical interplay of LIBs (taken with permission from [11]).	4
1.3	SEM morphologies of the precursors NMC: (a) overall low magnification view of the NMC cathode (b) high magnification view of the NMC particle, where the periphery revealing the individual grains (primary particles) in the form of ‘stacks’ of hexagonal plates (c) medium resolution imaging of the as-fabricated secondary particle before cycling (d) the presence of peripheral cracking in NMC particle after the first charge/discharge cycle (taken with permission from [13]).	6
2.1	(a) SEM image for NMC cathode materials (taken with permission from [11]), (b) Schematic illustration of the single NMC particle.	12
2.2	(Left) The schematic illustration of the NMC particle with multiple grains and GBs. (Right) The representing subdomain \mathcal{B}_1 and \mathcal{B}_2 with an interface Γ_I , where \vec{n}_I indicates the normal vector of the interface, while the GBs on each side are respectively denoted by (+) and (-).	13
2.3	The change of a body under multiple successive deformations.	14
2.4	The lattice gas model, where the particles are denoted by the black color, while the white color represents the holes.	28
2.5	The traction-separation law (TSL) under different α, β , with $\phi_n = \phi_t = 4\frac{J}{m}, \lambda_n = \lambda_t = 0.1, \sigma_{\max} = \tau_{\max} = 100\text{MPa}$	32
2.6	Damage functions for normal failure and mixed-mode failure with $\lambda_n = 0.2, \lambda_t = 0.1$	35
3.1	Outline of the two-level framework for the Lithium-ion battery with a half-cell structure.	40



- 4.1 The representative two-dimensional linear cohesive zone element in (a) the global coordinates and (b) the local coordinates. 55
- 4.2 Flowchart of the two-level framework. 56

- 5.1 The across-GB transport law and its impact on the chemical heterogeneity as well as fracture patterns of the NMC particle. 60
- 5.2 Two-level framework with the consideration of different particle shapes and diffusion dynamics, and their impact on the cell performance. 60

1 Introduction

The surging global warming and solutions to reduce their impediment were one of the most challenging topics that have been widely discussed during the 21st Century. For a lengthy time, the hydrocarbon-based vehicles have been one of the major contributors to the increasing levels of greenhouse gases, for instance, the carbon dioxide, sulfur, and other pollutants in the air. Therefore, the demand to develop eco-friendly vehicles has become more and more important to rebuild a healthy environment. Renewable energy sources, for instance, the wind, solar, and hydropower have been accepted as excellent alternatives to the current energy production. Compared to fossil fuels, renewable energy can reduce the negative impact of greenhouse gases (CO_2 or CH_4) emissions on earth. However, one of the major issues related to renewable energy supply is the strong fluctuation in time and requires a large-scale stable storage solution. Rechargeable batteries are one promising solution.

As one leading type of rechargeable batteries, which can convert the electrical energy and the chemical energy back and forth, Lithium-ion batteries (LIBs) have high power densities and energy densities, as shown in Fig. 1.1. Moreover, LIBs have low self-discharge and no memory effect, which is more advanced than other batteries, i.e. the Ni–MH batteries. LIBs enable the use of smaller and lighter battery units and have been widely used in the portable electronics. In 1991, Lithium-ion batteries (LIBs) were first commercialized by Sony Company for the application in portable devices [1]. With successful implementation of massive production through Giga factories, the cost of LIBs has decreased largely. Along with further performance improvement of the LIBs, LIBs have been considerably employed for electric vehicle (EV), led by the company Tesla. The substitution of internal combustion engine by the electric motors contributes to a reduction of CO_2 and CH_4 emissions, which can further reduce the oil dependency [2].

The electric vehicle batteries operate under relative extreme conditions such as operating temperatures, high cycle frequency, and high changing discharge rates. Thus, LIBs in EV applications are expected to degrade significantly after the several years of application. The degradation mechanisms are of strong research interest and are known in general to be related to electrochemistry, mechanics and their interplay. More details will be introduced in the following subsections. These EV batteries can live a second life,

after they fail to meet EV performance standards, because they typically still maintain 80 percent of total capacity and satisfactory power density. After remanufacturing, these batteries can serve less-demanding applications, such as stationary energy-storage services for renewable energy.

Nevertheless, conventional gasoline can provide up to 80 times higher gravimetric and 20 times higher volumetric energy densities than the current LIBs [3], as shown in Table 1.1. LIBs still have a long way to go to compete with gasoline. The criticality of the essential elements such as Lithium, Nickel and Cobalt in the current LIB system is also an issue. The demands on better performance and cell amount of LIBs become increasingly high and motivated research on the fundamental understanding and optimization of the LIBs.

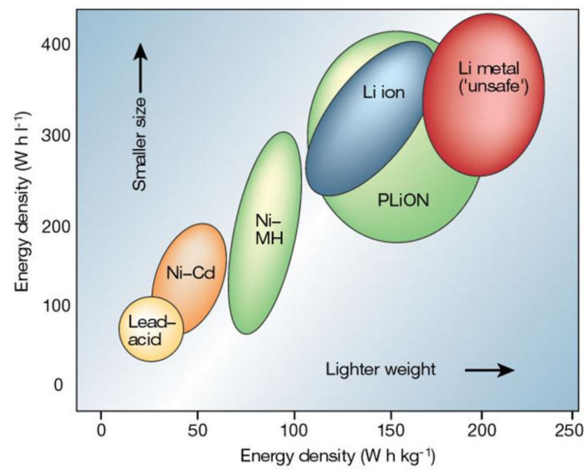


Figure 1.1: Comparison between different battery technologies in terms of volumetric and gravimetric energy densities (taken with permission from [2]).

	Nickel Cadmium	Nickel Metal Hydride	Lead Acid	Lithium-ion	Gasoline
Gravimetric Energy Density (Wh/kg)	45-80	60-120	30-50	100-160	12,200
Volumetric Energy Density (Wh/L)	120	240	30-50	350-450	9700

Table 1.1: Comparison of the gravimetric and volumetric energy densities between different batteries and gasoline (taken with permission from [3]).

1.1 Lithium-ion battery

As can be seen in Fig. 1.2(a), a classical Lithium-ion battery (LIB) cell consists of two composite electrodes (anode and cathode) sandwiched by a thin electron-insulating layer (namely the separator) soaked with the solid or liquid ionic conductive electrolyte in-between. Typically, the anode, namely the negative electrode, consists of a copper current collector foil coated with the carbonaceous active material. The most commonly used anode active material is graphite, since the carbon-based anodes have been successfully employed in the LIB produced by Sony company in 1991. Until nowadays, it is still the unbeatable anode material due to its high stability. One promising alternative to graphite as anode materials is the alloy type anodes, i.e. Aluminum and Silicon, with much higher theoretical energy density, safe operation potentials, and comparatively low cost [4, 5]. For instance, the promising Lithium-Silicon system can achieve a theoretical specific capacity of 4010 mAhg^{-1} . However, a severe volumetric swelling of 238% has been reported when the alloying process runs to the final stage with the composition of $\text{Li}_{22}\text{Si}_5$ [6], which can give rise to cracking as well as the contact loss, thus lead to the irreversible capacity fade. This will be discussed in the following subsection in more details. For solid-state batteries, Lithium metals are usually included as anode materials to have an optimal theoretical capacity.

The separator in a LIB cell is typically a porous polymer foil, where the pores of the active materials and the pores of the separator are filled with electrolyte. Commonly, the electrolyte contains the organic solvents, the conducting salt, and additives [7]. More recently, solid-state batteries, in which solid electrolytes have been applied to replace electrolyte solvent and the separator, has gained large research interest because of its potentially higher safety and higher energy density in comparison to the conventional LIBs.

While for the cathode, namely the positive electrode, the major components are the Aluminum current collector foil coated with the transition-metal-oxide active material, i.e. LiCoO_2 , LiMn_2O_4 or $\text{LiNi}_{1-x-y}\text{Mn}_x\text{Co}_y\text{O}_2$ (NMC). LiFePO_4 has also been widely used as cathode materials. However, it has relatively lower energy density than Lithium cobalt oxide chemistry, as well as a lower operating voltage. Since the progress in optimizing cathode materials is further than anode materials, the capacity of current LIBs is mainly determined by the cathode materials, for instance, for Lithium metal oxides LiMO_2 , i.e. LiCoO_2 , LiMn_2O_4 , LiFePO_4 and related materials with the specific capacity between 140 and 200 mAhg^{-1} have been widely reported [8].)

In particular, the widely used cathode materials $\text{LiNi}_x\text{Mn}_y\text{Co}_z\text{O}_2$ (NMC) have the so-called meatball structure, as shown in Fig. 1.3(a) and (c). Thereby the secondary spherical particle with the size around $10 \mu\text{m}$ is formed by small primary particles of

submicron size aggregate via van der Waals interactions [9]. Thereby, the mechanical strength of the secondary particle is much lower than the typical structure of the single-particle embedded in the conductive matrix. The ion transport across the grain boundary like interface is less studied. It can be related to the experimentally observed hot spots, in contrast to a gradual radial ion concentration variation.

During the charging process, Lithium stored in the cathode material is oxidized and deintercalated. Hence, Li^+ ions can go into the electrolyte solution, and move from the cathode to the anode. Meanwhile, the electrons are released to the external current at the positive current collector. Simultaneously, the electrons can reach the anode active materials from the external current path. Thereby, Li^+ ions from the electrolyte can be intercalated into the active materials, where the ions are reduced to neutral Lithium atoms. During the discharging, the process is reversed [10].

The overall charge and discharge kinetics are regulated by the electro-chemical reactions at the interface between active materials and electrolyte, given that the electron transport/supply is sufficient. In this scenario, the reversible electro-chemical reactions can be presented in the following:

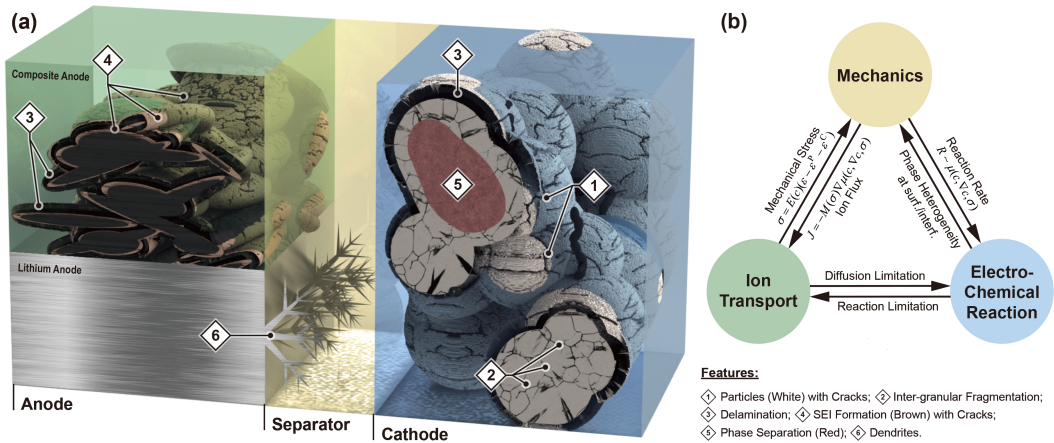
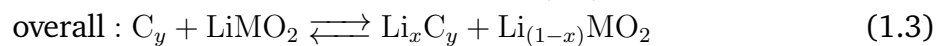
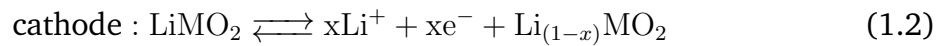


Figure 1.2: Schematics of (a) the structure of LIB as well as the mechanistic and mechanical degradation mechanisms (b) chemo-mechanical inter-play of LIBs (taken with permission from [11]).

1.2 Chemo-mechanics in LIBs

As explained above, during the charge/discharge cycles, Lithium or Li^+ shuttle between the cathode and the anode. Due to the chemical strain associated them, the battery materials experience breath-like deformation during cycling. The volume change can arrange from 12% to 300%, depending on the materials. The materials and the interfaces which exist both in the materials and between different functional components suffer from mechanical degradation. As it is summarized in Fig. Fig. 1.2(a)) taken from our review article [11], there could be various degradation mechanisms. For instance, the crack propagation can occur in the active material particles, along with intergranular fragmentation and the enhanced mechanical fields at phase interfaces of phase-separating materials. Moreover, delamination has been observed between active materials and other functional elements such as solid electrolytes or binders. All these degradations can lead to capacity fade and life time limitation of LIBs [12]. If Lithium metal is used electrode materials or at extreme charging conditions, Lithium dendrites can form on the surface of the active materials, penetrate through the electrolyte, reach the other electrode and thus leads to short-cut of the unit cell.

Particularly, take the commonly used $\text{LiNi}_{0.8}\text{Co}_{0.15}\text{Al}_{0.05}\text{O}_2$ (NCA) cathode materials as an example, a high degree of delithiation of NCA, i.e. above 50-60%, can lead to an irreversible distortion of the lattice structure, which can consequence in the irreversible capacity fade [14, 15]. Moreover, at both the high and low state of charge (SOC), the volumetric changes of NCA particles can cause mechanical stresses, result in the mechanical degradation [14, 15]. The increasing microcracks and smaller fragmented particles have been reported during cycling [16]. Parts of the particles may be detached from the binder, and due to the missing electron supply electrochemical reaction cannot happen. In other words, these parts become inactive and cannot host or release Lithium, which explains partially the capacity fade. Moreover, the Lithium deintercalation in LiFePO_4 nanoparticles can lead to the phase transformation, which can cause the strain mismatch [17].

Moreover, the microcracks generation at the grain boundary (GB) and intergranular cleavage during cycling has been widely reported [18, 19, 13]. The meatball structure of NMC cathode particles shown in Fig. 1.3 is known to experience disassembling or fragmentation. In contrast to the radial major cracking reported in the homogeneous particles, peripheral cracking or partial surface layer detachment (Fig. 1.3 (b) and (d)) have been observed in the meatball structure [19, 13, 20, 21]. The understanding of these unique features is rather limited. We believe they are closely related to the interface ion transport and interface damage. However, there is very few chemo-mechanical interface damage model and simulation available in the literature. Part of this thesis

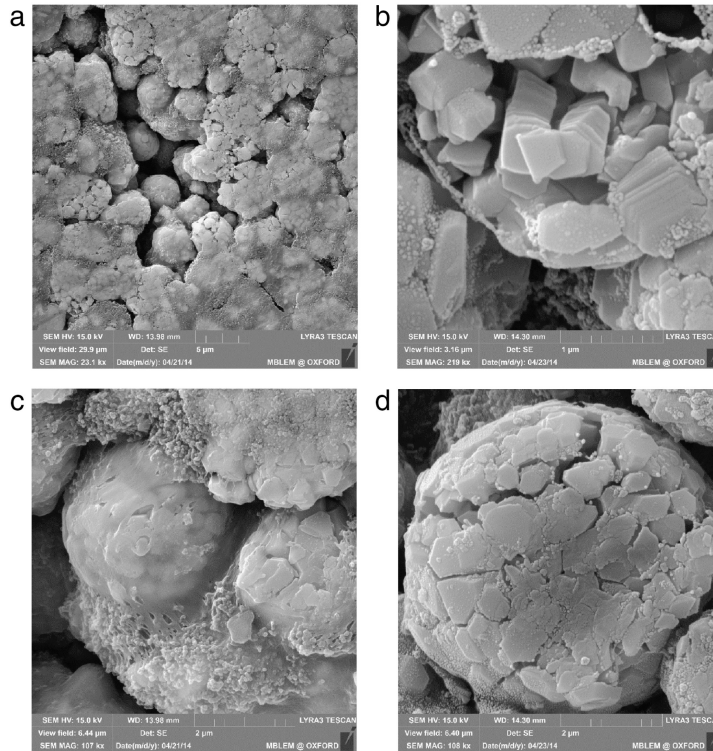


Figure 1.3: SEM morphologies of the precursors NMC: (a) overall low magnification view of the NMC cathode (b) high magnification view of the NMC particle, where the periphery revealing the individual grains (primary particles) in the form of 'stacks' of hexagonal plates (c) medium resolution imaging of the as-fabricated secondary particle before cycling (d) the presence of peripheral cracking in NMC particle after the first charge/discharge cycle (taken with permission from [13]).

confronts this challenge directly.

Besides degradation, mechanics has even large influence on the fundamental mechanisms in LIBs, particularly Li transport and electrochemical reactions, as shown in Fig. 1.2(b). The mechanical energy makes a contribution to the system free energy and thus to the chemical potential, which, in turn, regulates both the Li transport in the solid phases and the electrochemical reactions at the interfaces. It is known that in addition to the gradient chemical potential (or the gradient of the ion concentration in the case of dilute solution), the ion flux contains a drift contribution due to stress inhomogeneity. In the simple isotropic case, Li transport is sensitive to the gradient of

the hydrostatic pressure, since guest atoms tend to move to regions with sufficient space to accommodate them. Given purely elastic mechanical behavior, the outer layers of an electrode particle are compressed during intercalation, while its interior is stretched. Thus, the stresses can enhance lithium diffusion towards the interior of the particle, facilitating fast intercalation. This results in a change in surface concentration and hence in the chemical potential at the surface, which can in return impact the surface reactions and the surface screening effect, and thus the cell capacity. In phase-separating materials, the elastic energy contributions due to mismatch strains at the interface can outweigh the chemical energy contributions, resulting in a suppression of phase separation in the material. In nanostructured materials, surface effects become more prominent and can change the capacity and diffusivity of the particle through the surface tensions induced internal stresses. In summary, mechanics is thereby strongly correlated with the extrinsic features of the particles, such as size and shape. Understanding and controlling the effects of mechanics on fundamental mechanisms and degradation can guide optimal design of materials and composites for improving the performance and the durability of battery devices.

There are increasing work on multi-physics models involving the community of mechanics and electrochemistry [22, 23, 24, 11]. Whereby, the interplay between, e.g. the charge and mass transport, the electrochemical reaction, and also the mechanical fracture have been investigated in these theoretical works. Due to the complexity of the LIBs system, models have been formulated and focused on different scales with different aims.

For instance, at the cell level, models mainly focus on the transport of Li^+ ions and the prediction of cell performance. The pseudo-two-dimensional (P2D) model was first presented by Dolye et. al. [25, 26, 27] to estimate the electrochemical performance of LIBs with a half-cell structure, where the one dimensional transport from the Lithium anode through the separator into the cathode was modeled macroscopically based on the concentrated solution theory as well as the porous electrode theory [28], and where the kinetics of Lithium diffusion inside the cathode particles was simplified as 1D case along the radius direction for the symmetry of the spherical particles. Meanwhile, the electrochemical interaction between the active particles and electrolyte was successfully described via the Bultler–Volmer relation [29] in the P2D model. Later on, this model has been extended to consider the full cell [30]. Christensen et al. [31] combined the P2D model with their diffusion induced stress model to study the stresses generated during the galvanostatic operation, the significant impact of the pressure diffusion and lattice distortion on the cell performance has been confirmed. Moreover, the phase transformation inside the spherical particle also been modeled by Renganathan et al. [32]. Golmon et al. [33] extended the P2D model based on the multiscale approach, where

the mechanical response between the cell and active particles was coupled through the Mori–Tanaka (M–T) homogenization approach [34]. Later on, the thermal effect [35] and also the nickel-manganese-cobalt (NMC) particle with realistic 3D microstructures which were reconstructed from FIB-SEM and synchrotron X-ray tomography [36] have been studied.

On the particle level, the electro-chemo-mechanical models provide more insights in understanding the diffusion of Lithium, phase transformation, and also the grain boundary cracking. A mathematical model has been presented by Christensen et al. [37] to study the volume expansion and stress evolution of the isotropic spherical particles due to the Lithium insertion and extraction. Zhang et al. [38] developed a chemo-mechanical model to study the intercalation–induced stresses inside spherical and ellipsoidal LiMn_2O_4 particles. Later, Stein et al. [39] modified the Butler–Volmer relation to account for the chemo-mechanical interaction, where the impact of the surface tension on the electrochemical behavior of nanoscale spherical and ellipsoidal particles has also been investigated. The Cahn–Hilliard–type diffusion behavior inside the particle for the hyperelastic solids has been successfully studied by Zhao and Xu [40] via a mechanically coupled phase-field model. Later, this model has been successfully applied to study the fracture of LiMn_2O_4 particles [41]. Besides the single particle case, the fracture of polycrystalline materials like NMC has been investigated via a electro-chemo-mechanically coupled model presented by Wu and Lu [42]. Moreover, the cohesive zone model (CZM) have been widely used to study the crack initiation and propagation at the GBs (interface) between primary grains in NMC materials [43, 44, 21, 45, 13].

Though the aforementioned studies provided very useful insights on the crack propagation inside polycrystalline NMC, a chemo-mechanical grain boundary (GB) or interface model and the related numerical simulations are still missing. It is known that grain boundaries influence the ion transport path. The chemical process and the mechanical degradation of grain boundaries go hand-in-hand: the enhanced intergranular chemical inhomogeneity challenges the GB mechanical strength, while the GB damage influences in return the across grain ion transport as it is sensitive to or can be even blocked by GB delamination. The study on the influence of such degradation on the cell performance is also very limited, because most cell models assume very simple chemo-mechanical particle models.

1.3 Goal and outline

The goal of this thesis is to understand the chemo-mechanical interplay inside the cathode materials with internal interfaces as shown in Fig. 1.2(b), and to develop a

two-level simulation platform to study the influence of such chemo-mechanical interplay in the particles on the cell performance.

To derive a chemo-mechanically coupled bulk and interface model, the thesis extends first the thermodynamically consistent chemo-mechanical phase-field bulk model by considering additionally the internal work done at the internal interfaces, as well as the mass conservation across the interfaces. Thereby the nonlinear kinematics for large deformation, hyperelasticity, phase separation, and a potential-based cohesive law have been considered. As an application example, finite element simulations based on the model have been carried out on the NMC polycrystalline or meatball particles.

Moreover, on the basis of the P2D model, a two-level finite element simulation platform is proposed, which combine the cell model and the particle model with the most recent advances. The two-level model takes the advantages of both the cell model (e.g. numerical access to the cell performance and efficiency) and those of the particle models (e.g. chemo-mechanical diffusion, complex particle geometry, and consideration of the defects in the particles such as internal interfaces). Strategies is also proposed to further improve the computational efficiency.

Particularly, the model presented in this thesis includes the following aspects:

- The thermodynamically consistent framework is presented for both the grains and grain boundaries (GBs).
- The constitutive laws for the grains and GBs are derived from the system free energy.
- The across-GB interaction for both the transport of Lithium and also the traction-separation law is presented.
- The phase-separation and also the shapes of the particle have been considered, and their impact on the cell performance has been studied.
- A two-level simulation framework has been presented to incorporate the multi-physics model on the particle level to study the cell performance.

The remaining part of the thesis is organized as follows. In Chapter 2, the thermodynamically consistent model is presented for grains and grain boundaries. The models are developed to be as general as possible, instead of being confined to one particular material or electrode, the equations are developed for any choice of energy materials. The proposed two-level simulation platform is presented in the Chapter 3. Then, the details for the finite element implementation of the new particle model and the two-level

finite element implementations of the particle-cell coupling are presented in Chapter 4. The last chapter outlines the published work related to the thesis.

Even though the motivation of this thesis is the mechanically coupled issues in LIB electrode particles with internal interfaces and its influence on the cell performance, the essential knowledge and methodology are closely applicable to other battery chemistries such as Na-ion or Mg-ion batteries. In a more general sense, they are also helpful to understand the role of mechanics in other energy conversion and storage processes and in materials which involve diffusion and deformation or fracture.

2 Chemo-Mechanical Model for Particles with Interface

In this chapter, a thermodynamically consistent framework in the finite deformation region is first presented for both the grains and grain boundaries (GBs). Based on this framework, the chemical and mechanical processes are regarded in a fully coupled manner. Constitutive laws and coupled diffusion equations are derived for the grains and interfaces consistently from the system free energies. In particular, a chemo-mechanical interface model, which includes both the damage-dependent interface transport and a cohesive traction-separation law for mechanical degradation, is presented.

The model derived in this chapter is implemented with the finite element method, and implementation details can be found in the related section in Chapter 4. It serves as the basis of the finite element simulations in Publication A. Though the simulation examples are battery electrode materials, the proposed chemo-mechanical bulk and interface model is applicable to polycrystalline ion conductors.

2.1 Kinematics

The insertion and extraction of Li to the host material can involve the diffusion of species, as well as the volumetric swelling and shrinkage, which can cause the stresses and even the cracks for the mechanical failure. Therefore, the lithiation and delithiation process of the electrode materials naturally involve the interplay of chemo-mechanical coupling. Moreover, the energy materials can exhibit the polycrystalline structure, i.e., the secondary NMC particle contains hundred primary particles, as shown in Fig. 2.1. To this end, a thermodynamically consistent framework is presented to study the chemo-mechanical interplay in both the grains and the grain boundaries.

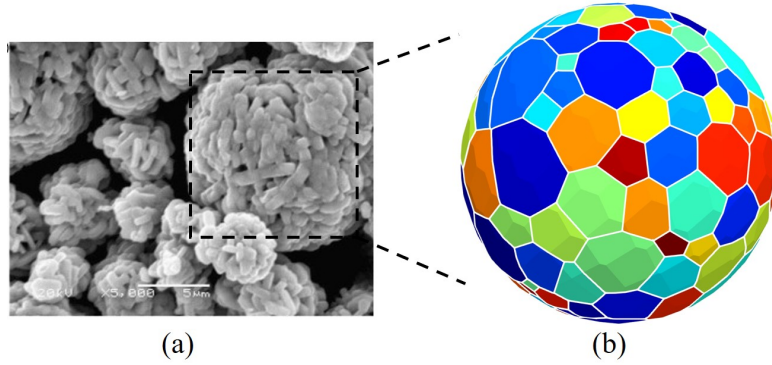


Figure 2.1: (a) SEM image for NMC cathode materials (taken with permission from [11]), (b) Schematic illustration of the single NMC particle.

2.1.1 The motion of grains

In order to make our model as general as possible, let us consider the commonly used electrode particle as a macroscopically homogeneous body \mathcal{B} with space it occupies in a fixed reference configuration. Therefore, the illustration of the particle can be considered as a body \mathcal{B} , which contains n non-overlapped subdomains. Wherein each subdomain accounts for the arbitrary individual grain, namely \mathcal{B}_i , in the reference body \mathcal{B} , as shown in Fig. 2.2. Therefore, for the arbitrary particle with a polycrystalline structure, one can have $\mathcal{B} = \cup_{i=1}^n \mathcal{B}_i$. While for the single-particle case, n can be reduced to $n \equiv 1$, namely the single-grain case.

Following the definition of modern continuum theory [46, 47], the motion of an arbitrary material point \mathbf{X} of the body \mathcal{B} can be described by the following smooth one-to-one mapping:

$$\mathbf{x} = \boldsymbol{\chi}(\mathbf{X}, t) = \mathbf{X} + \mathbf{U}, \quad (2.1)$$

where \mathbf{x} denotes the spatial position in the deformed (current) configuration at time t , and where $\mathbf{U}(\mathbf{X}, t)$ and \mathbf{X} are the displacement field and its related spatial position in the undeformed (reference) configuration, respectively. To this end, the related deformation gradient tensor $\mathbf{F}(\mathbf{X}, t)$ of material point \mathbf{X} can be written out as follows:

$$\mathbf{F}(\mathbf{X}, t) = \frac{\partial \boldsymbol{\chi}(\mathbf{X}, t)}{\partial \mathbf{X}} = \frac{\partial \mathbf{X}}{\partial \mathbf{X}} + \frac{\partial \mathbf{U}}{\partial \mathbf{X}} = \mathbf{I} + \nabla \mathbf{U}, \quad (2.2)$$

where \mathbf{I} is the identity rank two tensor, and where $\nabla \mathbf{U}$ denotes the gradient of the displacement field in the reference configuration.

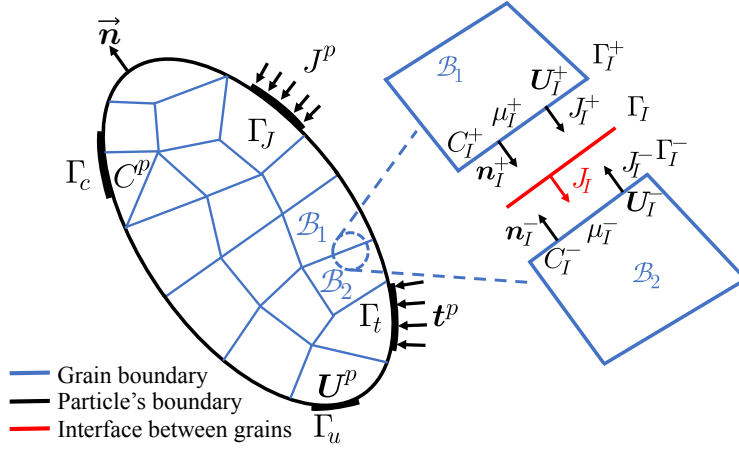


Figure 2.2: (Left) The schematic illustration of the NMC particle with multiple grains and GBs. (Right) The representing subdomain \mathcal{B}_1 and \mathcal{B}_2 with an interface Γ_I , where \vec{n}_I indicates the normal vector of the interface, while the GBs on each side are respectively denoted by (+) and (-).

Alternatively, denote by \mathbf{u} the displacement field described in the current configuration, the motion $\chi(\mathbf{x}, t)$ can also be stated as:

$$\mathbf{u}(\mathbf{x}, t) = \mathbf{x} - \mathbf{X}(\mathbf{x}, t), \quad (2.3)$$

then we can have the following expression:

$$\text{grad} \mathbf{u} = \text{grad} \mathbf{x} - \text{grad} \mathbf{X}(\mathbf{x}, t) = \mathbf{I} - \mathbf{F}^{-1}(\mathbf{x}, t), \quad (2.4)$$

where $d\mathbf{X} = \mathbf{F}^{-1}(\mathbf{x}, t)d\mathbf{x}$ denotes the transformation rule from the arbitrary spatial point to its related material point. In this thesis, we use grad and lap for the gradient and Laplace operators in the current (spatial) configuration. While ∇ and Δ are adopted for the related operators in the reference (material) configuration.

For the case with multiple successive deformations, for instance, suppose that two successive deformations are applied to the electrode particle, as shown in Fig. 2.3. Then we can have [48]:

$$d\mathbf{y} = \mathbf{F}^{(1)}d\mathbf{x} \quad d\mathbf{z} = \mathbf{F}^{(2)}d\mathbf{y}, \quad (2.5)$$

where $\mathbf{F}^{(1)} = \mathbf{y} \otimes \nabla_{\mathbf{x}}$ denotes the map from the original configuration to the first deformed shape, and where $\mathbf{F}^{(2)} = \mathbf{z} \otimes \nabla_{\mathbf{y}}$ represents the map from the first deformed shape to the second one. \otimes is the *dyad* operator. Then, by applying the chain rule [49,

50]:

$$dz_i = \frac{\partial z_i}{\partial y_j} \frac{\partial y_j}{\partial x_k} dx_k, \quad (2.6)$$

we can have the deformation gradient map that changes from the original configuration to the second one or the final one as follows:

$$dz = \mathbf{F} \cdot dx \quad \text{with} \quad \mathbf{F} = \mathbf{F}^{(2)} \cdot \mathbf{F}^{(1)}. \quad (2.7)$$

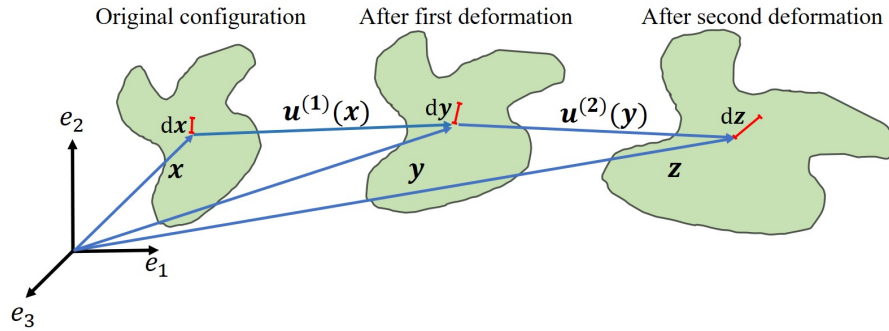


Figure 2.3: The change of a body under multiple successive deformations.

Therefore, for the chemo-mechanically coupled process of the electrode particle, we can split the deformation gradient tensor \mathbf{F} into the elastic distortion part \mathbf{F}_e as well as the volumetric (de-)swelling part \mathbf{F}_c as follows:

$$\mathbf{F} = \mathbf{F}_e \mathbf{F}_c \quad \text{with} \quad J = \det \mathbf{F} = J_e J_c, \quad (2.8)$$

and

$$\mathbf{F}_c = (J_c)^{\frac{1}{3}} \mathbf{I} \quad \text{with} \quad J_c = \det \mathbf{F}_c = 1 + \Omega C, \quad (2.9)$$

where \mathbf{F}_c represents the local distortion due to the volumetric swelling of the Lithium insertion and de-swelling of the extraction, and where J_c denotes the swelling stretch which is dependent on both the concentration of Lithium $C(\mathbf{X}, t)$ as well as the partial mole volume Ω in the reference configuration. \mathbf{F}_e denotes the subsequent stretching and rotation for the corresponding elastic distortion.

Similarly, the material velocity of an arbitrary material point in the body \mathcal{B} can be defined as follows:

$$\mathbf{V}(\mathbf{X}, t) = \frac{\partial \boldsymbol{\chi}(\mathbf{X}, t)}{\partial t} = \dot{\boldsymbol{\chi}}(\mathbf{X}, t), \quad (2.10)$$

and the time derivative of the deformation gradient tensor \mathbf{F} can be obtained as follows:

$$\dot{\mathbf{F}}(\mathbf{X}, t) = \frac{\partial}{\partial t} \left(\frac{\partial \boldsymbol{\chi}(\mathbf{X}, t)}{\partial \mathbf{X}} \right) = \frac{\partial}{\partial \mathbf{X}} \left(\frac{\partial \boldsymbol{\chi}(\mathbf{X}, t)}{\partial t} \right) = \frac{\partial \mathbf{V}}{\partial \mathbf{X}} = \nabla \mathbf{V}(\mathbf{X}, t), \quad (2.11)$$

then the spatial velocity gradient $\mathbf{l} = \text{grad} \mathbf{v}$ can be stated as follows:

$$\mathbf{l} = \frac{\partial \mathbf{v}}{\partial \mathbf{x}} = \frac{\partial \dot{\boldsymbol{\chi}}(\mathbf{X}, t)}{\partial \mathbf{X}} \frac{\partial \mathbf{X}}{\partial \mathbf{x}} = \frac{\partial}{\partial t} \left(\frac{\partial \boldsymbol{\chi}(\mathbf{X}, t)}{\partial \mathbf{X}} \right) \mathbf{F}^{-1} = \dot{\mathbf{F}} \mathbf{F}^{-1}. \quad (2.12)$$

Furthermore, based on Eqs. (2.8) and (2.9), one can have the time derivative of the deformation tensors as follows:

$$\dot{\mathbf{F}} = \dot{\mathbf{F}}_e \mathbf{F}_c + \mathbf{F}_e \dot{\mathbf{F}}_c, \quad (2.13)$$

then, by using Eq. (2.9), we can have the time derivative of the chemical distortion tensor \mathbf{F}_c as follows:

$$\dot{\mathbf{F}}_c = \frac{1}{3} J_c^{-\frac{2}{3}} \Omega \dot{\mathbf{C}} \mathbf{I}, \quad (2.14)$$

consequently, we can write out the velocity gradient tensor of the swelling part as follows:

$$\mathbf{l}_c = \dot{\mathbf{F}}_c \mathbf{F}_c^{-1} = \frac{1}{3} J_c^{-1} \Omega \dot{\mathbf{C}} \mathbf{I}. \quad (2.15)$$

In order to measure the strains in the reference configuration, we introduce the right Cauchy-Green tensor \mathbf{C} as follows:

$$\mathbf{C} = \mathbf{F}^T \mathbf{F} \quad \text{with} \quad \det \mathbf{C} = (\det \mathbf{F})^2 = J^2, \quad (2.16)$$

then the Green-Lagrange strain tensor \mathbf{E} can be written out as follows:

$$\mathbf{E} = \frac{1}{2} (\mathbf{F}^T \mathbf{F} - \mathbf{I}), \quad (2.17)$$

furthermore, we can write out the elastic Cauchy-Green deformation tensor \mathbf{C}_e and the elastic Green-Lagrange strain tensor \mathbf{E}_e as follows:

$$\mathbf{C}_e = \mathbf{F}_e^T \mathbf{F}_e \quad \mathbf{E}_e = \frac{1}{2} (\mathbf{F}_e^T \mathbf{F}_e - \mathbf{I}). \quad (2.18)$$

2.1.2 The motion of grain boundaries (GBs)

While for the grain boundaries (GBs), their motion can be described by the two neighboring domains, i.e. \mathcal{B}_1 and \mathcal{B}_2 , which are separated by a common interface (grain boundary) Γ_I in the reference configuration, as shown in Fig. 2.2. Similar to the grains (bulk), we denote by \mathbf{U}_I^\pm the displacement fields on the two sides of the interface, then the motion of these two GBs can be characterized as follows:

$$\mathbf{x}_I^\pm = \boldsymbol{\chi}_I^\pm = \mathbf{X}_I + \mathbf{U}_I^\pm \quad \text{on } \Gamma_I^\pm, \quad (2.19)$$

where \mathbf{x}_I^\pm are spatial positions of the upper GB Γ_I^+ and the lower GB Γ_I^- , respectively, and where \mathbf{U}_I^\pm respectively denote the displacement fields of these two GBs. \mathbf{X}_I represents an arbitrary material point at the interface. Then the displacement jump vector Δ of an arbitrary material point \mathbf{X}_I at the interface can be stated as:

$$\Delta = \mathbf{x}_I^+ - \mathbf{x}_I^- = \boldsymbol{\chi}_I^+ - \boldsymbol{\chi}_I^- = (\mathbf{X}_I + \mathbf{U}_I^+) - (\mathbf{X}_I + \mathbf{U}_I^-) = \llbracket \mathbf{U}_I \rrbracket, \quad (2.20)$$

where $\llbracket \mathbf{U}_I \rrbracket$ is the displacement jump vector at the interface. Following the same notation, the concentration at the two sides of the GBs can be denoted by C_I^+ and C_I^- , respectively. While μ_I^+ and μ_I^- respectively represent the chemical potentials at the upper and lower GBs. Moreover, as illustrated in Fig. 2.2, the flux at the two sides of the interface are denoted by \mathbf{J}_I^+ and \mathbf{J}_I^- respectively. Therefore, we can have the following relationships:

$$J_I = J_I^+ = -J_I^-, \quad (2.21)$$

$$J_I = \mathbf{J}_I \cdot \vec{\mathbf{n}}_I, \quad (2.22)$$

$$J_I^+ = \mathbf{J}_I^+ \cdot \vec{\mathbf{n}}_I^+, \quad (2.23)$$

$$J_I^- = \mathbf{J}_I^- \cdot \vec{\mathbf{n}}_I^-, \quad (2.24)$$

$$\vec{\mathbf{n}}_I = \vec{\mathbf{n}}_I^+ = -\vec{\mathbf{n}}_I^-, \quad (2.25)$$

where the mass conservation of Lithium at the interface is guaranteed by Eq. (2.21).

2.2 Governing equations

2.2.1 Mass conservation

As mentioned in Section 2.1, the concentration of Lithium in the reference configuration is described by $C(\mathbf{X}, t)$. Therefore, the changes of $C(\mathbf{X}, t)$ in a body \mathcal{B} can be

described by the diffusion of Lithium across its boundary $\partial\mathcal{B}$. To this end, the diffusion of Li inside the particle can be characterized by an external flux $\mathbf{J}(\mathbf{X}, t)$, which is defined as the number of moles of Lithium measured per unit reference area per unit time, such that

$$-\int_{\partial\mathcal{B}} \mathbf{J} \cdot \vec{\mathbf{n}} dA \quad (2.26)$$

represents the number of moles of Lithium entering \mathcal{B} across $\partial\mathcal{B}$ in a unit time. Therefore, by applying the Fick's second law [51, 52], the change of Lithium over time in the reference body \mathcal{B} can be stated as:

$$\int_{\mathcal{B}} \dot{C}(\mathbf{X}, t) dV = -\int_{\partial\mathcal{B}} \mathbf{J} \cdot \vec{\mathbf{n}} dA. \quad (2.27)$$

Then, by employing the divergence theorem [53, 54] to Eq. (2.27), we can have the following expression:

$$\int_{\mathcal{B}} \dot{C}(\mathbf{X}, t) dV + \int_{\mathcal{B}} \nabla \cdot \mathbf{J} dV = 0, \quad (2.28)$$

since this mass conservation law holds for the arbitrary point inside the body \mathcal{B} , we can write out the local balance law for Lithium as follows:

$$\dot{C}(\mathbf{X}, t) = -\nabla \cdot \mathbf{J}. \quad (2.29)$$

In order to find the solution of the concentration, the initial conditions and boundary conditions for the above equation are listed as below:

$$C = C_p \quad \text{on } \Gamma_c \times (0, \mathcal{T}), \quad (2.30)$$

$$\mathbf{J} \cdot \vec{\mathbf{n}} = J_p \quad \text{on } \Gamma_J \times (0, \mathcal{T}), \quad (2.31)$$

$$C(\mathbf{X}, 0) = C_0(\mathbf{X}) \quad \text{in } \mathcal{B} \times (0, \mathcal{T}), \quad (2.32)$$

$$\mathbf{J} \cdot \vec{\mathbf{n}}_I = J_I \quad \text{on } \Gamma_I \times (0, \mathcal{T}). \quad (2.33)$$

Eq. (2.30) represents the essential boundary condition, in which C_p indicates the prescribed concentration on the boundary Γ_c . Eq. (2.31) denotes the natural boundary condition, where J_p is the prescribed flux on Γ_J . The initial concentration C_0 is imposed on the Lithium concentration field $C(\mathbf{X}, t)$, which is given by Eq. (2.32). For the interface or the GBs, the continuity condition is given by the flux J_I in Eq. (2.33). It should be mentioned that, in this thesis, we mainly focus on the across-GB transport problem. The GB diffusion problem, as mentioned in Refs. [55, 56, 57], is beyond the scope of the current study and will be addressed in future work.

2.2.2 Mechanical equilibrium equation

Considering that the time scales for the mechanics' problem are much smaller than the one in the diffusion process, we neglect all the inertial effects and assume the quasi-static equilibrium condition for the body \mathcal{B} . Therefore, with the absence of body forces in any part of the body \mathcal{B} , the conservation of linear momentum can be stated as follows [58, 59, 47, 48]:

$$\nabla \cdot \mathbf{P} = \mathbf{0} \quad \text{in } \mathcal{B} \times (0, \mathcal{T}), \quad (2.34)$$

where \mathbf{P} is the first Piola-Kirchhoff stress tensor. Then the traction on the surface Γ_t can be written out as follows:

$$\mathbf{t}_p(\vec{\mathbf{n}}) = \mathbf{P} \cdot \vec{\mathbf{n}} \quad \text{on } \Gamma_t \times (0, \mathcal{T}), \quad (2.35)$$

with $\vec{\mathbf{n}}$ being the normal vector towards the outward surface of the body \mathcal{B} . The related boundary conditions for Eq. (2.34) are listed as below:

$$\mathbf{U} = \mathbf{U}_p \quad \text{on } \Gamma_u \times (0, \mathcal{T}), \quad (2.36)$$

$$\mathbf{P} \cdot \vec{\mathbf{n}} = \mathbf{t}_p \quad \text{on } \Gamma_t \times (0, \mathcal{T}), \quad (2.37)$$

$$\mathbf{P} \cdot \vec{\mathbf{n}}_I = \mathbf{t}^+ = -\mathbf{t}^- = \mathbf{t}_I \quad \text{on } \Gamma_I \times (0, \mathcal{T}), \quad (2.38)$$

where the prescribed displacement \mathbf{U}_p in Eq. (2.36) is given as the Dirichlet boundary condition, and where the prescribed traction \mathbf{t}_p in Eq. (2.37) is applied for the Neumann boundary condition. In Eq. (2.38), \mathbf{t}^+ and \mathbf{t}^- are the tractions on the upper and lower GBs, namely Γ_I^+ and Γ_I^- , respectively. \mathbf{t}_I represents the traction at the interface Γ_I . It should be mentioned that the traction \mathbf{t}_I is non-zero at the interface, but treated as zero elsewhere for the consideration of the traction free boundary conditions along the cracked surface.

Until now, we establish the governing equations for the chemo-mechanical coupling problem. However, the expressions of \mathbf{J} , J_I , \mathbf{P} and \mathbf{t}_I are still missing. In the next section, we will introduce the details of these physical quantities, namely the constitutive laws for our chemo-mechanically coupled framework.

2.3 Thermodynamics

In order to account for the chemo-mechanical interplay in both the grains (bulk) and GBs (interface), we treat each individual grain \mathcal{B}_i or the whole bulk domain \mathcal{B} and

also the interface (GBs) Γ_I as two independent thermodynamic systems. Therefore, the single-particle without any GBs can be easily regarded as a special case based on this framework.

By applying the quasi-static condition to the mechanical problem, the total kinetic energy \mathcal{K} can take the form as below:

$$\mathcal{K} = \int_{\mathcal{B}} \frac{1}{2} \rho \dot{\boldsymbol{\chi}} \cdot \dot{\boldsymbol{\chi}} dV \equiv 0. \quad (2.39)$$

Furthermore, by introducing the theory of microforce balance [60, 61, 62, 63, 46] to our framework, the related microscopic systems can be defined by:

1. a scalar microscopic stress $\bar{\omega}$ which expends the power over the change rate of the Lithium concentration \dot{C} ,
2. a vector microscopic stress $\boldsymbol{\xi}$ which expends the power over the gradient of the Lithium concentration change rate $\nabla \dot{C}$,
3. a scalar microscopic traction $\xi = \boldsymbol{\xi} \cdot \bar{\mathbf{n}}$ that expends the power over \dot{C} on the boundary.

It should be noted that the plastic deformation is not taken into consideration in our framework. Therefore, the scalar microscopic stress π that expends power over the equivalent plastic shear strain, as mentioned in Refs. [64, 60, 63], is treated as zero.

Therefore, the external expenditure of power for our polycrystalline particle can be written out as follows:

$$\begin{aligned} \mathcal{W}_{\text{ext}} &= \int_{\mathcal{B}} \mathbf{b} \cdot \dot{\boldsymbol{\chi}} dV + \int_{\partial \mathcal{B}} (\mathbf{P} \cdot \bar{\mathbf{n}}) \cdot \dot{\boldsymbol{\chi}} dS + \int_{\partial \mathcal{B}} \xi \cdot \dot{C} dS \\ &= \int_{\partial \mathcal{B}} (\mathbf{P} \cdot \bar{\mathbf{n}}) \cdot \dot{\boldsymbol{\chi}} dS + \int_{\partial \mathcal{B}} (\boldsymbol{\xi} \cdot \bar{\mathbf{n}}) \cdot \dot{C} dS \end{aligned} \quad (2.40)$$

Simultaneously, the corresponding internal expenditure of power with the mechanical contribution of GBs can be expressed as:

$$\begin{aligned} \mathcal{W}_{\text{int}} &= \int_{\mathcal{B}} \mathbf{S}_e : \dot{\mathbf{F}}_e dV + \int_{\mathcal{B}} \bar{\omega} \dot{C} dV + \int_{\mathcal{B}} \boldsymbol{\xi} \cdot \nabla \dot{C} dV + \int_{\Gamma_I^+} \mathbf{t}_I^+ \cdot \dot{\boldsymbol{\chi}}^+ d\Gamma + \int_{\Gamma_I^-} \mathbf{t}_I^- \cdot \dot{\boldsymbol{\chi}}^- d\Gamma \\ &= \int_{\mathcal{B}} \mathbf{S}_e : \dot{\mathbf{F}}_e dV + \int_{\mathcal{B}} \bar{\omega} \dot{C} dV + \int_{\mathcal{B}} \boldsymbol{\xi} \cdot \nabla \dot{C} dV + \int_{\Gamma_I} \mathbf{t}_I \cdot \dot{\boldsymbol{\Delta}} d\Gamma \end{aligned} \quad (2.41)$$

where \mathbf{S}_e denotes the stress tensor which is power-conjugated to the time derivative of the deformation tensor $\dot{\mathbf{F}}_e$. $\dot{\Delta}$ represents the time derivative of the displacement jump vector Δ , which can be read as:

$$\dot{\Delta} = \dot{\chi}_I^+ - \dot{\chi}_I^- = \dot{\mathbf{U}}_I^+ - \dot{\mathbf{U}}_I^- = \llbracket \dot{\mathbf{U}}_I \rrbracket, \quad (2.42)$$

where $\llbracket \dot{\mathbf{U}}_I \rrbracket$ represents the time derivative of the displacement jump defined in Eq. (2.20).

According to Refs. [61, 60], we can write out the definition of the stress tensor \mathbf{S}_e as follows:

$$\mathbf{S}_e = \mathbf{P}\mathbf{F}_c^T = J\boldsymbol{\sigma}\mathbf{F}_c^{-T} \quad \mathbf{P} = \mathbf{S}_e\mathbf{F}_c^{-T}, \quad (2.43)$$

where $\boldsymbol{\sigma}$ represents the Cauchy stress tensor. Therefore, the relationship between \mathbf{S}_e and the second Piola-Kirchhoff stress tensor \mathbf{S} [60] can be stated as follows:

$$J_c\mathbf{S} = \mathbf{F}_e^{-1}\mathbf{S}_e \quad \mathbf{S}_e : \dot{\mathbf{F}}_e = (J_c\mathbf{S}) : (\mathbf{F}_e^T\dot{\mathbf{F}}_e) = \frac{1}{2}(J_c\mathbf{S}) : \dot{\mathbf{C}}_e \quad \mathbf{S} = J_e\mathbf{F}_e^{-1}\boldsymbol{\sigma}\mathbf{F}_e^T. \quad (2.44)$$

Furthermore, we can write out the Mandel stress tensor \mathbf{M}_e as follows:

$$\mathbf{M}_e = \mathbf{C}_e\mathbf{S} = J_e\mathbf{F}_e^T\boldsymbol{\sigma}\mathbf{F}_e^{-T} \quad \mathbf{F}_e^T\mathbf{S}_e = J_c\mathbf{M}_e, \quad (2.45)$$

then, by using the second microscopic force balance in Ref. [60], the scalar microscopic stress $\bar{\omega}$ can be read as:

$$\bar{\omega} = \frac{\Omega}{3}\text{tr}(\mathbf{M}_e) + \nabla \cdot \boldsymbol{\xi}, \quad (2.46)$$

then, by substituting Eq. (2.44)₂ into Eq. (2.41), we can have:

$$\mathcal{W}_{\text{int}} = \int_{\mathcal{B}} \frac{1}{2}(J_c\mathbf{S}) : \dot{\mathbf{C}}_e dV + \int_{\mathcal{B}} \bar{\omega}\dot{\mathbf{C}} dV + \int_{\mathcal{B}} \boldsymbol{\xi} \cdot \nabla\dot{\mathbf{C}} dV + \int_{\Gamma_I} \mathbf{t}_I \cdot \dot{\Delta} d\Gamma. \quad (2.47)$$

Similarly, the thermal power \mathcal{Q}_b for the bulk can be stated as:

$$\mathcal{Q}_b = - \int_{\partial\mathcal{B}} \mathbf{q} \cdot \bar{\mathbf{n}} dS + \int_{\mathcal{B}} Q dV, \quad (2.48)$$

where \mathbf{q} represents the heat flux per unit reference area of the body \mathcal{B} , and where Q denotes the external heat supply per unit reference volume in \mathcal{B} . While for the GBs, we ignore the heat supply, thereby, the thermal power for the interface can be written out as follows:

$$\mathcal{Q}_I = - \int_{\Gamma_I^+} \mathbf{q}_I^+ \cdot \bar{\mathbf{n}}_I^+ d\Gamma - \int_{\Gamma_I^-} \mathbf{q}_I^- \cdot \bar{\mathbf{n}}_I^- d\Gamma = - \int_{\Gamma_I} \mathbf{q}_I \cdot \bar{\mathbf{n}}_I d\Gamma, \quad (2.49)$$

where \mathbf{q}_I is the heat flux per unit reference area of the interface (GBs). Therefore, the total thermal power of the whole system can be written out as follows:

$$\mathcal{Q} = \mathcal{Q}_b + \mathcal{Q}_I = - \int_{\partial\mathcal{B}} \mathbf{q} \cdot \vec{\mathbf{n}} dS + \int_{\mathcal{B}} Q dV - \int_{\Gamma_I} \mathbf{q}_I \cdot \vec{\mathbf{n}}_I d\Gamma, \quad (2.50)$$

Following the same procedure, the diffusion power for the transport of Li in the body \mathcal{B} can be written out as follow:

$$\mathcal{J} = - \int_{\partial\mathcal{B}} \mu \mathbf{J} \cdot \vec{\mathbf{n}} dS - \int_{\Gamma_I} \mu_I \mathbf{J}_I \cdot \vec{\mathbf{n}}_I d\Gamma, \quad (2.51)$$

where μ_I represents the chemical potential of Li at the interface, and where \mathbf{J}_I denotes the flux at the interface.

Thereby, the balance law for internal energy \mathcal{U} of the system can be found as [65, 66]:

$$\dot{\mathcal{U}} = \dot{\mathcal{U}}_b + \dot{\mathcal{U}}_I = \mathcal{W}_{\text{ext}} + \mathcal{Q} + \mathcal{J}, \quad (2.52)$$

where $\dot{\mathcal{U}}_b$ and $\dot{\mathcal{U}}_I$ respectively denote the time derivative of the internal energy density per unit mass associated with the bulk (grains) and the interface. Considering that, $\mathcal{W}_{\text{ext}} = \mathcal{W}_{\text{int}}$ must be held for an arbitrary part of the body \mathcal{B} , we can rewrite Eq. (2.52) as follows:

$$\begin{aligned} \dot{\mathcal{U}} &= \mathcal{W}_{\text{int}} + \mathcal{Q} + \mathcal{J} \\ &= \int_{\mathcal{B}} \frac{1}{2} (J_c \mathbf{S}) : \dot{\mathbf{C}}_e dV + \int_{\mathcal{B}} \bar{\omega} \dot{C} dV + \int_{\mathcal{B}} \boldsymbol{\xi} \cdot \nabla \dot{C} dV + \int_{\Gamma_I} \mathbf{t}_I \cdot \dot{\boldsymbol{\Delta}} d\Gamma \\ &\quad - \int_{\partial\mathcal{B}} \mathbf{q} \cdot \vec{\mathbf{n}} dS - \int_{\Gamma_I} \mathbf{q}_I \cdot \vec{\mathbf{n}}_I d\Gamma + \int_{\mathcal{B}} Q dV, \\ &\quad - \int_{\partial\mathcal{B}} \mu \mathbf{J} \cdot \vec{\mathbf{n}} dS - \int_{\Gamma_I} \mu_I \mathbf{J}_I \cdot \vec{\mathbf{n}}_I d\Gamma \end{aligned}, \quad (2.53)$$

On the other side, the bulk and interface are considered as two independent thermodynamics systems in our framework. Therefore, the second laws of thermodynamics for these two irreversible systems, namely the Clausius-Duhem inequality [67, 68, 69, 66, 70], can be stated in the following forms:

$$\int_{\mathcal{B}} \dot{\eta}_b dV \geq - \int_{\partial\mathcal{B}} \frac{\mathbf{q} \cdot \vec{\mathbf{n}}}{T} dS + \int_{\mathcal{B}} \frac{Q}{T} dV, \quad (2.54)$$

and for the interface

$$\int_{\Gamma_I} \dot{\eta}_I d\Gamma \geq - \int_{\Gamma_I} \frac{\mathbf{q}_I \cdot \vec{\mathbf{n}}_I}{T} d\Gamma, \quad (2.55)$$

where $\dot{\eta}_b$ and $\dot{\eta}_I$ denote the time derivative of the entropy density associated with the bulk (grains) and the interface between grains, respectively. Therefore, the entropy imbalance [71] of the whole system can be written out as follows:

$$\int_{\mathcal{B}} \dot{\eta} dV = \int_{\mathcal{B}} \dot{\eta}_b dV + \int_{\Gamma_I} \dot{\eta}_I d\Gamma \geq - \int_{\partial\mathcal{B}} \frac{\mathbf{q} \cdot \vec{\mathbf{n}}}{T} dS + \int_{\mathcal{B}} \frac{Q}{T} dV - \int_{\Gamma_I} \frac{\mathbf{q}_I \cdot \vec{\mathbf{n}}_I}{T} d\Gamma. \quad (2.56)$$

Since our chemo-mechanical coupling system is considered as an isothermal system and the temperature profile is smooth across the GBs, namely

$$T_I = T_I^+ = T_I^- = T, \quad (2.57)$$

where T_I^\pm denote the temperature at the upper and lower GBs and where T_I represents the temperature at the interface. Since no temperature jump is allowed at the interface, one can have:

$$T \equiv \text{constant} \quad \text{with} \quad \dot{T} \equiv 0, \quad (2.58)$$

thereby, by multiplying the entropy imbalance in Eq. (2.56) by T , we can have:

$$\int_{\mathcal{B}} \dot{\eta} T dV \geq - \int_{\partial\mathcal{B}} \mathbf{q} \cdot \vec{\mathbf{n}} dS - \int_{\Gamma_I} \mathbf{q}_I \cdot \vec{\mathbf{n}}_I d\Gamma + \int_{\mathcal{B}} Q dV. \quad (2.59)$$

Meanwhile, the Helmholtz free energy per unit reference volume can be defined by:

$$\Psi = \mathcal{U} - \eta T, \quad (2.60)$$

which can be split into the bulk part Ψ_b and the interface part Ψ_I as follows:

$$\Psi = \Psi_b + \Psi_I, \quad (2.61)$$

thereby, the energy conservation can be obtained via:

$$\dot{\Psi} = \dot{\Psi}_b + \dot{\Psi}_I = \dot{\mathcal{U}} - \dot{\eta} T - \eta \dot{T} = \dot{\mathcal{U}} - \dot{\eta} T. \quad (2.62)$$

Then, upon substituting Eqs. (2.53) and (2.62) into Eq. (2.59), we can have the Clausius-Planck inequality or the dissipation of the system as follows:

$$\begin{aligned} \mathcal{D} = & \int_{\mathcal{B}} \left[\frac{1}{2} (J_c \mathbf{S}) : \dot{\mathbf{C}}_e + \bar{\omega} \dot{C} + \boldsymbol{\xi} \cdot \nabla \dot{C} - \dot{\Psi}_b \right] dV - \int_{\partial\mathcal{B}} \mu \mathbf{J} \cdot \vec{\mathbf{n}} dS \\ & + \int_{\Gamma_I} [\mathbf{t}_I \cdot \dot{\boldsymbol{\Delta}} - \mu_I \mathbf{J}_I \cdot \vec{\mathbf{n}}_I - \dot{\Psi}_I] d\Gamma \geq 0 \end{aligned} \quad (2.63)$$

In order to formulate the equations for the bulk and interface independently, we decompose the total dissipation as $\mathcal{D} = \mathcal{D}_b + \mathcal{D}_I$. Then, by applying the divergence theorem to Eq. (2.63), the bulk dissipation \mathcal{D}_b can be written out as follows:

$$\begin{aligned}\mathcal{D}_b &= \int_{\mathcal{B}} \left[\frac{1}{2} (J_c \mathbf{S}) : \dot{\mathbf{C}}_e + \bar{\omega} \dot{C} + \boldsymbol{\xi} \cdot \nabla \dot{C} - \dot{\Psi}_b \right] dV - \int_{\partial \mathcal{B}} \mu \mathbf{J} \cdot \bar{\mathbf{n}} dS \\ &= \int_{\mathcal{B}} \left[\frac{1}{2} (J_c \mathbf{S}) : \dot{\mathbf{C}}_e + \bar{\omega} \dot{C} + \boldsymbol{\xi} \cdot \nabla \dot{C} - \dot{\Psi}_b \right] dV - \int_{\mathcal{B}} \nabla \cdot (\mu \mathbf{J}) dV \geq 0\end{aligned}\quad (2.64)$$

Since Eq. (2.64) must be held for an arbitrary point inside the body \mathcal{B} , then we can remove the volume integral $\int()dV$. Furthermore, by applying the mass conservation $\dot{C} + \nabla \cdot \mathbf{J} = 0$, we can rewrite Eq. (2.64) as follows:

$$\begin{aligned}\mathcal{D}_b &= \frac{1}{2} (J_c \mathbf{S}) : \dot{\mathbf{C}}_e + \bar{\omega} \dot{C} + \boldsymbol{\xi} \cdot \nabla \dot{C} - \dot{\Psi}_b + \mu \dot{C} - \mathbf{J} \cdot \nabla \mu \\ &= \frac{1}{2} (J_c \mathbf{S}) : \dot{\mathbf{C}}_e + \mu_{\text{net}} \dot{C} + \boldsymbol{\xi} \cdot \nabla \dot{C} - \dot{\Psi}_b - \mathbf{J} \cdot \nabla \mu \geq 0\end{aligned}\quad (2.65)$$

where the net chemical potential μ_{net} is defined as follows:

$$\mu_{\text{net}} = \mu + \bar{\omega}. \quad (2.66)$$

While for the interface, we assume the GB with an infinitely small width w . Thereby, we can have the following relationship:

$$\int_{\mathcal{B}_I} () dV = w \int_{\Gamma_I} () d\Gamma, \quad (2.67)$$

where \mathcal{B}_I denotes the "volume" of the interface. By applying a similar process as the bulk, together with the mass conservation at the interface

$$\dot{C}_I + \nabla \cdot \mathbf{J}_I = 0, \quad (2.68)$$

as well as the divergence theorem, the interface dissipation \mathcal{D}_I can be written out as follows:

$$\begin{aligned}\mathcal{D}_I &= \int_{\Gamma_I} \mathbf{t}_I \cdot \dot{\boldsymbol{\Delta}} d\Gamma - \int_{\Gamma_I} \mu_I \mathbf{J}_I \cdot \mathbf{n}_I d\Gamma - \int_{\Gamma_I} \dot{\Psi}_I d\Gamma \\ &= \int_{\Gamma_I} \mathbf{t}_I \cdot \dot{\boldsymbol{\Delta}} d\Gamma - \int_{\mathcal{B}_I} \nabla \cdot (\mu_I \mathbf{J}_I) dV - \int_{\Gamma_I} \dot{\Psi}_I d\Gamma \\ &= \int_{\Gamma_I} \mathbf{t}_I \cdot \dot{\boldsymbol{\Delta}} d\Gamma + \int_{\Gamma_I} w (\mu_I \dot{C}_I - \mathbf{J}_I \cdot \nabla \mu_I) d\Gamma - \int_{\Gamma_I} \dot{\Psi}_I d\Gamma \geq 0\end{aligned}\quad (2.69)$$

Since Eq. (2.69) is held for an arbitrary point at the interface, we can thereby remove the surface integration $\int()d\Gamma$, then the final expression of the interface dissipation can be stated as:

$$\mathcal{D}_I = \mathbf{t}_I \cdot \dot{\Delta} + w(\mu_I \dot{C}_I - \mathbf{J}_I \cdot \nabla \mu_I) - \dot{\Psi}_I \geq 0. \quad (2.70)$$

2.4 Constitutive laws and ion transport equations

For the fully coupled multi-physics process, the free energy of the bulk contains the contribution from the stresses as well as the species diffusion. Therefore, the bulk free energy per unit reference volume takes a form $\Psi_b = \Psi_b(\mathbf{C}_e, C, \nabla C)$. To this end, the time derivative of Ψ_b can be determined by the chain rule as follows:

$$\dot{\Psi}_b = \frac{\partial \Psi_b}{\partial \mathbf{C}_e} : \dot{\mathbf{C}}_e + \frac{\partial \Psi_b}{\partial C} \dot{C} + \frac{\partial \Psi_b}{\partial \nabla C} \cdot \nabla \dot{C}, \quad (2.71)$$

therefore, by substituting Eq. (2.71) into the bulk dissipation inequality, namely Eq. (2.65), we can have:

$$\mathcal{D}_b = \left(\frac{1}{2} J_c \mathbf{S} - \frac{\partial \Psi_b}{\partial \mathbf{C}_e} \right) : \dot{\mathbf{C}}_e + (\mu_{\text{net}} - \frac{\partial \Psi_b}{\partial C}) \dot{C} + \left(\boldsymbol{\xi} - \frac{\partial \Psi_b}{\partial \nabla C} \right) \cdot \nabla \dot{C} - \mathbf{J} \cdot \nabla \mu \geq 0. \quad (2.72)$$

Since Eq. (2.72) must be held for all admissible deformation and concentration at an arbitrary time point, then by employing the Coleman-Noll procedure [72, 73, 74], the expression for the second Piola-Kirchhoff stress tensor \mathbf{S} , the net chemical potential μ_{net} for the bulk, and the microscopic stress vector $\boldsymbol{\xi}$ can be written out as follows:

$$\mathbf{S} = \frac{1}{J_c} \frac{\partial \Psi_b}{\partial \mathbf{C}_e}, \quad (2.73)$$

and

$$\mu_{\text{net}} = \frac{\partial \Psi_b}{\partial C}, \quad (2.74)$$

and

$$\boldsymbol{\xi} = \frac{\partial \Psi_b}{\partial \nabla C}. \quad (2.75)$$

Then, by using the second microscopic force balance in Eq. (2.46) as well as the expression of the net chemical potential in Eq. (2.74), we can write out the final form of the chemical potential as follows:

$$\mu = \mu_{\text{net}} - \bar{\omega} = \frac{\partial \Psi_b}{\partial C} - \nabla \cdot \frac{\partial \Psi_b}{\partial \nabla C} - \frac{1}{3} \text{tr}(\mathbf{M}_e) \Omega. \quad (2.76)$$

Next, by substituting Eqs. (2.73) to (2.75) into Eq. (2.72), the bulk dissipation can be further reduced:

$$\mathcal{D}_b = -\mathbf{J} \cdot \nabla\mu \geq 0. \quad (2.77)$$

In order to ensure the positiveness of Eq. (2.77), a convex type dissipation potential ϕ_b of the bulk can be adopted such that [46]:

$$\mathbf{J} = -\frac{\partial\Phi_b}{\partial\nabla\mu}. \quad (2.78)$$

For the multiphysics coupling, the bulk dissipation potential function ϕ_b can be split into the mechanical part ϕ_b^e and the chemical part ϕ_b^c as follows:

$$\phi_b = \phi_b^e + \phi_b^c \quad \text{with} \quad \phi_b^e = f(\mathbf{S}), \quad (2.79)$$

in which $f(\mathbf{S})$ can be a function of the plastic deformation [75, 76, 75, 77], which is treated as zero in this thesis. According to the work presented in Refs. [78, 79, 80], the chemical dissipation potential function ϕ_b^c can be considered as follows:

$$\phi_b^c = \frac{1}{2}\mathbf{M}(C) : (\nabla\mu \otimes \nabla\mu), \quad (2.80)$$

where \otimes is the operator for the vector dyadic product, and where \mathbf{M} denotes the symmetric and positively defined mobility tensor, expressed as:

$$\mathbf{M}(C) = M(C)[\mathbf{N} \otimes \mathbf{N} + \zeta(\mathbf{I} - \mathbf{N} \otimes \mathbf{N})], \quad (2.81)$$

where \mathbf{N} denotes the unit normal vector to the crystallographic plane, and where ζ represents the degree of the anisotropy. In this thesis, the isotropic mobility is taken into consideration, namely $\zeta = 1$ is applied. Therefore, the isotropic mobility tensor can be written out as follows:

$$\mathbf{M}(C) = M(C)\mathbf{I}. \quad (2.82)$$

Then, by using Eqs. (2.78) and (2.80), we can have the expression for the flux in Eq. (2.29) as follows:

$$\mathbf{J} = -\frac{\partial\Phi_b}{\partial\nabla\mu} = -M(C)\mathbf{I}\nabla\mu = -M(C)\nabla\mu, \quad (2.83)$$

where the concentration dependent mobility of Lithium is considered as:

$$M(C) = \frac{D}{RT}C(1 - \bar{C}), \quad (2.84)$$

where R and T respectively denote the gas constant and temperature, and where D is the diffusion coefficient of Lithium inside the particle. $\bar{C} = C/C_{\max}$ represents the normalized concentration of Lithium and C_{\max} denotes the maximum concentration of Li that the host material can hold.

Following the same procedure as the bulk, the free energy density functional of the interface takes a form $\Psi_I = \Psi_I(C_I, \Delta)$. By applying the same process as the bulk to the interface, the time derivative of Ψ_I can be written out as follows:

$$\dot{\Psi}_I = \frac{\partial \Psi_I}{\partial \Delta} \cdot \dot{\Delta} + \frac{\partial \Psi_I}{\partial C_I} \dot{C}_I + \frac{\partial \Psi_I}{\partial \nabla C_I} \cdot \nabla \dot{C}_I. \quad (2.85)$$

By putting Eq. (2.85) into the interface dissipation, namely Eq. (2.70), we can obtain:

$$\mathcal{D}_I = (\mathbf{t}_I - \frac{\partial \Psi_I}{\partial \Delta}) \cdot \dot{\Delta} + (w\mu_I - \frac{\partial \Psi_I}{\partial C_I} + \nabla \cdot \frac{\partial \Psi_I}{\partial \nabla C_I}) \cdot \dot{C}_I - \mathbf{J}_I \cdot \nabla \mu_I \geq 0. \quad (2.86)$$

Then, by applying the Coleman-Noll procedure to Eq. (2.86), we can have the expressions for the traction \mathbf{t}_I at the interface and also the interface chemical potential μ_I as follows:

$$\mathbf{t}_I = \frac{\partial \Psi_I}{\partial \Delta}, \quad (2.87)$$

and

$$\mu_I = \frac{1}{w} \frac{\partial \Psi_I}{\partial C_I} - \frac{1}{w} \nabla \cdot \frac{\partial \Psi_I}{\partial \nabla C_I}. \quad (2.88)$$

Thus the interface dissipation \mathcal{D}_I can thereby be further reduced to:

$$\mathcal{D}_I = -\mathbf{J}_I \cdot \nabla \mu_I \geq 0. \quad (2.89)$$

Similar to the bulk, a convex type dissipation potential $\phi_I = \phi_I^e + \phi_I^c$ is adopted to ensure the positiveness of \mathcal{D}_I , in which the chemical dissipation potential ϕ_I^c is expressed as follows:

$$\phi_I^c = \frac{1}{2} M_I(C) \mathbf{I} : (\nabla \mu_I \otimes \nabla \mu_I), \quad (2.90)$$

where $M_I(C)$ denotes the mobility of the interface. Since the elastic dissipation potential ϕ_I^e is independent on μ_I , then the interface flux \mathbf{J}_I can be read as:

$$\mathbf{J}_I = -\frac{\partial \phi_I}{\partial \nabla \mu_I} = -\frac{\partial \phi_I^c}{\partial \nabla \mu_I} = -M_I(C) \nabla \mu_I. \quad (2.91)$$

2.5 Free energies

Phase separation has been widely reported in energy materials, such as crystalline Silicon [81], Antimony (Sb) and their oxides for anodes [5, 82], Li_xFePO_4 [17, 83, 84], $\text{Li}_x\text{Mn}_2\text{O}_4$ [85, 86, 87] and LiCo_2O_4 [88] for cathode materials. In order to account for the phase separation, the Cahn–Hilliard phase-field model presented in Refs. [89, 90] has been employed to investigate the diffusion of Lithium inside the particle. Thereby, in this section, the free energies with the consideration of phase separation as well as the mechanical deformation for the grains and GBs of polycrystalline materials are formulated.

2.5.1 Helmholtz free energy for the grains

Considering a lattice gas model of Lithium intercalation in host layered oxide, as shown in Fig. 2.4. We can assume a "lattice gas" of N indistinguishable finite-sized particles confined to the lattice with N_s available fixed lattice sites. Thus, the indistinguishable holes can be denoted by $N - N_s$. Therefore, for the "ideal solution" or "ideal mixture" case, the entropy of the system can be specified as follows [91, 92, 93]:

$$S = k_B \ln \Omega, \quad (2.92)$$

where k_B is the Boltzmann's constant, and where Ω denotes the number of distinguishable (degenerate) states of the system, expressed as follows:

$$\Omega = \binom{N_s}{N} = \frac{N_s!}{N!(N_s - N)!}. \quad (2.93)$$

Since N_s has the same magnitude as the Avogadro constant [94], we can use the Stirling approximation [95, 96]

$$\ln(A!) = A \ln(A) - A. \quad (2.94)$$

Next, by substituting Eqs. (2.93) and (2.94) into Eq. (2.92), we can write out the entropy S of the system as follows:

$$\begin{aligned} S &= k_B \{ \ln(N_s!) - \ln(N!) - \ln[(N_s - N)!] \} \\ &= k_B \{ N_s \ln(N_s) - N_s - N \ln(N) + N - (N_s - N) \ln(N_s - N) + (N_s - N) \} \\ &= k_B \{ N_s \ln(N_s) - N \ln(N) - (N_s - N) \ln(N_s - N) \} \\ &= k_B \{ N_s [\ln(N_s) - \ln(N_s - N)] + N [-\ln(N) + \ln(N_s - N)] \} \\ &= k_B \left\{ -N_s \ln\left(\frac{N_s - N}{N_s}\right) + N \ln\left(\frac{N_s - N}{N}\right) \right\} \end{aligned} \quad (2.95)$$

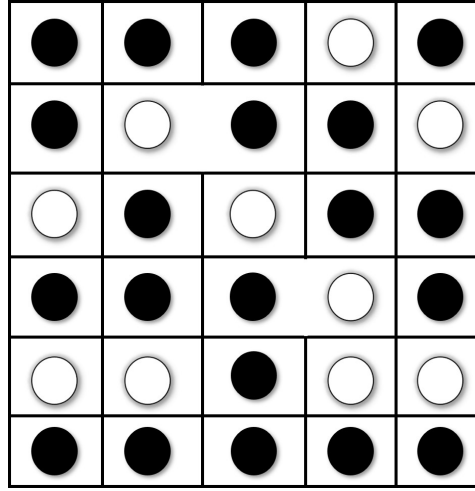


Figure 2.4: The lattice gas model, where the particles are denoted by the black color, while the white color represents the holes.

Furthermore, denoting by x the fraction of sites occupied by cations (the fraction of Lithium inside the particle):

$$x = \frac{N}{N_s}, \quad (2.96)$$

we can rewrite Eq. (2.95) as follows:

$$S = -k_B N_s \{x \ln(x) + (1 - x) \ln(1 - x)\}, \quad (2.97)$$

then the Gibbs free energy [97] per site can be written out as follows:

$$g = \frac{H - TS}{N_s} = h - Ts = h + k_B T \{x \ln(x) + (1 - x) \ln(1 - x)\}, \quad (2.98)$$

where H is the enthalpy and where h denotes the enthalpy per site. Simultaneously, s is defined as the entropy per site. Considering that the particle-hole repulsion can result in the immiscibility between the Li and its host, we introduce the enthalpic term as follows:

$$h = h_0 x(1 - x), \quad (2.99)$$

where h_0 represents the coefficient for the interaction between phases. Then the expression for the free energy per site can be stated as:

$$g = h_0 x(1 - x) + k_B T \{x \ln(x) + (1 - x) \ln(1 - x)\}. \quad (2.100)$$

Considering that, it is more common to determine the free energy per unit reference volume. Then, by applying the following relationships to Eq. (2.100):

$$R = k_B N_s \quad C = \frac{N}{N_s V}, \quad (2.101)$$

where C denotes the molar concentration of Lithium inside the particle and where V represents the volume of the particle. We can thereby write out the Gibbs free energy per unit reference volume as follows:

$$\Psi_b = \Psi_b^c = RTC_{\max} \{ \bar{C} \ln(\bar{C}) + (1 - \bar{C}) \ln(1 - \bar{C}) + \chi \bar{C}(1 - \bar{C}) \}, \quad (2.102)$$

where C_{\max} represents the maximum molar concentration of Lithium inside the particle, and where χ is the parameter for the intercalation between two phases. The single-phase system can be investigated by setting $\chi < 2$, while for the coexistence of the two-phases system, $\chi > 2$ is adopted. Following the work presented in Ref. [89], the final expression for the free energy with the consideration of interfacial energy contribution can be stated as follows:

$$\Psi_b = \Psi_b^c + \Psi_b^i = RTC_{\max} \{ \bar{C} \ln(\bar{C}) + (1 - \bar{C}) \ln(1 - \bar{C}) + \chi \bar{C}(1 - \bar{C}) \} + C_{\max} \frac{1}{2} \kappa |\nabla C|^2, \quad (2.103)$$

where κ is the gradient energy coefficient which is proportional to the thickness of the interface.

As mentioned in Section 1.1, during (de-)lithiation process, the electrode can experience changes in lattice dimensions as well as crystal structures, which are associated with overall volume changes and phase transformation. Besides, the formation of the two-phases system can result in high stresses, in particular at the phase interface. Therefore, in order to account for the large deformation of electrodes, the hyperelastic strain energy density is introduced [40, 98, 99]:

$$\Psi_b^e(C, \mathbf{C}_e) = J_c \left[\frac{K}{2} (J_e - 1)^2 + \frac{G}{2} (\bar{I}_1 - 3) \right], \quad (2.104)$$

where

$$\bar{I}_1 = \text{tr}(\bar{\mathbf{C}}_e) = J^{-\frac{2}{3}} \text{tr}(\mathbf{C}_e), \quad (2.105)$$

is the modified invariant, following the standard definition of the continuum mechanics [47]. Thereby, the Helmholtz free energy for the bulk as mentioned in Section 2.3

can be written out as follows:

$$\begin{aligned}\Psi_b &= \Psi_b^c + \Psi_b^i + \Psi_b^e \\ &= RT C_{\max} \{ \bar{C} \ln(\bar{C}) + (1 - \bar{C}) \ln(1 - \bar{C}) + \chi \bar{C} (1 - \bar{C}) \} + C_{\max} \frac{1}{2} \kappa |\nabla C|^2. \quad (2.106) \\ &+ J_c \left[\frac{K}{2} (J_e - 1)^2 + \frac{G}{2} (\bar{I}_1 - 3) \right]\end{aligned}$$

Then, by applying Eqs. (2.73) and (2.76), we can have the stress and the chemical potential as follows:

$$\mathbf{S} = \frac{1}{J_c} \frac{2\partial\Psi_b}{\partial\mathbf{C}_e} = [K J_e (J_e - 1) \mathbf{C}_e^{-1} + G J^{-\frac{2}{3}} (\mathbf{1} - \frac{1}{3} I_1 \mathbf{C}_e^{-1})], \quad (2.107)$$

and

$$\begin{aligned}\mu &= \frac{\partial\Psi_b}{\partial C} + \nabla \cdot \frac{\partial\Psi_b}{\partial\nabla C} - \frac{1}{3} \text{tr}(\mathbf{M}_e) \Omega \\ &= RT [\ln \bar{C} - \ln(1 - \bar{C}) + \chi(1 - 2\bar{C})] - \kappa \nabla^2 \bar{C}. \quad (2.108) \\ &+ \frac{\Omega K}{2} [1 - (J^e)^2] + \frac{\Omega G}{2} (\bar{I}_1 - 3) - \frac{1}{3} \Omega \text{tr}(\mathbf{M}_e)\end{aligned}$$

Wherein, the chemical potential μ can be split into the chemical part μ^c , the interfacial part μ^i and the mechanical part μ^e , defined as follows:

$$\mu^c = RT [\ln \bar{C} - \ln(1 - \bar{C}) + \chi(1 - 2\bar{C})], \quad (2.109)$$

$$\mu^i = -\kappa \nabla^2 \bar{C}, \quad (2.110)$$

$$\mu^e = \frac{\Omega K}{2} [1 - (J^e)^2] + \frac{\Omega G}{2} (\bar{I}_1 - 3) - \frac{1}{3} \Omega \text{tr}(\mathbf{M}_e). \quad (2.111)$$

2.5.2 Helmholtz free energy for interfaces

The intergranular cracking or the grain boundary (GB) cracking has been widely reported in polycrystalline materials [100, 101, 13]. Furthermore, the cracks of primary particles can lead to newly opened surfaces, deteriorate the layer-to-cubic phase transformation during cycling, thus the capacity becomes worse [102, 103]. Moreover, the insertion of Lithium into the particle can lead to the lattice expansion and volume change, which can cause both the normal and tangential failure at the GBs. Meanwhile, the cracks at the GBs can cut off the flux, weak the transport of Lithium across the GBs. Thereby, in order to investigate the impact of the interfacial debonding on the GBs as well as the Lithium transport across the GBs, a degradation function $g(d)$ is introduced

at the interface. Moreover, once the damage occurs, the stiffness of the cohesive element can be subsequently reduced even on the unloading state. Thus the interface Helmholtz free energy can be defined as follows:

$$\Psi_I = g(d)\Psi_I^e(\mathbf{\Delta}) + g(d)\Psi_I^c(C_I, \mu_I), \quad (2.112)$$

where the interface free energy for the mechanical contribution is introduced as the cohesive-zone energy, namely $\Psi_I^e = \Psi_{CZM}$. While $\Psi_I^c(C_I, \mu_I)$ is the chemical free energy contribution due to the transport of Lithium across the GB. Moreover, we introduce d as the damage state variable for the irreversible fracture of the GBs. To account for the mixed-mode failure and also the flexibility of modeling different fracture behavior of materials, i.e. brittle, quasi-brittle and ductile materials, the PPR model has been used. For more details, one is referred to the work presented in Refs. [104, 105, 106]. The mechanical free energy for the interface can thereby be expressed as follows [104, 105, 106]:

$$\begin{aligned} \Psi_{CZM}(\mathbf{\Delta}) = \Psi_{CZM}(\Delta_n, \Delta_t) = & \min(\phi_n, \phi_t) \\ & + [\Gamma_n(1 - \frac{\Delta_n}{\Delta_t})^\alpha (\frac{m}{\alpha} + \frac{\Delta_n}{\delta_n})^m + \langle \phi_n - \phi_t \rangle], \\ & \cdot [\Gamma_t(1 - \frac{|\Delta_t|}{\delta_t})^\beta (\frac{n}{\beta} + \frac{|\Delta_t|}{\delta_t})^n + \langle \phi_t - \phi_n \rangle] \end{aligned} \quad (2.113)$$

where ϕ_n and ϕ_t represent the fracture energies for the normal and tangential failures, respectively. $\mathbf{\Delta} = [\Delta_n, \Delta_t]$ is the displacement jump vector in the local coordinates (n, s) . It should be mentioned that, $\mathbf{\Delta}$ in Eq. (2.20) is defined in global coordinates, namely \mathbf{X} or (X, Y, Z) in cartesian coordinates, which is different from the one used in Eq. (2.113). Accordingly, Δ_n and Δ_t being the normal and tangential displacement jumps, respectively. δ_n and δ_t are the normal and tangential final crack opening widths, respectively. $\langle \cdot \rangle$ denotes the *Macaulay bracket*, which can be defined as follows:

$$\langle x \rangle = \begin{cases} 0 & x < 0 \\ x & x \geq 0 \end{cases}. \quad (2.114)$$

Γ_n and Γ_t are the related energy constants, which can be obtained as follows:

$$\Gamma_n = \begin{cases} (-\phi_n)^{\frac{\langle \phi_n - \phi_t \rangle}{\phi_n - \phi_t}} (\frac{\alpha}{m})^m & \phi_n \neq \phi_t \\ -\phi_n (\frac{\alpha}{m})^m & \phi_n = \phi_t \end{cases} \quad \Gamma_t = \begin{cases} (-\phi_t)^{\frac{\langle \phi_t - \phi_n \rangle}{\phi_t - \phi_n}} (\frac{\beta}{n})^n & \phi_n \neq \phi_t \\ (\frac{\beta}{n})^n & \phi_n = \phi_t \end{cases}, \quad (2.115)$$

where m and n are the non-dimensional exponents, defined as follows:

$$m = \frac{\alpha(\alpha - 1)\lambda_n^2}{(1 - \alpha\lambda_n^2)} \quad n = \frac{\beta(\beta - 1)\lambda_t^2}{(1 - \beta\lambda_t^2)}, \quad (2.116)$$

Here we introduce the variables α and β as the shape parameters in Eq. (2.116) to account for different material softening responses, for instance, $\alpha, \beta < 2$ can be used for the plateau type, while for the quasi-brittle material, $\alpha, \beta > 2$ are adopted. The related traction-separation profiles are shown in Fig. 2.5. Furthermore, λ_n and λ_t are given as the initial slope indicators, which are the ratio of the critical crack opening width δ_{nc}, δ_{tc} to the final crack opening width δ_n, δ_t , therefore, we can have:

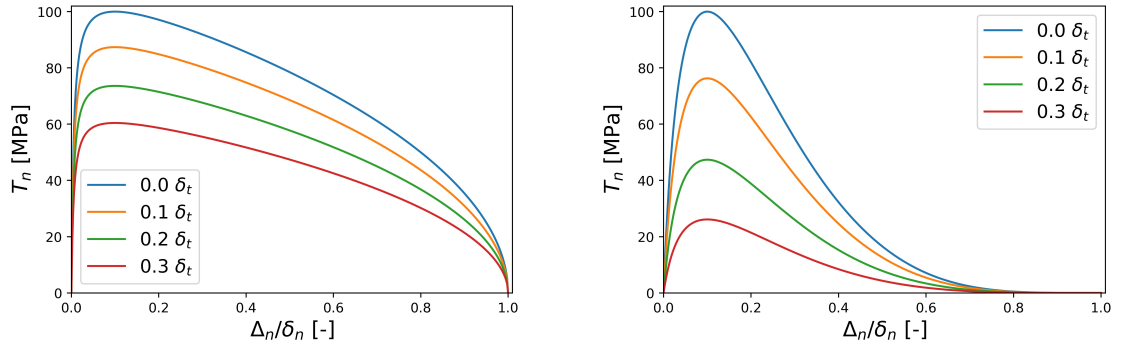
$$\lambda_n = \delta_{nc}/\delta_n \quad \lambda_t = \delta_{tc}/\delta_t. \quad (2.117)$$

Next, by applying the normal and tangential cohesive strengths σ_{\max} and τ_{\max} , the final crack opening width δ_n and δ_t can be expressed as follows:

$$\delta_n = \frac{\phi_n}{\sigma_{\max}} \alpha \lambda_n (1 - \lambda_n)^{\alpha-1} \left(\frac{\alpha}{m} + 1\right) \left(\frac{\alpha}{m} \lambda_n + 1\right)^{m-1}, \quad (2.118)$$

and

$$\delta_t = \frac{\phi_t}{\tau_{\max}} \beta \lambda_t (1 - \lambda_t)^{\beta-1} \left(\frac{\beta}{n} + 1\right) \left(\frac{\beta}{n} \lambda_t + 1\right)^{n-1}. \quad (2.119)$$



(a) $\alpha, \beta = 1.5$ for the plateau type

(b) $\alpha, \beta = 5.0$ for the convex type

Figure 2.5: The traction-separation law (TSL) under different α, β , with $\phi_n = \phi_t = 4 \frac{\text{J}}{\text{m}}, \lambda_n = \lambda_t = 0.1, \sigma_{\max} = \tau_{\max} = 100 \text{MPa}$.

Considering that, the total displacement jump vector Δ can be decomposed into the normal and tangential part as follows:

$$\begin{aligned}\Delta &= \Delta_n + \Delta_t \\ \Delta_n &= (\vec{n}_I \otimes \vec{n}_I)\Delta \quad \Delta_n = \Delta \cdot \vec{n}_I, \\ \Delta_t &= \Delta - \Delta_n \quad \Delta_t = \Delta \cdot \vec{s}_I\end{aligned}\quad (2.120)$$

where \vec{s}_I is the vector of tangential direction. Moreover, since $\Psi_I^e(C_I, \mu_I)$ is independent on the displacement jump, we can thereby write out the traction vector as follows:

$$\mathbf{t}_I = \frac{\partial \Psi_I}{\partial \Delta} = \frac{\partial \Psi_I^e}{\partial \Delta} = T_n \vec{n}_I + T_t \vec{s}_I, \quad (2.121)$$

therefore, by using Eqs. (2.87) and (2.120), the traction vector $\mathbf{t}_I = [T_n, T_t]$ can thus be obtained from the derivative of the interfacial energy as follows:

$$\begin{aligned}T_n(\Delta_n, \Delta_t) &= \frac{\partial \Psi_I}{\partial \Delta_n} = g(d) \frac{\partial \Psi_{CZM}}{\partial \Delta_n} = g(d) \frac{\partial \Psi_I^e}{\partial \Delta_n} \\ &= g(d) \frac{\Gamma_n}{\delta_n} \left[m \left(1 - \frac{\Delta_n}{\delta_n} \right)^\alpha \left(\frac{m}{\alpha} + \frac{\Delta_n}{\delta_n} \right)^{m-1} - \alpha \left(1 - \frac{\Delta_n}{\delta_n} \right)^{\alpha-1} \left(\frac{m}{\alpha} + \frac{\Delta_n}{\delta_n} \right)^m \right], \\ &\quad \cdot \left[\Gamma_t \left(1 - \frac{|\Delta_t|}{\delta_t} \right)^\beta \left(\frac{n}{\beta} + \frac{|\Delta_t|}{\delta_t} \right)^n + \langle \phi_t - \phi_n \rangle \right]\end{aligned}\quad (2.122)$$

and

$$\begin{aligned}T_t(\Delta_n, \Delta_t) &= \frac{\partial \Psi_I}{\partial \Delta_t} = g(d) \frac{\partial \Psi_{CZM}}{\partial \Delta_t} = g(d) \frac{\partial \Psi_I^e}{\partial \Delta_t} \\ &= g(d) \frac{\Gamma_t}{\delta_t} \left[n \left(1 - \frac{|\Delta_t|}{\delta_t} \right)^\beta \left(\frac{n}{\beta} + \frac{|\Delta_t|}{\delta_t} \right)^{n-1} - \beta \left(1 - \frac{|\Delta_t|}{\delta_t} \right)^{\beta-1} \left(\frac{n}{\beta} + \frac{|\Delta_t|}{\delta_t} \right)^n \right], \\ &\quad \cdot \left[\Gamma_n \left(1 - \frac{\Delta_n}{\delta_n} \right)^\alpha \left(\frac{m}{\alpha} + \frac{\Delta_n}{\delta_n} \right)^m + \langle \phi_n - \phi_t \rangle \right] \frac{\Delta_t}{|\delta_t|}\end{aligned}\quad (2.123)$$

For the 3D case, the tangential jump contains two components, namely Δ_{t_1} and Δ_{t_2} , thus we can have:

$$\Delta_t = \sqrt{\Delta_{t_1}^2 + \Delta_{t_2}^2}, \quad (2.124)$$

and

$$\frac{\partial}{\partial \Delta_{t_1}} = \frac{\partial}{\Delta_t} \frac{\partial \Delta_t}{\partial \Delta_{t_1}} \quad \frac{\partial}{\partial \Delta_{t_2}} = \frac{\partial}{\Delta_t} \frac{\partial \Delta_t}{\partial \Delta_{t_2}}. \quad (2.125)$$

Therefore, the shear traction in 3D case can be obtained via:

$$T_{t_1} = T_t(\Delta_n, \Delta_t) \frac{\Delta_{t_1}}{\Delta_t} \quad T_{t_2} = T_t(\Delta_n, \Delta_t) \frac{\Delta_{t_2}}{\Delta_t}. \quad (2.126)$$

Furthermore, the interface debonding is determined by the displacement jump. To this end, the complete normal failure occurs when the normal separation Δ_n reaches the final crack opening width δ_n . Simultaneously, the complete tangential failure happens when $\Delta_t = \delta_n$. In this work, the fracture of the interface is a combination of both the normal and tangential failure. Therefore, the mode-mixity for GB cracking can be considered by the effective displacement jump Δ_{eff} , which is defined as follows:

$$\Delta_{\text{eff}} = \sqrt{\Delta_n^2 + \Delta_t^2}. \quad (2.127)$$

The damage evolution functions for the normal failure and mode-mixity failure are defined as follows:

$$d_n = \begin{cases} 0 & \Delta_n \leq \delta_{nc} \\ \frac{\delta_n}{\Delta_n} \frac{\Delta_n - \delta_{nc}}{\delta_n - \delta_{nc}} & \Delta_n > \delta_{nc} \end{cases} \quad d = \begin{cases} 0 & \Delta_{\text{eff}} \leq \delta_{c,\text{eff}} \\ \frac{\delta_{\text{eff}}}{\Delta_{\text{eff}}} \frac{\Delta_{\text{eff}} - \delta_{c,\text{eff}}}{\delta_{\text{eff}} - \delta_{c,\text{eff}}} & \Delta_{\text{eff}} > \delta_{c,\text{eff}} \end{cases}, \quad (2.128)$$

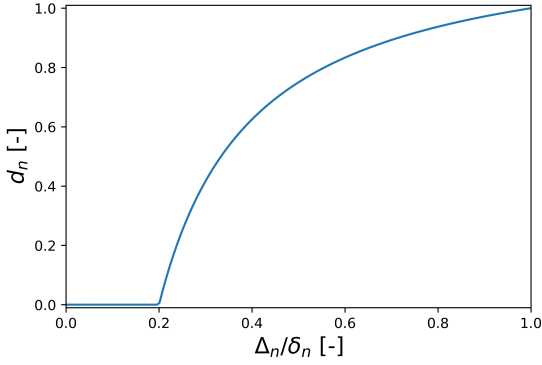
where $\delta_{\text{eff}} = \sqrt{\delta_n^2 + \delta_t^2}$ is the effective final crack opening width, $\delta_{c,\text{eff}} = \sqrt{\delta_{nc}^2 + \delta_{tc}^2}$ denotes the effective critical crack opening width. For the damage evolution, $\dot{d} \geq 0$ is considered for the irreversible crack propagation. In this work, the damage parameter d is introduced as the history-dependent state variable, namely $d = \max_{s \in [0, t]} \hat{d}(x, s)$ over

the full temporal history $s \in [0, \mathcal{T}]$ of damage state \hat{d} . Fig. 2.6 plots the normal and mixed-mode failure functions, respectively. In this work, the degradation function is introduced as a linear function as $g(d) = 1 - d$. The discussion of the degradation function's influence on the interface debonding will be presented in future work.

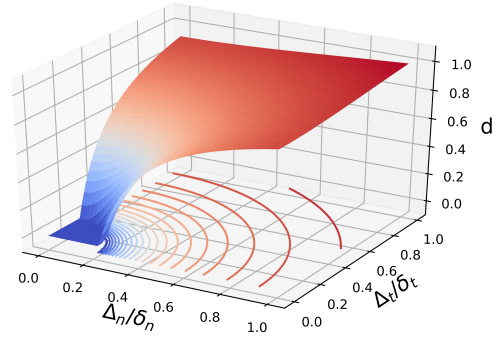
While for the chemical part, we can extract the interfacial free energy from the bulk one, namely Eq. (2.106), as follows:

$$\Psi_I^c = w \Psi_b(C_I, \nabla C_I). \quad (2.129)$$

Therefore, the damage dependent interface chemical potential can be obtained as



(a) damage function for normal failure



(b) damage function for mixed-mode failure

Figure 2.6: Damage functions for normal failure and mixed-mode failure with $\lambda_n = 0.2$, $\lambda_t = 0.1$.

follows:

$$\begin{aligned}
 \mu_I &= g(d) \frac{1}{w} \left(\frac{\partial \Psi_I^c}{\partial C_I} - \nabla \cdot \frac{\partial \Psi_I^c}{\partial \nabla C_I} \right) \\
 &= g(d) \left(\frac{\partial \Psi_b(C_I, \nabla C_I)}{\partial C_I} - \nabla \cdot \frac{\partial \Psi_b(C_I, \nabla C_I)}{\partial \nabla C_I} \right), \quad (2.130) \\
 &= g(d) \{ RT [\ln \bar{C}_I - \ln(1 - \bar{C}_I) + \chi(1 - 2\bar{C}_I)] - \kappa \nabla^2 \bar{C}_I \\
 &\quad + \frac{\Omega K}{2} [1 - (J^e)^2] + \frac{\Omega G}{2} (\bar{I}_1 - 3) \}
 \end{aligned}$$

Then the interface flux \mathbf{J}_I in Eq. (2.91) can be expressed as:

$$\begin{aligned}
 \mathbf{J}_I &= -M_I(C_I) \nabla \mu_I \\
 &= -g(d) M_I(C_I) \nabla \cdot \{ RT [\ln \bar{C}_I - \ln(1 - \bar{C}_I) + \chi(1 - 2\bar{C}_I)] - \kappa \nabla^2 \bar{C}_I, \quad (2.131) \\
 &\quad + \frac{\Omega K}{2} (1 - J_e^2) + \frac{\Omega G}{2} (\bar{I}_1 - 3) \}
 \end{aligned}$$

however, Eq. (2.131) evolves the high order derivative of the concentration field, which make the calculation not so straightforward. Moreover, in this thesis, we mainly focus on the across-GB diffusion. Therefore, by assuming no transport of Lithium along the tangential direction of the interface Γ_I , the net Lithium migration flux across the GB can be obtained as follows:

$$J_I = \mathbf{J}_I \cdot \vec{\mathbf{n}}_I. \quad (2.132)$$

Physically, the across-GB flux is proportional to the jump of the chemical potential at the interface. Therefore, by using the Taylor expansion, the net flux on the two sides of the interface can be written out as follows:

$$\begin{aligned} J_I^+ &\approx J_I + \frac{w}{2} \nabla J_I \cdot \vec{\mathbf{n}}_I \\ J_I^- &\approx J_I - \frac{w}{2} \nabla J_I \cdot \vec{\mathbf{n}}_I, \end{aligned} \quad (2.133)$$

thus, by using Eq. (2.131), we can have the across-GB flux as follows:

$$\begin{aligned} J_I &= \mathbf{J}_I \cdot \vec{\mathbf{n}}_I = \frac{1}{2}(J_I^+ + J_I^-) \\ &= \frac{1}{2}g(d)(-M_I^+ \nabla \mu_I^+ \cdot \vec{\mathbf{n}}_I^+ - M_I^- \nabla \mu_I^- \cdot \vec{\mathbf{n}}_I^-) \\ &= \frac{1}{2}g(d)(-M_I^+ \nabla \mu_I^+ + M_I^- \nabla \mu_I^-) \cdot \vec{\mathbf{n}}_I \\ &= \frac{1}{2}g(d) \left[-\frac{D_I^+ C_I^+}{RT} (1 - \bar{C}_I^+) \nabla \mu_I^+ + \frac{D_I^- C_I^-}{RT} (1 - \bar{C}_I^-) \nabla \mu_I^- \right] \cdot \vec{\mathbf{n}}_I \end{aligned} \quad (2.134)$$

where $D_I^+ = D_I^- = D_I$ are the diffusion coefficient of the GB.

As a special case, we can also choose a simpler expression of the interface free energy density for the single species case as presented in Ref. [45]. Thus one can write out the Ψ_I^c as follows:

$$\Psi_I^c = w\Psi_I^{c0} = w[\mu_I^0 C_I + RT C_I (\ln C_I - 1)], \quad (2.135)$$

where Ψ_I^{c0} is the bulk free energy, and where μ_I^0 denotes the reference chemical potential at the interface. In this scenario, the interface chemical potential μ_I can be written out as follows:

$$\mu_I = \frac{1}{w} \frac{\partial \Psi_I}{\partial C_I} = g(d) [\mu_I^0 + RT \ln C_I]. \quad (2.136)$$

Therefore, the flux J_I can be written out as follows:

$$J_I = -g(d) \frac{RT M_I}{C_I} \nabla C_I \cdot \vec{\mathbf{n}}_I = -g(d) \frac{RT D_I C_{\max} \bar{C}_I (1 - \bar{C}_I)}{C_I} \nabla C_I \cdot \vec{\mathbf{n}}_I, \quad (2.137)$$

considering that, the concentration at the two sides of the interface can be approached by using the Taylor expansion, thus we can have:

$$C_I^+ \approx C_I + \frac{w}{2} \nabla C_I \cdot \mathbf{n}_I, \quad (2.138)$$

$$C_I^- \approx C_I - \frac{w}{2} \nabla C_I \cdot \mathbf{n}_I, \quad (2.139)$$

then we can write out the relationship between the interface concentration gradient ∇C_I and the interface concentration jump $\llbracket C \rrbracket$ as follows:

$$\llbracket C \rrbracket = C_I^+ - C_I^- = w \nabla C_I \cdot \vec{\mathbf{n}}_I, \quad (2.140)$$

then, by substituting Eq. (2.140) into Eq. (2.137), we can write out the across-GB flux J_I as follows:

$$J_I = -g(d) \frac{RT M_I \llbracket C \rrbracket}{C_I w} = -g(d) \frac{RT D_I C_{\max}(1 - \bar{C}_I)}{w} \llbracket \bar{C} \rrbracket. \quad (2.141)$$

Next, denoting by

$$\gamma = \frac{RT D_I C_{\max}(1 - \bar{C}_I)}{w}, \quad (2.142)$$

an exchange kinetics parameter for the interface, we can rewrite Eq. (2.141) as follows:

$$J^d = -g(d) \gamma \llbracket \bar{C} \rrbracket. \quad (2.143)$$

Since $w \ll 1$, we can also treat γ as a constant value in the simulation. It should be mentioned that, current model is different from the cases presented in Refs. [43, 21, 13], where a smooth concentration profile across the GB is assumed, no concentration jump and flux jump are allowed at the interface. However, the smoothed profile can not well explain the experimentally observed chemical heterogeneity. Besides, Eq. (2.141) requires the formula of a newly created interface free energy, in which both the information of stresses and also the phase-interface contribution are missing. Moreover, it can be easily considered as a special case of Eq. (2.134). Therefore, to make our framework general and flexible enough, Eq. (2.134) is adopted for the simulation.

3 Two-level Modeling of Particle and Cell

A classical LIB cell can be decomposed into scales of different lengths, for instance, the macro-scale and the micro-scale. The kinetics and transport phenomena at the micro-scale, which is referred to the particle level, have been presented in details in Chapter 2. While at the macro-scale, namely the cell level, a simple layout of the LIB cell includes a negative (anodic) current collector, a Lithium foil anode, a solid or liquid electrolyte, a porous intercalation cathode, and a positive (cathodic) current collector. Since in this thesis, we mainly focus on the cathode materials as well as their chemical and mechanical impact on the cell. Therefore, a half-cell structure, as shown in Fig. 3.1, has been presented for the following discussion.

The two-level finite element implementation of the model presented in this chapter is explained in details in the related section of Chapter 4. It serves as the basis of Publication B.

3.1 Concentrated solution

Most of the widely used commercial LIBs are fabricated with Li^+ salt solution as the electrolyte, for instance, the poly-ethylene oxide (PEO) dissolved with alkali metal salt [107], LiPF_6 [108], the superconcentrated $\text{LiN}(\text{SO}_2\text{F})_2$ [109], and also the promising solid electrolyte material $\text{Li}_7\text{La}_3\text{Zr}_2\text{O}_{12}$ (LLZO) for the all-solid-state battery (ASSB) [110]. These salts can provide a wider electropositive potential window as well as a better Li ion conductivity than other solutions. Thus the batteries can facilitate a very high energy density and better cell performance. Considering that, in most of the batteries, the salt concentrations are generally large [111, 112, 113, 114]. Therefore, the transport of the electrolyte is treated rigorously by using the concentrated solution theory, in which the driving force for the mass transfer is proportional to the gradient of the electrochemical potential. Thereby, the driving force for the i -th species of the electrolyte under the constant temperature and pressure can be given as follows [28,

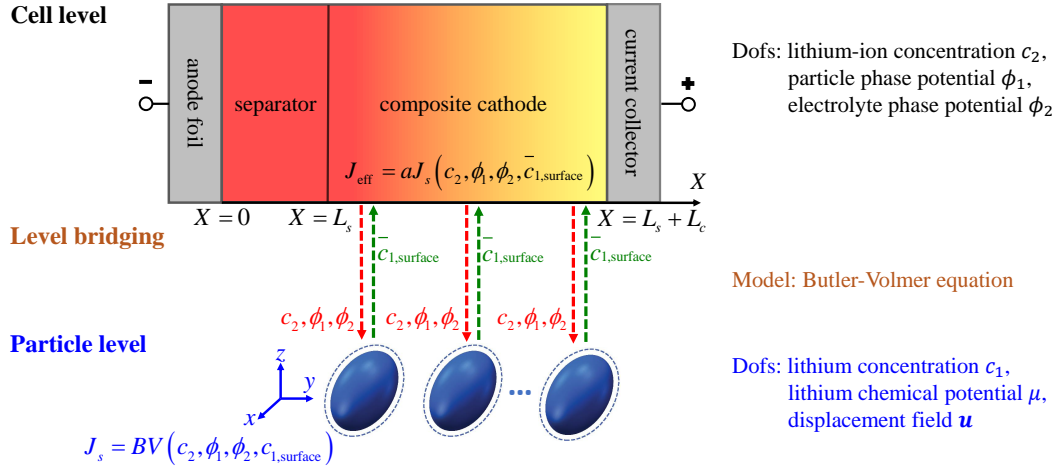


Figure 3.1: Outline of the two-level framework for the Lithium-ion battery with a half-cell structure.

115]:

$$c_i \nabla \mu_i = RT \sum_j \frac{c_i c_j}{c_T \mathcal{D}_{ij}} (\mathbf{v}_j - \mathbf{v}_i), \quad (3.1)$$

where c_i is the concentration of i -th species and where μ_i is the related electrochemical potential. \mathbf{v}_i denotes the velocity of species i , \mathcal{D}_{ij} is the diffusion coefficient describing the interaction between the i -th and j -th species. Next, by applying the Onsager reciprocal relationship [116, 117], the diffusion coefficients can be assumed as $\mathcal{D}_{ij} = \mathcal{D}_{ji}$. The total concentration c_T can be determined by the summation of all the species as follows:

$$c_T = \sum_i c_i. \quad (3.2)$$

Moreover, the mass conservation of each species can be ensured via:

$$\frac{\partial c_i}{\partial t} = -\nabla \cdot \mathbf{N}_i + R_i, \quad (3.3)$$

where \mathbf{N}_i denotes the flux of i -th species, and where R_i represents the production of species i due to the homogeneous chemical reaction.

In order to obtain the flux in terms of driving forces for the material balance, namely Eq. (3.3), we consider a binary electrolyte including anions, cations and solvent.

Then by considering the solvent velocity as the reference one, namely \mathbf{v}_0 , we can have:

$$c_+ \nabla \mu_+ = K_{0+}(\mathbf{v}_0 - \mathbf{v}_+) + K_{+-}(\mathbf{v}_- - \mathbf{v}_+), \quad (3.4)$$

$$c_- \nabla \mu_- = K_{0-}(\mathbf{v}_0 - \mathbf{v}_-) + K_{-+}(\mathbf{v}_+ - \mathbf{v}_-), \quad (3.5)$$

where K_{ij} denotes the drag coefficient defined as follows:

$$K_{ij} = \frac{RTc_i c_j}{c_T \mathcal{D}_{ij}}. \quad (3.6)$$

Considering that, the current density can be defined as:

$$\mathbf{i} = F \sum_i z_i \mathbf{N}_i, \quad (3.7)$$

then, by rearranging Eqs. (3.4) and (3.5), the flux density $\mathbf{N}_i = \mathbf{v}_i c_i$ of each species can be given as follows:

$$\mathbf{N}_+ = c_+ \mathbf{v}_+ = -\frac{\nu_+ \mathcal{D}}{\nu RT} \frac{c_T}{c_0} c \nabla \mu_e + \frac{\mathbf{i}^0_+}{z_+ F} + c_+ \mathbf{v}_0, \quad (3.8)$$

$$\mathbf{N}_- = c_- \mathbf{v}_- = -\frac{\nu_- \mathcal{D}}{\nu RT} \frac{c_T}{c_0} c \nabla \mu_e + \frac{\mathbf{i}^0_-}{z_- F} + c_- \mathbf{v}_0, \quad (3.9)$$

where c_0 is the concentration of the solvent, and where $\nu = \nu_+ + \nu_-$ is the number of ions produced by the dissociation of one molecule of electrolyte. ν_+ and ν_- respectively denote the number of cations and anions obeying the following relationship:

$$c = \frac{c_+}{\nu_+} = \frac{c_-}{\nu_-}, \quad (3.10)$$

where c represents the concentration of the electrolyte. μ_e is the electrochemical potential of the electrolyte, defined as follows:

$$\mu_e = \nu_+ \mu_+ + \nu_- \mu_- = \nu RT \ln(c f_{\pm} a_{\pm}^{\theta}) \quad (3.11)$$

where f_{\pm} represents the mean molar activity coefficient, and where a_{\pm}^{θ} denotes the activity. Considering that, the diffusion coefficient of the electrolyte can be defined as follows:

$$\mathcal{D} = \frac{\mathcal{D}_{0+} \mathcal{D}_{0-} (z_+ - z_-)}{z_+ \mathcal{D}_{0+} - z_- \mathcal{D}_{0-}}, \quad (3.12)$$

and the transference numbers t_+^0 can be given as follows:

$$t_+^0 = 1 - t_0^- = \frac{z_+ \mathcal{D}_{0+}}{z_+ \mathcal{D}_{0+} - z_- \mathcal{D}_{0-}}, \quad (3.13)$$

then, the commonly used and measured diffusion coefficient D of the electrolyte can be written out as follows:

$$D = \mathcal{D} \frac{c_T}{c_0} \left(1 + \frac{d \ln \gamma_{\pm}}{d \ln m}\right). \quad (3.14)$$

Thereby, the gradient of the chemical potential can be stated as follows:

$$\frac{\mathcal{D}}{\nu RT} \frac{c_T}{c_0} c \nabla \mu_e = D \left(1 - \frac{d \ln c_0}{d \ln c}\right) \nabla c, \quad (3.15)$$

then, by substituting Eqs. (3.8), (3.9) and (3.15) into Eq. (3.3) and vanishing the reaction source term, we can have:

$$\frac{\partial c}{\partial t} + \nabla \cdot (c \mathbf{v}_0) = \nabla \cdot \left[D \left(1 - \frac{d \ln c_0}{d \ln c}\right) \nabla c \right] - \frac{\mathbf{i} \cdot \nabla t_+^0}{z_+ \nu_+ F}, \quad (3.16)$$

where $\mathbf{i} = F \sum_i z_i \mathbf{N}_i$ is the current density with z_i being the charge number of species i .

Furthermore, the potential in the solution obeys the following relationship:

$$-nF \nabla \phi = s_- \mu_- + s_+ \mu_+ + s_0 \mu_0 \quad \text{with} \quad s_+ z_+ + s_- z_- = -n, \quad (3.17)$$

where n represents the number of transferred electrons for the reaction, and s_i denotes the stoichiometric coefficient of species i . Then, by substituting Eqs. (3.8) and (3.9) into Eq. (3.1), we can have:

$$\frac{\nabla \mu_-}{z_-} = -\frac{F}{k} \mathbf{i} - \frac{t_+^0}{z_+ \nu_+} \nabla \mu_e, \quad (3.18)$$

where k is the conductivity of the solution defined as follows:

$$\frac{1}{k} = \frac{-RT}{c_T z_+ z_- F^2} \left(\frac{1}{\mathcal{D}_{+-}} + \frac{c_0 t_-^0}{c_+ \mathcal{D}_{0-}} \right). \quad (3.19)$$

Then by substituting Eq. (3.18) into Eq. (3.17) and eliminating $\nabla \mu_0$, we can have:

$$\mathbf{i} = -k \nabla \phi - \frac{k}{F} \left(\frac{s_+}{n \nu_+} + \frac{t_+^0}{z_+ \nu_+} - \frac{s_0 c}{n c_0} \right) \nabla \mu_e, \quad (3.20)$$

then for the reaction $\text{Li} \rightleftharpoons \text{Li}^+ + \text{e}^-$, we will have:

$$\nabla \phi = -\frac{\mathbf{i}}{k} + \frac{2RT}{F} \left(1 + \frac{d \ln c_0}{d \ln c}\right) (1 - t_+^0) \nabla \ln c. \quad (3.21)$$

Thereby, the transport of Lithium-ions and the related potential in the solution can be described by Eqs. (3.16) and (3.21).

3.2 Porous electrode theory

The microstructure of the LIB electrode has a significant impact on the cell performance by providing specific interfacial surface area, Lithium-ion diffusion path as well as the active material connectivity [118, 119]. Nevertheless, the complex geometry of electrode makes it difficult to model the physical behavior of the battery. Thereby, the porous electrode theory has been presented [28], where the homogenous description of the electrode structure was used. Following this theory, the porous electrode can be considered as a superposition of the continuous electrode phase and solution phase, respectively. Thus the porous electrode can be described by its specific interfacial area a and also the volume fractions ϵ of each phase. Moreover, the geometric details of the cathode can be disregarded in this macroscopic treatment. Therefore, we can define two different potentials, namely ϕ_1 and ϕ_2 , for the solid conducting matrix material (electrode phase) and the pore-filling electrolyte (electrolyte phase), respectively. Following the work of Refs. [25, 28, 26, 27], we denote by the subscript 1 for the properties of the electrode phase while the subscript 2 is utilized for the quantities in the solution phase.

Thus, by applying Eq. (3.16) with the average quantities, the material balance of the salt in the pore can be stated as [120]:

$$\begin{aligned} \epsilon \frac{\partial c}{\partial t} + \mathbf{v}_0 \cdot \nabla c = \nabla \cdot \left[\epsilon D \left(1 - \frac{d \ln c_0}{d \ln c} \right) \nabla c \right] - \frac{\mathbf{i} \nabla t_+^0}{z_+ \nu_+ F} \\ + (1 - t_+^0) \frac{a j_{+n}}{\nu_+} + (1 - t_+^0) \frac{a j_{-n}}{\nu_-}, \end{aligned} \quad (3.22)$$

where j_{ij} denotes the average pore wall flux over the interfacial area between the matrix and solution in pores. Since each phase is considered independently, therefore, the current density \mathbf{i} in the pore phase can be changed to \mathbf{i}_2 . Moreover, since only the Lithium-ions participate in the chemical reaction, thus we can have $j_{-n} = j_{0n} = 0$. Then, by assuming $v_0 = 0$, we can have the material balance of the salt as follows:

$$\epsilon \frac{\partial c}{\partial t} = \nabla \cdot \left[D_{\text{eff}} \left(1 - \frac{d \ln c_0}{d \ln c} \right) \nabla c \right] + (1 - t_+^0) \frac{a j_{+n}}{\nu_+} - \frac{\mathbf{i}_2 \nabla t_+^0}{z_+ \nu_+ F}. \quad (3.23)$$

Besides, by applying Eq. (3.21) for the pore phase, we can have:

$$\nabla \phi_2 = -\frac{\mathbf{i}_2}{k_{\text{eff}}} + \frac{RT}{F} \left(1 + \frac{d \ln c_0}{d \ln c} \right) (1 - t_+^0) \nabla \ln c, \quad (3.24)$$

while for the matrix phase, the movement of electrons is governed by Ohm's law [121, 122]:

$$\mathbf{i}_1 = -\sigma_{\text{eff}} \nabla \phi_1, \quad (3.25)$$

where σ_{eff} represents the effective conductivity of the matrix, which is dependent on the volume fraction of the conducting phase.

Since our cell model is operated under the galvanostatic charge/discharge process, thus for the homogeneous electrode, we can have:

$$\nabla \cdot \mathbf{i}_1 + \nabla \cdot \mathbf{i}_2 = 0, \quad (3.26)$$

considering that, for a single electrode reaction, the Faraday's law can be expressed as:

$$aj_{in} = -\frac{as_i}{nF}i_n = -\frac{s_i}{nF}\nabla \cdot \mathbf{i}_2, \quad (3.27)$$

thus, by defining the effective pore wall flux as:

$$j_{\text{eff}} = aj_{+n}, \quad (3.28)$$

and using Eqs. (3.26) and (3.27), we can have the expressions for the two different currents as follows:

$$\nabla \cdot \mathbf{i}_1 + Fj_{\text{eff}} = 0, \quad (3.29)$$

$$\nabla \cdot \mathbf{i}_2 - Fj_{\text{eff}} = 0, \quad (3.30)$$

where Eqs. (3.29) and (3.30) are the ones presented in Refs. [33, 98]. Accordingly, the mass conservation of the salt can be rewritten as follow:

$$\epsilon \frac{\partial c}{\partial t} = \nabla \cdot [D_{\text{eff}}(1 - \frac{d \ln c_0}{d \ln c})\nabla c] + (1 - t_+^0)j_{\text{eff}} - \frac{\mathbf{i}_2 \nabla t_+^0}{F}. \quad (3.31)$$

For the separator, $\epsilon = 1$ is applied. Moreover, since no chemical reaction occurs, $j_{\text{eff}} = 0$ is applied in the equations mentioned above.

Wherein, the effective quantities for the porous electrode can be obtained via the Bruggeman's relationship [11, 98, 123], which is defined as follows:

$$k_{\text{eff}} = \epsilon^{1.5}k, \quad (3.32)$$

$$D_{\text{eff}} = \epsilon D, \quad (3.33)$$

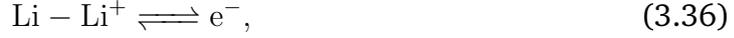
$$\sigma_{\text{eff}} = \epsilon \sigma. \quad (3.34)$$

3.3 Electrochemical reaction

The charge-transfer reaction between the electrolyte and the active particle can be written out as follows:



by rewriting Eq. (3.35) in the standard form, we can have:



where the stoichiometric coefficients can be listed as: $s_{\text{Li}} = 1$ and $s_{\text{Li}^+} = -1$, with $n = 1$. Following the definition of thermodynamics, the electrochemical potential of species i can be stated as:

$$\mu_i = \mu_i^\theta + RT \ln(a_i) + z_i F \phi, \quad (3.37)$$

where μ_i^θ is the standard electrochemical potential of species i and where a_i is the activity. Thereby, the electrochemical potential for Li, Li^+ and e^- can be given as follows:

$$\mu_{\text{e}^-} = \mu_{\text{e}^-}^\theta + RT \ln(a_{\text{e}^-}) - F \phi_{\text{e}^-}, \quad (3.38)$$

$$\mu_{\text{Li}^+} = \mu_{\text{Li}^+}^\theta + RT \ln(a_{\text{Li}^+}) + F \phi_{\text{Li}^+}, \quad (3.39)$$

$$\mu_{\text{Li}} = \mu_{\text{Li}}^\theta + RT \ln(a_{\text{Li}}), \quad (3.40)$$

where ϕ_{e^-} denotes the potential of the electrode or ϕ_1 as mentioned in the previous section, and where ϕ_{Li^+} is the potential of the solution phase, namely ϕ_2 in Section 3.2. Thus the Nernst potential or the interfacial voltage drop between the electrode and the electrolyte can be given as follows:

$$\Delta\phi = \phi_{\text{e}^-} - \phi_{\text{Li}^+} = \phi_1 - \phi_2, \quad (3.41)$$

thereby, the overpotential η for the reaction in Eq. (3.35) can be expressed as follows:

$$\eta = \frac{\mu_{\text{Li}} - \mu_{\text{Li}^+} - \mu_{\text{e}^-}}{F} = \frac{\mu_{\text{Li}}^\theta - \mu_{\text{Li}^+}^\theta - \mu_{\text{e}^-}^\theta}{F} - \frac{RT}{F} \ln\left(\frac{a_{\text{Li}}}{a_{\text{Li}^+} a_{\text{e}^-}}\right) + \Delta\phi. \quad (3.42)$$

For the half-cell reaction $\text{Li} \rightleftharpoons \text{Li}^+ + \text{e}^-$ that occurs in the cathode, we can write out the Nernst equation [124, 125] as follows:

$$\Delta\phi = \Delta\phi^\theta - \frac{RT}{F} \ln\left(\frac{a_{\text{Li}}}{a_{\text{Li}^+} a_{\text{e}^-}}\right), \quad (3.43)$$

where $\Delta\phi^\theta$ denotes the standard potential defined as follow:

$$\Delta\phi^\theta = \frac{\mu_{\text{e}^-}^\theta + \mu_{\text{Li}^+}^\theta - \mu_{\text{Li}}^\theta}{F}. \quad (3.44)$$

Next, by using the Nernst equation, the open-circuit voltage V_{oc} , which indicates the voltage at the terminal of the cell when no current flows, can be defined as follows:

$$V_{oc} = \Delta\phi^\theta + \frac{RT}{F} \ln\left(\frac{a_{\text{Li}}}{a_{\text{Li}^+} a_{\text{e}^-}}\right), \quad (3.45)$$

then, by substituting Eq. (3.45) into Eq. (3.42), we can have the final form of the over-potential η as follows:

$$\eta = -V_{oc} + \Delta\phi = \phi_1 - \phi_2 - V_{oc}, \quad (3.46)$$

in which V_{oc} can be measured from the experimental data. Next, we introduce the exchange current density i_0 for the reaction which is defined as follows:

$$i_0 = Fk_c\sqrt{(c_{\max} - c)c}, \quad (3.47)$$

where k_c represents the chemical reaction rate and where c_{\max} denotes the maximum concentration of salt. Thus the flux for the reaction in the cathode can be written out via the Butler–Volmer equation [29] as follows:

$$j = \frac{i_0}{F}C_{\max}[\bar{C} \exp(\frac{1}{2} \frac{F\eta}{RT}) - (1 - \bar{C}) \exp(-\frac{1}{2} \frac{F\eta}{RT})]. \quad (3.48)$$

3.4 Bridging of the cell level and the particle level

The modeling details for both the particle level and the cell level have been presented in Chapter 2 and Section 3.2, respectively. However, the interaction between the particle and the cell is still missing. Therefore, in this section we will present the level bridging between the cell and the particle.

For each point of interest at the cell level, we introduce the concentration c_2 for Lithium-ions in the solution phase, as well as the two potentials ϕ_1 and ϕ_2 for the electrode phase and the solution phase, respectively. Moreover, the normalized concentration of Li inside the particle (electrode phase) is denoted by \bar{C}_1 . Thus, in the given state of c_2^I , ϕ_1^I and ϕ_2^I at the time t^I , and the averaged surface concentration $\bar{C}_{1,\text{surface}}^I$ of the particles with general geometry, one can obtain the effective pore wall flux J_{eff} by using the Butler–Volmer reaction model and the definition of effective flux, namely, Eqs. (3.28) and (3.48).

In present work, the pore wall flux J_s is treated as a dependent quantity, where the calculation depends on the quantities from both the cell level and particle level. For the model at the particle level, J_s is applied as a flux boundary condition. While for the problem of the cell level, the effective pore wall flux J_{eff} is applied as the source term in Eqs. (3.21), (3.29) and (3.30). Following the same notation of Doyle's work [26, 25], the relationship between these two fluxes can be expressed as follow:

$$J_{\text{eff}} = aJ_s, \quad (3.49)$$

where a is defined as the specific surface area per unit volume. To account for particles with a complex geometry, let's consider n identical particles with arbitrary shape, which are embedded in a cubic cathode domain with the length L_c and the cross section area A . For each individual particle, its volume and surface area are denoted by V and S , respectively. Once the volume fraction coefficient ϵ of the cathode is given, we can write out the following relationship:

$$L_c A (1 - \epsilon) = n \times V, \quad \text{and} \quad a = \frac{n \times S}{L_c A} = \frac{S}{V} (1 - \epsilon). \quad (3.50)$$

For the particles with general geometry, the following relationship is applied:

$$J_{\text{eff}} = a J_s = \frac{S}{V} (1 - \epsilon) J_s. \quad (3.51)$$

Since the size of the particle is so small compared to the length of the cell, the averaged surface concentration $\bar{C}_{1,\text{surface}}$ is adopted for the particles with the general geometry, which is defined as follow:

$$\bar{C}_{1,\text{surface}} = \frac{\int_{\partial\Omega} C_1 dA}{\int_{\partial\Omega} dA}. \quad (3.52)$$

Then, as a special case, the volume and surface area of the spherical particle with radius r can be expressed as $V = \frac{4}{3}\pi r^3$ and $S = 4\pi r^2$, respectively. Consequently, the effective pore wall flux can be obtained by

$$J_{\text{eff}} = \frac{3}{r} (1 - \epsilon) J_s, \quad (3.53)$$

moreover, since the surface is smooth and symmetric in the spherical particle, we can use $C_{1,\text{surface}}$, instead of $\bar{C}_{1,\text{surface}}$ for the calculation of Eq. (3.48). While for the particles with the general geometry, $C_{1,\text{surface}}$ should be replaced by $\bar{C}_{1,\text{surface}}$ in Eq. (3.48) at the cell level.

4 Finite Element Implementation

The models mentioned in Chapters 2 and 3 can result in a set of coupled partial/ordinary differential equations (PDEs/ODEs), wherein the solutions of these equations can be solved under the given geometrical domain and the specific physical conditions or boundary conditions. Due to the complexity of the coupled equations, analytical solutions are not always available. To this end, the numerical approximations are thus introduced to solve those equations. As one of the most widely used numerical methods for solving equations, the finite element method (FEM) gains excellent success in engineering and mathematical modeling. In this chapter, we will introduce the fundamentals of FEM and the numerical implementations of the proposed models of Publications A and B.

4.1 Basics of the finite element method

Considering the classical Poisson equation defined in the body \mathcal{B} :

$$\Delta u(x) = f(x) \quad \text{in } \mathcal{B}, \quad (4.1)$$

where $u(x)$ denotes the unknown field variables to be solved, and where $f(x)$ represents a given function for the equation. The related boundary conditions can be list as follows:

$$\nabla u \cdot \vec{n} = g \quad \text{on } \Gamma_N, \quad (4.2)$$

$$u = \bar{u} \quad \text{on } \Gamma_D, \quad (4.3)$$

where Eq. (4.2) is the *Neumann boundary condition* on boundary Γ_N , and where Eq. (4.3) represents the *Dirichlet boundary condition* on boundary Γ_D .

Next, by using the weighted residual method [47, 126], we can multiply Eq. (4.1) with a weight function or a test function δu and integrate over the domain \mathcal{B} yields:

$$\int_{\mathcal{B}} \Delta u(x) \delta u dV = \int_{\mathcal{B}} f(x) \delta u dV. \quad (4.4)$$

Then, by using the divergence theorem and integrating by parts, we can have:

$$\int_{\partial\mathcal{B}} \nabla u(x) \cdot \vec{n} \delta u dS - \int_{\mathcal{B}} \nabla u(x) \nabla \delta u dV - \int_{\mathcal{B}} f(x) \delta u dV = 0. \quad (4.5)$$

Thus, by substituting the corresponding equations, namely Eq. (4.2), into Eq. (4.5), we can obtain:

$$\int_{\partial\mathcal{B}} g \delta u dS - \int_{\mathcal{B}} \nabla u(x) \nabla \delta u dV - \int_{\mathcal{B}} f(x) \delta u dV = 0, \quad (4.6)$$

where Eq. (4.6) is called the *weak form* of the Poisson equation, and where the solution of Eq. (4.6) is exactly the solution of the related strong formulation, namely Eqs. (4.1) to (4.3). It should be noted that, Eq. (4.3) is often imposed on the boundary where the weighting function δu vanishes on Γ_D .

Considering that, the body \mathcal{B} can be decomposed into finite pieces of domains \mathcal{B}_e , namely the *elements*, as follows:

$$\mathcal{B} \approx \sum_e \mathcal{B}_e, \quad (4.7)$$

and similarly for the boundaries:

$$\partial\mathcal{B} = \Gamma_N + \Gamma_D \approx \sum_e \Gamma_{N_e} + \sum_e \Gamma_{D_e}. \quad (4.8)$$

Thus, the Eq. (4.6) can be discretized as follows:

$$\sum_e \int_{\partial\mathcal{B}_e} g \delta u dS - \sum_e \int_{\mathcal{B}_e} \nabla u(x) \nabla \delta u dV - \sum_e \int_{\mathcal{B}_e} f(x) \delta u dV = 0 \quad (4.9)$$

Considering that, each element has nodes that are associated with the local basis functions. Therefore, each position $\mathbf{x}(\xi)$ in the element \mathcal{B}_e can be interpolated as follows:

$$\mathbf{x}(\xi) = \mathbf{x}^I N^I(\xi), \quad (4.10)$$

where \mathbf{x}^I is the spatial coordinates of the I-th node, and where N^I is the related shape function. ξ is the coordinates in the parametric space for the integration. Similarly, we can write out the expressions for $u(\xi)$, δu and also the gradients as follows:

$$u(\xi) = u^I N^I(\xi), \quad (4.11)$$

$$\delta u = \delta u^I N^I(\xi), \quad (4.12)$$

$$\nabla u = u^I \nabla N^I, \quad (4.13)$$

$$\nabla \delta u = \delta u^I \nabla N^I \quad (4.14)$$

where u^I is the unknown nodal variable of I-th node, which is also referred to the degree of freedom (DoF). Next, by applying Eqs. (4.11) to (4.14) into Eq. (4.9), we can have:

$$\sum_e \int_{\partial B_e} g \delta u^I N^I dS - \sum_e \int_{B_e} u^J \nabla N^J \delta u^I \nabla N^I dV - \sum_e \int_{B_e} f(x) \delta u^I N^I dV = 0. \quad (4.15)$$

Since Eq. (4.15) must be held for the arbitrary δu^I , thus the residual for the system equations within each element can be read as:

$$R_u^I = \int_{\partial B_e} g N^I dS - \int_{B_e} u^J \nabla N^J \nabla N^I dV - \int_{B_e} f(x) N^I dV, \quad (4.16)$$

where the subscript u in R_u^I denotes the contribution of the Poisson equation to the residual.

For the nonlinear problems, the Newton-Raphson iteration procedure [47, 126] is employed, where the iteration of the system residual \mathbf{R}_k at current iteration obeys the following rules:

$$\mathbf{R}_{k+1} = \mathbf{R}_k + \mathbf{K}_k d\mathbf{u}_k = 0, \quad (4.17)$$

where $k + 1$ denotes the quantities for the next iteration, and where \mathbf{K} denotes the tangential or the stiffness matrix of the system, which can be defined as follows:

$$\mathbf{K}_k = -\left(\frac{\partial \mathbf{R}}{\partial \mathbf{u}}\right)_k. \quad (4.18)$$

Then the solution for the next iteration can be updated through

$$\mathbf{u}_{k+1} = \mathbf{u}_k + d\mathbf{u}_k, \quad (4.19)$$

until the convergence is reached, we can obtain the solution for the current step.

4.2 Finite element implementation for the cell model

The governing equations for the cell level problem, which is considered as the 1D case in Publication B, as introduced in Chapter 3 are summarized as below:

$$\varepsilon \frac{\partial c_2}{\partial t} = D_{\text{eff}} \nabla^2 c_2 - \frac{1}{F} \frac{\partial t_+^0}{\partial c_2} \nabla c_i \mathbf{i}_2 + (1 - t_+^0) J_{\text{eff}}, \quad (4.20)$$

$$\nabla \cdot \mathbf{i}_1 + F J_{\text{eff}} = \nabla(-\sigma_{\text{eff}} \nabla \phi_1) + F J_{\text{eff}} = 0, \quad (4.21)$$

$$\nabla \cdot \mathbf{i}_2 - F J_{\text{eff}} = \nabla[-k_{\text{eff}} \nabla \phi_2 + k_{\text{eff}} \frac{RT}{F} (1 - t_+^0) \nabla \ln c] - F J_{\text{eff}} = 0, \quad (4.22)$$

and the related boundary conditions are read as:

$$-D_{\text{eff}}\nabla c_2 \cdot \vec{\mathbf{n}} = \frac{I(1-t_+^0)}{F} \quad \text{at } X=0, \quad (4.23)$$

$$-D_{\text{eff}}\nabla c_2 \cdot \vec{\mathbf{n}} = 0 \quad \text{at } X=L_s+L_c, \quad (4.24)$$

$$-\sigma_{\text{eff}}\nabla\phi \cdot \vec{\mathbf{n}} = 0 \quad \text{at } X=0, \quad (4.25)$$

$$-\sigma_{\text{eff}}\nabla\phi \cdot \vec{\mathbf{n}} = I \quad \text{at } X=L_s+L_c, \quad (4.26)$$

$$-k_{\text{eff}}\left[\nabla\phi_2 - \frac{RT}{F}(1-t_+^0)\nabla\ln c\right] \cdot \vec{\mathbf{n}} = I \quad \text{at } X=0, \quad (4.27)$$

$$-k_{\text{eff}}\left[\nabla\phi_2 - \frac{RT}{F}(1-t_+^0)\nabla\ln c\right] \cdot \vec{\mathbf{n}} = 0 \quad \text{at } X=L_s+L_c, \quad (4.28)$$

where L_c is the length of the separator domain, and where L_c represents the length of the cathode domain. I is the applied current density for the galvanostatic discharge process. Next, by choosing the test functions δc_2 , $\delta\phi_1$ and $\delta\phi_2$ for Eqs. (4.20) to (4.22), we can write the related *weak forms* as follows:

$$\begin{aligned} \int_{\mathcal{B}} \varepsilon \dot{c}_2 \delta c_2 dV &= - \int_{X=0} \frac{I(1-t_+^0)}{F} \delta c_2 dS - \int_{\mathcal{B}} D_{\text{eff}} \nabla c_2 \nabla \delta c_2 dV \\ &\quad - \int_{\mathcal{B}} \frac{1}{F} \frac{\partial t_+^0}{\partial c_2} \mathbf{i}_2 \cdot \nabla c_2 \delta c_2 dV + \int_{\mathcal{B}} (1-t_+^0) J_{\text{eff}} \delta c_2 dV \end{aligned} \quad (4.29)$$

and

$$\int_{X=L_s+L_c} I \delta\phi_1 dS + \int_{\mathcal{B}} \sigma_{\text{eff}} \nabla\phi_1 \nabla\delta\phi_1 dV + \int_{\mathcal{B}} F J_{\text{eff}} \delta\phi_1 dV = 0 \quad (4.30)$$

and

$$\int_{X=0} I \delta\phi_2 dS + \int_{\mathcal{B}} k_{\text{eff}} \left[\nabla\phi_2 - \frac{RT}{F}(1-t_+^0)\nabla\ln c \right] \nabla\delta\phi_2 dV - \int_{\mathcal{B}} F J_{\text{eff}} \delta\phi_2 dV = 0 \quad (4.31)$$

thus, the residuals for the system equations can be written out as follows:

$$\begin{aligned} R_{c_2}^I &= \int_{\mathcal{B}} \varepsilon \dot{c}_2 N^I dV + \int_{X=0} \frac{I(1-t_+^0)}{F} N^I dS + \int_{\mathcal{B}} D_{\text{eff}} \nabla c_2 \nabla N^I dV \\ &\quad + \int_{\mathcal{B}} \frac{1}{F} \frac{\partial t_+^0}{\partial c_2} \mathbf{i}_2 \cdot \nabla c_2 N^I dV - \int_{\mathcal{B}} (1-t_+^0) J_{\text{eff}} N^I dV \end{aligned} \quad (4.32)$$

and

$$R_{\phi_1}^I = \int_{X=L_s+L_c} I N^I dS + \int_{\mathcal{B}} \sigma_{\text{eff}} \nabla\phi_1 \nabla N^I dV + \int_{\mathcal{B}} F J_{\text{eff}} N^I dV \quad (4.33)$$

and

$$R_{\phi_2}^I = \int_{X=0} \text{I}N^I dS + \int_{\mathcal{B}} k_{\text{eff}} \left[\nabla \phi_2 - \frac{RT}{F} (1 - t_+^0) \nabla \ln c \right] \nabla N^I dV - \int_{\mathcal{B}} F J_{\text{eff}} N^I dV \quad (4.34)$$

then, by letting the system residual $\mathbf{R}^I = [R_{c_2}^I, R_{\phi_1}^I, R_{\phi_2}^I]$ equals to zero, we can obtain the solution for c_2 , ϕ_1 and ϕ_2 .

4.3 Finite element implementation for the chemo-mechanical particle model

For the problems at the particle level, the chemo-mechanically coupled equations, as mentioned in Chapter 2, can be list as below:

$$\frac{\partial C_1}{\partial t} = \nabla \cdot (M \nabla \mu), \quad (4.35)$$

$$\mu = \mu^c + \mu^i + \mu^e, \quad (4.36)$$

$$\nabla \cdot \mathbf{P} = \mathbf{0}, \quad (4.37)$$

the related boundary conditions are given as:

$$-M \nabla \mu \cdot \vec{\mathbf{n}} = J_s \quad \text{in } \partial \mathcal{B}_c \times (0, \mathcal{T}), \quad (4.38)$$

$$\nabla C_1 \cdot \vec{\mathbf{n}} = 0 \quad \text{in } \partial \mathcal{B} \times (0, \mathcal{T}), \quad (4.39)$$

$$\mathbf{t} = \mathbf{P} \cdot \vec{\mathbf{n}} = \mathbf{0} \quad \text{in } \partial \mathcal{B}_t \times (0, \mathcal{T}), \quad (4.40)$$

$$\mathbf{u} = \hat{\mathbf{u}} \quad \text{in } \partial \mathcal{B}_u \times (0, \mathcal{T}). \quad (4.41)$$

Next, by using the test functions δC_1 , $\delta \mu$ and δu_i , we can write out the *weak forms* as follows:

$$\int_{\mathcal{B}} \dot{C}_1 \delta C_1 dV = - \int_{\partial \mathcal{B}_c} J_s \delta C_1 dS - \int_{\mathcal{B}} M \nabla \mu \nabla \delta C_1 dV, \quad (4.42)$$

and

$$\int_{\mathcal{B}} \mu \delta \mu dV = \int_{\mathcal{B}} \mu^c \delta \mu dV + \int_{\mathcal{B}} \mu^i \delta \mu dV + \int_{\mathcal{B}} \mu^e \delta \mu dV, \quad (4.43)$$

and

$$\int_{\mathcal{B}} P_{iJ} \delta u_{i,J} dV + \int_{\Gamma_1} t_i \delta \Delta_i dS = 0. \quad (4.44)$$

Therefore, the residuals for each equation can be expressed as:

$$R_{c_1}^I = \int_{\mathcal{B}} \dot{C}_1 N^I dV + \int_{\partial \mathcal{B}_c} J_s N^I dS + \int_{\mathcal{B}} M \nabla \mu \nabla N^I dV, \quad (4.45)$$

and

$$R_{\mu}^I = \int_{\mathcal{B}} \mu N^I dV - \int_{\mathcal{B}} \mu^c N^I dV - \int_{\mathcal{B}} \mu^i N^I dV - \int_{\mathcal{B}} \mu^e N^I dV, \quad (4.46)$$

and

$$R_{u_i}^I = \int_{\mathcal{B}} P_{iJ} N_{,J}^I dV + \int_{\Gamma_1^+} t_i^+ N^I dS - \int_{\Gamma_1^-} t_i^- N^I dS. \quad (4.47)$$

It should be mentioned that, the traction t_i^+ and t_i^- at the interface are defined on the global coordinates. However, the calculation is carried out in the local coordinates system. Therefore, the global to local coordinates transformation operator Λ and the rotation matrix \mathbf{R} are introduced as:

$$\mathbf{x} = \Lambda \cdot \mathbf{X}, \quad (4.48)$$

and

$$\hat{\mathbf{U}} = \mathbf{R} \cdot \mathbf{U}, \quad (4.49)$$

where \mathbf{x} represents the local coordinates of a cohesive zone element and where \mathbf{X} is the global one. \mathbf{U} and $\hat{\mathbf{U}}$ are the global and local displacements, respectively. Therefore, the local displacement jumps Δ can be easily calculated via the following expression:

$$\Delta = \mathbf{L} \cdot \mathbf{U}, \quad (4.50)$$

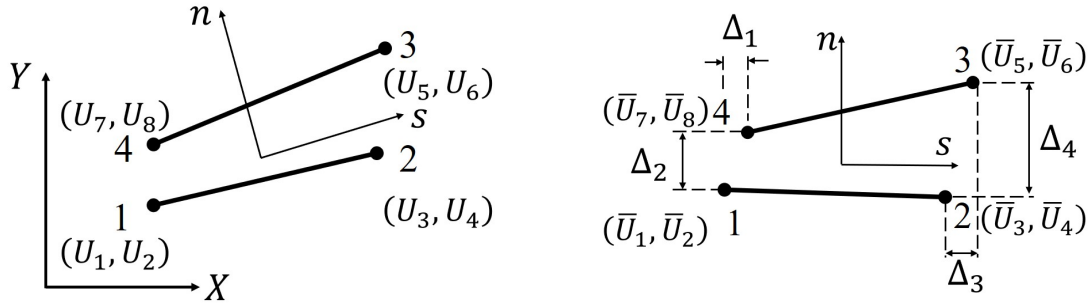
where \mathbf{L} represents the local displacement–separation relation matrix. Thus the global traction at the interface can be found as:

$$\mathbf{T} = \mathbf{B} \cdot \mathbf{T}_{\text{loc}}, \quad (4.51)$$

where \mathbf{T} is the global traction vector at the interface, and where $\mathbf{B} = \mathbf{N}\mathbf{L}\mathbf{R}$ is the global displacement-separation relation matrix, \mathbf{N} is the shape functions of the interface. The local traction \mathbf{T}_{loc} can be calculated from Eqs. (2.122) and (2.123) based on the local displacement jump Δ .

Take the two-dimensional 4 nodes quadratic element as an example, the interface of the two neighboring element is a two-node line element as shown in Fig. 4.1. Thus the transformation matrix Λ can be given as:

$$\Lambda = \begin{bmatrix} \cos \theta & \sin \theta \\ -\sin \theta & \cos \theta \end{bmatrix} \quad (4.52)$$



(a)

(b)

Figure 4.1: The representative two-dimensional linear cohesive zone element in (a) the global coordinates and (b) the local coordinates.

then the rotation matrix \mathbf{R} can be expressed as:

$$\mathbf{R} = \begin{bmatrix} \Lambda & 0 & 0 & 0 \\ 0 & \Lambda & 0 & 0 \\ 0 & 0 & \Lambda & 0 \\ 0 & 0 & 0 & \Lambda \end{bmatrix}. \quad (4.53)$$

As shown in Fig. 4.1b, the local displacement jump Δ can be obtained from the local displacements as follows:

$$\Delta_1 = \bar{U}_7 - \bar{U}_1, \quad \Delta_2 = \bar{U}_8 - \bar{U}_2, \quad \Delta_3 = \bar{U}_5 - \bar{U}_3, \quad \Delta_4 = \bar{U}_6 - \bar{U}_4, \quad (4.54)$$

where \bar{U}_i denotes the displacements in the local coordinates, then the local transformation matrix \mathbf{L} can be read as:

$$\mathbf{L} = \begin{bmatrix} -1 & 0 & 0 & 0 & 0 & 0 & 1 & 0 \\ 0 & -1 & 0 & 0 & 0 & 0 & 0 & 0 \\ 0 & 0 & -1 & 0 & 1 & 0 & 0 & 0 \\ 0 & 0 & 0 & -1 & 0 & 1 & 0 & 0 \end{bmatrix} \quad (4.55)$$

Thus, one can easily get the global traction and its derivatives for the cohesive-zone element.

4.4 Data transfer between two levels

In order to explain the framework in more details, a flowchart for this two-level framework is given in Fig. 4.2. For the implementation of this two-level framework,

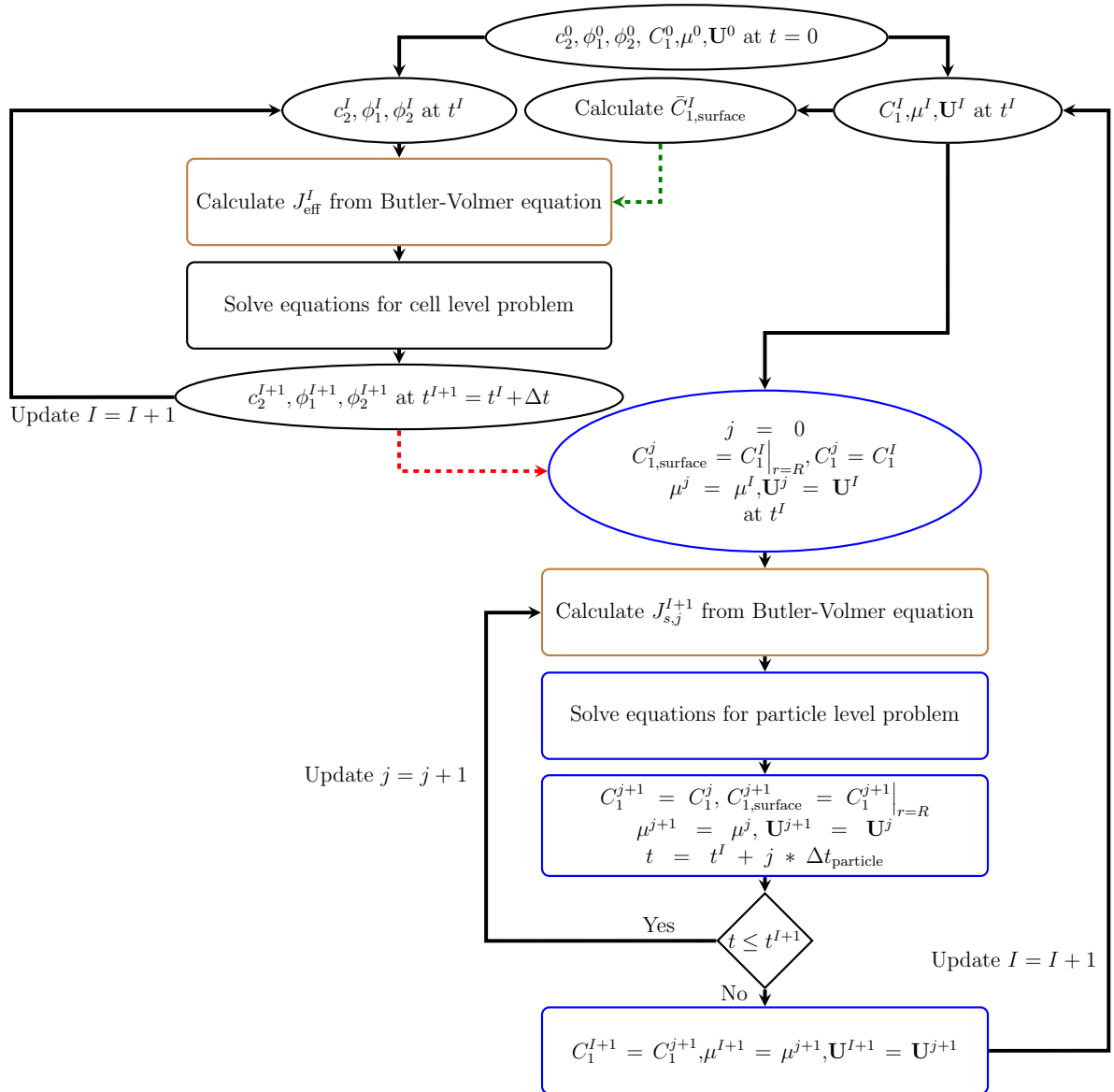


Figure 4.2: Flowchart of the two-level framework.

we only involve one time scale for the simulation, where the backward Euler (BE) time integration scheme with the adaptive capability is applied for the time stepping. Moreover, we introduce the staggered solution procedures to solve the problems of the cell level and the particle level.

At the beginning of the simulation, c_2^0 , ϕ_1^0 , ϕ_2^0 and C_1^0 are given as the initial conditions for both the cell level and particle level. Once the simulation starts, for instance, as illustrated in Fig. 4.2, c_2^{I+1} , ϕ_1^{I+1} and ϕ_2^{I+1} of the cell level are solved at the time t^{I+1} , and then being transferred to the particle level to solve the diffusion problem of the particle. After the calculation of the diffusion problem of the particle reaches the time t^{I+1} , the updated C_1^{I+1} , μ^{I+1} , \mathbf{U}^{I+1} and $\bar{C}_{1,\text{surface}}^{I+1}$ are passed back to the cell level for the next time step's simulation. This time stepping loop will continue until the cell voltage drops below some certain value, i.e. 3.5V, where we assume the discharge process is finished.

However, the governing equations of the cell level and the particle level are employed in two different spatial scales. For the problem of the cell level, the 1D uniform mesh is adopted to discretize the domain of separator and cathode, where the 1D linear Lagrange mesh is used for the discretization. While at the particle level, we use the open-source package Gmsh [127] to generate the 3D tetrahedral mesh for the spherical and spheroidal particles. Moreover, in order to reduce the computation costs of our implementation, the simulation of the particle is solved at the attached nodal points of the cathode domain at the cell level, and the C_1^{I+1} , μ^{I+1} , \mathbf{U}^{I+1} and $\bar{C}_{1,\text{surface}}^{I+1}$ are projected back to the corresponding nodes at the cell level. This is different from Golmon's work [33], where each integration point inside the element is attached with a particle model. Since the number of the nodal point is smaller than that of the integration points, the current model could be more efficient.

Furthermore, in order to further improve the computational efficiency, we use the open-source parallel computational framework MOOSE [128, 129] and libMesh [130] to implement the model we mentioned above. The MultiApps and Transfer systems [131] of MOOSE are also introduced to do the two-level coupling and data transfer between the two different levels. Moreover, the scalable (parallel) open-source solver PETSc [132, 133] has been used to solve our coupled partial differential equations (PDEs) based on the MPI parallelism. Calculations for this thesis and publications were conducted on the Lichtenberg high performance computer of the TU Darmstadt.

5 Results and Publications

In this chapter, the specific problems and challenges from among those listed previously are addressed via our thermodynamic consistent models as well as the two-level framework, and calculated by means of finite element method (FEM) software MOOSE.

5.1 Considered Problems

A. The across-GB transport and its impact on the crack patterns of polycrystalline materials

In this problem, a chemo-mechanical grain boundary model is formulated based on our thermodynamically consistent framework to study the GB cracking problem in polycrystalline energy materials in LIBs.

A. A chemo-mechanical grain boundary model and its application to understand the damage of Li-ion battery materials

[Y. Bai, K.-J. Zhao, Y. Liu, P. Stein, B.-X. Xu, A chemo-mechanical grain boundary model and its application to understand the damage of Li-ion battery materials, *Scr. Mater* 183 (2020):45-49]

The NMC particles with different numbers of grains, as shown in Fig. 5.1, have been considered to demonstrate the chemo-mechanical interplay inside the individual grain, and also between the GB.

The goal of this work is to understand that, how can the intergranular chemical inhomogeneity challenges the GB mechanical strength, and how can the GB damage influence or even block the across-grain transport.

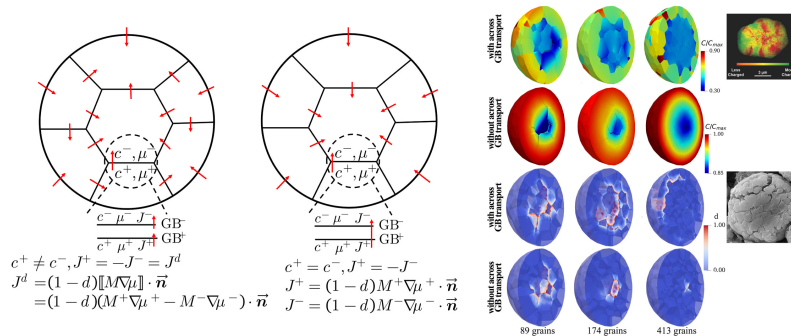


Figure 5.1: The across-GB transport law and its impact on the chemical heterogeneity as well as fracture patterns of the NMC particle.

B. Influence of Particle on Cell Performance

In this problem, the impact of the chemo-mechanical coupling and also the shapes of the particle on the cell performance are studied.

B. Two-level modeling of lithium-ion batteries

[Y. Bai, Y. Zhao, W. Liu, B.-X. Xu, Two-level modeling of lithium-ion batteries, J. Power Source 422 (2019) 92-103]

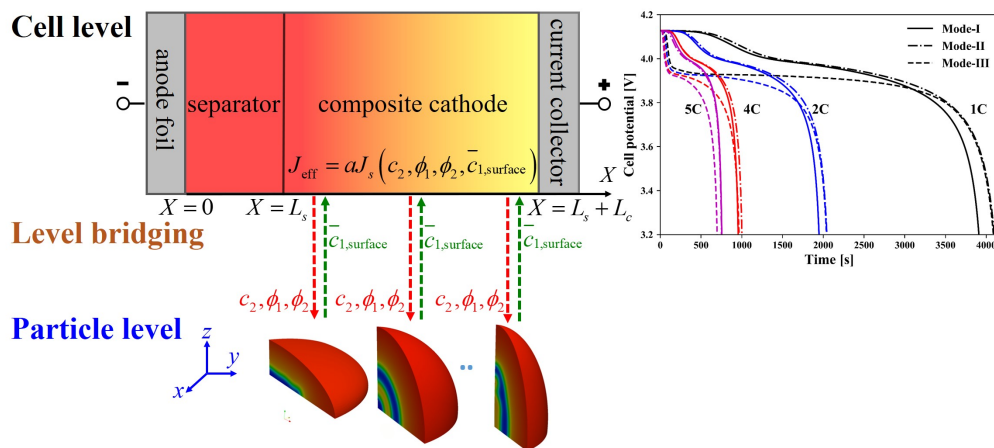


Figure 5.2: Two-level framework with the consideration of different particle shapes and diffusion dynamics, and their impact on the cell performance.

The mechanically coupled Cahn–Hilliard type diffusion model is considered for the

particle, where the cases with and without the phase-separation are compared. Moreover, the particles with the same volume but different shapes as shown in Fig. 5.2 are adopted to investigate the impact of the particle shape on the cell performance. Furthermore, the different elastic modulus of the particle have been studied. The goal of this paper is to demonstrate how flexible and robust the framework can be to reveal the impact of particle shape, finite deformation elasticity, and phase separation in particles on cell performance. It also allows the consideration of particles with interfaces and their influence on cell performance.

C. A review on modeling of electro-chemo-mechanics in lithium-ion batteries

In this set of problems, we reviewed the model development of the LIB cell.

C. A review on modeling of electro-chemo-mechanics in lithium-ion batteries

[Y. Zhao, P. Stein, Y. Bai, M. Al-Siraj, Y. Yang, B.-X. Xu, A review on modeling of electro-chemo-mechanics in lithium-ion batteries, *J. Power Sources* 413 (2019):259-283]

In this work, the P2D model and its extensions with the consideration of the mechanical coupling, phase separation as well as fracture have been summarized. Besides, the rigorous 2D and 3D models for the LIB cell have been investigated. The goal of this work is to give a comprehensive overview of the approaches for modeling the coupled chemo-mechanical behavior of LIBs at three different scales, namely the particle, the electrode, and the battery cell levels.

5.2 Author's contribution to the publications

In publication A, the author performed all the FEM modeling, and densely contributed to the analysis of its results, the work is supervised by Prof. Dr. Bai-Xiang Xu. The discussion of the anisotropic properties of NMC material was made by Prof. Dr. Kejie Zhao, who are gratefully acknowledged.

In the work B, all the numerical calculations and the analysis have been performed by the author, under the supervision of Prof. Dr. Bai-Xiang Xu.

For publication C, the author carried the simulation results of mechanical influence on the cell capacity. The author also reviewed the battery cell modeling in the literature which is mainly focused on the P2D model and its extension to chemo-mechanical coupling, along with rigorous 2D and 3D cell modeling.

5.3 Publication A

A chemo-mechanical grain boundary model and its application to understand the damage of Li-ion battery materials

Yang Bai, Kejie Zhao, Yao Liu, Peter Stein, Bai-Xiang Xu, A chemo-mechanical grain boundary model and its application to understand the damage of Li-ion battery materials, *Scripta Materialia* 183 (2020) 45-49.



Contents lists available at ScienceDirect

Scripta Materialia

journal homepage: www.elsevier.com/locate/scriptamat

A chemo-mechanical grain boundary model and its application to understand the damage of Li-ion battery materials

Yang Bai^a, Kejie Zhao^b, Yao Liu^a, Peter Stein^a, Bai-Xiang Xu^{a,*}

^a *Mechanics of Functional Materials Division, Department of Materials Science, TU Otto-Berndt-Straße 3 Darmstadt, Germany*

^b *School of Mechanical Engineering, Purdue University, West Lafayette, IN 47907, USA*

ARTICLE INFO

Article history:
Received 10 December 2019
Revised 6 March 2020
Accepted 11 March 2020

Keywords:
Grain boundary
Fragmentation
Ion transport
NMC particles
Crack propagation

ABSTRACT

Although the unique mechanical and transport features of grain boundaries (GBs) in polycrystalline ion conductors have been recognized, the understanding of the chemo-mechanical interplay and its impact is insufficient. We present a coupled GB model which includes both the damage-dependent across-grain transport and a mechanical cohesive zone law. 3D simulations on $\text{LiNi}_x\text{Mn}_y\text{Co}_z\text{O}_2$ demonstrate that the chemical process and the mechanical degradation go hand-in-hand: the enhanced intergranular chemical inhomogeneity challenges the GB mechanical strength, while the GB damage influences or even blocks the across-grain transport. Results explain well the experimentally observed features including chemical hot spots and surface layer delamination.

© 2020 Acta Materialia Inc. Published by Elsevier Ltd. All rights reserved.

Most ion conductors in energy applications like cathode materials and solid-state electrolytes in Li-ion batteries have polycrystalline or multi-grains structure. Compared to the bulk, the grain boundaries (GBs) play thereby significant roles for both their functional and mechanical properties. The unique mechanical and chemical properties of the GBs have been long recognized. For instance, the intergranular cleavage has been widely reported in cathode polycrystalline materials under cyclic charging/discharging. Besides, GBs can influence the ion transport path. However the chemical process and mechanical degradation go hand-in-hand. Their interplay is essential for understanding the functional and mechanical degradation of those materials.

Though the issue we address in this letter is for polycrystalline ion conductors in general, we take the widely used polycrystalline cathode materials $\text{LiNi}_x\text{Mn}_y\text{Co}_z\text{O}_2$ (NMC) [1,2] as an example. The NMC polycrystal is synthesized as an aggregate of many small grains with the size around 500nm [3,4]. The mechanical strength of the aggregates is determined by the adhesion of grains via Van der Waals interactions. It is thus much weaker than the intrinsic material strength of grains and thus the decohesion of GBs is the major contribution to mechanical degradation. Several numerical efforts have been made to predict the degradation of NMC particles during (de)lithiation [4–6]. A cohesive zone model (CZM) was thereby employed to simulate the intergranular fracture within the polycrystal. Later the competition between the energy

release rate and fracture resistance during crack growth of NMC material [7] was examined. This showed that the Li extraction can induce material embrittlement, increases the energy release rate, and reduces the fracture toughness. The aforementioned studies provided very useful insights on the crack propagation inside polycrystalline NMC.

However, there are still interesting experimental observations to be explained. One is the prominent lithium inhomogeneities or hot spots, as shown in the transmission X-ray microscopy image by Gent et al. [8], reprinted in Fig. 1b, which can be caused by the inter-grain chemical process [9]. This goes beyond the smooth concentration profile predicted in previous works.

Moreover, the SEM image [4] reprinted in Fig. 1a shows that the fragmentation or disassembly of grains can be restricted to the outside layer of the polycrystal. Such surface layer delamination cannot be predicted by previous models since the calculated diffusion-induced stress favors major radial cracks [10].

Both the hot spots across grains and the surface layer disassembly can be related to chemical interactions between grains. Different than in the grain interior, the lithium concentration at two sides of the GBs can be discontinuous and is merely governed by the chemical potential jumps across GBs [9]. Thus the GB kinetics should be formulated in general with the chemical potential jumps. Sharing similar research interest with ours, Singh and Pal [11] proposed a chemo-mechanical GB model in more recent work. Nevertheless the GB transport is formulated with respect to the concentration jump across GBs, which is suitable for the case of dilute solution. Their two-dimensional results of multi-grains do

* Corresponding author.

E-mail address: xu@mfm.tu-darmstadt.de (B.-X. Xu).

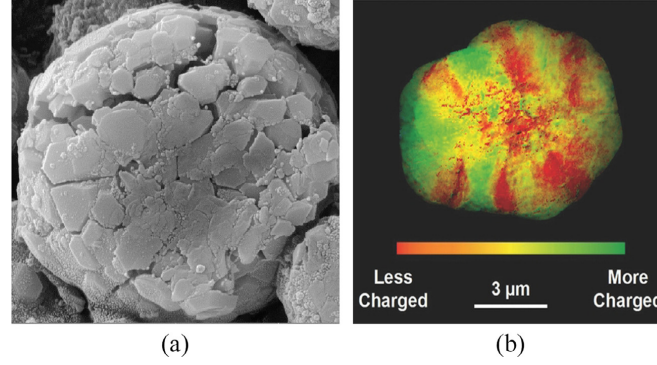


Fig. 1. (a) SEM image of cracks in a NMC particle after the first cycle of charge/discharge (Reproduced with permission from Sun et al. [4], Copyright 2016 by Elsevier), (b) the elemental mapping from ex situ transmission X-ray microscopy (Reproduced with permission from Gent et al. [8], Copyright 2016 by Wiley Online Library).

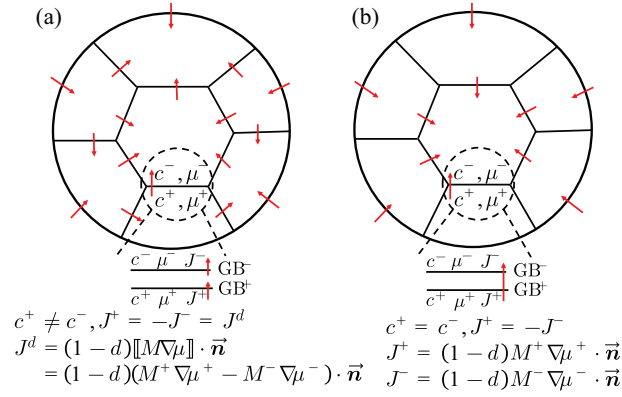


Fig. 2. Illustration of the GB models with (a) and without (b) the across-grain boundary transport.

not show the prominent chemical inhomogeneity observed in experiments, indicating the requirement of a more general GB kinetics. This chemical inhomogeneity resembles the mechanical displacement discontinuity due to GB delamination. Furthermore, if GBs are separated wide enough, the flux across them can even be switched off. Thus the mechanical damage of GBs should be considered in modeling the across-GB transport. The two mentioned issues can lead in the aggregate a highly inhomogeneous concentration distribution which deviates from the classical core-shell type smooth varying concentration profile. The enhanced inhomogeneity is further expected to change the diffusion-induced stress distribution and ultimately the fracture path. In the following, we present a chemo-mechanical grain boundary model and simulations for three-dimensional polycrystalline NMC particles. We contrast the simulated fragmentation patterns and the concentration distribution for cases with and without GB transport, and conclude that the former case leads to results much closer to experimental observations. Besides, we find the anisotropy of elasticity and chemical strain can slightly retard the damage once the GB transport is regarded.

In this letter, we present a chemo-mechanical model, which includes the damage-dependent across-GB transport for lithium transport, and also the cohesive traction-separation law for mechanical degradation. The model is illustrated in Fig. 2, contrasted with a counterpart without the across-GB transport. The ion flux

across the GBs is defined as

$$J^+ = -J^- = J^d, \quad J^d = (1-d)[M^+ \nabla \mu^+ - M^- \nabla \mu^-] \cdot \vec{n} \quad (1)$$

where J , M and μ indicate the normal ion flux, the mobility and the chemical potential, respectively. ∇ is the gradient operator. The superscripts + and - indicate the parameters defined on the two sides of each GB, respectively. The variable d represents the damage state of the GB, which is related to the interface separation in the later context. Any variable with the superscript d denotes that this quantity is damage-dependent. Accordingly, J^d is the damage-dependent flux across the GB. Mass conservation is guaranteed by the first expression in Eq. 1. Once complete failure occurs, namely for $d = 1$, the flux at the GB is cut off. The ion diffusion along the GB is beyond the present work and will be addressed in the future. As for the mechanical part, the continuity equation reads,

$$T_n^+ = T_n^- = T_n(\Delta_n, \Delta_t), \quad T_t^+ = T_t^- = T_t(\Delta_n, \Delta_t) \quad (2)$$

where T_n , T_t are the normal and tangential traction, respectively. Thereby Δ_n , Δ_t are the normal and tangential interface separation, respectively. According to Refs. [12,13], the traction-separation law can be derived from a potential, i.e., $T_n(\Delta_n, \Delta_t) = \delta \Psi_{CZM} / \delta \Delta_n$ and $T_t(\Delta_n, \Delta_t) = \delta \Psi_{CZM} / \delta \Delta_t$. The potential Ψ_{CZM} for a mixed-mode

Table 1
Material parameters of LiNi_xMn_yCo_zO₂ (NMC).

Name	Symbol and unit	Value
Diffusion coefficient	D [m ² s ⁻¹]	7.0×10^{-15}
Max. conc. of NMC particle	C_{\max} [mole m ⁻³]	38320
Youngs modulus	E [GPa]	140
Poisson coefficient	ν [-]	0.3
Partial molar volume	Ω [m ³ mol ⁻¹]	4.566×10^{-6}
Fracture energy	ϕ_n, ϕ_t [J m ⁻²]	2
Cohesive strength	$\sigma_{\max}, \tau_{\max}$ [MPa]	100
Non-ideality parameter	χ [-]	2.0
Applied C-rate	-	1C

fracture is thereby expressed as

$$\Psi_{\text{CZM}}(\Delta_n, \Delta_t) = \min(\phi_n, \phi_t) + \left[\Gamma_n \left(1 - \frac{\Delta_n}{\delta_n} \right)^\alpha \left(\frac{m}{\alpha} + \frac{\Delta_n}{\delta_n} \right)^m + (\phi_n - \phi_t) \right] \cdot \left[\Gamma_t \left(1 - \frac{|\Delta_t|}{\delta_t} \right)^\beta \left(\frac{n}{\beta} + \frac{|\Delta_t|}{\delta_t} \right)^n + (\phi_t - \phi_n) \right], \quad (3)$$

where ϕ_n and ϕ_t are the normal and tangential fracture energies, and where δ_n and δ_t further represent the final crack opening widths in the normal and tangential direction, respectively. The symbol $\langle \cdot \rangle$ denotes the *Macaulay bracket*, namely $\langle x \rangle = 0$ if $x < 0$, and $\langle x \rangle = x$ if $x \geq 0$. Whereby, the damage variable is expressed as $d = (\Delta_{\text{eff}} - \Delta_c) / (\delta_{\text{eff}} - \Delta_c)$. $\Delta_{\text{eff}} = \sqrt{\Delta_n^2 + \Delta_t^2}$ and $\delta_{\text{eff}} = \sqrt{\delta_n^2 + \delta_t^2}$ are the effective separation and crack opening width for the mixed case, and Δ_c denotes the critical separation for damage initiation.

For the grain interior, we employ a mechanically coupled diffusion model used in our previous publications [14–17]. The mechanical equilibrium and the ion diffusion equation are

$$\nabla \cdot \boldsymbol{\sigma} = \mathbf{0}, \quad \frac{\partial c}{\partial t} = \nabla \cdot (M \nabla \mu), \quad (4)$$

where $\boldsymbol{\sigma}$ is the Cauchy stress tensor, $M = Dc(1 - c)$ describes the concentration-dependent mobility with D being the diffusion coefficient. In a thermodynamic consistent formulation, the chemical potential and the stress can be obtained from the corresponding variational derivatives of the system free energy, i.e., $\mu = \delta \psi / \delta c$, $\boldsymbol{\sigma} = \delta \psi / \delta \mathbf{E}$, with \mathbf{E} being the Green–Lagrange strain tensor. Accordingly, the free energy $\psi = \psi^c + \psi^e$ with the bulk free energy and the elastic energy have the following form:

$$\psi^c = c \ln c + (1 - c) \ln(1 - c) + \chi c(1 - c), \quad (5)$$

$$\psi^e = \det \mathbf{F}^c \left[\frac{K}{2} \left(\frac{\det \mathbf{F}}{\det \mathbf{F}^c} - 1 \right)^2 + \frac{G}{2} (\bar{I}_1 - 3) \right]. \quad (6)$$

Here, χ is a parameter for non-ideal solution, K and G respectively denote the bulk and shear moduli. \bar{I}_1 is the first invariant of the right Cauchy–Green deformation tensor. $\det \mathbf{F}$ and $\det \mathbf{F}^c$ are the Jacobian determinants of the deformation gradient tensor \mathbf{F} and its chemical part, respectively. Note that the structural transition is neglected.

The finite element software MOOSE [18,19] is applied to implement the outlined model. The Discontinuous Galerkin method is applied for the discontinuity of displacement and concentration at GBs. Aggregates with radius $R = 5 \mu\text{m}$ comprising 89, 174 and 413 grains are considered separately, to achieve representative statements. The 1C-rate discharge process is applied for all the aggregates. The material properties of NMC are taken from Refs. [6,7,20–23] and listed in Table 1.

We first demonstrate the impact of the across-GB transport between grains on the fracture pattern of the aggregates by comparing the results with and without the across-GB transport, as illustrated in Fig. 2. Thereby the anisotropy of the grains is ignored, its influence is demonstrated in later examples. Fig. 3 compares the concentration and damage fields within the considered aggregates. It can be seen that for all the grain sizes, the across-GB transport results in stronger concentration inhomogeneities, together with noticeable concentration hot spots and higher degrees of interface damage, which is confirmed by the elemental mapping in Fig. 3c resulting from experiments. Furthermore, we can recognize pronounced concentration jumps towards inner grains. These result in a larger volume expansion of the outer grains and hence in a strong strain mismatch along GBs between neighboring grains. Once cracks open up wide enough, the flux between neighboring grains is cut off and the lithium cannot diffuse towards the center of the aggregate. Instead, the lithium will accumulate in the outer grain layer, which can further accelerate the damage of NMC particles. Several small grains are even “squeezed” out from their environment. Moreover, for the case with smaller grain size (higher number of grains), the aggregates experience stronger surface delamination, which can be observed from the SEM image of NMC particles shown in Fig. 3d. We attribute this effect to the shorter interaction distance of the stresses between neighboring grains. In the cases without the across-GB transport, on the other hand, the concentration field varies much smoother along the aggregate’s radius. The strain mismatch is hence comparatively small and cracks mainly form in the core of the aggregate, similar to the results shown in the mentioned literature. Subsequently, several small cracks will grow away from the main crack. The surface delamination is thereby suppressed due to the absence of surface layer blocking effects. On the other hand, experiments also confirm that by adding a glue-nanofiller between the grains [24] or performing nanoscale surface treatment of grains with a mixed ethanol solution [25], the interfacial bonding can be enhanced and the cracks can be suppressed. Thereby, both the GBs with stronger mechanical strength (namely a higher fracture energy) and the GBs with better ion conductivity (resulting in a stronger across-GB transport with fewer concentration jumps) are suggested to alleviate cracks and improve the chemo-mechanical performance of the particle.

We now analyze the influence of the anisotropy of elasticity and chemical strain on the crack patterns of NMC particles, and thereby the GB model with across-GB transport is regarded. The elastic strain energy is treated as $\psi^e = \frac{1}{2} \mathbf{E} : \mathbb{C} : \mathbf{E}$, where \mathbf{E} denotes the Green–Lagrange strain tensor and where \mathbb{C} represents the anisotropic elasticity tensor [26]. Following [27], we employ a stiffness of the in-plane axis that is two times larger than that of the out-of-plane axis. Thus the Young’s modulus of different axes is considered as $E_{xx} = E_{yy} = 2E_{zz} = 140 \text{GPa}$ locally. In addition, the anisotropic eigenstrain is introduced as $c\Omega/3\mathbf{I}$ for the anisotropic volume expansion, where $\mathbf{I} = [-0.02 \quad -0.02 \quad 0.01 \quad 0 \quad 0 \quad 0]$ is an anisotropic tensor in Voigt notation. Aggregation of randomly oriented grains thus results in macroscopically isotropic properties, whereas the properties of individual grains remain locally anisotropic.

If the aggregate is modeled as a uniform continuum and the across-GB transport is ignored, a domain wall migrates through the aggregate in the radial direction, separating the exterior regions of high concentration from those with a low concentration in the interior. The strain mismatch is concentrated along the concentration gradient, as are the first principal stresses (σ_{sp1}). During initial states of discharge, a tensile stress state is established in the aggregate center, which is relaxed by the formation and the subsequent (low) growth of cracks. The introduction of anisotropy changes the behavior insofar as that the grains now try to expand along their randomly oriented lattice directions. The regular distribution of

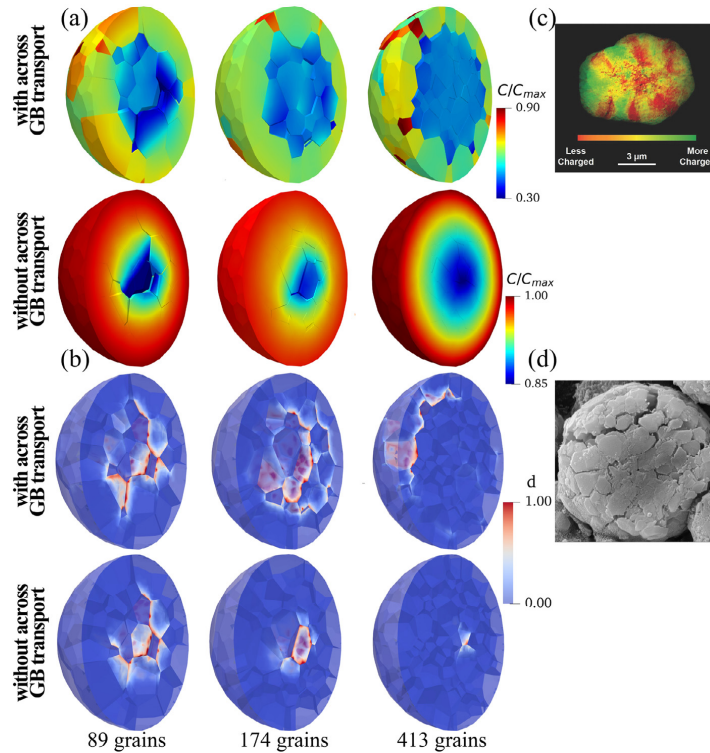


Fig. 3. Comparison of the concentration distribution and the resulting crack patterns between the cases with (a) and without (b) across-GB transport. Concentration hot spots and surface layer delamination are visible in the cases with this interaction, which are confirmed by (c) reprint of the elemental mapping from *ex situ* transmission X-ray microscopy (Reproduced with permission from Gent et al. [8]. Copyright 2016 by Wiley Online Library), (d) reprint of cracks in NMC particle after the first cycle of charge/discharge using SEM imaging (Reproduced with permission from Sun et al. [4]. Copyright 2016 by Elsevier).

σ_{sp1} along phase interfaces is now replaced by a scattered distribution, and the stresses show a much wider range compared to the isotropic case. In particular, the outermost grains show a “local” core-shell distribution of stresses, with compressive stresses in the outer layers and strong tensile stresses towards the center of the aggregate. This induces a strong strain mismatch along the GBs. The cracks formed at the aggregate center are thus “pulled” away from the interior of the grain agglomerate. Along the main crack branches, the stress relaxation results in a redistribution of ions due to stress-assisted diffusion effects [28].

However, the behavior changes once the across-GB transport is included, although the scattered distribution of σ_{sp1} is sustained. During the initial stages of discharge, cracks nucleate in the aggregate center and are pulled outward by the strain mismatch in its outer layers. The crack growth thereby proceeds faster than the diffusion process. Consequently, the ion transport towards the aggregate center is cut off, resulting in the aforementioned surface layer blocking effect. The strong strain mismatch between the outermost grains and their neighbors towards the aggregate center thereby attracts the cracks to radiate outwards. Concurrently, some of the outermost grains de-laminate from the agglomerate. The introduction of the piecewise anisotropic elastic behavior appears to reduce the severity of this damaging process. The anisotropic chemical expansion of neighbor grains appears to accommodate the strain mismatch between neighbor grains. The distribution of σ_{sp1} is now shifted towards a more concentric arrangement, and the magni-

tude of stresses is slightly reduced. As a result, the amount of damage in the grain aggregate is slightly reduced, as shown in Fig. 4.

To further understand and summarize the difference, we determined the damage fraction as shown in Fig. 4c. The damage fraction is defined as $\frac{1}{A_{\Gamma}} \int_{\Gamma} dA$, where Γ denotes the GB surface area. It is clear that the across-GB transport enhances significantly the damage for both cases with and without anisotropy. Nevertheless, the anisotropy plays a different role depending on the fact whether the across-GB transport is regarded or not. If this interaction is ignored, the anisotropy obviously promotes the damage development, as it is shown by the comparison between the solid red line and dashed red line. This is in contrast to the results if the across-GB transport is considered, as shown by the comparison of the black solid and dashed lines. More particularly, the anisotropy retards the damage development slightly. This is likely due to the random/scattered nature of the anisotropy mismatch, which partially relaxes the mismatch strain induced by the hot spots.

A chemo-mechanical damage model has been developed to study the fracture of cathode materials with polycrystalline structure. It includes the across-GB transport and the cohesive traction-separation law along GBs. Simulation results of NMC polycrystals indicate that if the diffusion of the aggregate is modeled as a single homogeneous particle, the diffusion-induced damage is comparable to that induced by the anisotropy mismatch. However, this significantly underestimates the damage since the model cannot reproduce the enhanced chemical inhomogeneity and thus the

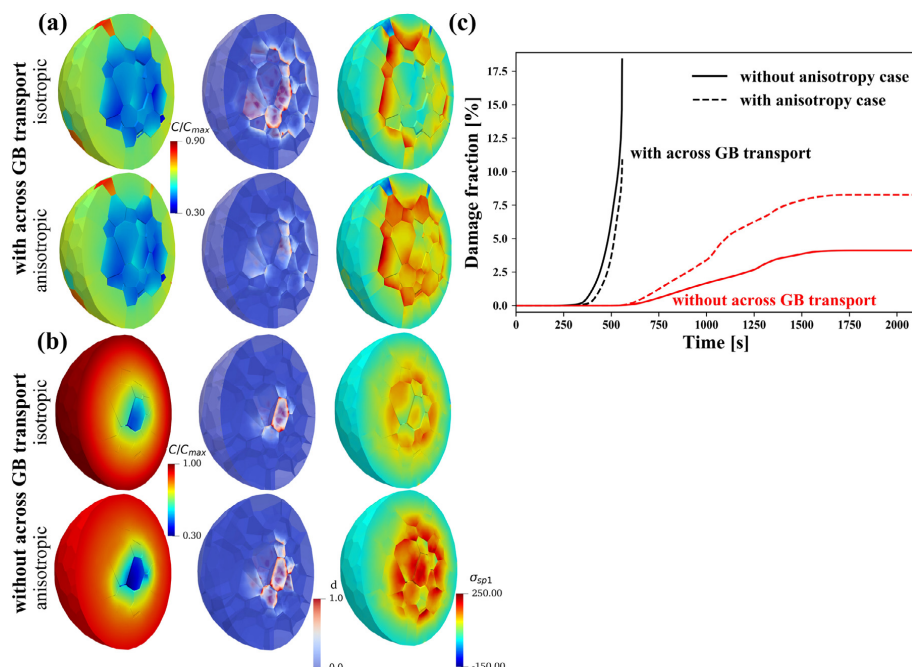


Fig. 4. Influence of the anisotropy on the distribution of the concentration, damage state, and the maximum principal stress σ_{sp1} (MPa) in aggregates with (a) and without (b) across-GB transport, (c) the accumulated damage within an aggregate (with 174 grains) for the cases with/without anisotropy or across-GB transport.

surface layer delamination. For this purpose, one should consider the across-GB transport and its dependency on the interface damage. Interestingly, the anisotropy of the elasticity and chemical strain tends to retard the damage induced by this transport.

Declaration of Competing Interest

The authors declare that they have no known competing financial interests or personal relationships that could have appeared to influence the work reported in this paper.

Acknowledgment

The authors gratefully acknowledge the computing time granted on the Hessian High-Performance Computer "Lichtenberg".

Supplementary materials

Supplementary material associated with this article can be found, in the online version, at doi:10.1016/j.scriptamat.2020.03.027

References

- [1] C. Daniel, D. Mohanty, J. Li, D. L. Wood, in: AIP, pp. 26–43.
- [2] J.E. Harlow, X. Ma, J. Li, E. Logan, Y. Liu, N. Zhang, L. Ma, S.L. Glazier, M.M.E. Cormier, M. Genovese, S. Buteau, A. Cameron, J.E. Stark, J.R. Dahn, J. Electrochem. Soc. 166 (2019) A3031–A3044.
- [3] D.J. Miller, C. Proff, J. Wen, D.P. Abraham, J. Bareño, Adv. Energy Mater. 3 (2013) 1098–1103.
- [4] G. Sun, T. Sui, B. Song, H. Zheng, L. Lu, A.M. Korsunsky, Extreme Mech. Lett. 9 (2016) 449–458.
- [5] Y. Zhang, C. Zhao, Z. Guo, Int. J. Mech. Sci. 155 (2019) 178–186.
- [6] R. Xu, L. de Vasconcelos, J. Shi, J. Li, K. Zhao, Exp. Mech. 58 (2018) 549–559.
- [7] R. Xu, K. Zhao, J. Mech. Phys. Solids 121 (2018) 258–280.
- [8] W.E. Gent, Y. Li, S. Ahn, J. Lim, Y. Liu, A.M. Wise, C.B. Gopal, D.N. Mueller, R. Davis, J.N. Weker, J.-H. Park, D. Seok-Kwang, C. William, Adv. Mater. 28 (2016) 6631–6638.
- [9] Y. Zhao, L.R. De Jesus, P. Stein, G.A. Horrocks, S. Banerjee, B.X. Xu, RSC Adv. 7 (2017) 41254–41264.
- [10] H.-H. Sun, A. Manthiram, Chem. Mater. 29 (2017) 8486–8493.
- [11] A. Singh, S. Pal, Int. J. Plast. (2019).
- [12] K. Park, G.H. Paulino, J.R. Roesler, J. Mech. Phys. Solids 57 (2009) 891–908.
- [13] K. Park, G.H. Paulino, Eng. Fract. Mech. 93 (2012) 239–262.
- [14] Y. Zhao, P. Stein, B.X. Xu, Comput. Methods Appl. Mech. Engrg. 297 (2015) 325–347.
- [15] Y. Bai, Y. Zhao, W. Liu, B.X. Xu, J. Power Sources 422 (2019) 92–103.
- [16] Y. Zhao, P. Stein, Y. Bai, M. Al-Siraj, Y. Yang, B.X. Xu, J. Power Sources 413 (2019) 259–283.
- [17] B.-X. Xu, Y. Zhao, P. Stein, GAMM-Mitteilungen 39 (2016) 92–109.
- [18] D. Gaston, C. Newman, G. Hansen, D. Lebrun-Grandie, Nucl. Eng. Des. 239 (2009) 1768–1778.
- [19] B.S. Kirk, J.W. Peterson, R.H. Stogner, G.F. Carey, Eng. Comput. 22 (2006) 237–254.
- [20] L. de Vasconcelos, N. Sharma, R. Xu, K. Zhao, Exp. Mech. 59 (2019) 337–347.
- [21] R. Xu, H. Sun, L.S. de Vasconcelos, K. Zhao, J. Electrochem. Soc. 164 (2017) A3333–A3341.
- [22] K. Min, E. Cho, Phys. Chem. Chem. Phys. 20 (2018) 27115–27124.
- [23] Y. Bai, C. Dong, Z. Liu, Compos. Struct. 128 (2015) 54–69.
- [24] H. Kim, S. Lee, H. Cho, J. Kim, J. Lee, S. Park, S.H. Joo, S.H. Kim, Y.-G. Cho, H.K. Song, et al., Adv. Mater. 28 (2016) 4705–4712.
- [25] H. Kim, M.G. Kim, H.Y. Jeong, H. Nam, J. Cho, Nano Lett. 15 (2015) 2111–2119.
- [26] T. Belytschko, W.K. Liu, B. Moran, K. Elkhodary, Nonlinear Finite Elements for Continua and Structures, John Wiley & Sons, 2013.
- [27] H. Sun, K. Zhao, J. Phys. Chem. C 121 (2017) 6002–6010.
- [28] P. Stein, B. Xu, Comput. Methods Appl. Mech. Engrg. 268 (2014) 225–244.

5.4 Publication B

Two-level modeling of lithium-ion batteries

Yang Bai, Ying Zhao, Wei Liu, Bai-Xiang Xu, Journal of Power Sources 422 (2019) 92-103.



Contents lists available at ScienceDirect

Journal of Power Sources

journal homepage: www.elsevier.com/locate/jpowsour

Two-level modeling of lithium-ion batteries

Yang Bai^a, Ying Zhao^b, Wei Liu^a, Bai-Xiang Xu^{a,*}

^a *Mechanics of Functional Materials Division, Department of Materials Science, TU Darmstadt, Otto-Berndt-Straße 3, 64287, Darmstadt, Germany*

^b *Department of Engineering, University of Cambridge, Trumpington Street, CB2 1PZ, Cambridge, UK*



HIGHLIGHTS

- Two-level framework incorporate multiphysical particle level modeling to cell mode.
- The existence of stresses can enhance the bulk diffusion improve the cell performance.
- The ellipsoidal particles have better cell performance than spherical particles.
- Diffusion dynamic has a larger impact on the cell performance than particle shapes.
- Capacity can be improved as the stiffness of the particle increase.

ARTICLE INFO

Keywords:

Pseudo 2D model
Mechanical coupling
Phase separation
Lithium-ion battery
Two-level modeling

ABSTRACT

The widely used Pseudo-Two-Dimensional (P2D) cell model for Li-ion batteries is generally based on a simplified lithium diffusion model of active particles with certain geometry. In this work, we propose a two-level framework, which extends the P2D cell model and incorporates a mechanically coupled phase-field Cahn–Hilliard diffusion model of active particles. The phase-field model allows more detailed diffusion study in particles of general geometry and includes the full coupling of the mechanics and phase separation. To improve the computational efficiency, we manage to reduce one degree of freedom at the cell level by treating the ion flux between the electrolyte and active particle as a dependent quantity. The two-level framework is validated against the original one and applied to study the impact of particle geometry, finite deformation elasticity and phase separation on the cell performance. Results show that the oblate particle has better cell performance than other spheroidal particles. It is attributed to the mechanical drifting at the higher curvature.

1. Introduction

The lithium-ion batteries (LIB) are widely used in electronic devices and electric vehicles, and are a promising solution for the storage of renewable energy, because of their high energy and power density. Theoretical and numerical efforts have contributed greatly to the understanding of both the mechanism and degradation, and serve as effective tools for battery designs.

On one hand, there are efficient cell models for the simulation of the electrochemical performance of a unit cell. Thereby the surface concentration of the active particles, and the flux between the electrolyte and active particles are usually obtained through the simplified particle diffusion models or even the approximate solution. In 1993, Doyle et al. [1–3] presented a pseudo-two-dimensional (P2D) model to estimate the electrochemical performance of lithium-ion battery, where the one-dimensional transport from the lithium anode through the separator into

the cathode was modeled macroscopically based on the concentrated solution theory. While the kinetics of lithium diffusion inside the cathode particles was simplified as 1D case along the radius direction for the symmetry of the spherical particles. The electrochemical interaction between the active particles and electrolyte was described via the Butler–Volmer relation. Later a full cell model has been presented by Fuller [4]. For the models listed above, the coupling between the electrolyte and particles only depends on the flux calculated from the Butler–Volmer equation, where the mechanical influence and phase separation are disregarded. Christensen et al. [5] combined the P2D model with their diffusion induced stress model to study the stresses generated during the galvanostatic operation. Their results show that the pressure diffusion and lattice distortion have more significant impact on the electrochemical performance if the finite deformation theory is regarded rather than the small deformation kinematics. Besides stresses, the phase transformation inside the spherical particle has

* Corresponding author.

E-mail address: xu@mfm.tu-darmstadt.de (B.-X. Xu).

<https://doi.org/10.1016/j.jpowsour.2019.03.026>

Received 18 September 2018; Received in revised form 19 February 2019; Accepted 8 March 2019

0378-7753/ © 2019 Elsevier B.V. All rights reserved.

also been modeled by Renganathan et al. [6]. In their work the P2D model was employed at the cell level, while the mechanically coupled diffusion behavior in the coexisting two phases was considered at the cathode particle level. Due to the complexity of the large set of the coupled partial differential equations (PDEs), the simulation using this model is computationally rather expensive. In order to improve the computational efficiency, Golmon et al. [7] extended the P2D model based on the multiscale approach. In their work the kinetics of the battery cell was analyzed through a 3D battery model, which was modeled at the cell level, while the diffusion behavior of the active particles embedded in the deformable matrix was modeled at the particle level. The electro-chemo-mechanical interactions between the active particles and host materials were considered, the mechanical response between the battery cell and active particles was coupled through the Mori–Tanaka (M–T) homogenization approach [8]. However, their studies were limited to the spherical particles, and the implementation was simplified to 1D case at both the cell level and particle level. Xiao and coworkers [9] extended this multiscale approach to study the stress distribution of the separator in battery cell. Fu et al. [10] further coupled this model with thermal effect and applied it in a lithium ion polymer battery. Wu and coworkers [11] extended this model by considering the 2D multiphysical and microstructural resolved model with the realistic electrode geometry for a $\text{Li}_x\text{C}_6/\text{PP}/\text{Li}_y\text{Mn}_2\text{O}_4$ cell, the stress distribution in the active particles and binder has been discussed in details. Later, the stress generation caused by the phase transitions and lithium intercalation inside the nickel-manganese-cobalt (NMC) particle with realistic 3D microstructures, which were reconstructed from FIB-SEM and synchrotron X-ray tomography, has been modeled [12]. Behrou et al. [13] extended this multiscale model to consider the damage of the active particle in a solid state battery, their results show that the damage evolution inside the particle has a significant contribution to capacity fade. Even though this multiscale model has been widely applied to consider the multiphysics coupling and the influence of phase transition of particles with complex micro-structure on the battery [14], the study including the impact of the active particle's phase heterogeneity and the related mechanics on battery cell performance is absent.

On the other hand, the study focusing on the particle level has been carried out extensively. They can be used to include the multiphysics and defects at the particle level. Christensen et al. [15] presented a mathematical model to study the volume expansion and stress evolution of the isotropic spherical particles due to the lithium insertion and extraction. The fracture of the active electrode particle has been predicted based on this model, where the solid state diffusion in a one-phase material and moving boundary insertion in a two-phases material have been considered [16]. The intercalation-induced stresses inside spherical and ellipsoidal LiMn_2O_4 particles have been modeled and simulated by Zhang et al. [17]. Park et al. [18] presented a volume expansion and diffusion model to evaluate stresses arising due to phase transition of the 3D LiMn_2O_4 particles based on the finite element approach. Their results show that phase transition leads to a larger stress than solid-state intercalation dose. Stein et al. [19] presented a three-dimensional chemo-mechanical coupled model to study the intercalation-induced stresses inside the ellipsoidal particle based on the finite element method with the newly developed isogeometric analysis (IGA) [20,21]. Later the impact of the surface tension on the electrochemical behavior of nanoscale spherical and ellipsoidal particles has also been investigated through a modified Butler–Volmer relation to account for the chemo-mechanical interaction [22,23]. The electrode particle models which account for the phase separation and mechanical stresses have also been proposed and simulated in great depth. To account for the phase separation, a sharp interface between two phases has been presented in several models and the lithium insertion reactions were considered to occur at the interface between the phases [24–26]. Since the track of the interface is crucial in these models, advanced computational techniques are needed, which is a challenge in

the numerical simulations, especially when the geometry is complex. To overcome this issue, the phase-field models based on the Cahn–Hilliard equation [27,28] have been developed, which assume a diffuse interface between phases [29–36]. This method avoids the track of the interface, which evolves naturally so that the overall energy is minimized. In these models, the mechanical stresses arising during lithiation and delithiation can be well predicted under different charging/discharging conditions, with different particle geometries and electrode materials. The mechanically coupled phase-field model has been successfully applied for the hyperelastic solids by Zhao and Xu [35,37], where a single particle was investigated to study the stress coupled Cahn–Hilliard-type diffusion behavior inside the particle. The phase-field model of the fracture coupled with anisotropic Cahn–Hilliard-type diffusion in the large deformation regime has also been developed [38]. Later the interconnected electrode particles have been considered to study the lithium transport in the particles and interface reactions across the particle network [39,40].

While the battery cell models and the particle models have been successfully applied and become successful separately, there are insufficient efforts, which combine the two levels' modeling with the most recent advances. Such modeling can, however, take the advantages of both the cell models (e.g. numerical access to the cell performance and efficiency) and those of the particle models (e.g. accuracy of the diffusion solution, complex particle geometry, and consideration of the defects in the particles). In this work, we aim at a framework to incorporate our multiphysical modeling at the particle level into the P2D cell model. To further improve the computational efficiency, we manage to reduce one degree of freedom (DoF) at the cell level by treating the lithium-ion flux between the electrolyte and active particles as a dependent quantity. As examples, we demonstrate how the framework can be used directly to reveal the impact of particle shape, finite deformation elasticity, and phase separation in particles on the cell performance.

The article is organized as follows. In Section 2.1, the two-level framework is presented, with details of the modified cell model given in Section 2.2, and of the mechanically coupled Cahn–Hilliard-type diffusion model at the particle level in Section 2.3. In particular, the bridging between the two levels is detailed in Section 2.4. After the proposed framework is benchmarked against the results of the original P2D model, the representative results are provided in Section 3 to demonstrate the capability of the extended model. Finally, concluding remarks are given.

2. Model

2.1. The two-level framework

The schematic in Fig. 1 outlines the two-level framework. In the following, the framework is presented on a battery half cell, but the extension to a full cell is straightforward. The cell consists of a Li foil as the negative electrode, a composite positive electrode and a separator with the liquid electrolyte throughout. The diffusion and electrostatics at the cell level are described in the X coordinate. As illustrated in Fig. 1, the diffusion and electrostatic variation at the cell level are assumed only occur along one direction, which is denoted by X. Although the presented framework is based on the 1D case, it can be extended to account for 2D and 3D configurations. The degrees of freedom (DoFs) at this level are denoted by the Li^+ concentration c_2 in electrolyte phase, the potential ϕ_2 in electrolyte phase, and the potential ϕ_1 in particle phase, respectively. According to Doyle's work [1], the subscripts 1,2 represent the particle phase and electrolyte phase, respectively. They are governed by an electrochemical cell model. At each point of interest at the cell level, a representative particle is attached and the particle simulation will be carried out concurrently. To describe the electro-chemo-mechanical model at the particle level, the lithium concentration c_1 , the lithium chemical potential μ and the displacement field \mathbf{u} are

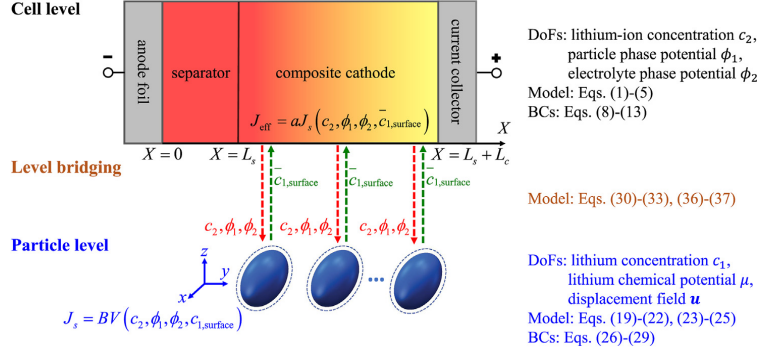


Fig. 1. Outline of the two-level framework.

adopted as the DoFs for the point of interest inside an active particle, respectively. They are spatially resolved by the particle coordinates \mathbf{x} . Note that the simulations at both levels share the same time scale. Thereby the bridging between two levels has to be done for each corresponding point at the cell level at each time step.

In order to explain the framework in more details, a flowchart of the two-level framework is given in Fig. 2. For each point of interest at the cell level, given the state c_2^t , ϕ_1^t and ϕ_2^t at time t^t , and the averaged surface concentration $\bar{c}_{1,\text{surface}}^t$ of the particles with general geometry, one can obtain the effective pore wall flux J_{eff} by using the Butler–Volmer reaction model and the definition of effective flux, namely, Eqs. (30) and (37). Applying J_{eff} to the electrochemical model in the cell, for which the governing equations and the boundary conditions are given in details in Section 2.2, one obtains the update for the DoFs c_2^{t+1} , ϕ_1^{t+1} and ϕ_2^{t+1} at the next time $t^{t+1} = t^t + \Delta t$, as described in Fig. 2, where Δt denotes the time increment at the cell level. Simultaneously, the DoFs c_2^{t+1} , ϕ_1^{t+1} and ϕ_2^{t+1} will be passed down to the attached particle simulation, as illustrated by the dashed ‘L’ shaped arrow in the flowchart. These quantities are required to calculate the averaged surface concentration $\bar{c}_{1,\text{surface}}^{t+1}$ of the particle at time t^{t+1} . More particularly, the particle level’s simulation starts with the previous state c_1^t , μ^t and \mathbf{u}^t at time t^t , and is subjected to a gradually changing flux till the time t^{t+1} is reached. In principle, any mechanically coupled particle model can be applied here to achieve the numerical solution of the diffusion and the deformation of the particles. In this work, an example model is given in details in Section 2.3. Note that both the diffusion inside the particle and the electrochemical reaction on the surface of the particle are time dependent. To obtain a more accurate solution, the integration between the time t^t and t^{t+1} is refined through the time step $\Delta t_{\text{particle}}$, as indicated by the j loop in the flowchart. After each time increment of $\Delta t_{\text{particle}}$, the flux on the surface of the particle is recalculated, until the time $t = t^t + j * \Delta t_{\text{particle}}$ reaches $t = t^{t+1}$. It passes c_1^{t+1} , μ^{t+1} and \mathbf{u}^{t+1} , and particularly the averaged surface concentration $\bar{c}_{1,\text{surface}}^{t+1}$ back to the cell level calculation, ready for the iteration in the next time step. In general, any applicable numerical methods can be applied here to solve the problems of the cell level and particle level. In current work, the finite element methods are applied to both.

In order to improve the computational efficiency, we treat the lithium-ion flux J_s between the electrolyte and active particles as a dependent quantity. This is different from Doyle’s work [1], where instead of solving the diffusion equation of the particle, the surface concentration of the particle was adopted and expressed via a semi-analytical solution based on J_s , and also the current and history value of $c_{1,\text{surface}}$. In other words, both the $c_{1,\text{surface}}$ and J_s were treated as two independent degrees of freedom (DoFs).

2.2. Electrochemical model at cell level

At the cell level, the electrochemical transport behavior of Li^+ ions through the electrolyte and the current contributions come from the particle phase and electrolyte phase are described by the following equations [1,7]:

$$\varepsilon \frac{\partial c_2}{\partial t} = D_{\text{eff}} \frac{\partial^2 c_2}{\partial X^2} - \frac{1}{F} \frac{\partial t_+^0}{\partial c_2} \frac{\partial c_2}{\partial X} + (1 - t_+^0) J_{\text{eff}}, \quad (1)$$

$$\frac{\partial i_1}{\partial X} + F J_{\text{eff}} = 0, \quad (2)$$

$$\frac{\partial i_2}{\partial X} - F J_{\text{eff}} = 0. \quad (3)$$

where t_+^0 is the transference number which can be obtained from the experimental data. The source term J_{eff} denotes the effective pore wall flux, which equals to zero in the separator domain. i_1 and i_2 represent the currents in the particle phase and electrolyte phase, respectively, defined as [1,7]:

$$i_1 = -\lambda \frac{\partial \phi_1}{\partial X} \quad (4)$$

$$i_2 = -\kappa_{\text{eff}} \left[\frac{\partial \phi_2}{\partial X} - \frac{RT}{F} (1 - t_+^0) \frac{\partial \ln c_2}{\partial X} \right] \quad (5)$$

where λ denotes the conductivity coefficient of the particle phase, κ_{eff} represents the effective conductivity coefficient of the electrolyte phase based on the porosity coefficient ε . R , T and F are the gas constant, temperature and faraday constant, respectively. In Eq. (5), a modified Ohm’s law is applied, where $\frac{RT}{F} (1 - t_+^0) \frac{\partial \ln c_2}{\partial X}$ denotes the contribution of Li^+ ion to the current of electrolyte phase. The bruggeman relation is adopted for the effective transport properties in the porous cathode [1,2]:

$$D_{\text{eff}} = D_2 \varepsilon \quad (6)$$

$$\kappa_{\text{eff}} = \kappa_{\infty} \varepsilon^{\text{Brugg}} \quad (7)$$

where D_2 represents the diffusion coefficient of the electrolyte phase, in this work a constant D_2 is applied in the simulation. κ_{∞} denotes the conductivity coefficient of the electrolyte phase.

The related boundary conditions for the equations at the cell level are listed as below:

$$-D_{\text{eff}} \frac{\partial c_2}{\partial X} = \frac{I(1 - t_+^0)}{F} \quad \text{at} \quad X = 0 \quad (8)$$

$$-D_{\text{eff}} \frac{\partial c_2}{\partial X} = 0 \quad \text{at} \quad X = L_s + L_c \quad (9)$$

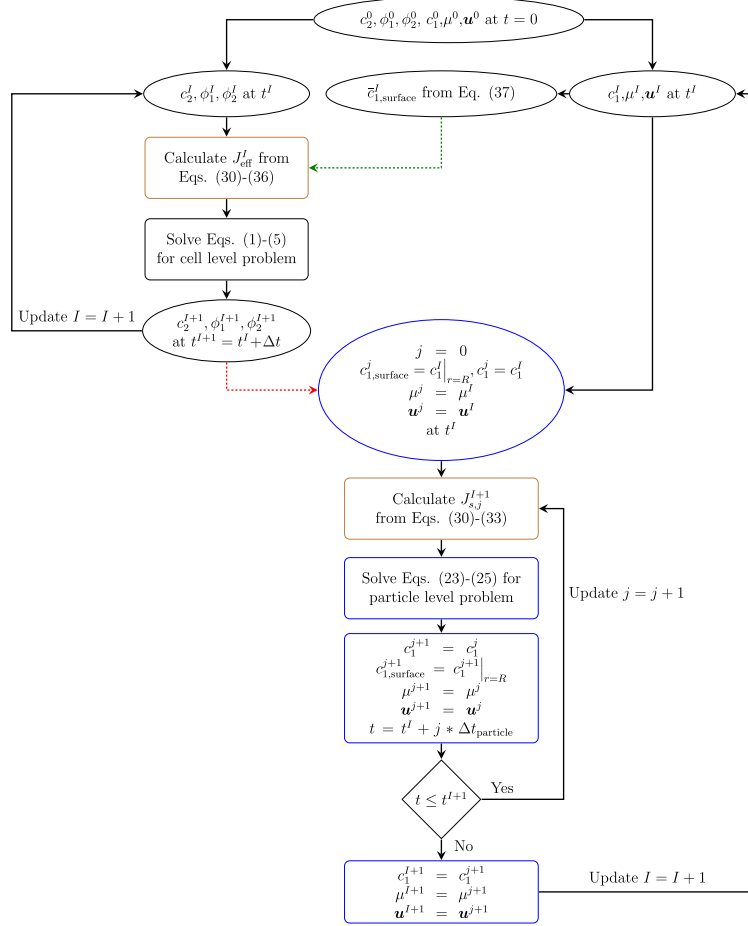


Fig. 2. Flowchart of two-level framework. The color and line style of the arrows and boxes match with those used in Fig. 1. (For interpretation of the references to color in this figure legend, the reader is referred to the Web version of this article.)

$$-\lambda \frac{\partial \phi_1}{\partial X} = 0 \quad \text{at} \quad X = 0 \quad (10)$$

$$-\lambda \frac{\partial \phi_1}{\partial X} = I \quad \text{at} \quad X = L_s + L_c \quad (11)$$

$$-\kappa_{\text{eff}} \left[\frac{\partial \phi_2}{\partial X} - \frac{RT}{F} (1 - l_+^0) \frac{\partial \ln c_2}{\partial X} \right] = I \quad \text{at} \quad X = 0 \quad (12)$$

$$-\kappa_{\text{eff}} \left[\frac{\partial \phi_2}{\partial X} - \frac{RT}{F} (1 - l_+^0) \frac{\partial \ln c_2}{\partial X} \right] = 0 \quad \text{at} \quad X = L_s + L_c \quad (13)$$

where I denotes the applied constant current density for the galvanostatic discharge process. $X = 0$ represents the boundary between the anode foil and separator, $X = L_s + L_c$ represents the boundary between the cathode and current collector.

2.3. Electro-chemo-mechanical model at particle level

In this section, we adopt Zhao's model [35] for modeling the diffusion behavior at the particle level, where the mechanically coupled

Cahn–Hilliard–type diffusion model is taken into consideration inside the particles. For the sake of completeness, the model is summarized in the following. For the points inside the particle, the lithium concentration c_1 , the lithium chemical potential μ and the displacement field \mathbf{u} are the independent DoFs, respectively. During the charge and discharge process, stresses will arise due to the changes in the lattice dimensions and crystal structures, which are associated with the overall volume changes and phase transformation, respectively. In addition, the formation of the two phases system can also lead to high stresses, in particular at the phase interface in cathode materials [41,42]. As a consequence, the finite deformation theory is applied for the mechanics. The deformation gradient $\mathbf{F} = \mathbf{I} + \nabla \mathbf{u}$ can thus be decomposed into the elastic distortion part \mathbf{F}^e and the (de-)intercalation-induced swelling part \mathbf{F}^c as follow:

$$\mathbf{F} = \mathbf{F}^e \mathbf{F}^c \quad \text{with} \quad J = \det \mathbf{F} = J^e J^c \quad (14)$$

where $J^e = \det \mathbf{F}^e$ and $J^c = 1 + \Omega c_1^R$, the system free energy density of the cathode particle is defined as follow:

$$\psi_R(c_1^R, \nabla_R c_1^R, \mathbf{C}) = \psi_R^c(c_1^R) + \psi_R^i(\nabla_R c_1^R) + \psi_R^e(c_1^R, \mathbf{C}) \quad (15)$$

where $\psi_R^c(c_1^R)$, $\psi_R^i(\nabla_R c_1^R)$ and $\psi_R^e(c_1^R, \mathbf{C})$ denote the bulk free energy, the interface free energy and the elastic free energy, respectively. Here the symbol R for both the superscript and the subscript indicates those parameters are defined on the reference configuration, c_1^R represents the normalized concentration of lithium in the cathode particle, and $\mathbf{C} = \mathbf{F}^T \mathbf{F}$ is the right Cauchy–Green deformation tensor [43]. According to Zhao's work [35], these three different contributions of free energies are defined in:

$$\psi_R^c = c_1^R \ln c_1^R + (1 - c_1^R) \ln(1 - c_1^R) + \chi c_1^R (1 - c_1^R) \quad (16)$$

$$\psi_R^i(\nabla_R c_1^R) = \frac{1}{2} \kappa |\nabla_R c_1^R|^2 \quad (17)$$

$$\psi_R^e(c_1^R, \mathbf{C}) = J^c \left[\frac{K}{2} \left(\frac{J}{J^c} - 1 \right)^2 + \frac{G}{2} (\bar{I}_1 - 3) \right] \quad (18)$$

To allow for the coexistence of two phases, $\chi = 2.5$ is used in this work, the single phase diffusion is applied by setting $\chi = 1.0$ in the simulation, κ denotes the interface parameter. The neo–Hookean model is employed in Eq. (18) for the cathode particles under large deformation, which can be easily extended to consider other type hyperelastic materials. K and G are the bulk modulus and shear modulus, respectively. $\bar{I}_1 = \text{tr}(\mathbf{C}) = J^{-\frac{2}{3}} \text{tr}(\mathbf{C})$ is the modified invariant, following the standard definition of the continuum mechanics [43]. Based on the free energies defined above, one can obtain the second Piola–Kirchhoff stress tensor and the chemical potentials as follow respectively:

$$\mathbf{S} = \frac{\partial \psi_R}{\partial \mathbf{E}} = \frac{2 \partial \psi_R^e}{\partial \mathbf{C}} = J^c \left[K J^e (J^e - 1) \mathbf{C}^{-1} + G J^{-\frac{2}{3}} \left(1 - \frac{1}{3} \bar{I}_1 \mathbf{C}^{-1} \right) \right] \quad (19)$$

$$\mu^c = \frac{\partial \psi_R^c}{\partial c_1^R} = \ln c_1^R (1 - c_1^R) + \chi (1 - 2c_1^R) \quad (20)$$

$$\mu^i = \frac{\partial \psi_R^i}{\partial c_1^R} = -\kappa \nabla_R^2 c_1^R \quad (21)$$

$$\mu^e = \frac{\partial \psi_R^e}{\partial c_1^R} = \frac{\Omega K}{2} [1 - (J^e)^2] + \frac{\Omega G}{2} (\bar{I}_1 - 3) \quad (22)$$

where $\mathbf{E} = \frac{1}{2}(\mathbf{C} - 1)$ is the Green–Lagrange strain tensor. The Cauchy stress can be obtained by $\boldsymbol{\sigma} = \frac{1}{J} \mathbf{F} \mathbf{S} \mathbf{F}^T$. The lithium concentration of the particles on the current configuration is then defined as $c_1 = c_1^R / J$. For each cathode particle, the mechanically coupled Cahn–Hilliard–type diffusion model is applied. In order to solve the fourth order Cahn–Hilliard equation, we use the mixed finite element formulation to split the fourth order equation into 2 second order equations:

$$\nabla \cdot \boldsymbol{\sigma} = 0 \quad \text{in } B \times (0, \mathcal{T}), \quad (23)$$

$$\frac{\partial c_1}{\partial t} = \nabla \cdot (\mathbf{M} \nabla \mu) \quad \text{in } B \times (0, \mathcal{T}), \quad (24)$$

$$\mu = \mu^c + \mu^i + \mu^e \quad \text{in } B \times (0, \mathcal{T}). \quad (25)$$

the related boundary conditions and initial conditions are listed below:

$$-\mathbf{M} \nabla \mu \cdot \mathbf{n} = J_s \quad \text{on } \partial B_c \times (0, \mathcal{T}), \quad (26)$$

$$\nabla c_1 \cdot \mathbf{n} = 0 \quad \text{on } \partial B \times (0, \mathcal{T}), \quad (27)$$

$$c_1(\mathbf{x}, 0) = c_1^0(\mathbf{x}) \quad \text{in } B \times (0, \mathcal{T}), \quad (28)$$

$$\mathbf{u} = \hat{\mathbf{u}} \quad \text{on } \partial B_u \times (0, \mathcal{T}). \quad (29)$$

the equations mentioned above at the particle level are described on the current configuration in the \mathbf{x} coordinate. \mathbf{M} is concentration-dependent mobility defined as $\mathbf{M} = D_1 c_{1,\max} c_1 (1 - c_1)$, where D_1 represents the diffusion coefficient of the particle and $c_{1,\max}$ denotes the maximum concentration of lithium inside the particle. The pore wall flux J_s is described by a Butler–Volmer equation based on the c_2 , ϕ_1 and ϕ_2 from the cell level, and the surface concentration of the particles from the

particle level, which is define as follow [1,2]:

$$J_s = \frac{i_0}{F} \left[c_{1,\text{surface}} \exp\left(\frac{1}{2} \frac{F \eta}{RT}\right) - (1 - c_{1,\text{surface}}) \exp\left(-\frac{1}{2} \frac{F \eta}{RT}\right) \right] \quad (30)$$

with

$$i_0 = F k_2 \sqrt{(c_{2,\max} - c_2) c_2} \quad (31)$$

$$\eta = \phi_1 - \phi_2 - U(c_{1,\text{surface}}) \quad (32)$$

where k_2 denotes the reaction rate for (de-)lithiation reaction, $c_{2,\max}$ represents the maximum concentration of the electrolyte phase. Initially, we assume all the cathode particles have homogeneous concentration. $U(c_{1,\text{surface}})$ is the open circuit potential (OCP), for LiMn_2O_4 material the following function is adopted in our simulation [2]:

$$\begin{aligned} U(c_{1,\text{surface}}) = & 4.06279 + 0.0677504 \tanh[-21.8502 c_{1,\text{surface}} + 12.8268] \\ & - 0.105734 [(1.00167 - c_{1,\text{surface}})^{-0.379571} - 1.575994] \\ & - 0.045 \exp[-71.69 (c_{1,\text{surface}})^2] \\ & + 0.01 \exp[-200 (c_{1,\text{surface}} - 0.19)] \end{aligned} \quad (33)$$

Note that, the calculation of the over potential η is based on the OCP, which is fitted from the experimental data. Following the thermodynamic definition, the OCP can also be calculated via:

$$FU_{\text{ocp}} = \mu^{\text{electrolyte}} - \mu^{\text{particle}} \quad (34)$$

where $\mu^{\text{electrolyte}}$ denotes the chemical potential of the electrolyte, while μ^{particle} represents the chemical potential of the particle defined in Eq. (25). The discussion of the local chemical potential based calculation is beyond the scope of this work, the details will be presented in future work.

2.4. Bridging of the cell level and the particle level

In present work, the pore wall flux J_s is treated as a dependent quantity, where the calculation depends on the quantities from both the cell level and particle level. For the model at the particle level, J_s is applied as a flux boundary condition. While for the problem of the cell level, the effective pore wall flux J_{eff} is applied as the source term in Eqs. (1)–(3). Following the same notation of Doyle's work [1,2], the relationship between these two fluxes can be expressed as follow:

$$J_{\text{eff}} = a J_s, \quad (35)$$

where a is defined as the specific surface area per unit volume. For more general cases, let's consider n identical particles with arbitrary shape, embedded in a cubic cathode with length L_c and cross section area A . For each particle, its volume and surface area are denoted by V and S , respectively. Once the porosity coefficient ε of the cathode is given, one can have the following relations:

$$L_c A (1 - \varepsilon) = n \times V, \quad \text{and} \quad a = \frac{n \times S}{L_c A} = \frac{S}{V} (1 - \varepsilon). \quad (36)$$

For the particles with general geometry, the following relation is applied:

$$J_{\text{eff}} = a J_s = \frac{S}{V} (1 - \varepsilon) J_s. \quad (37)$$

Since the size of the particle is so small compared with the length of the cell, the averaged surface concentration $\bar{c}_{1,\text{surface}}$ is adopted for the particles with general geometry, which is defined as follow:

$$\bar{c}_{1,\text{surface}} = \frac{\int_{\partial \Omega} c_1 dA}{\int_{\partial \Omega} dA}. \quad (38)$$

For the spherical particle with radius r , its volume and surface area can be expressed as $V = \frac{4}{3} \pi r^3$ and $S = 4 \pi r^2$, respectively. Consequently, the effective pore wall flux can be obtained by $J_{\text{eff}} = \frac{3}{r} (1 - \varepsilon) J_s$. In the

spherical case, $\bar{c}_{1,\text{surface}} = c_{1,\text{surface}}$ is applied, while for the particles with general geometry, $c_{1,\text{surface}}$ should be replaced by $\bar{c}_{1,\text{surface}}$ in Eqs. (30)–(33) at the cell level.

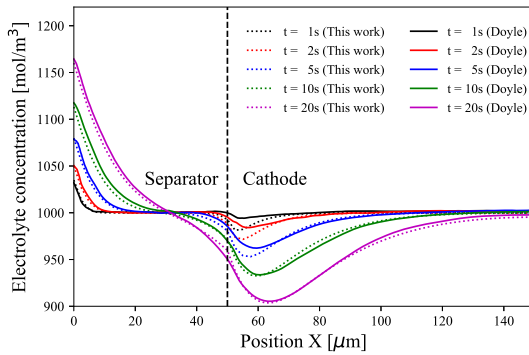
In order to bridge these two levels, the two-level simulation approach is adopted in present work as shown in Fig. 2. Temporally, only one scale is considered in the two-level simulation, where the backward Euler (BE) integration scheme with the adaptive time stepping algorithm is applied. Staggered solution procedures are applied for the problems of the cell level and the particle level. c_2^{j+1} , ϕ_1^{j+1} and ϕ_2^{j+1} are solved at time t^{j+1} , and then transferred to the particle level to solve the diffusion problem of the particle. After the calculation of the diffusion problem of the particle reaches the time t^{j+1} , c_1^{j+1} , μ^{j+1} , \mathbf{u}^{j+1} and $\bar{c}_{1,\text{surface}}^{j+1}$ are passed back to the cell level for the next time step's simulation. Spatially, the governing equations of the cell level and the particle level are employed in two different scales. For the problem of the cell level, the 1D uniform mesh is adopted to discretize the domain of separator and cathode. While at the particle level, the Gmsh package [44] is used to generate the 3D tetrahedral mesh for the spherical and spherical particles. In present work, the simulation of the particle is solved at the attached nodal points of the cathode domain at the cell level, and the c_1^{j+1} , μ^{j+1} , \mathbf{u}^{j+1} and $\bar{c}_{1,\text{surface}}^{j+1}$ are projected back to the corresponding nodes at the cell level. This is different from Golmon's work [7], where each integration point inside the element is attached with a particle model. Since the number of the nodal point is smaller than that of the integration points, the current model is more efficient. The parallel computational framework MOOSE [45] has been adopted to solve the coupled PDEs, the MultiApps and Transfer systems [46] of MOOSE are used to do the two-level coupling and data transfer between the two different levels.

3. Results and discussions

The proposed two-level framework is first benchmarked against the results of the P2D model presented by Doyle et al. [1]. The battery consists of the separator and cathode, with width $L_s = 50\mu\text{m}$ and $L_c = 100\mu\text{m}$, respectively. For the electrolyte PEO – LiCF_3SO_3 is taken into consideration, and the TiS_2 cathode particle with radius $r = 1\mu\text{m}$ is considered. Following Doyle et al. [1], the Fickian diffusion without phase separation and mechanics, which is defined as Mode-I in Table 2, is considered as follow:

$$\frac{\partial c_1}{\partial t} = \nabla(D_1 \nabla c_1) \quad (39)$$

with the flux boundary condition described in Eq. (26), and $I = 10\text{ A/m}^2$



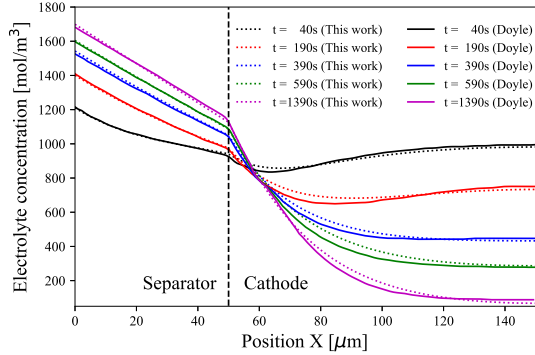
(a) discharge for short time

Table 1
Parameters used in the simulation. All the parameters are taken from the work of Doyle et al. [1,2], Golmon et al. [7] and Zhao et al. [47].

Parameters for the model at the cell level			
Description	Unit	Cathode	Separator
Length	μm	$L_c = 75$	$L_s = 60$
Porosity	–	$\epsilon_c = 0.3$	$\epsilon_s = 1.0$
Initial concentration	mol m^{-3}	$c_2(X, t = 0) = 2000$	
Li-ion diffusivity	$\text{m}^2 \text{s}^{-1}$	$D_2 = 7.5 \times 10^{-11}$	
Conductivity of particle	S m^{-1}	$\lambda = 3.8$	
Conductivity of electrolyte	S m^{-1}	$\kappa_{\text{oe}} = 1.5 \times 10^{-1}$	
Parameters for the model at the particle level			
Description	Unit	LiMn ₂ O ₄	
Particle radius	μm	$r = 8.0$	
Initial concentration	mol m^{-3}	$c_1(\mathbf{x}, t = 0) = 14870$	
Max. concentration	mol m^{-3}	$c_{1,\text{max}} = 22860$	
Li diffusivity	$\text{m}^2 \text{s}^{-1}$	$D_1 = 1.0 \times 10^{-13}$	
Young's modulus	GPa	$E = 10$	
Poisson's ratio	–	$\nu = 0.3$	
Partial molar volume	$\text{m}^3 \text{mol}^{-1}$	$\Omega = 3.499 \times 10^{-6}$	
Phase parameter	–	$\chi = 2.5$	
Interface parameter	$\text{J m}^2 \text{mol}^{-1}$	$\kappa = 1.0 \times 10^{-10}$	
Other constants			
Gas constant		$R = 8.314 \text{ Jmol}^{-1} \text{ K}^{-1}$	
Temperature		$T = 298.15 \text{ K}$	
Faraday's constant		$F = 96487 \text{ Cmol}^{-1}$	
Bruggeman exponent		$\text{Brug} = 1.5$	
Li-ion transference number		$t_+^0 = 0.0107907 + 1.48837 \times 10^{-4} c_2$	
Reaction rate constant		$k_2 = 1 \times 10^{-10} \text{ m}^2 \text{ mol}^{-0.5} \text{ s}^{-1}$	

is applied in this simulation. Fig. 3 shows the concentration distribution of c_2 in the electrolyte. Our simulation results agree well with Doyle's result [1] for both the short time and long time discharge process. Slight difference is captured at the domain close to the interface between the separator and cathode in the short time discharge process. This is due to the different numerical treatment, where an artificial diffusion term based on the upwinding scheme is adopted in Doyle's work to stabilize the diffusion at the interface.

The two-level framework is adopted in the following to simulate the $\text{LiPF}_6/\text{LiMn}_2\text{O}_4$ battery half cell system. Particularly, the phase separation and mechanics in the LiMn_2O_4 particles are regarded in the particle



(b) discharge for long time

Fig. 3. Comparison between the results of the proposed two-level framework and the one from the P2D model [1].

Table 2
The diffusion models used in current work.

Diffusion dynamics inside the particle		
Model type	Model description	Governing equations
Mode-I	Fickian diffusion without mechanics and phase separation	Eq. (39)
Mode-II	Fickian diffusion with mechanics	Eqs. (23)–(25), with $\chi = 1.0$
Mode-III	Fickian diffusion with mechanics and phase separation	Eqs. (23)–(25)

simulation. The simulation parameters are listed in Table 1, the models listed in Table 2 are applied in the following sections. Note that the framework is not restricted to the LiMn_2O_4 material. In order to apply the galvanostatic discharge process under different C-rate, a current density 17.5Am^{-2} is considered [2], and the current density for different C-rate is described by the following equation:

$$I = C - \text{rate} \times 17.5\text{Am}^{-2} \quad (40)$$

3.1. Influence of particle shapes on cell performance

We investigate five particles with the same volume: a spherical particle with $r = 8\ \mu\text{m}$ and four spheroidal particles with different semi-axis along z-direction $a_3 = 4\ \mu\text{m}$, $6\ \mu\text{m}$, $10\ \mu\text{m}$ and $12\ \mu\text{m}$, respectively. The semi-axes of other two dimensions for spheroidal particle can be calculated by $a_1 = a_2 = \sqrt{\frac{r^3}{a_3}}$. The mechanically coupled Cahn–Hilliard–type diffusion model, which is described in Section 2.3 and referred as the Mode-III in Table 2, is applied for different spheroidal particles. The averaged surface concentration $\bar{c}_{1,\text{surface}}$ defined in Eq. (38) is investigated, where the surface integration for the particle is calculated at the end of each time step.

Fig. 4a shows the averaged surface concentration $\bar{c}_{1,\text{surface}}$ of different particles. From the results we can see that for the spherical particle, the slope of the averaged surface concentration profile is much steeper than that of the spheroidal particles. As a consequence, the cell potential of the spherical particle drops faster than the spheroidal cases as shown in Fig. 4b. The reason is that for the spheroidal particles, the non-uniform surface curvature can lead to a higher stress gradient inside the particle, which can enhance the diffusion of lithium into the particle. Thus, the surface concentration increases slower than that in

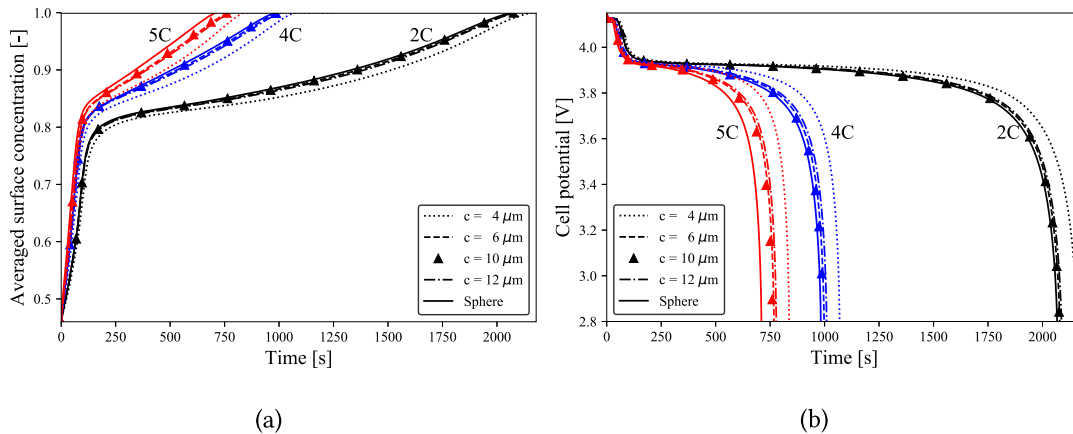


Fig. 4. Evolution of the averaged surface concentration distribution and the cell potential change over time for the spherical particle and the spheroidal particles under different C-rate discharge process.

the spherical case. This can be seen in Fig. 5, where the concentration c_1 and the hydrostatic stress σ_h in the spheroidal particles are plotted for the cases under 5C-rate discharge process. Fig. 5a–e shows the concentration of lithium inside the spherical and spheroidal particles, one can see that the Li-rich and Li-poor phase pairs appear inside the particle. Compared with Fig. 5f–j, the phase pairs are associated with the compressive and tensile stresses. For the oblate spheroidal particle, especially for the case with $a_3 = 4\ \mu\text{m}$ in Fig. 5f, the magnitude of stress is higher than the prolate cases as shown in Fig. 5i and j, and also the spherical case as shown in Fig. 5h. Consequently, even though the diffusion path is shorter than the prolate cases, the existence of the higher stress gradient can supply a stronger push to the lithium into the particle, which makes the lithium not so easy to accumulate at the surface as the prolate cases. Thus a better cell performance is achieved due to the mechanical drifting at higher curvature. For all the spheroidal cases and spherical case, the hydrostatic stresses show a compressive effect at the outside surface, while in the center of the particle, the tensile effect is captured. The prolate particles show a stronger compressive effect around their equatorial plane than the tip part, while for the oblate particle, the tip part experiences the highest compressive stress. Results show that the spheroidal particles can improve the attainable capacity of the battery cell.

3.2. Influence of phase separation and mechanics on cell performance

In order to demonstrate the influence of the phase separation and the mechanical stresses inside the particle on the cell performance, the particle simulations with three different models as mentioned in Table 2 are investigated in this section. The phase separation is disregarded in Mode-II by setting $\chi = 1.0$ for the single phase diffusion. The LiMn_2O_4 particles with radius $r = 8.0\ \mu\text{m}$ are considered in this section, different C-rate discharge processes are investigated for each cases.

Fig. 6a shows the electrolyte concentration c_2 of each cases at the time when the discharge process reaches the final stage. Here $t = 3600\text{s}$, 1800s , 900s and 720s are chosen for 1C, 2C, 4C and 5C discharge processes, respectively. In this way, one can compare them with each other under the same state of charge (SOC) condition. We can see that at the final stage of discharge process, the mechanical stresses and the phase separation have limited influence on the electrolyte concentration profile. Only small difference is captured for the 2C-rate case and 5C-rate case. Fig. 6b shows the pore wall flux distribution of each cases, where the slight difference is captured in the low C-rate

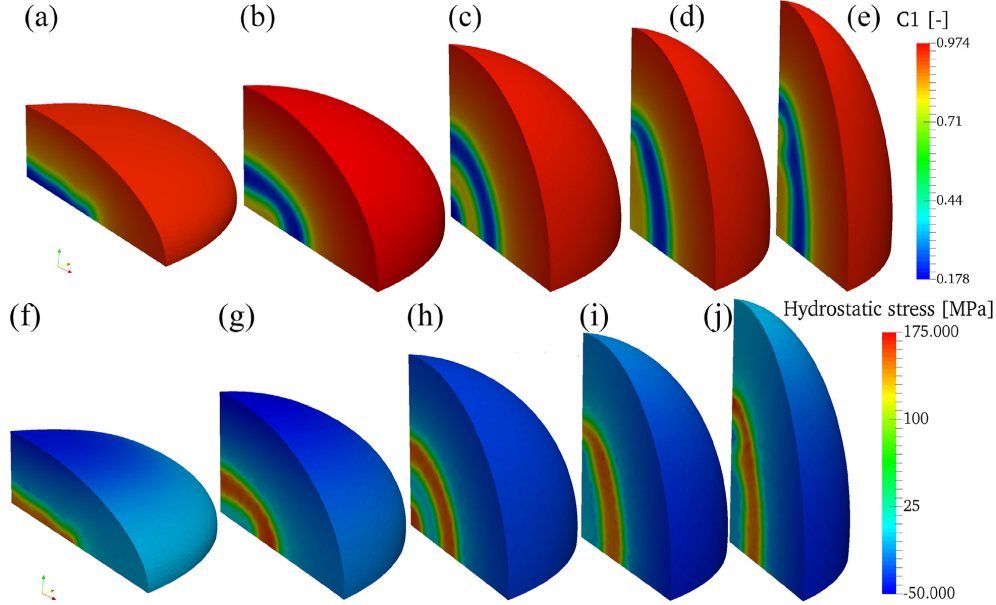


Fig. 5. Distribution of (a)–(e) the lithium concentration c_1 at $t = 300$ s for the spherical and the spheroidal particles where $a_3 = 4\mu\text{m}$, $6\mu\text{m}$, $8\mu\text{m}$, $10\mu\text{m}$, $12\mu\text{m}$ are applied, respectively. The case with $a_3 = 8\mu\text{m}$ represents the spherical particle. (f)–(j) the hydrostatic stress for different particles at $t = 300$ s. C-rate = 5C is applied in this simulation.

discharge process. When the C-rate increases to 4C and 5C, the cases with Mode-II and Mode-III show a lower and steeper flux profile than the other cases with Mode-I at the domain close to the interface between the separator and cathode, while a higher and more flattened profile is captured at the end of cathode. One can conclude that the existence of the stresses shows an enhanced effect on the pore wall flux for the high C-rate discharge process.

The state of charge (SOC) of the cell can be evaluated by integrating the $\bar{c}_{1,\text{surface}}$ along the cathode domain at the cell level, which is defined as follow:

$$\text{SOC} = \frac{\int_{L_s}^{L_s+L_c} \bar{c}_{1,\text{surface}} dX}{\int_{L_s}^{L_s+L_c} dX} \quad (41)$$

Fig. 6c shows the response of SOC of each cases under different C-rate discharge process. If the phase separation is disregarded, a linear increment of SOC is captured. While for the cases with Mode-III, the SOC will experiences a dramatically increase at the beginning of discharging. Which means the surface concentration will increase to the Li-rich phase quickly at the beginning, once the Li-rich phase is formed at the surface of the particle, a stable phase state will be kept. Then the increment of the SOC for the cases with Mode-III is slower than the case with Mode-I and Mode-II. Consequently, the cell potential drops dramatically at the beginning but flattens for a long time in the cases with Mode-III. Fig. 6d shows the cell potential change over time for each cases. We can see that for the low C-rate discharge processes, e.g. 1C and 2C, the existence of stresses can significantly improve the capacity of the battery. While for the high C-rate discharge cases, the influence is limited.

Besides the stresses, the phase separation can also associate with the large strain-mismatch at the interface, which is the primary cause for the mechanical degradation of the particle as reported in Refs. [48–50]. The formation of cracks can hinder the diffusion of lithium inside the active particle. As a consequence, the lithium will accumulate at the

surface layer, which can lead to a faster increase of the surface concentration than in the undamaged case. A shorter discharge time is expected. In addition, the crack can lead to the disintegration of the particle, then capacity fades directly due to the loss of active materials.

3.3. Comparison between particle shapes and diffusion dynamics

To investigate which feature, among the particle geometry and the diffusion dynamics, has a stronger impact on the cell performance, the Mode-II and Mode-III as mentioned in Table 2 are applied for different ellipsoidal particles, respectively. Following the work of Zhang et al. [17], the aspect ratio $\alpha = \frac{a_3}{a_1}$ is introduced to indicate the particle shapes with the same volume, as introduced in Section 3.1.

Fig. 7a plots the discharge time of particles with different aspect ratios in two models before the cell potential drops to 3.0V under 5C discharge process. The results show similar tendencies in both two models: when $\alpha > 1.0$, increasing α can improve the capacity of the battery; while for cases with $\alpha < 1.0$, decreasing α can enhance the cell performance. When α approaches 0, the particle turns to be an infinite plane surface, and leads to an infinite capacity increase. Whereas, $\alpha \rightarrow +\infty$ corresponds to the infinite long cylindrical particle with zero radius, and leads to an upper bound for the capacity increase. Around the critical points $\alpha_l \approx 0.48$ and $\alpha_r \approx 2.23$, two lines intersect with each other and the performances of the diffusion models are not so different from each other. For the particles with aspect ratio in the range of $\alpha_l < \alpha < \alpha_r$, a better cell performance is obtained in Mode-II, where the single phase diffusion is applied. For very flat oblate spheroidal ($\alpha < \alpha_l$) or very slender prolate spheroidal ($\alpha > \alpha_r$) particles, however, the Mode-III shows a great positive impact on the cell performance.

$$\bar{\sigma}_{\text{vonMises,max}} = \frac{\int_{L_s}^{L_s+L_c} \sigma_{\text{vonMises,max}} dX}{\int_{L_s}^{L_s+L_c} dX} \quad (42)$$

The averaged max von Mises stress $\bar{\sigma}_{\text{vonMises,max}}$, as defined in Eq.

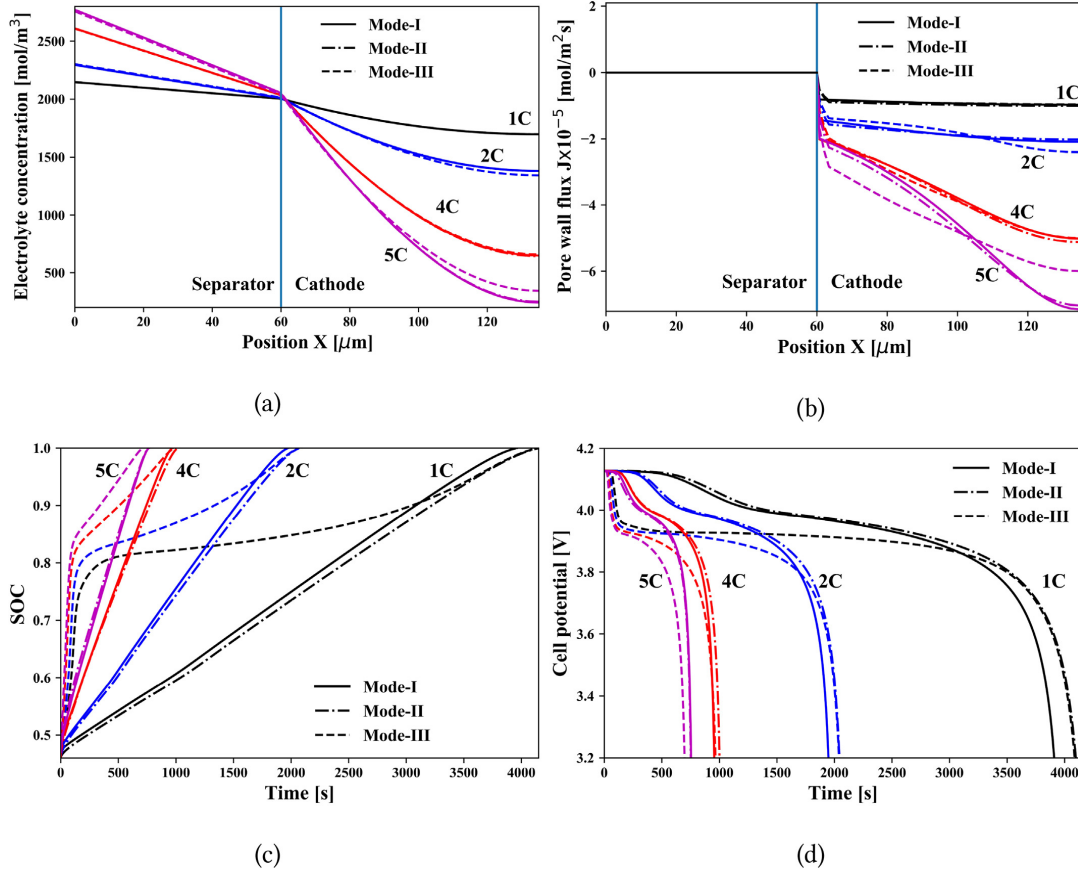


Fig. 6. Evolution of the quantities for different cases under different C-rate discharge process: a) concentration distribution of c_2 in the electrolyte phase, b) pore wall flux, c) SOC, d) cell potential.

(42), and the surface concentration are plotted in Fig. 7b and c to investigate the differences, respectively. The $\sigma_{\text{vonMises,max}}$ is the max von Mises stress of each particle, which is projected from the particle level to the cell level for the calculation of $\sigma_{\text{vonMises,max}}$. As shown in Fig. 7b, the max von Mises stress of the cases with Mode-III is larger than the cases with Mode-II. For the $\alpha > 1.0$ cases, as α increases, the von Mises stress will reach a peak value then decrease, which is in good agreement with Zhang et al. [17]. The same conclusion still holds for the cases with $\alpha < 1.0$, where the peak value is approached by reduction of the aspect ratio.

The max von Mises stresses $\sigma_{\text{vonMises,max}}$ of the particle which is located at the interface between separator and cathode are plotted in Fig. 7d. Different from Zhang et al. [17], the dynamic pore wall flux from the cell level, instead of the constant one, is applied at the surface of the particle during the simulation. Result shows that, once the phase separation is disregarded in Mode-II, the stress will experience the peak value then decrease to zero. While for the cases with phase separation in Mode-III, the sharp increase of the stress is captured at the beginning. As the Li-poor and Li-rich phase pairs arise inside the particle, the stress inside the oblate and prolate particles will reach a peak value, then decrease with the phase pairs move towards the center. At the end the stress will decrease to zero, where only the Li-rich phase exist inside the

particle. The peak value of the stress in both the oblate particles and prolate particles is larger than the one in the spherical particle. One can also conclude this from Fig. 7c, where the surface concentration of the cases with Mode-III experiences a dramatically increase at the beginning then keep a slower increase than other cases. While for the spherical particle, the existence of the phase interface can lead to the dramatically increase of the stress, then the high plateau of the stress is kept for a long time, at the end the stress decreases to zero. As a consequence, the diffusion of lithium into the particle is slower than the oblate particle and prolate particle, which provides a faster increase of the surface concentration as shown in Fig. 7c, then a shorter discharge time is achieved. In this section we can conclude that, when the value of α is close to the critical aspect ratio value α_l and α_r , the different diffusion models have almost the same performance, while for cases where the α is far away from the critical value, the diffusion dynamics have much larger impact on the cell performance than the particle shapes.

3.4. Influence of elastic properties on cell performance

In order to investigate the influence of elastic properties, spherical particles with different elastic properties are simulated. The particle radius is taken as $r = 8\mu\text{m}$, and Young's modulus E varies among

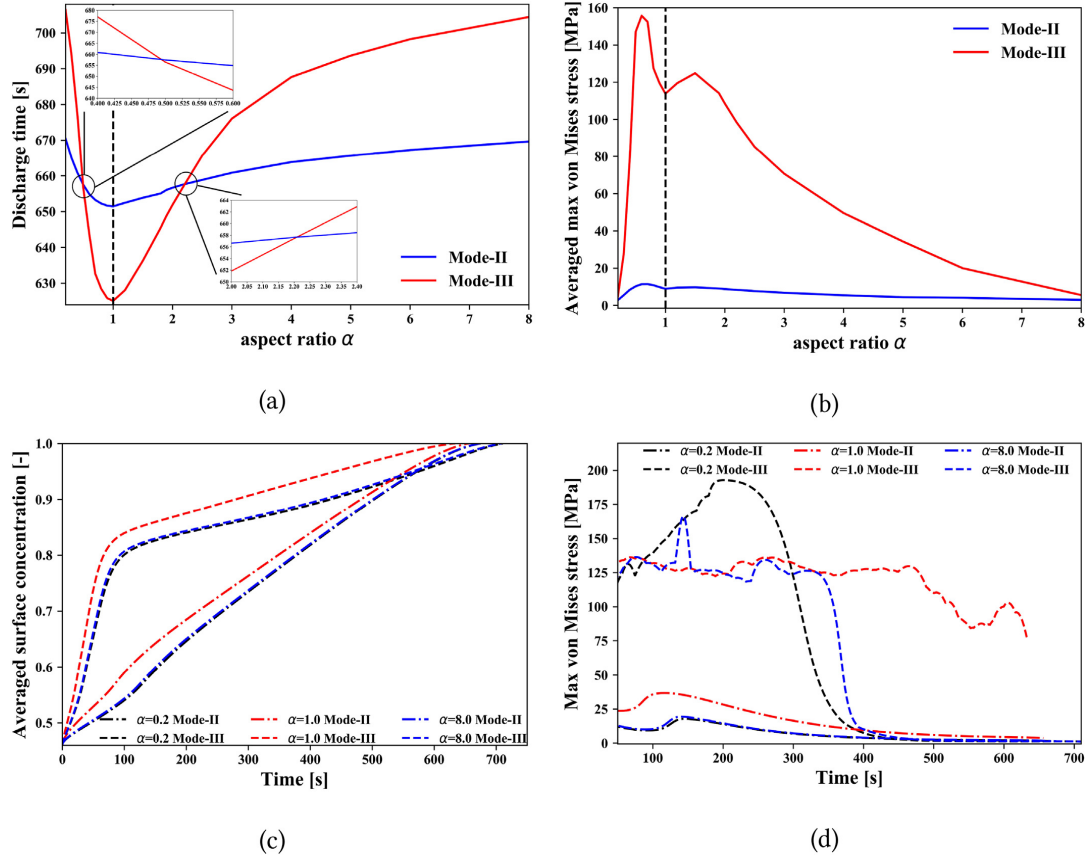


Fig. 7. Distribution of: a) discharge time under different aspect ratio α when cell voltage drops below 3.0 V. b) averaged max von Mises stress $\sigma_{\text{vonMises,max}}$ under different aspect ratio when cell voltage equals to 3.0 V. c) averaged surface concentration change over time. d) max von Mises stress $\sigma_{\text{vonMises,max}}$ change over time of different particles.

$E = 1\text{GPa}$, 10GPa , 50GPa and 100GPa . For the particle located at the interface between separator and cathode, its concentration c_1 and the related hydrostatic stress are plotted.

Fig. 8a and b shows that the lithium concentration c_1 inside the soft particles ($E = 1\text{GPa}$ and 10GPa) and stiff particles ($E = 50\text{GPa}$ and 100GPa), respectively. In soft particles, the Li-poor and Li-rich phase pairs still appear inside the particle during discharging, which means the phase separation occurs. In stiff particles, however, the phase separation behavior is suppressed. As a consequence, the concentration of the lithium inside the particle gradually increases from the center outwards to the surface. Fig. 8c and d shows the hydrostatic stress inside the particles. Even though the material is much more stiff, where $E = 50\text{GPa}$ and $E = 100\text{GPa}$ are applied as shown in Fig. 8d, the existence of phase interface can lead to a higher stress state for $E = 10\text{GPa}$ case as shown in Fig. 8c. In all the particles, the tensile part of the hydrostatic stress mainly takes place in the center while the compressive stress occurs in the outer layer. For the cases with phase separation, the repeated Li-poor and Li-rich phase pairs appear inside the particle, associated with the tensile and compressive stress.

Fig. 8e and f plot the SOC and the cell performance under different C-rate discharge processes. For the cases with phase separation, where particles are softer ($E = 1\text{GPa}$ and 10GPa), the SOC still increases

dramatically at the beginning. It leads to a dramatic drop of the cell potential in a short time. The linear increment is still captured if phase separation is disregarded. For the low C-rate cases, where 2C is applied, the influence of stresses on the cell performance is not so significant. While for the high C-rate discharge process, the cases without phase separation, where particles are stiffer ($E = 50\text{GPa}$ and 100GPa), show a better cell performance than the cases with phase separation, as shown in 8f. Once the particle becomes stiff enough, the improvement for each C-rate discharge process is not so significant. We can conclude that stresses have a significant positive impact on the cell performance, especially for the high C-rate discharge process, the stresses can postpone the cell potential drop time, increase the attainable capacity.

4. Conclusion

In this work, we proposed a two-level framework for modeling the battery cell performance on the basis of the multiphysics particle simulation. It is numerically more efficient than the rigorous microstructure-based battery cell models, but inherits the full advantages of the particle models, such as the accuracy of the diffusion solution and accessibility to the complex particle geometry and defects in particles.

In particular, we incorporate our multiphysical particle level

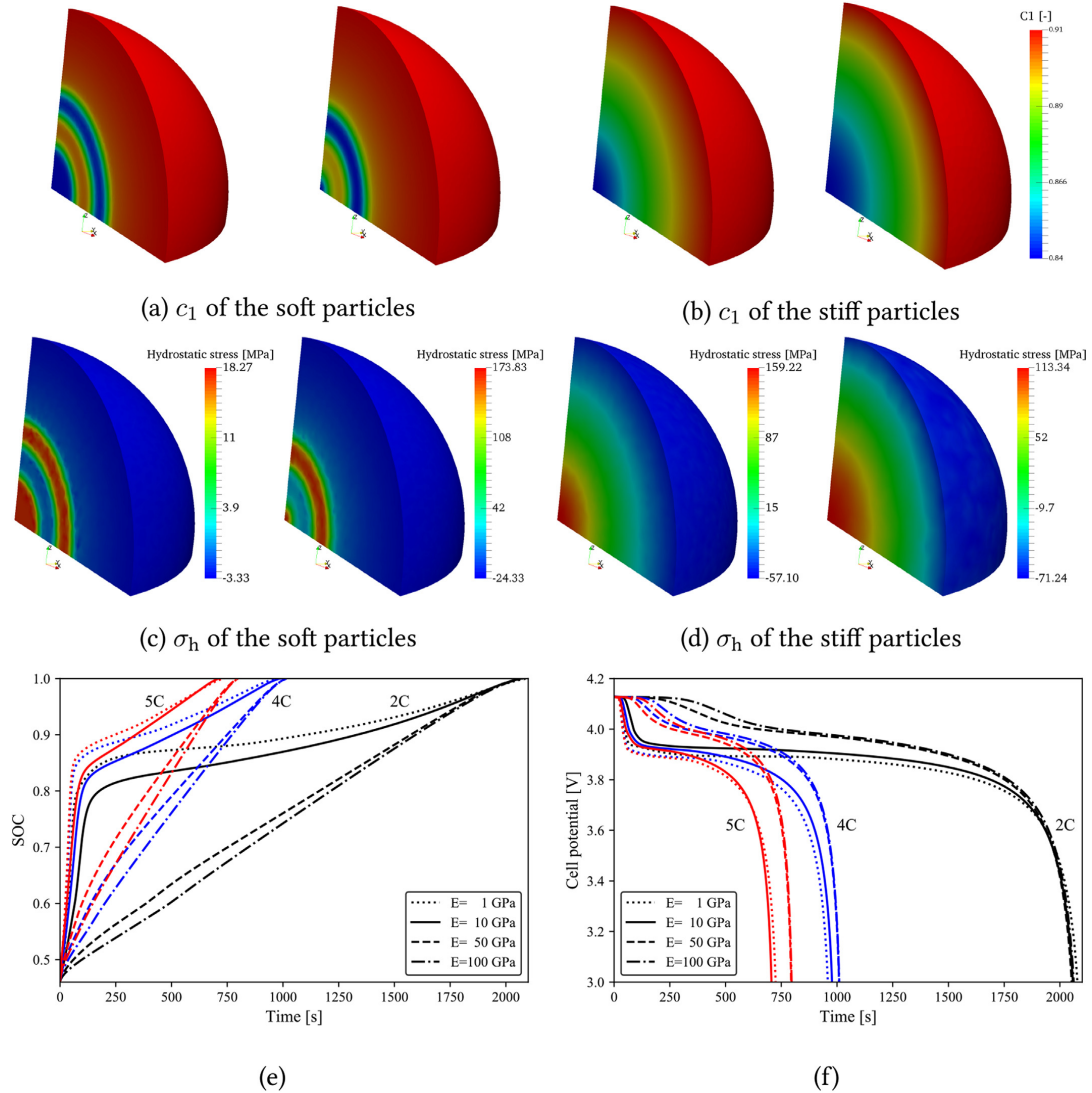


Fig. 8. Distribution of a) c_1 for the soft particles with $E = 1$ GPa and $E = 10$ GPa at $t = 400$ s respectively, b) c_1 for the stiff particles with $E = 50$ GPa and $E = 100$ GPa at $t = 400$ s respectively, c) hydrostatic stress σ_h for the soft particles at $t = 400$ s, d) hydrostatic stress σ_h for the stiff particles at $t = 400$ s respectively, e) SOC change over time, f) the cell potential change over time. C-rate = 5C is applied in this simulation.

modeling into the P2D cell model. To further improve the computational efficiency, we manage to reduce one degree of freedom on the cell level by treating the lithium-ion flux between the electrolyte and active particles as the dependent quantity. The two-level framework is adopted to solve the PDEs of the cell level and the particle level with the finite element method. We proposed to bridge the two levels on the attached finite element node of the cell mesh, instead of on its integration points. It further increases the efficiency.

We have verified our two-level model with a benchmark available in the literature, and applied it to study the influence of the particle shape, mechanics and phase separation on the cell performance. Simulation

results show that the existence of the stresses can enhance the bulk diffusion inside the particles, so that the surface concentration of the particle changes slower than the cases without stresses. It can increase the attainable capacity. Moreover, the oblate particles show a better cell performance than the prolate particles and the spherical particles for the higher stress gradient, which can attribute to the mechanical drifting at higher curvature. Compare to the particle shapes, the diffusion behavior inside the particle has a larger impact on the cell performance when the aspect ratio is far away from the critical value. The mechanically coupled Cahn–Hilliard–type diffusion is much more sensitive to the change of aspect ratio than other type diffusion dynamics.

As the stiffness of the particle increase, the attainable capacity can be improved. Once the particle is stiff enough, it has a very limited improvement for the cell performance. Besides the influence of the shape, the phase separation behavior associated with the high stress gradient in the phase interface can also keep the surface concentration under a slow increment until the particle is fully lithiated. As a consequence, the cell potential experiences a dramatic drop at the beginning. Afterwards it decreases much slower than the cases without phase separation, where a higher capacity is achieved. In the near future, the two-level model will be applied to study the impact of defects (e.g. the voids, grain boundaries and dislocation) in the particle on the cell performance. The strain mismatch and the resulted defects due to the phase interface will be investigated, and the contribution of local chemical potential to the Butler-Volmer reaction between particles and electrolyte will also be demonstrated.

Acknowledgement

The authors gratefully acknowledge the computing time granted on the Hessian High Performance Computer "Lichtenberg". The author Bai and Xu would particularly like to thank the Adolf Messer Foundation for awarding them the Adolf Messer Prize and for financial support.

References

- [1] M. Doyle, T.F. Fuller, J. Newman, Modeling of galvanostatic charge and discharge of the lithium/polymer/insertion cell, *J. Electrochem. Soc.* 140 (1993) 1526–1533.
- [2] C.M. Doyle, Design and Simulation of Lithium Rechargeable Batteries, Ph.D. thesis University of California at Berkeley, 1995.
- [3] M. Doyle, J. Newman, The use of mathematical modeling in the design of lithium/polymer battery systems, *Electrochim. Acta* 40 (1995) 2191–2196.
- [4] T.F. Fuller, Simulation and optimization of the dual lithium ion insertion cell, *J. Electrochem. Soc.* 141 (1994) 1.
- [5] J. Christensen, Modeling diffusion-induced stress in li-ion cells with porous electrodes, *J. Electrochem. Soc.* 157 (2010) A366–A380.
- [6] S. Renganathan, G. Sikha, S. Santhanagopalan, R.E. White, Theoretical analysis of stresses in a lithium ion cell, *J. Electrochem. Soc.* 157 (2010) A155–A163.
- [7] S. Golmon, K. Maute, M.L. Dunn, Numerical modeling of electrochemical-mechanical interactions in lithium polymer batteries, *Comput. Struct.* 87 (2009) 1567–1579.
- [8] T. Mori, K. Tanaka, Average stress in matrix and average elastic energy of materials with misfitting inclusions, *Acta Metall.* 21 (1973) 571–574.
- [9] X. Xiao, W. Wu, X. Huang, A multi-scale approach for the stress analysis of polymeric separators in a lithium-ion battery, *J. Power Sources* 195 (2010) 7649–7660.
- [10] R. Fu, M. Xiao, S.-Y. Choe, Modeling, validation and analysis of mechanical stress generation and dimension changes of a pouch type high power li-ion battery, *J. Power Sources* 224 (2013) 211–224.
- [11] W. Wu, X. Xiao, M. Wang, X. Huang, A microstructural resolved model for the stress analysis of lithium-ion batteries, *J. Electrochem. Soc.* 161 (2014) A803–A813.
- [12] L. Wu, X. Xiao, Y. Wen, J. Zhang, Three-dimensional finite element study on stress generation in synchrotron X-ray tomography reconstructed nickel-manganese-cobalt based half cell, *J. Power Sources* 336 (2016) 8–18.
- [13] R. Behrou, K. Maute, Numerical modeling of damage evolution phenomenon in solid-state lithium-ion batteries, *J. Electrochem. Soc.* 164 (2017) A2573–A2589.
- [14] B. Wu, W. Lu, A battery model that fully couples mechanics and electrochemistry at both particle and electrode levels by incorporation of particle interaction, *J. Power Sources* 360 (2017) 360–372.
- [15] J. Christensen, J. Newman, Stress generation and fracture in lithium insertion materials, *J. Solid State Electrochem.* 10 (2006) 293–319.
- [16] J. Christensen, J. Newman, A mathematical model of stress generation and fracture in lithium manganese oxide, *J. Electrochem. Soc.* 153 (2006) A1019–A1030.
- [17] X. Zhang, W. Shyy, A.M. Sastry, Numerical simulation of intercalation-induced stress in Li-ion battery electrode particles, *J. Electrochem. Soc.* 154 (2007) A910–A916.
- [18] J. Park, W. Lu, A.M. Sastry, Numerical simulation of stress evolution in lithium manganese dioxide particles due to coupled phase transition and intercalation, *J. Electrochem. Soc.* 158 (2011) A201–A206.
- [19] P. Stein, B. Xu, 3D Isogeometric Analysis of intercalation-induced stresses in Li-ion battery electrode particles, *Comput. Methods Appl. Mech. Eng.* 268 (2014) 225–244.
- [20] T. Hughes, J. Cottrell, Y. Bazilevs, Isogeometric analysis: CAD, finite elements, NURBS, exact geometry and mesh refinement, *Comput. Methods Appl. Mech. Eng.* 194 (2005) 4135–4195.
- [21] Y. Bai, C. Dong, Z. Liu, Effective elastic properties and stress states of doubly periodic array of inclusions with complex shapes by isogeometric boundary element method, *Compos. Struct.* 128 (2015) 54–69.
- [22] P. Stein, B.-X. Xu, Isogeometric analysis of surface elasticity: a comparison with isoparametric fem, *Proc. Appl. Math. Mech.* 15 (2015) 427–428.
- [23] P. Stein, Y. Zhao, B.-X. Xu, Effects of surface tension and electrochemical reactions in Li-ion battery electrode nanoparticles, *J. Power Sources* 332 (2016) 154–169.
- [24] Y. Liu, P. Lv, J. Ma, R. Bai, H.L. Duan, Stress fields in hollow core-shell spherical electrodes of lithium ion batteries, *Proc. Roy. Soc. Lond.: Math. Phys. Eng. Sci.* 470 (2014) 20140299.
- [25] X. Zhang, S.W. Lee, H.-W. Lee, Y. Cui, C. Linder, A reaction-controlled diffusion model for the lithiation of silicon in lithium-ion batteries, *Extreme Mech. Lett.* 4 (2015) 61–75.
- [26] X. Zhang, A. Krischok, C. Linder, A variational framework to model diffusion induced large plastic deformation and phase field fracture during initial two-phase lithiation of silicon electrodes, *Comput. Methods Appl. Mech. Eng.* 312 (2016) 51–77.
- [27] J.W. Cahn, J.E. Hilliard, Free energy of a nonuniform system. I. Interfacial free energy, *J. Chem. Phys.* 28 (1958) 258–267.
- [28] J.W. Cahn, On spinodal decomposition, *Acta Metall.* 9 (1961) 795–801.
- [29] M. Huttin, M. Kamlah, Phase-field modeling of stress generation in electrode particles of lithium ion batteries, *Appl. Phys. Lett.* 101 (2012) 133902.
- [30] A.-C. Walk, M. Huttin, M. Kamlah, Comparison of a phase-field model for intercalation induced stresses in electrode particles of lithium ion batteries for small and finite deformation theory, *Eur. J. Mech. A Solid.* 48 (2014) 74–82.
- [31] S. Gladkov, B. Svendsen, Thermodynamic and rate variational formulation of models for inhomogeneous gradient materials with microstructure and application to phase field modeling, *Acta Mech. Sin.* (2015) 1–11.
- [32] C. Miehe, F.E. Hildebrand, L. Böger, Mixed variational potentials and inherent symmetries of the Cahn-Hilliard theory of diffusive phase separation, *Proc. Roy. Soc. Lond.: Math. Phys. Eng. Sci.* 470 (2014) 20130641.
- [33] L. Anand, A Cahn-Hilliard-type theory for species diffusion coupled with large elastic-plastic deformations, *J. Mech. Phys. Solids* 60 (2012) 1983–2002.
- [34] C.V. Di Leo, E. Rejovitzky, L. Anand, A Cahn-Hilliard-type phase-field theory for species diffusion coupled with large elastic deformations: application to phase-separating Li-ion electrode materials, *J. Mech. Phys. Solids* 70 (2014) 1–29.
- [35] Y. Zhao, P. Stein, B.-X. Xu, Isogeometric analysis of mechanically coupled Cahn-Hilliard phase segregation in hyperelastic electrodes of Li-ion batteries, *Comput. Methods Appl. Mech. Eng.* 297 (2015) 325–347.
- [36] S. Kaesmair, P. Steinmann, Comparative computational analysis of the Cahn-Hilliard equation with emphasis on C^1 -continuous methods, *J. Comput. Phys.* 322 (2016) 783–803.
- [37] B.-X. Xu, Y. Zhao, P. Stein, Phase field modeling of electrochemically induced fracture in li-ion battery with large deformation and phase segregation, *GAMM-Mitteilungen* 39 (2016) 92–109.
- [38] Y. Zhao, B.-X. Xu, P. Stein, D. Gross, Phase-field study of electrochemical reactions at exterior and interior interfaces in Li-ion battery electrode particles, *Comput. Methods Appl. Mech. Eng.* 312 (2016) 428–446.
- [39] Y. Zhao, L.R. De Jesus, P. Stein, G.A. Horrocks, S. Banerjee, B.-X. Xu, Modeling of phase separation across interconnected electrode particles in lithium-ion batteries, *RSC Adv.* 7 (2017) 41254–41264.
- [40] L.R. De Jesus, Y. Zhao, G.A. Horrocks, J.L. Andrews, P. Stein, B.-X. Xu, S. Banerjee, Lithiation across interconnected v 2 o 5 nanoparticle networks, *J. Mater. Chem.* 5 (2017) 20141–20152.
- [41] C. Delacourt, P. Poizot, J.-M. Tarascon, C. Masquelier, The existence of a temperature-driven solid solution in Li_xFePO_4 for $0 \leq x \leq 1$, *Nat. Mater.* 4 (2005) 254–260.
- [42] M. Ebner, F. Marone, M. Stampanoni, V. Wood, Visualization and quantification of electrochemical and mechanical degradation in Li ion batteries, *Science* 342 (2013) 716–720.
- [43] T. Belytschko, W.K. Liu, B. Moran, K. Elkhodary, *Nonlinear Finite Elements for Continua and Structures*, John Wiley & Sons, 2013.
- [44] C. Geuzaine, J.-F. Remacle, Gmsh: A 3-d finite element mesh generator with built-in pre-and post-processing facilities, *Int. J. Numer. Methods Eng.* 79 (2009) 1309–1331.
- [45] D. Gaston, C. Newman, G. Hansen, D. Lebrun-Grandie, Moose: a parallel computational framework for coupled systems of nonlinear equations, *Nucl. Eng. Des.* 239 (2009) 1768–1778.
- [46] D.R. Gaston, C.J. Permann, J.W. Peterson, A.E. Slaughter, D. Andriš, Y. Wang, M.P. Short, D.M. Perez, M.R. Tonks, J. Ortensi, et al., Physics-based multiscale coupling for full core nuclear reactor simulation, *Ann. Nucl. Energy* 84 (2015) 45–54.
- [47] Y. Zhao, P. Stein, B.-X. Xu, Phase field simulation of the intercalation-induced stresses in the hyperelastic solids via isogeometric analysis, *Proc. Appl. Math. Mech.* 15 (2015) 443–444.
- [48] A. Verma, P.P. Mukherjee, Mechanistic analysis of mechano-electrochemical interaction in silicon electrodes with surface film, *J. Electrochem. Soc.* 164 (2017) A3570–A3581.
- [49] P. Barai, B. Huang, S.J. Dillon, P.P. Mukherjee, Mechano-electrochemical interaction gives rise to strain relaxation in sn electrodes, *J. Electrochem. Soc.* 163 (2016) A3022–A3035.
- [50] P. Barai, P.P. Mukherjee, Mechano-electrochemical stochasticity in high-capacity electrodes for energy storage, *J. Electrochem. Soc.* 163 (2016) A1120–A1137.

5.5 Publication C

A review on modeling of electro-chemo-mechanics in lithium-ion batteries

Ying Zhao, Peter Stein, Yang Baia, Mamun Al-Siraj, Yangyiwei Yang, Bai-Xiang Xu,
A review on modeling of electro-chemo-mechanics in lithium-ion batteries, Journal of
Power Sources 413 (2019):259-283



Contents lists available at ScienceDirect

Journal of Power Sources

journal homepage: www.elsevier.com/locate/jpowsour



Review article

A review on modeling of electro-chemo-mechanics in lithium-ion batteries

Ying Zhao^{a,b,*}, Peter Stein^a, Yang Bai^a, Mamun Al-Siraj^a, Yangyiwei Yang^a, Bai-Xiang Xu^{a,**}



^a *Mechanics of Functional Materials Division, Department of Materials and Earth Sciences, Technische Universität Darmstadt, Otto-Berndt-Straße 3, 64287, Darmstadt, Germany*

^b *Department of Engineering, University of Cambridge, Trumpington Street, CB2 1PZ, Cambridge, UK*

HIGHLIGHTS

- Comprehensive review of electro-chemo-mechanical modeling of lithium-ion batteries.
- Step-by-step instruction of the model for interested newcomers to the field.
- Modeling on three length scales: particle, composite electrode and battery cell.
- Review and perspective on the mechanically coupled modeling of solid-state batteries.

ARTICLE INFO

Keywords:

Lithium-ion battery
Electro-chemo-mechanical coupling
Electrode active particle model
Composite electrode model
Battery cell model
Solid-state battery

ABSTRACT

Investigations on the fast capacity loss of Lithium-ion batteries (LIBs) have highlighted a rich field of mechanical phenomena occurring during charging/discharging cycles, to name only a few, large deformations coupled with nonlinear elasticity, plastification, fracture, anisotropy, structural instability, and phase separation phenomena. In the last decade, numerous experimental and theoretical studies have been conducted to investigate and model these phenomena. This review aims, on one hand, at a comprehensive overview of the approaches for modeling the coupled chemo-mechanical behavior of LIBs at three different scales, namely the particle, the electrode, and the battery cell levels. Focus is thereby the impact of mechanics on the cell performance and the degradation mechanisms. We point out the critical points in these models, as well as the challenges towards resolving them. Particularly, by outlining the milestones of theoretical and numerical models, we give a step-by-step instruction to the interested readers in both electrochemical and mechanical communities. On the other hand, this review aims to facilitate the knowledge transfer of mechanically coupled modeling to the study of all-solid-state batteries, where the mechanical issues are expected to play even more diverse and essential roles due to the additional mechanical constraint imposed by the solid electrolytes.

1. Introduction

Rechargeable lithium-ion batteries (LIBs) are widely used in portable electronic devices and electric vehicles, and are prominent solutions for the storage of intermittent renewable energies [1,2]. The working principle of LIBs lies essentially in the electrochemical-potential-driven redox reaction in the electrode active materials, involving lithium ions and electrons. Electrons flow through conductive agents and current collectors to the external circuit, while lithium cations shuttle between the anode and cathode through the electrolyte.

Mechanics can have a critical influence on the performance and the lifetime of LIBs. It is well known that LIBs suffer from considerable

chemo-mechanical degradation, which is one of the bottleneck issues for current commercial batteries failing to meet the increasing demand in wide application [3]. In pursuit of larger capacity and longer cycle/calendar life, numerous efforts have been made in the community of electrochemistry and related fields, to develop next-generation battery systems with novel electrode materials. Nevertheless, most material candidates with promising electrochemical properties have insufficient chemo-mechanical stability. That is, electrode materials with a high theoretical capacity suffer from irreversible mechanical degradation already after few cycles due to high internal stress [4]. This is the long recognized dilemma between capacity and cyclability of LIBs.

There are various types of mechanical degradation in LIBs which

* Corresponding author. Department of Engineering, University of Cambridge, Trumpington Street, CB2 1PZ, Cambridge, UK.

** Corresponding author. Mechanics of Functional Materials Division, Department of Materials and Earth Sciences, Technische Universität Darmstadt, Otto-Berndt-Straße 3, 64287, Darmstadt, Germany.

E-mail addresses: yz575@cam.ac.uk (Y. Zhao), xu@mfm.tu-darmstadt.de (B.-X. Xu).

<https://doi.org/10.1016/j.jpowsour.2018.12.011>

Received 20 October 2018; Received in revised form 4 December 2018; Accepted 5 December 2018
0378-7753/ © 2018 Published by Elsevier B.V.

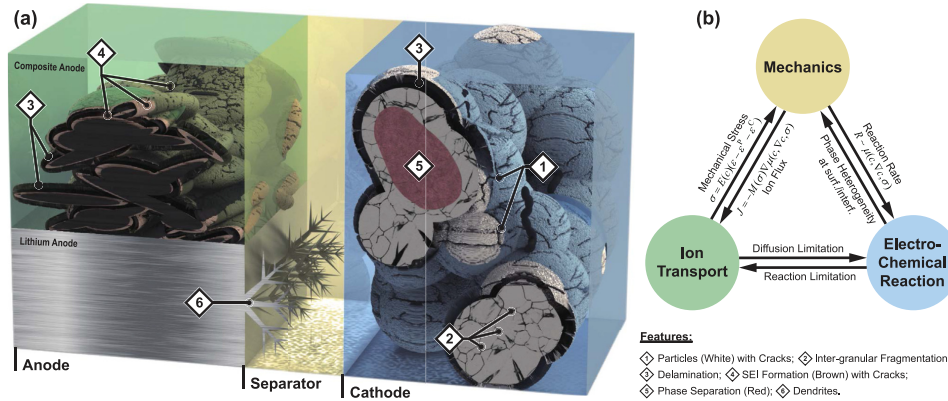


Fig. 1. Schematics of (a) mechanistic and (b) mechanical degradation mechanisms of a lithium-ion battery cell with a composite anode and a lithium metal anode, respectively.

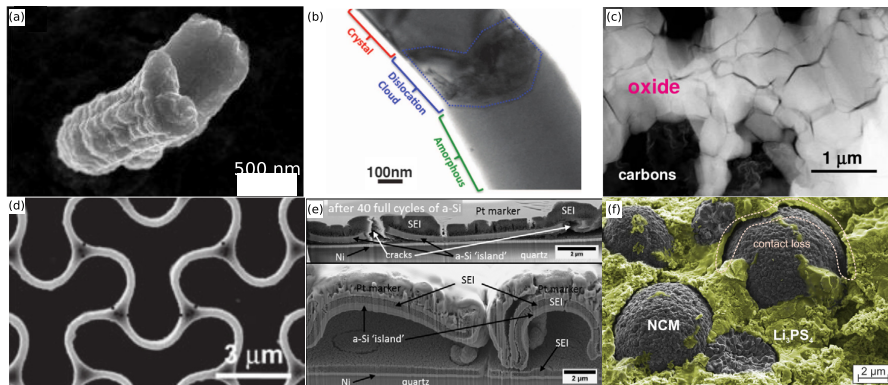


Fig. 2. (a) Fracture in a Si nanopillar [10]. (b) Formation and propagation of a dislocation cloud at the reaction front in a SnO nanowire during lithiation [11]. (c) Fragmentation of $\text{LiNi}_{0.8}\text{Co}_{0.15}\text{Al}_{0.05}\text{O}_2$ secondary particles [3]. (d) Buckling of a planar silicon honeycomb anode [12]. (e) Fracture in the SEI [13]. (f) Delamination of a particle from solid electrolyte [14]. (For interpretation of the references to colour in this figure legend, the reader is referred to the Web version of this article.)

contribute significantly to capacity fade and impedance increase of a battery over charge/discharge cycles. A selection of mechanical phenomena and degradation mechanisms are illustrated in Fig. 1 (a). In electrode active materials, Li insertion/extraction is, in general, accompanied by local deformation and volume change of the materials. Nowadays, commercial batteries usually employ graphite as active material for the battery anode (with a theoretical capacity of 372 mA h g^{-1} [5]), which exhibits volume changes of 10% under intercalation [6]. Si and Sn, on the other hand, two promising candidate materials with higher theoretical capacities of 4200 mA h g^{-1} [7] and 873 mA h g^{-1} [8], respectively, show corresponding volume changes of 310% and 260% [9]. Due to the intrinsic non-equilibrium working condition of LIBs, this deformation is inhomogeneous in the materials, giving rise to high internal stress that eventually lead to fracture, fragmentation, or pulverization. A selection of the observed damage phenomena is given in Fig. 2(a–d).

Due to a loss of contact to conductive agents or electrolyte, the active materials may become partially inactive, thus contributing to the overall capacity and power loss. Besides the aforementioned fracture within the active materials, the mismatch between active and inactive materials also tends to promote fracture or delamination at the interface. The solid-electrolyte-interphase (SEI), which is formed on the

surface of active materials due to irreversible side reactions of active materials with the electrolyte, further contributes to capacity fade. These side reactions are widely believed to be able to chemically stabilize themselves as the formed SEI layer prevents further side reactions. However, the mechanical mismatch between the active particles and the SEI layer promotes cracking at the particle surface. Consequently, more active material is exposed to the electrochemical reactions at the fresh crack surface, which leads to formation of new SEI and hence to a loss in capacity fade and increase in resistivity. This positive feedback between SEI formation and cracking brings on a progressive failure [15,16] (Fig. 2(f)). In the case of solid electrolyte, delamination between the particle and the electrolyte can become more prominent than in the case of liquid electrolyte (Fig. 2(e)). The formation of micro-cracks within the solid electrolyte is expected to reduce its effective ionic conductivity, and micro-cracks may provide a pathway for Li dendrite growth, eventually causing the cell to short-circuit [17]. On the cell level, fracture and delamination can further take place between electrode and current collector [18], which can be alleviated to some degree by introducing additional buffer layers in the material [13].

In addition to degradation, mechanics can have a significant influence on both Li transport and electrochemical reactions, which are two

essential mechanisms of the working principle of LIBs, as shown in Fig. 1(b). The mechanical energy makes a contribution to the system's free energy and thus to the chemical potential, which, in turn, regulates both the Li transport in the solid phases and the electrochemical reactions at the interfaces. The driving force for the Li transport in solid phases does not only comprise a diffusion contribution but also a drifting force due to stress inhomogeneity. In the simple isotropic case, Li transport is sensitive to the gradient of the hydrostatic pressure, since guest atoms tend to move to regions with sufficient space to accommodate them. Assuming purely elastic mechanical behavior, the outer layers of an electrode particle are compressed during intercalation, while its interior is stretched. Thus, the stresses can enhance lithium diffusion towards the interior of the particle, facilitating fast intercalation [19]. This results in a change in surface concentration and hence in the chemical potential at the surface, which can further impact the surface reactions. Mechanical stresses can also regulate the cell potential so that it evolves more stably during charge and discharge, which is beneficial to the functionality of a battery. In phase-separating materials, the elastic energy contributions due to mismatch strains at the interface can outweigh the chemical energy contributions, resulting in a suppression of phase separation in the material. It has further been reported that stresses can help to suppress lithium dendrite formation in a lithium-metal battery [20,21]. In nanostructured materials, surface stresses become more prominent and can change the capacity and diffusivity of the particle through the induced internal stresses. The mechanical stresses are thereby strongly correlated with the extrinsic features of the particles, such as size and shape. Understanding and controlling the effects of stress and strain on ion transport, phase transformations, and catalytic pathways in energy materials can be a key for improving the performance and the durability of battery devices.

In the last two decades, a vast amount of studies has been undertaken concerning the role and the impact of mechanics in the performance and degradation of LIBs. Advanced experiments characterized and provided evidence for the chemo-mechanical behavior and fracture of electrodes, as summarized in the review article by Cheng and Pecht [22]. The understanding and the prediction of the lithiation behavior has concurrently been expanded by a number of theoretical works, both with regard to modeling and numerical simulations. These form the bases for an optimization of batteries at the level of individual particles, the electrode, and a whole battery cell.

The subset of studies regarding modeling of LIBs has been reviewed in several papers. These reviews focus on multiscale modeling and homogenization techniques [23,24], particle-level modeling [4,25,26], and combined experimental-theoretical approaches [27–30]. However, there is no review article in the literature which summarizes the extensive mechanically coupled modeling of LIBs and the knowledge acquired thereby. In the review by Grazioli et al. [24], modeling of micro-mechanical effects in active materials was addressed at the particle level. However, the influence of mechanics extends over different regions and length scales and is not limited to the active particles. Xu and Zhao [26] also provided a brief yet in-depth overview on different theories and observations of electro-chemo-mechanics of electrode particles in LIBs. They focused, however, only on a phenomenological and conceptual description with schematic illustrations. A detailed survey of the extensive literature is missing. Herein lies the motivation for this review article. The present paper reviews the modeling and simulation work on the impact of mechanics, particularly in terms of mechanisms and degradation on particle, electrode and cell scales. On one hand, we outline the theoretical and numerical development of mechanically coupled investigation of LIBs. On the other hand, we highlight the results on mechanical impact obtained in the reviewed papers, to make the knowledge accessible to the readers with different background.

With the present paper we aim to fulfill two goals. Firstly, we want to give a comprehensive overview of the approaches to modeling the

coupled electro-chemo-mechanical behavior of LIBs at three different scales: the particle, the electrode, and the battery cell levels. Focus is thereby the impact of mechanics on the mechanisms for operation and degradation at these length scales. Secondly, we outline the evolution of theoretical and numerical models for the mechanically coupled investigation of LIBs in the hope of aiding newcomers to the field and experts alike. We highlight noteworthy results and critical points in these models, as well as the challenges towards resolving them. This should provide pointers towards the future development of the field. Furthermore, a special section is devoted to all-solid-state lithium batteries, which have emerged as promising alternatives to current liquid-electrolyte LIBs. These raise more profound mechanical issues during operation and thus deserve more attention from mechanics community.

In order to facilitate this ambitious endeavor, we need to limit the scope of our considerations. In this paper we will therefore exclude thermal runaway related to dendrite penetration in metal-air and metal-sulfur rechargeable batteries. Moreover, we will not regard safety issues stemming from mechanical abuse of battery cells. Such effects have however found attention in the recent review by Kerami and Sahraei [18]. We also restrict our study to a continuum view, which ranges from the particle level (microns and sub-microns) to the battery scale. The models based on first principles are out of scope for this review paper but have been reviewed in the article by Islam and Fisher [364].

Even though this review focuses on the mechanically coupled issues in LIBs, the essential knowledge and methodology on mechanical degradation and the contribution of mechanics to ion transport and electrochemical reactions are well applicable to other battery chemistries such as Na-ion or Mg-ion batteries. In a more general sense, they are also helpful to understand the role of mechanics in other energy conversion and storage processes in materials, for instance photovoltaics and catalysis.

We begin the review at the electrode particle level in Section 2 with an introduction to a basic model accounting for the electro-chemo-mechanics of a single stand-alone particle of active material in order to provide the reader with a general understanding of the multi-physics phenomena taking place within an active particle during charge and discharge. Based on the limitations of this basic model, we discuss its extensions for different mechanical behavior and degradation mechanisms. Section 3 and Section 4 are then dedicated to the modeling of mechanical influence at two larger scales: the electrode level and the cell level. Due to the complexity of the battery structure, a full modeling with all particles is possible on neither of the two scales. Therefore, simplified models are proposed. At the electrode level, there are two different approaches: micro-structurally resolved models and homogenized models. The former resolves all the details but is limited to countable particles with the surroundings, whereas the latter employs micromechanics-based homogenization techniques to obtain effective quantities for the composite electrodes with different microstructures. At the cell level, model variations that are adapted from battery cell theory from the electrochemistry community [31] are extended in order to incorporate mechanical effects. However, due to the compliant nature of liquid electrolyte, mechanical issues are at this level not as significant as others, for instance electrical, chemical and thermal effects. The mechanically coupled modeling research is thus also lacking. However, a recent trend is towards replacing the liquid electrolyte with solid electrolyte, where mechanical effects play a more pronounced role in batteries. This poses a big challenge not only to the electrochemistry, but also to the mechanics community. Consequently, we address this enhanced importance of mechanical effects separately in Section 5.

2. Particle level

Electrode active materials are crucial to batteries because they directly influence battery capacity. Lithium ion intercalation and de-intercalation in an electrode particle will give rise to, among other

phenomena, stress generation, phase separation, volumetric expansion, and particle fragmentation. In this section, mechanistic models are firstly introduced for a better understanding of the functioning of active particles during lithiation and delithiation. On this basis, various degradation models are given to discuss the failure of electrode particles.

2.1. Modeling of diffusion-induced stresses and stress-assisted diffusion: the basic model

Modeling of chemically induced stresses can be dated back to the 1960s, beginning with the work of Prussin [32] who described the stresses developing in Si wafers using an analogy to thermal stresses, an ansatz which finds application to the present day. The thermodynamics of diffusion interacting with stresses has later been formulated by Li [33] and, in a series of papers, by Larché and Cahn [34–36], which have later been extended to account for concentration-dependent material parameters [37]. A general theory for diffusion in stressed solids has been described by Aifantis [38]. Analytical solutions for this model have been derived in Refs. [39,40]. Extension towards diffusion in viscoelastic media and within solids undergoing large elastic deformations are described by Taylor and Aifantis [41] and by Stephenson [42], respectively. Early applications of these stress-diffusion models can be found, for instance to modeling hydrogen embrittlement, by Girrens and Smith [43]. Modeling of lithium intercalation induced stresses in lithium batteries has, however, not found attention until 2005, when García et al. [44] developed a mechanically coupled 2D battery cell model with spatially varied porous electrode microstructures beyond the mean-field methods. In their work, they split the total strain (ϵ) into elastic strain (ϵ^{el}) and inelastic strain (ϵ^{ch}) due to lithium insertion. Following Vegard's law, the chemical strain is proportional to lithium concentration inside the particle,

$$\epsilon^{\text{ch}} = (c - c_{\text{ref}})\beta, \quad (1)$$

where β denotes the Vegard coefficient, c the lithium concentration, and c_{ref} a reference strain-free concentration. With that model, they captured the overall stress distribution across a group of representative particles during discharge.

Meanwhile, Christensen and Newman [19] derived a stand-alone electrode particle model in which they considered mechanical stresses and fracture in lithium insertion materials. In their model, instead of strain decomposition, the total stress is split into an elastic stress and a thermodynamic pressure, that is, an equivalent elastic pressure to deform the particle by a chemically induced volumetric strain. In this model, the thermodynamic pressure also contributes to the diffusion of lithium inside the particle, thus establishing a two-way coupling between chemical and mechanical behavior. This means that, at any instance of time, the transport of lithium will give rise to distributed stresses, which, in turn, affect the diffusion of lithium in the electrode active material. The chemical and mechanical fields are thus dependent on each other.

For simplicity, this effect of the stresses on the chemical behavior is ignored in many of the early models. By introducing an eigenstrain (or stress-free transformation strain) expressed as Eq. (1) in an analogue to the thermal strain, the problem is thus reduced to a purely mechanical problem. The lithium concentration distribution is thereby either prescribed through a steady-state function or it is computed independently by solving Fick's diffusion equation, with the stresses generated here being known as *diffusion-induced stresses* (DIS). Since a constant homogeneous concentration field in a free-standing solid will only give rise to homogeneous and stress-free swelling, gradients or discontinuities in the lithium concentration are necessary to generate a stress field.

However, mechanical stresses also play an important role in assisting the diffusion process. An alternative approach to that of Christensen and Newman, that is, considering the stress-assisted diffusion, is to modify the diffusivity in Fick's diffusion law in the light of

thermodynamics. As an example, consider the mechanical confinement of the active electrode material which has been identified as a strategy to mitigate the large volumetric expansion of materials such as Si [45–47]. This necessarily causes compressive stresses within the active material and hence an overpotential which can limit the accessible capacity of the material [48–50] and the rate of lithiation [51]. Mechanical stress can thus be used to enhance the diffusivity of the active material [365], for instance in LiCoO_2 [52,53], $\text{Li}_x\text{V}_2\text{O}_5$ [54], and LiFePO_4 [366]. A full consideration of the interaction between electrochemistry and mechanics (two-way coupling) is thus very important for a better understanding of the coupled behavior in an electrode active particle and for the correct prediction of stress levels in the active material [55] and for surface reaction rates. In particular the latter are increasingly affected by surface stresses upon progression towards nanoscale electrodes, a fact that so far has only found scarce attention in the scientific community [367–369].

In this section, a simple yet practical two-way coupled model is summarized that considers mechanical stresses and lithium diffusion inside the particle. It is mostly based on the work of Zhang et al. [56] and is built based on the following assumptions:

- Electron transfer is fast enough compared with lithium transport so that electrons can always equilibrate at any time instant. This is valid during normal operation of a battery since the diffusion under direct current pulse (or slow alternating current pulse) is the dominant mechanism. The electronic conductivity is several orders of magnitude larger than lithium diffusivity in active materials such as LiMnO_2 [57]. This assumption helps to eliminate the governing equations for the electron transport. Moreover, since we assume the electrode material to be electronically conductive, the whole electrode particle is in isotropic state, which again helps to cut down the efforts for solving the governing equation for electro-static potential throughout the electrode particle. Electrons are thus disregarded.

- The diffusion model is adapted from a dilute solution model, which can be valid only if lithium migrates among interstitial sites. Li vacancy sites are thus not conserved.
- Since only interstitial intercalation is assumed in the model, it is natural to also assume that the structure of host materials is only slightly affected and can fully recover. With this assumption, plastic strains and phase transformation of the host material are disregarded. The particles show only small deformations under the coupled diffusion process, and material properties remain constant under lithiation and delithiation.
- It is assumed that the host material is either polycrystalline or amorphous, possessing homogeneous and isotropic chemical and mechanical properties. The particles are considered to be large enough so that surface stresses can be disregarded. The particles are free-standing, that is, there is no interaction with neighbor particles.

Since lithium transport inside the electrode is a complex process, involving not only lithium but also other species such as electrons, host atoms, and vacancies, these assumptions can be violated in some specific systems. We will elaborate this point in more detail in Section 2.2.

In the model, the chemical potential gradient is employed as the driving force for the movement of lithium ions, following the idea of Verbrugge and Koch [58] and Botte and White [59]. The chemical potential of 1 mol lithium inside an active particle body \mathcal{B} is expressed as

$$\mu = \mu_0 + RT \ln c - \Omega \sigma_{\text{n}}, \quad (2)$$

where μ_0 , R , T , and c are reference chemical potential, gas constant, absolute temperature, and lithium molar fraction, respectively. Ω is the lithium partial molar volume, which represents the volume change of an active particle upon adding 1 mol lithium into it. Further, σ_{n} denotes the hydrostatic stress, expressed as $(\sigma_{11} + \sigma_{22} + \sigma_{33})/3$. Equation (3) can potentially include further terms, describing, for instance the non-

ideality of solution [370]. The lithium transport inside the particle (assuming the particle to be an ideal electronic conductor and being in an isopotential state) is then expressed as

$$\frac{\partial c}{\partial t} = -\nabla \cdot \mathbf{J} = \nabla \cdot \left(\frac{Dc}{RT} \nabla \mu \right) = \nabla \cdot \mathbf{D} \left(\nabla c - \frac{\Omega c}{RT} \nabla \sigma_h \right) \text{ in } \mathcal{A}, \quad (3)$$

where D denotes the diffusion coefficient and where \mathbf{J} is the lithium molar flux. Here, Ω can be interpreted as a chemo-mechanical coupling coefficient. Its derivation from nano-indentation experiments has been described recently by Papakyriakou et al. [60]. This non-classical diffusion can be modified further, including, for instance, drift terms due to electrostatic interaction or due to local deformation velocity, which can even outweigh the flux due to a concentration gradient [61,371].

For the mechanical part, a linear elastic material is assumed, whose constitutive relation reads

$$\boldsymbol{\sigma} = \frac{E\nu}{(1+\nu)(1-2\nu)} \text{tr} \boldsymbol{\varepsilon}^{\text{el}} \mathbf{1} + \frac{E}{1+\nu} \boldsymbol{\varepsilon}^{\text{el}} \quad (4)$$

where E and ν are Young's modulus and Poisson's ratio, respectively, and where $\mathbf{1}$ is the second-order unit tensor. The elastic strain is expressed as $\boldsymbol{\varepsilon}^{\text{el}} = \boldsymbol{\varepsilon} - \boldsymbol{\varepsilon}^{\text{ch}}$, where $\boldsymbol{\varepsilon} = (\nabla \mathbf{u} + (\nabla \mathbf{u})^T)/2$. Starting from Eq. (1), we can derive a simplified expression for $\boldsymbol{\varepsilon}^{\text{ch}}$ upon assuming isotropic lithiation-induced deformations:

$$\boldsymbol{\varepsilon}^{\text{ch}} = \frac{\Omega}{3} (c - c_{\text{ref}}) \mathbf{1}. \quad (5)$$

The local force balance is then

$$\nabla \cdot \boldsymbol{\sigma} = 0 \text{ in } \mathcal{A}. \quad (6)$$

The virtue of this model lies in the fact that, for stand-alone particles with simple geometries and sufficient symmetry (such as spheres and cylinders), a closed-form expression of hydrostatic stress σ_h with respect to the concentration c can be derived [56,62,372,397]. One can thus recast Eq. (3) into

$$\frac{\partial c}{\partial t} = \nabla \cdot [D(1 + \gamma c) \nabla c] \text{ in } \mathcal{A}, \quad (7)$$

where $\gamma = (2\Omega^2 E)/[9RT(1 - \nu)]$ is a parameter representing the coupling between mechanical stresses and concentration. In other words, for such simple geometries, the chemical and the mechanical problems can be decoupled. It can further be observed from this model that the effective lithium diffusivity is actually enhanced by mechanical stresses from D to $D(1 + \gamma c)$, and that the effective diffusivity increases with increasing concentration.

Based on this model, the lithium diffusion and the mechanical stresses in spherical and cylindrical particles can be determined by the finite difference method. However, this simple approach falls short in simulating complex geometries and boundary conditions, which warrants use of the finite element method. Considering the aforementioned isotropic material and the strain decomposition shown in Eq. (5), the gradient of hydrostatic stress can be expressed by primal variables (displacement \mathbf{u} and molar fraction c) as

$$\nabla \sigma_h = \frac{E}{1-2\nu} [\nabla(\nabla \cdot \mathbf{u}) - \Omega \nabla c], \quad (8)$$

which renders Eq. (3) a third-order partial differential equation. A direct treatment using C^1 -continuous shape functions is described by Stein and Xu [63], where the force balance and the diffusion equations are solved monolithically for the primal unknowns. Alternatively, one can also solve this problem using a mixed formulation or a staggered scheme [64–66]. For the former approach, a proper combination of discretization of the concentration field and the extra field (usually σ_h or μ) is crucial for the convergence of the solution. For the staggered method, care should be taken of the choice of the time step size for a more accurate solution.

For the electrode surface, proper boundary conditions need to be given. Mechanically, traction-free boundary conditions are commonly

applied on the outer surface and a fixed central point is imposed to prevent rigid-body movements. For a finite element treatment, an octant of a 3D sphere or a quarter of a 2D disc is generally constrained by symmetry boundary conditions [63].

The chemical boundary conditions are highly dependent on the experimental electrochemical setups to be simulated. To characterize different electrochemical properties of insertion materials, experiments are conducted with different electrochemical methods [30,67,68]. These conditions need to be carefully treated in the simulation in order to reproduce the experimental results. To simulate galvanostatic charge/discharge, the Neumann boundary condition

$$-\mathbf{J} \cdot \mathbf{n} = \frac{\hat{i}}{zF} \text{ on } \partial \mathcal{A}_{\text{galvano}} \quad (9)$$

is applied on the electrode-electrolyte interface with the normal vector \mathbf{n} pointing towards the electrolyte. \hat{i} is the applied current density flowing into the electrode particle, z is the charge number of an inserted/extracted ion and F is Faraday's constant. On the electrode-substrate interface, which is impermeable to the ions of active species, \hat{i} is set to be zero. For a potentiostatic charge/discharge process the Dirichlet boundary condition

$$c = \hat{c} \text{ on } \partial \mathcal{A}_{\text{potentio}} \quad (10)$$

is often employed in simulations under the assumption that the surface reactions are kinetically sufficiently fast such that the equilibrium concentration \hat{c} of the active species is instantly reached on the surface. Consequently, the overall insertion/extraction rate is governed by bulk lithium diffusion (diffusion-limited dynamics) [69]. Alternatively, the surface flux can also be computed by considering the simple reaction



where \mathcal{M} is the host active material. A phenomenological Butler–Volmer expression can thus be given as the boundary condition [31].

$$-\mathbf{J} \cdot \mathbf{n} = \frac{i_0}{F} \left\{ \exp\left(\frac{(1-\beta)F\eta}{RT}\right) - \exp\left(-\frac{\beta F\eta}{RT}\right) \right\}, \quad (12)$$

with i_0 being the exchange current density, β a symmetry factor representing the fraction of the applied potential that promotes forward reaction in Eq. (11), and η the electro-chemical over-potential, expressed as [70–73].

$$\eta = V(\mathbf{x}, t) - U(c_s), \quad (13)$$

where V is the space- and time-dependent applied potential and U is the equilibrium potential, a function of the surface concentration c_s . In this approach, no assumptions of fast reaction kinetics is required and numerical experiments can be carried out with different reaction-diffusion relations. This boundary condition is particularly suitable for describing potentiostatic and -dynamic loading. It is also widely used in different cell models as shown in the following sections, where electrolyte potentials can be calculated at the battery level.

2.2. Model variations based on deformation/lithiation mechanism

The model described in the preceding section is a good starting point to understand the coupling between chemical intercalation and mechanical stresses and it can offer a reasonable explanation of the electro-chemo-mechanical behaviors of electrode particles. However, due to over-simplified assumptions as described in the last section, it needs to be extended for different material systems which are influenced by additional mechanisms.

Remark: It is well accepted that electrode materials can be classified into two main categories based on lithiation/delithiation reaction: intercalation and conversion (including alloying) materials. The former includes graphite, TiO_2 , LiCoO_2 , LiFeO_4 , whose crystal structures remain unchanged or which experience only slight distortion. The latter

includes alloy anodes such as Si and Sn as well as metal halides, which undergo structural change, accompanied by chemical bond breaking and recombination. In this review, however, we do not follow this classification for the mechanical models. The reason is twofold: firstly, different mechanical mechanisms can be present within one material category. Secondly, materials from different categories can also exhibit the same mechanical mechanisms. For instance, phase transformation is much less obvious in materials such as graphite, LiCoO₂ and a-Si than in materials like LiFeO₄ and c-Si. Therefore, the focus of the classification in this review is the mechanical significance during lithiation/delithiation.

2.2.1. Host material lattice distortion and plastic strain

It is very desirable for an intercalation material to maintain minimal volume changes during charge and discharge in order to ensure stable cyclability. Cathode materials usually exhibit relatively small volumetric deformation ($\approx 5\%$). Graphite—which is by far the most successful commercial anode material—shows a volume expansion up to 10%. The observed strains are already beyond the linear kinematic assumption (small deformation). It is thus inappropriate to use linear elasticity theory for such materials. Moreover, many high-capacity anode materials can expand to several times their original size when fully lithiated. For instance, the particle volume of Si can increase up to 310% with an uptake of 4.4 Li atoms per Si atom. Furthermore, accumulated evidence has shown that part of the incurred strain is inelastic and irreversible even for amorphous Si (a-Si) [74–78], indicating a possible plastic strain. Yield stresses of ca. -1.75 GPa (compression) and 1 GPa (tension) have been estimated for a silicon thin film electrode by Sethuraman et al. [76].

In order to account for this phenomenon, Bower et al. [79,80,373] employed a multi-component Larche–Cahn model [81] which permits unoccupied Si lattice sites to be created or destroyed. They found that there is a large irreversible deformation change when initially unoccupied Si sites are introduced. Similar models considering the interdiffusion between the host and guest atoms have been proposed by Gao et al. [82] and Baker et al. [83]. They formulated a mechanically coupled three-field problem of the elastic deformation, the concentration of lithium, and the concentration of host atoms (in this case, silicon) and described its mixed-variational Finite Element implementation. Their results show that interdiffusion can reduce the intercalation-induced stresses even below yielding threshold for plasticity.

Recently, Salvadori et al. [84] proposed a coupled model for heat and mass transfer, mechanics, chemical reactions, and trapping of the mobile species. Their model considers trapping of mobile species in the host material, inducing inelastic straining of the host material, and it is applied to the analysis of vacancy redistribution in metals, hydrogen embrittlement, and the insertion/extraction into a spherical LiCoO₂ electrode particle. Singh and Bhandakkar [85] studied the stresses developing in a free-standing elastic-perfectly plastic spherical electrode particle covered by viscoelastic binder. They found that high binder stiffness and viscosity may lead to yielding of the encapsulated particle.

In continuum models, the plastic strain (ϵ^{pl}) is an additional contribution to the total strain. In the large deformation regime, a multiplicative decomposition of total deformation gradient $\mathbf{F} = \mathbf{F}^{\text{el}}\mathbf{F}^{\text{pl}}\mathbf{F}^{\text{ch}}$ is introduced, where \mathbf{F}^{el} , \mathbf{F}^{pl} , and \mathbf{F}^{ch} are the elastic, plastic, and the lithium-intercalation-induced contributions to the deformation gradient, respectively [86,374]. To determine the plastic strain, a standard rate-dependent or rate-independent plastic rule can be employed, which is based on a von Mises yield criteria and an associated flow rule stemming from the 2nd invariant J_2 of the stress deviator σ_{dev} [65,79,86–90,375,376]. However, it can also be argued that in some materials such as silicon, the yield surface depends on both the mechanical and chemical history. Consequently, the chemical reactions taking place in the material would change the yield resistance and hence promote plastic flow. This approach denoted as “reactive flow” was put forward by Zhao et al. [78] and found consideration in a series

of papers [91–95].

A related factor is the formation of dense dislocation clouds under lithiation of SnO nanowire anodes [96,97] and LiCoO₂ cathodes after high-rate charging [96,97], see Fig. 2(b). The high density of dislocations results in the loss of crystal structure of the host material. Although the dislocations themselves do not seem to cause any performance decay, they can at least be seen as a symptom for the structural degradation of the electrode material [11,98]. On the other hand, dislocations have been known for a long time to constitute paths of enhanced diffusion, particularly in metals [99], and it has been hypothesized that a similar beneficial effect will arise in the electrodes of Li-ion batteries [100–102].

One of the earliest works to incorporate dislocations and their effects into models for electrode particles was described by Wei et al. [103]. In their model, as in the later approaches that followed, dislocations are regarded merely as an additional source of stresses that have no influence on diffusion. Following Prussin [32], the dislocation density is assumed to evolve proportional to the concentration gradients. Using a result of Estrin [104], they describe a *scalar stress* that develops due to the dislocation density and which is subsequently superimposed onto the radial and tangential diffusion-induced stresses in a spherical particle. The additional stresses due to the dislocations lead to a reduction of tensile stresses that develop during intercalation. Furthermore, these dislocation-induced stresses can convert tensile stresses to compressive stresses and hence reduce the tendency for crack initiation.

However, this approach has been disputed by Yang [105] on the grounds that the resulting stress fields violated the stress-free boundary conditions described by Wei et al. [103]. As an alternative, he proposed an elastic-plastic approach wherein the dislocation density affects the deviatoric stress components via the plastic strain. In his approach, the dislocation density would evolve with the curl of the concentration field instead of its gradient. Unfortunately, he only outlined his approach and did not give any results. In a separate paper, however, Yang [106] describes a simple model for the evolution of dislocation density in lithiated particles. By this, he demonstrated a size effect in the incurred dislocation density: he predicts a growing dislocation density due to lithiation with decreasing particle size. The eigenstrains caused by the formation of dislocations are further shown to reduce the intercalation-induced stresses.

Nevertheless, models using the approach by Wei et al. [103] have been applied for the computation of stresses in thin films [107], hollow spherical particles [108], or cylinders [109]. Chen et al. [110] applied this approach for the description of a phase transformations in a spherical particle and compared the resulting stress profiles with that of a simple phase-transforming particle and a single-phase material. Thereby, they expressed the dislocation density in terms of the lattice mismatch at the moving sharp phase boundary. They later used this model to derive stress intensity factors for a phase-transforming material [111]. The model proposed by Wei et al. [103] was further modified to include strains from forward and backward intercalation reactions [112] or, following the approach described in Refs. [113,114], to analyze the effects of surface stress in nanospheres [115] and nanowires [116], both of which affect the stress profiles within the considered electrode particles. The model has found further application by Ma et al. [117] for the analysis of irradiation-induced changes in the elastic constants and the plastic behavior of active electrode materials. The shown results agree well with the described experimental data, despite the aforementioned shortcomings of the underlying model.

Wang et al. [118] established a theoretical framework for relating the indentation hardness of a material sample to its state of charge. They make use of Prussin's relation between concentration gradients and dislocation density, from which they directly compute the material hardness by virtue of the Taylor orientation factor. An extension of their work considering elastic softening has been done by Ma et al. [119].

Huang and Wang [120] analyzed the stress fields due to several

dislocations in LiFePO₄ and discussed the onset of fracture in this material in terms of dislocation interaction. An analytical model for the generation of misfit dislocations has been proposed by Li et al. [121], where the generation rate is proportional to the strain energy within the layers of a thin film.

2.2.2. Phase separation

Phase transformation occurs in both anode and cathode materials. At the anode side, during the first cycle, crystalline silicon (c-Si) undergoes phase transformation to a-Si [122–127]. Even in a-Si, a two-step lithiation mechanism is observed, where two phases of a-Si coexist during the first lithiation, with single-phase lithiation in subsequent cycles [128,129]. Cathode materials such as LiFePO₄ and LiMnO₂ are also phase-separating materials, where two phases can coexist in a single crystal during (de-)lithiation [130,131]. Differential strains at phase interfaces lead to large mechanical stresses, which will not necessarily disappear even with open circuit condition. Moreover, Huang et al. [132] and Yang et al. [133] found that phase separation can change the sign of the stresses at the shell of a spherical Si particle. A particle under lithiation can hence experience tensile shell stresses, which runs against the common belief of compressed outer layers during ion insertion (e.g. Ref. [19]). They argued that the large compressive stresses in the shell at the onset of lithiation cause an immediate plastification of the shell and hence the release of compressive stresses.

In order to account for phase-separating behavior, two different models are employed: sharp-interface and phase-field (diffuse-interface) models. In the former, a discontinuity is imposed at the interface, and a subsequent strain mismatch will give rise to stress concentration at the interface [134]. This discontinuity can be described explicitly by a jump condition on an interface layer between two different domains (e.g. Ref. [135]); it can also be achieved by assuming a non-linear diffusivity that is infinitely large when $c = 1$, which effectively promotes a sharp reaction front [136]. These models have been employed in order to compute the stress build-up both in the bulk and at the interface in spherical and in hollow spherical particles [135,137,138] as well as in thin films [139]. They can also capture the velocity of a migrating interface in combination with reaction models such as the Butler–Volmer equation and bond-breaking kinetics at the interface [140,141]. It has further been found that lithiation-induced elastic softening of a-Si at the first cycle mitigate stresses in the following cycles [142]. Further, it has been found that external mechanical loading regulates lithiation and can lead to isotropic deformation even with anisotropic reaction kinetics in Si nano pillars, as shown in Fig. 3(a).

However, these sharp-interface models in general require sophisticated interface-tracking techniques when a solution with a moving interface is sought numerically. Phase-field models are thus employed as an alternative to sharp-interface models. Here, the interface is captured by a field variable, a so-called “order parameter”, and the tracking of the interface by an adaptive mesh can be avoided [72,86,145]. In phase-field methods, the expression of chemical potential Eq. (2) is modified so that it allows for two-phase coexistence. A simplest expression considering linear elasticity and a regular-solution model is given by Refs. [145,146].

$$\mu = \mu_0 + RT[\ln c - \ln(1 - c)] + RT\chi(1 - 2c) - \kappa\Delta c - \Omega\sigma_n, \quad (14)$$

where spinodal decomposition of two phases can occur for $\chi > 2$. The term containing the Laplacian of concentration (Δc) is an energetic penalty of forming a phase interface, with κ being a parameter related to this interfacial thickness. A Cahn–Hilliard-type equation is thus in place to govern lithium concentration evolution

$$\frac{\partial c}{\partial t} = \nabla \cdot \frac{Dc(1 - c)}{RT} \nabla \mu = \nabla \cdot D \left\{ [1 - 2\chi c(1 - c)] \nabla c - \nabla(\kappa\Delta c) - \frac{\Omega c(1 - c)}{RT} \nabla \sigma_n \right\} \text{ on } \mathcal{A}. \quad (15)$$

Since Eq. (15) is a fourth-order non-linear partial differential equation, numerical treatment is challenging in solving this, in particular for finite element method. One can use a mixed formulation [147], isogeometric analysis [144], or a staggered scheme for the numerical solution.

In specific applications, Eq. (14) needs to be modified for different materials. For instance for silicon, Eq. (14) needs to be formulated in a large deformation regime, potentially with consideration of plastic deformations [144,147,148,377–379]. Zhao et al. [149] extended this model to consider large deformation and Butler–Volmer-type surface reaction. They found through a simulation with a spherical particle that phase separation can be very different in a diffusion-limit regime and a reaction-limit one. Zhang and Kamlah [398] studied the impact of particle size and elastic parameters on the miscibility gap in Li_xMn₂O₄ and Li_xFePO₄ nanoparticles and discussed the inhibiting conditions for inphase separation. Cogswell and Bazant [150] modified Eq. (14) with an orientation-informed elastic energy for the coherency strain between two phases in order to capture a striped pattern during lithium intercalation, known as a “domino-cascade” phenomenon [130]. A recent contribution by Nadkarni et al. [151] considered an anisotropic interface thickness tensor κ and studied its impact on phase stability in Li_xFePO₄ nanoparticles under lithiation and delithiation. Apart from strains, the diffusion mobility tensor can also be modified to capture the anisotropy of the interface [152].

Experimental observations indicate that nanosized olivine electrode particles exhibit amorphization in addition to phase separation. In order to study the conditions for amorphization, Chiang et al. formulated a phase-field model with the three state variables local concentration, crystallinity, and displacement [153–155]. Their model considers the interaction between diffusion and mechanical stresses, and its results indicate a critical particle size below which a particle will undergo amorphization in order to relieve stresses. As they show further, this behavior is driven by the applied overpotential and the lattice misfit between lithium-rich and lithium-poor phases. Their model finally contains an asymmetry in the energy barriers for the transition from a crystalline to an amorphous phase, which leads, over several charge-discharge cycles, to a gradual loss of crystalline structure of the active material.

2.2.3. Host material elastic stiffening/softening

The elastic properties of both cathode and anode materials vary with lithium concentration [156–159]. Deshpande et al. [160] used a concentration-dependent Young’s modulus in the simulation of a cylindrical electrode particle and found that lithium stiffening is beneficial to avoid surface cracking during delithiation, and that a moderate lithium softening can alleviate particle cracking from the center under lithiation. Yang et al. [161] concluded that the composition-dependent modulus plays a significant role in determining the diffusion process as well as the stress field. First principal studies also suggest the consideration of change of Young’s modulus in continuum level models. For graphite negative electrode, Qi et al. [6] have shown a softening in carbon-carbon bonds within the basal plane and a stiffening of inter-layer bonds during lithiation. This results in three-fold increase in the elastic moduli. On the other hand, lithiation can also cause monotonic decrease/softening of elastic modulus for LiSn alloy negative electrodes material along with increase of Li concentration, as shown by Stournara et al. [5]. Guo et al. [162] presented a continuum model for a cylindrical Li-ion battery. In their contribution, the hydrostatic stress and concentration-dependent elastic moduli were taken into account. They found that the hydrostatic stress, other than the variable elastic

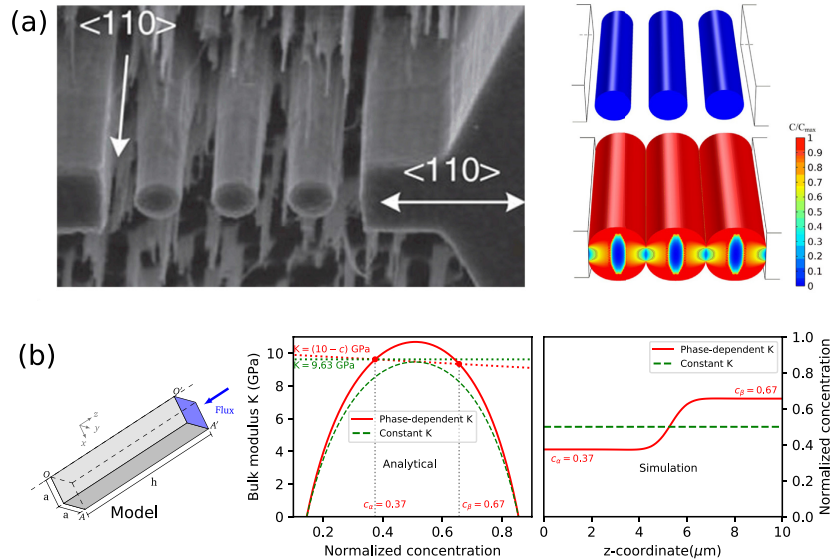


Fig. 3. (a) Experimental and modeling study of multiple Si nanowires lithiation and mechanical interaction. The geometrical confinement transform typical anisotropic lithiation behavior in Si to an isotropic one in the first cycle. Such modification should lead to lesser stress inhomogeneity and degradation of the Si anode. The results were then captured by finite element simulation [143]. (b) The influence of the mechanical constraint on a bar-shaped particle under fixed displacement boundaries. Analytical calculations and numerical simulations show that the phase separation behavior in equilibrium can be different with or without consideration of phase-dependent elastic moduli [144].

modulus, has little effect on the distribution of hoop stresses and radial stresses. Zhao et al. [144] used concentration-dependent elastic moduli in a phase-separating material, and found that variable elastic moduli admit a phase-separation where concentration-independent parameters would allow only for a homogeneous phase, as shown in Fig. 3 (b).

2.2.4. Anisotropy

Due to their anisotropic crystalline structure, nano-scale particles in general exhibit anisotropic properties. Lithiation of a c-Si nanoparticle is always associated with an a-Si shell and a polyhedral c-Si core crack initiation [138,163–166].

Levitas and Attariani [167] proposed a model which considered nonhydrostatic (deviatoric) stress contributions to the chemical potential of a-Si during lithiation and delithiation. They concluded that, despite the material isotropy of a-Si, deviatoric stresses cause anisotropic (tensorial) compositional expansion/contraction during Li insertion/extraction. Yang et al. [168,169] developed a model to study the phase and morphology evolution in silicon nanowires during lithiation. In their work, while the elastic modulus and bulk diffusion in two respective phases were treated as isotropic, the diffusivity inside the interface layer was assumed to depend on the local crystallographic orientation of the exposed c-Si surface. Anisotropic lithiation lead to stress inhomogeneities and fracture. In order to mitigate anisotropy-induced mechanical stresses, An et al. [170] engineered anisotropic morphologies of pristine c-Si particles that are deliberately designed to counteract the anisotropy in the crystalline/amorphous interface velocity.

LiFePO₄ crystals exhibit strong orthotropic behaviors. They offer exclusive 1D channels for lithium intercalation at interfaces between LiFePO₄ and FePO₄ phases [130]. Cogswell and Bazant [150], Tang et al. [152] employed phase-field models with orthotropic interfacial energy, diffusion models with orthotropic mobility, and elastic models with orthotropic elastic moduli in order to capture orthotropic phase

separation during lithiation and delithiation. Recently, Li et al. [380] extended these models by surface diffusion effects and discussed, how these can circumvent the low ionic diffusivity across phase boundaries in strongly anisotropic phase-separating intercalation compounds.

In polycrystalline particles, due to the different orientations of different grains, the mismatch strains at grain boundaries give rise to large stresses and an increased electrical resistance. Hu et al. [171] presented a phase-field model for a composite with multiple aggregated rutile TiO₂ single crystals. They found that, the anisotropic diffusivity in a randomly distributed aggregates will result in inhomogeneous lithium distribution and smaller capacity. Moreover, the diffusion along the grain boundary is also different from inside bulk. Han et al. [172] studied the effect of grain boundary upon the generated stress inside particles. They have shown that the fast diffusion pathways along the grain boundary network minimize stress evolution inside the grains and result in higher accessible capacities.

2.2.5. Particle morphology and size effects

Within the common active electrode materials for LIBs, Li ions exhibit a rather low diffusivity. This results in high concentration gradients, and by virtue of the misfit strain, in high stresses, which can cause mechanical degradation of the electrodes. Vanimisetti and Ramakrishnan [173] performed a general survey on the impact of particle size and shape on the magnitude of the DIS. To that end, they calculated the stored strain energy as a function of the particle sphericity and found that fibrous or flake-like particles exhibit reduced stress levels. Similar observations have been made by Stein and Xu [63] who performed parameter studies on prolate and oblate ellipsoidal electrode particles under galvanostatic conditions. They could show that a belt-like zone of high mechanical stresses develops around the particles' equator. With increasing distance to this belt region, the stress levels decay rapidly, as can be seen in Fig. 4(a and b).

A reduction of diffusion path lengths can, for instance be realized by

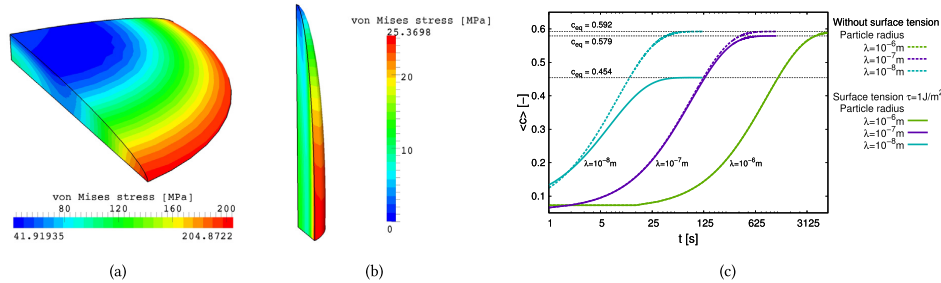


Fig. 4. Maximum von Mises stress distributions in oblate (a) and prolate (b) ellipsoidal particles for different aspect ratios Stein and Xu [63]. (c) Influence of the surface-stress-induced pressure in spherical electrode particles on the achievable state-of-charge. Through increase of the particles' electrochemical potential, the equilibrium concentration for a given potential will be reduced for a given stress. For smaller particle sizes, the relative impact of surface stresses (and hence the magnitude of the induced pressure) increases, yielding the particle-size-dependence of the capacity as shown above [174].

adopting hollow particles. Corresponding stress analyses have been performed by Harris et al. [175] and, under consideration of phase transitions, by Jia and Li [176]. Purkayastha and McMeeking [177] analyzed the intercalation into cubic electrode particles. The behavior of composite slabs/cylinders/spheres has been investigated by Suthar and Subramanian [178]. A common feature of these approaches is the use of analytical geometries such as spheres or cylinders [179].

It is clear that these idealized geometries are unable to reproduce the stress concentrations that emerge in the rugged, rough surfaces of realistic particles. These enhance the probability of fracture over the charge cycles. Studies on realistic particle shapes, for instance obtained from computer tomography (CT) scans, have been performed by Lim et al. [180], Chung et al. [181], Malavé et al. [182], and Hun et al. [183]. From their works it can be seen that the stresses in actual electrode particles exceed those in analytical geometries by as much as 410% [180]. Furthermore, these works demonstrated that irregular particles can fail locally even when the overall stress level in a particle is low.

However, such a fine-grained investigation of electrode particles requires huge computational efforts. In order to somewhat lessen these computational requirements, and to incorporate the immediate particle surroundings, phase-field methods can be adopted. Such frameworks have been described by Hu et al. [171] and by Lu and Ni [184]. Both groups describe the (agglomerate) particle geometry in terms of a phase-field model, where an order parameter describes the transition from electrolyte to active material. Hu et al. [171] extend this by further order parameters describing individual particle domains and their respective orientation. These models have been applied for the study of plasticity [184] and for charge transport [171] in agglomerate particles.

In recent years, nanostructuring of the battery electrodes has been proposed in the literature as a means to reduce DIS and to overcome the inherent low diffusivity of Li in the bulk material [185–190,381]. This trend is supported by experimental data indicating a high reversible capacity and stable cycling behavior [191] as well as a higher robustness against diffusion-induced mechanical degradation [7]. Accordingly, one can find studies on various nanoparticle morphologies such as nanowires [7], nanoflakes [192], nanowalls [193], inverse opal structures [194,195,382,383], hierarchical porous particles [196], or nanoporous electrodes [197]. This trend is further supported by additive manufacturing techniques which drastically widen the design space for electrode structures [198].

The size-dependent material behavior can be attributed not only to a lower defect density [384] and to reduced diffusion path lengths in the micro-structured material, but also to the effects of surface stresses, which gain an increasing influence with decreasing electrode particles size [199,200].

Classical models of elasticity cannot represent such size-dependent

effects. However, they can be extended correspondingly through incorporation of surface elasticity models [201,202]. Said models trace their origins back to the work of Gibbs [203] and the contributions of Shuttleworth [204] and Herring [205]. The fundamental mathematical theory of surface elasticity has been established by Gurtin and Murdoch [206], who assumed the surface to be an infinitesimally thin layer around a solid body. In order to capture its behavior, they formulated elastic relations analogous to solid elasticity. A nonlinear thermo-mechanical diffusion model incorporating viscoelasticity and surface effects has been formulated by McBride et al. [207].

The first group to consider surface effects in modeling the behavior of nanostructured electrode particles have been Cheng and Verbrugge [113]. They set up an analytical model for the diffusion in spherical nanoparticles under surface stress. In their model, the effect of surface stress was considered as a particle-size-dependent pressure boundary condition. For convex particles, this (average) pressure can be determined from the particle's surface-to-volume ratio and the acting surface stresses using the Weismüller–Cahn equation [208]. This caused a shift of the DIS towards the compressive regime, inducing an asymmetry between the charge and discharge behavior of the particle. However, in their model, they considered the diffusion to be decoupled from the stress field. This model has been later applied to the analysis of stresses in nanowire electrodes by Deshpande et al. [114].

The impact of surface stresses on the stress levels in insertion particles has later on been regarded by Hao et al. [209], DeLuca et al. [210], Gao and Zhou [385], and Zang and Zhao [211] in simulations of (hollow) nanowires and, in the case of the latter two, hollow nanospheres. Gao et al. [386] describe a model framework for the stress-coupled diffusion with surface stresses and applied it to the analysis of nanoporous materials. Liu et al. [135] extended these considerations by phase separation effects and showed that, despite the compressive stresses exerted on the hollow nanosphere by the surface stresses, strong tensile stresses can develop at the moving phase interface within the particle.

These approaches regarded spherical and cylindrical geometries, in which surface stresses will cause a homogeneous pressure. As in the case of DIS, the particle shape has a significant influence on the magnitude and distribution of the pressure field within the particle. Stein et al. [174] studied the interaction of constant surface stresses, stress-assisted diffusion, and electrochemical surface reactions in spherical and ellipsoidal electrode nanoparticles. They have shown that due to surface stresses, a pressure gradient arises in ellipsoidal particles which makes an appreciable contribution to the diffusional driving forces. Moreover, this pressure leads to a shift of the electrochemical potential which further affects the intercalation reactions at the surface (here modeled through a modified Butler–Volmer equation). Their results show that the interior pressure due to surface stress, while providing

mechanical stabilization, actually reduces the accessible capacity of the nanoparticles, as shown in Fig. 4 (c). Similar results have been obtained by Lu et al. [212] for spherical electrode particles under surface stress, considering variable surface stresses.

Stein et al. [213] recently calculated the migration energy barriers for Li vacancies in faceted LiCoO₂ nanoparticles which features strongly anisotropic surface stresses. Using finite element simulations and the defect dipole tensor concept, they could show that a heterogeneous pressure field develops in the nanoparticle under surface stress. Although this pressure distribution is expected to have a large impact on the diffusion of ions in the material, its energetic impact in migration barriers was shown to be negligible.

2.2.6. Buckling and wrinkling

Nanostructured electrodes usually exhibit slender features which, in combination with the intercalation-induced stresses, possess an inherent risk of mechanical instability, viz. “buckling”. This can be clearly seen in the work of Bagetto et al. [12], who produced planar silicon honeycomb structures as battery anodes. The morphology changes due to lithiation are illustrated in Fig. 2(d). Upon delithiation, the thin struts return *nearly* to their initial shape, with some struts showing cracks at the center of the ligaments. This work motivated Bhandakkar and Johnson [214] to analyze the stability of these structures using an elastoplastic model, and to study the impact of a stabilizing, conductive scaffold within the structure. This has shown that buckling can be exploited so as to reduce diffusion-induced stresses in the microstructure. The critical buckling length of constrained nanowires was examined by Chakraborty et al. [215], who describe a large-deformation, elastoplastic model for diffusion-induced swelling and stress-drift. Zhang et al. [216] compared the critical state of charge for buckling with different diffusion paths, and they concluded that both nanowire length and current density play important roles in determining the critical state of charge when the buckling occurs. Zhang et al. [217] have extended this model to regard binary phase separation and could demonstrate that both single-phase and two-phase segregation possess, given identical geometry and loading parameters, an identical critical buckling time. Similarly, the critical buckling length depends only the prescribed constraints and the applied charge rate, not on the lithiation mechanism.

Yu et al. [218] reported that thin-film electrodes on compliant substrates can mitigate mechanical degradation and maintain a good cyclability. They further offer a way to mitigate lithium dendrite growth [219]. Jia and Li [220] attribute the enhanced cycling performance to wrinkling-induced stress relaxation. They also pointed out through modeling and calculation that a risk of necking bands near wrinkling troughs or peaks can occur, which may lead to fragmentation of the anode (e.g. Fig. 2(e)).

2.3. Model variations based on degradation mechanism

The preceding discussions focused on the extensions of the basic model based solely on the mechanism of lithiation and the incurred

mechanical stresses. Right from the beginning of the collected modeling efforts, degradation has been a key issue in modeling LIBs. In this section, our discussion now rests on extensions of the basic model regarding specific degradation mechanisms.

2.3.1. Fracture

Fracture and delamination are critical factors that account for the deterioration of LIBs. High-capacity anode materials such as Si tend to fracture already during the initial few cycles whereas anode materials such as graphite in general exhibits stable cyclability. Large volumetric deformation of Si is also likely to give rise to delamination of Si from the current collector [221,222]. Commercial cathodes are usually fabricated as secondary particles, consisting, in turn, of crystallites with different orientations, also known as primary particles. Unless specified otherwise, all the particles to which we refer in this review are secondary particles, sometimes denotes as “meatball electrodes”. In two recent papers, Xu and Zhao investigate the disintegration of such electrode particles by means of cohesive-zone models for the separation of the primary particles and found that it is primarily the charging rate that drives the damage evolution in the aggregate particle [223,224].

Experiments have shown that both inter- and intragranular cracking of cathode particles are major failure mechanisms of cathodes at high voltage [225–227], especially for materials that undergo a phase change [228]. Due to the crystalline heterogeneity and microcracks, the mechanical properties of these particles, for instance the elastic modulus or the fracture toughness, span a wide range in the literature [229–231].

Extensive fracture models have been developed in an effort to find a proper description of the fracture of high-capacity anode materials, in particular for Si. Conventional cohesive zone models have been employed to study the fracture of Si nanowires [232], strip-shaped Si particles [233], Si nanopillars [234], and cylindrical graphite particles [235], as well as to the delamination of plate-like Si particles from the substrate [236–238,387]. This allows the determination of critical particle sizes and comparison with experiments.

Phase-field fracture models have been developed in order to simulate the crack propagation during cyclic charging of the particles [149,239–242], as shown in Fig. 5(a). These models can also predict crack propagation with different lithium content due to initial point defects in nano-sized anode materials, as shown in Fig. 5(c). Using a phase-field crack model, Zhao et al. [149] and Xu et al. [240] prescribed Butler–Volmer-type electrochemical reactions on both the initial particle surface as well as on the fresh crack surfaces. Based on phase-field models, Klinsmann et al. [241,242] concluded that a crack would initiate from a particle's surface and propagate inwards during delithiation (and vice versa). It is however worth noting that while this conclusion does agree with some experimental observations (e.g. Ref. [10]), it contradicts others (e.g. Ref. [138]), where visible cracks initiate from the surface and propagate inwards during lithiation rather than delithiation. There are several possibly reasons for this unexpected behavior. Firstly, the particles in the aforementioned experiments are, other than in the simulations, not free-standing, and inhomogeneous

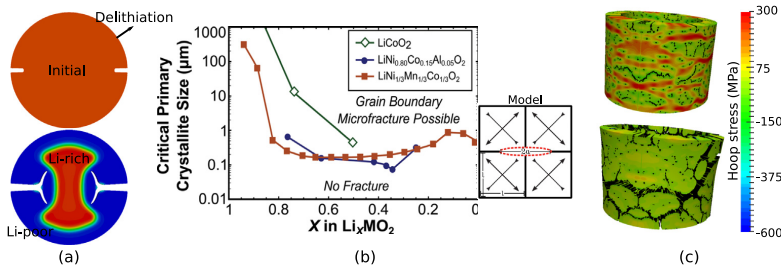


Fig. 5. Particle fracture due to different initial defects. (a) Crack propagation and branching of phase-separating material with initial notches under delithiation [149,240]. (b) Intergranular microcrack critia for secondary particles of selected LiMO₂ compounds. M stands for Co, Ni, Al and Mn. For a given SOC, crack can occur when the actual primary crystallite size exceeds the critical value [245]. (c) Crack propagation in a TiO₂ nanotube with randomly distributed initial point defects by an application of 1.26% strain due to lithium insertion.

mechanical/electrochemical boundary conditions can greatly affect the stress distribution inside the particles. Secondly, it can be argued that Si is a phase-separating material which will immediately deform plastically in the Li-rich phase in the shell, thus converting compressive stresses to tension in the shell region [132,136]. Finally, an anisotropic microstructure can increase the tensile stress in the shell so that a crack from the surface can become possible [169].

As an alternative to the two methods mentioned above, Barai and Mukherjee [243,244,388,389] described a stochastic computational methodology to model the crack propagation inside Si nanoparticles, using a lattice spring network to represent the particle.

The basic model in Section 2.1 is based on smeared-out microstructures, which yields a good estimation of stress levels, but which cannot predict stress concentrations across primary particles. Wu and Lu [246] developed a coupled mechanical and electrochemical model to predict intercalation-induced stress in a secondary particle with an agglomerate structure. Woodford et al. [247] derived a fracture criterion for a single LiMnO₂ particle with respect to different charge rates (C-rates) and particle sizes based on a continuum model and stress intensity factors. They also derived C-rate-independent criteria for grain boundary microcracks of the particles based on a microstructure-informed model [245], as shown in Fig. 5(b). In a series of papers, Zhao et al. [391–393] investigated the stability and growth of pre-existing cracks in electrode particles under diffusion-induced stresses and derived critical sizes below which the crack growth would be arrested. Similarly, Haftbaradaran et al. [390] investigated the delamination of Si thin films from the current collector using a fracture mechanics model. Gao et al. [394] formulated a J-integral for coupled deformation and diffusion and analyzed driving forces for crack growth in thin-film Si electrodes. Zhang et al. [395] recently employed a combined experimental-numerical approach to analyze the failure of coin-cell electrodes. Sun et al. [248] studied the fragmentation of granular cathode particles and pointed out that intergranular cracking is most severe in the first cycle. They performed sequential diffusion and deformation analysis upon the secondary electrode particles model to understand the mechanical decohesion and fracture between primary particles. Such degradation is clearly related to capacity fade as this would expose fresh electrode surface to electrolyte which will cause mobile Li consumption. To understand the damage between different domains (or particles), the contact area is described with a cohesive zone model. A linear traction-separation law was imposed which is sufficient to locate the crack initiation regions inside the 2D framework of spherical shaped secondary particles.

2.3.2. Solid-electrolyte interphase formation

The solid-electrolyte interphase (SEI) is a passivating layer formed on the electrode/electrolyte interface, which, under ideal conditions, is stable during cycling, permits fast lithium transport and, at the same time, is an electronic insulator. While the SEI is often referred to as the layer formed at the anode side, it can also form on the surface of the cathode particle, where is denoted as cathode-electrolyte interphase (CEI) [249]. In this section, we will consider only battery cells with liquid electrolytes; SEI formation for solid electrolytes will be discussed in Section 5.

Traditionally, SEI formation is more a chemical than a mechanical issue, depending heavily on the choice of the electrolyte. For a review on modeling of SEI formation from a chemical point of view, one can refer to the work of Wang et al. [250]. Nonetheless, mechanical problems arise when active materials with large volumetric change under (de-)lithiation are used. Due to the swelling and shrinkage of the active particles, SEI repeatedly forms and breaks down, resulting in a very thick SEI layer, capacity fade, and an increase in resistance [15]. For the description of the growing SEI and the stresses arising within, Revjitzky et al. [251] formulated a continuum model, described its finite element implementation, and investigated the stresses on the SEI/anode-particle interface for spherical- and spheroidal-shaped graphite

particles. Guan et al. [252] developed a phase-field model to simulate the morphological evolution of the SEI. With a prescribed contact angle between the newly produced SEI species and the graphite anode, they were able to capture the microstructure evolution of the SEI formation.

2.4. Concluding remarks

Lithium (de-)intercalation from and into an active electrode particle is a core mechanism for the functioning of a LIB, involving appreciable mechanical effects. Research into the degradation of battery electrodes has gained significant traction with the proposition of Si as anode material. This material promised to deliver a jump in available battery capacity, but its application highlighted a disappointing cycling performance due to mechanical degradation. Combined experimental and theoretical studies have identified a couple of mechanisms contributing to the behavior of Si particles, including large inelastic deformation, amorphization of the crystal structure, phase separation, anisotropy, fracture, and SEI formation.

Despite the intensive studies and the numerous modeling approaches, there remain several open issues that warrant further attention:

- The intercalation of lithium into a host material potentially leads to large inelastic deformations and the amorphization of the crystal structure. Through this mechanism, intercalation-induced stresses can be mitigated. A host of models has been described in the literature in order to capture this behavior. Based on observations made on metals, it has been hypothesized that the solid-state diffusion of Li ions can be potentially enhanced by a dislocation-rich microstructure. Current modeling approaches consider dislocations only insofar as they generate additional stresses in the bulk material, with the diffusion of ions being decoupled from the (evolving) dislocation density. The challenges that need to be overcome in order to follow this line of work involve the specification of dislocation systems at the microscale and the consistent homogenization towards the larger scales.
- The elastic properties of the active electrode materials have been shown to depend on the concentration of lithium. The resulting softening/stiffening effects can reduce the danger of crack initiation/growth and play a major role in the formation and stability of phases. Under lithiation, Sn exhibits a series of phases with different lattice parameters and elastic properties. The models discussed here have so far assumed a linear relationship between elastic properties and lithium concentration and deserve an extension towards more faithful, nonlinear relations between elastic properties and lithium concentration.
- Anisotropic properties are common in nano-scale particles due to lattice structures. These will influence diffusion directions, elastic stretching, and phase separation. They can also induce mismatch strains in polycrystalline particles among grains. Anisotropic elastic and chemical properties are readily incorporated into continuum models through the corresponding tensors. A factor that so far has found scarce attention is that fact that the chemical eigenstrain due to intercalation may have non-spherical components. The required information can be gained from atomistic simulations and can be integrated into continuum-level models by means of the defect dipole tensor concept [53,213,253].
- The impact of surface stresses on the chemo-mechanical behavior has predominantly focused on the pressure induced by the surface stress, which provides mechanical stabilization. However, the interaction of the, in general, heterogeneous pressure field with the ion transport has only found scarce attention. The studies so far concentrate on simple, analytic particle geometries and mostly on isotropic, deformation-independent surface stress. Realistic electrode nanostructures with surface stress effects have not been investigated yet. We do not expect the extension of the considered

surface stress models to pose significant problems. Further attention, however, has to be paid to the determination of suitable surface-elastic parameters from atomistic computations and their incorporation into the continuum setting.

- With the trend towards slender nanostructured electrode morphologies arises the risk of mechanical instability and failure through buckling. For elastic materials, this can be beneficial, allowing to relax stresses through a structure's evasion from the stressed initial state. Current studies focus on honeycomb structures and constrained nanowires, and first steps have been made in deriving critical buckling lengths and charge conditions for nanowire electrodes. The growing field of additive manufacturing also opens up new design directions for electrode microstructures, for instance in the form of inverse opal structures or microlattice frameworks. Although their high stiffness at relatively low weight and their high surface-to-volume ratio renders them interesting candidates for application as battery electrodes, these morphologies have not found attention in the mechanical community yet.
- Formation of the solid-electrolyte interphase is a major degradation mechanism in Li-ion batteries, featuring a loss of Li through formation of a passivating layer. Phase-field models again prove to be very efficient means for the description of this phenomenon. Despite the suitability of these model for the description of crack formation and propagation, studies on the formation and cracking of the SEI have not been undertaken yet. The dendritic growth of metallic lithium is a related factor, which can, through penetration of the separator layer, result in short-circuiting of the battery cell. Although it is generally believed that lithium dendrite formation is related to mechanical constraints in solid-state electrolyte, a convincing mechanism is not yet ready.

3. Composite electrode level

Most commercial batteries employ composite electrodes for both anodes and cathodes. These composite electrodes comprise, in general, active particles with a wide variation of sizes and morphology. These particles are supported by binders and conductive agents for improved mechanical integrity and electrical conductivity, respectively. The pores of this structure are filled by liquid electrolyte which wets the surface of the active material and provides continuous pathways for conducting lithium ions. This structure slightly differs for solid electrolytes, which will be discussed in Section 5. The inherent heterogeneity of the structure naturally leads to inhomogeneous distributions of lithium salt concentration, mechanical stresses, and electric potential in the electrode during the charge/discharge cycles. This, in turn, has a fundamental impact on the coupled electrochemical, thermal, and mechanical behavior of the composite electrodes. The discussed electrode models in the current section are formulated at a length-scale of several micrometers, which is sufficient to capture the heterogeneity. In order to evaluate the influence of this heterogeneity on the performance of the battery and to optimize its structural design, a proper composite electrode model is necessary. Spatially resolved models are thus employed in order to represent the different physical fields and their interactions in a heterogeneous structure under specific battery operating conditions.

Nonetheless, the physical processes taking place inside a composite electrode span several length- and time-scales, which renders straightforward modeling of a complete electrode very demanding. This drives the development of homogenization models based on the theory of micromechanics, where the relevant fields are averaged over a representative volume element (RVE). These models allow to bridge the gap in different spatial and temporal scales and can further provide effective quantities for cell-level calculations. Both approaches are discussed in the following sections.

3.1. Spatial field calculation of electrode models

Spatially resolved calculation upon composite electrode models can be considered as a natural extension of the single particle models, where the individual particles are embedded into solid matrices and their surfaces are wetted with electrolyte. These models however exceed the models for single, free-standing particles in that they are able to describe additional electrochemical and mechanical behaviors stemming from the electrode microstructures. Electrode microstructures are reported to be greatly affected by manufacturing processes, such as sintering temperature, compaction pressure, slurry composition, and particle size and shape distributions [254]. By electrochemical simulation upon composite models from actual tomographic or sectioned sample data, these effects can be assessed, aiding the optimization of the corresponding manufacturing processes.

3.1.1. Particle spatial distribution and size polydispersity

Experiments have shown that, through engineering the particle spatial distribution, an electrode's ionic resistance can be decreased concurrently with an improvement of the electronic transport behavior [255]. García et al. [44] carried out calculations based on synthetic two-dimensional microstructures. By varying particle spatial arrangement for a fixed particle volume fraction and for homogeneous particle radii, they evaluated microstructural effects in power density and stress evolution inside the electrode during discharge. Particles in different regions are thereby subjected to different Li intercalation mechanisms: particles close to the anode take on lithium mainly due to the potential drop. For particles far away from anode, on the other hand, the concentration difference is the driving force for intercalation since these particles are electrically shielded from potential gradients. This has an impact on the state of lithiation and on the stress state for different regions within the electrode, resulting in different cycle life expectancies for the constituent particles. Based on this model, Chung et al. [256] assessed the influence of particle size polydispersity and surface roughness on the electro-chemical and mechanical response of an electrode. They showed that, due to a reduced area density, the power density of the battery would be lowered for increasing particle size dispersity, whereas the energy density would be higher in a poly-disperse electrode than in a monodisperse electrode. Based on simulations of two-dimensional electrode geometries, Ji et al. [257] showed further that the mechanical stresses in composite electrodes can show a local variation for a given state of charge and that smaller particles experience faster charge/discharge.

The impact of particle size polydispersity on the electrochemical behavior is even more pronounced in phase-separating electrode materials. In order to simulate the inter-particle behavior in a cathode made of phase-separating active material, phase-field models have been employed by Zhao et al. [258], Jesus et al. [259] and Li et al. [260]. Their results showed that phase separation in a particle ensemble can differ greatly from that in stand-alone particles. In particular, it seems to be energetically favorable to establish phase interfaces not only within particles but also across particle-particle contact points, as illustrated in Fig. 6(a and b).

3.1.2. Particle-matrix interaction

In porous electrodes, particles are mechanically connected and supported by binders, which are in general electrochemically stable, well adhesive to particles and current collectors, and sufficiently compliant to compensate particle deformation. Aifantis et al. [262–264] considered cylindrical or spherical particles embedded into a glassy matrix. In their model, the concentration field is not explicitly given but implicitly described through the volumetric expansion. When embedded particles are fully lithiated, the exterior matrix experiences tensile circumferential stresses due to the swelling of the active particles, which can result in radial cracks nucleating at the interface between active particle and matrix. Using a 2D plane stress model, Rahani

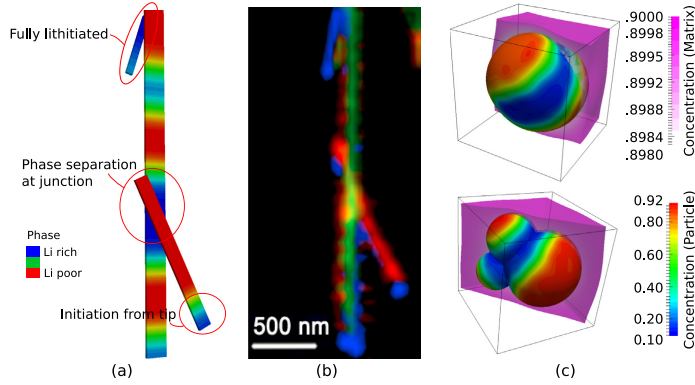


Fig. 6. (a–b) Inter-particle phase separation. (left) simulation results of a connected network of three particles. (right) a reconstructed compositional and phase heterogeneity across the interconnected network based on scanning transmission X-ray microscopy (STXM) maps [259]. (c) Concentration distribution of the deformed composite electrode with spherical and Mickey-mouse-shaped particles embedded in the polymer matrix at one time instance during lithiation [261].

and Shenoy [265] studied the stress distribution inside a graphite-based porous electrode subject to different charge-discharge regimes and graphite diffusivities. In their model, they considered two different microstructures of binder connecting the spherical graphite particles: binder bridges and binder shells. An extension to a 3D model allowed them to derive upper bounds for compressive and tensile stress generated at the binder-particle interface. Xu et al. [266] developed a finite element model simulating the coupled Li diffusion and mechanical stresses for three-dimensional composite electrodes. Based on this model, they simulated $\text{LiNi}_x\text{Mn}_y\text{Co}_z\text{O}_2$ (NMC) cathodes and SnO anodes and demonstrated that the mechanical confinement through the inactive matrix and the inter-particle contact can give rise to significant capacity losses. Zhao et al. [261] studied a 3D porous cathode comprising an irregular-shaped particle immersed in a polymer matrix with the finite cell method, as shown in Fig. 6 (c). The particles thereby exhibit a phase-separating behavior. A Butler–Volmer-type reaction is imposed at the particle-matrix interface, which governs the flux across the interface through the electro-chemical and mechanical status in both phases. Wang et al. [267] developed a model to study the stress evolution at the contact points and the binder/particle interface of spherical Si particles under cyclic electrochemical condition and thus highlighted the effect of binder mechanical properties, binder fraction, and charge/discharge strategy due to inelastic shape change of Si anodes. Motivated by experimentally observed battery degradation, Kim and Huang [268] studied the stresses on the cathode-electrolyte interface due to the fluid-structure interaction of active material and electrolyte.

3.1.3. Image-based reconstruction of electrode microstructure

In spatially resolved models, microstructures can be either generated artificially, based on porosity and particle size distribution [269,270], or they can be created using image-based methods [271]. Whereas the latter approach is computationally more expensive, in particular for 3D simulations, it preserves the geometric characteristics of the electrodes. This is important insofar as studies have shown that the electrode morphology has a significant influence on the electro-chemo-mechanical behavior of the electrodes. To reconstruct the 3D geometry for calculation, images extracted from micro/nano CT scans or from Focused-Ion Beam (FIB) sectioning are stacked in order to form a 3D voxel structure. This data set is subsequently processed by segmentation, smoothing, filtering, and geometrical reconstruction to yield a model of the geometry. The image-based reconstruction relies heavily upon proper segmentation or identification of different phases such as active particles, binder, or conductive agents and is potentially highly demanding for a better isolation of these intermingled phases. Roberts et al. [272] presented a computational framework that directly resolves the microstructure of many cathode particles and the surrounding

electrolyte. They also investigated the particle-to-particle contacts and they found that the largest stresses are located at the particle-to-particle contacts. A similar simulation with a conformal decomposition finite element method was performed by Mendoza et al. [273] on microstructures as illustrated in Fig. 7. In their model, they regarded the mechanical effects of the electrochemically inactive binder and showed that the binder helps to mitigate stress generation between the particles. Kim et al. [274] performed micro-scale simulation on representative volumes generated from actual FIB micrographs. The boundary conditions have thereby been derived from 1D macroscale electrochemical models. With these conditions, they computed both the diffusion-induced stress and the thermal stresses for different macroscale discharge rates and hence, could assess and compare the relative local evolution of DIS and thermal stresses. Wu et al. studied the stress generation inside different regions of reconstructed NMC [275] and LiCoO_2 [276] half-cells due to phase transition and Li intercalation. They considered an additional term for phase volume mismatch in the mechanical part which causes high stress state.

3.2. Homogenization of electrode models: effective properties

The electrode models described in the previous section, be they generated artificially or from micrographic images, are subjected to electro-chemo-mechanical modeling under suitable boundary conditions. The heterogeneity of structures is thereby explicitly addressed, and its effect is reflected in the solution fields. In homogenization studies of electrode models, on the other hand, the details of the microstructure are incorporated by RVE models, where effective quantities such as diffusivity, tortuosity, and elastic constants are calculated based on micromechanics theory.

Homogenization of the chemical and electrical properties of composite electrodes have been studied intensively [277–280]. A significant contribution was made by Newman et al. [281–283], who presented one of the first frameworks homogenization of a complete composite electrode. In their model, the porous electrode is assumed to consist of three phases: the electrode phase, the electrolyte phase, and the conductive filler, each characterized through the volume fractions ε_s , ε_e , and ε_f , respectively. For simplified cases, electrode particles were all assumed spheres with an identical radius R_s that are distributed homogeneously across the electrode. Similarly, the conductive filler is also assumed to be homogeneously distributed, with the electrolyte filling up the remaining space. The effective conductivity k_{eff} and diffusivity D_{eff} inside the electrolyte are then approximated by

$$k_{\text{eff}} = \frac{\varepsilon_e k_e}{\tau} = k_e \varepsilon_e^{1.5}, \quad D_{\text{eff}} = \frac{\varepsilon_e D_e}{\tau} = D_e \varepsilon_e^{1.5}, \quad (16)$$

where k_e and D_e are the respective quantities in a pure electrolyte. τ is

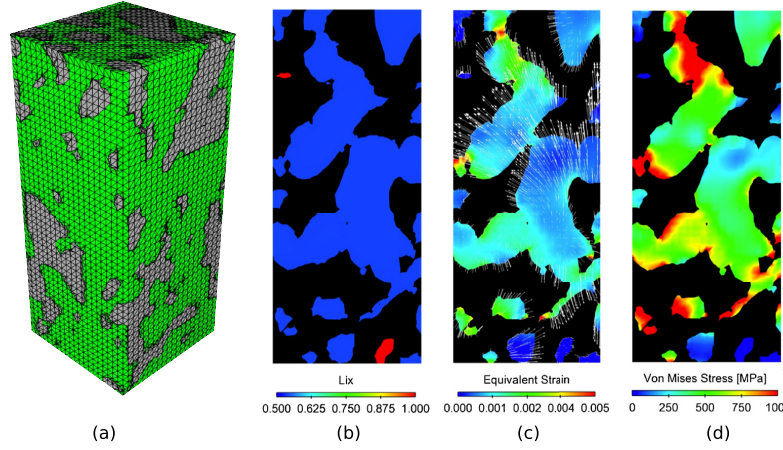


Fig. 7. (a) Numerical mesh for the reconstructed electrode. Distribution of (b) lithium fraction (Lix), (c) equivalent strain and (d) von Mises stress [GPa] at a cross section for baseline case (1C) at a SOC = 1 [273].

the tortuosity, taken as $\varepsilon_e^{-0.5}$. Note that the choice of τ is empirical, which accounts for the actual path length of the species in an electrode with spherical particles. There exist other empirical relations that are extensively used in porous electrode models, but they are limited by the assumptions made in their derivation, such as Bruggeman's relation [284,285]. In the early works, the porosity ε_e can also vary with the extent of reaction, without the consideration of expansion and compression of electrode particles (e.g. Eq. (11) in Ref. [281]). The volume change in porous electrodes was considered in the work of Weidner and coworkers [286–289], who based their model on the assumption that solid-phase reaction product during operation contributes to the change of porosity as well as stress-free electrode dimensional change.

Homogenization using reconstructed microstructures have, for instance, been undertaken numerically by Yan et al. [290] and by Wiedemann et al. [291]. Following micromechanics theory, a linear Poisson equation is solved over the solid and electrolyte phases in the reconstructed geometries using certain predefined boundary conditions, enforcing, for instance, an average concentration gradient in the sample. Effective conductivity and diffusivity can then be obtained by dividing the average flux vector by the prescribed average concentration gradient. This approach has been pursued by Hutzenlaub et al. [292], who employed a hybrid segmentation method for a 3D reconstruction for a LiCoO₂ composite electrodes consisting of three phases: active material, binder, and pores space. Ebner and Wood [293] used scanning electron microscopy (SEM) micrographs to develop a tortuosity estimation method based on differential effective medium approximation. They validated their methods using different particle shapes with known Bruggeman's estimation. Similarly, Cooper et al. [294] used an image-based modeling method to compare tortuosity factors estimated from Bruggeman's method with geometrical and numerical methods.

For the homogenization of an electrode's mechanical properties, Golmon et al. [295] followed Mori–Tanaka's theory [296], assuming the effective elasticity tensor \mathbf{C}_{eff} to read

$$\mathbf{C}_{\text{eff}} = \mathbf{C}_m + (1 - \varepsilon_e)(\mathbf{C}_s - \mathbf{C}_m)\mathbf{A}_s, \quad (17)$$

where

$$\mathbf{A}_s = \mathbf{A}_D[\varepsilon_e \mathbf{1} + (1 - \varepsilon_e)\mathbf{A}_D]^{-1}, \quad \mathbf{A}_D = [\mathbf{1} + \mathcal{S} \mathbf{C}_m^{-1}(\mathbf{C}_s - \mathbf{C}_m)]^{-1}.$$

Here, ε_e is the volume fraction of the electrolyte, \mathbf{C}_s and \mathbf{C}_m denote the stiffness tensors for the active particle and matrix with the electrolyte, respectively, $\mathbf{1}$ is the identity tensor and \mathcal{S} is the Eshelby tensor.

The effect of a macroscopic eigenstrain due to lithium insertion can also be obtained from the micro-scale eigenstrain as shown by Inoue et al. [297].

Apart from analytical expressions, effective coupled chemo-mechanical properties can also be obtained numerically. To that end, Awarke et al. [298] performed two-scale finite element (FE²) simulations of a composite LiFePO₄ cathode and evaluated its displacement field, potential field, and SOC distribution when subjected to external loads and diffusion-induced stress. Its effective elastic modulus and SOC-dependent volumetric expansion were calculated on an RVE, which has a microstructure with monodisperse spheres based on the known material densities, porosity, and particle sizes. The interstitial voids between spheres were assumed to be filled by polymeric binder phase, and periodic boundary conditions were applied for the RVE.

3.3. Concluding remarks

Models for composite electrodes are valuable for evaluating the particle-particle, particle-matrix and particle-electrolyte interactions. In that, they extend the narrow focus made by the particle-level models discussed in the previous section. This allows to identify the effects of (dis-)charge “hot-spots”, inhomogeneous mechanical constraints, chemically inactive binder, and of the heterogeneous chemical reactions taking place throughout the electrode structure and their combined impact on cycle life expectancy of the electrode structure. Current models are however restricted to stress analyses of the considered structures. Thereby, the diffusion is usually considered to be decoupled from mechanical stresses, which excludes a significant driving force from the chemical problem, as was discussed in Section 2. Moreover, due to computational cost, the models currently do not account for mechanical degradation such as fracture of particles or the delamination of the composite structure.

Homogenization techniques are essential for bridging the gap between the electrode scale and the cell scale. The effective quantities calculated from such techniques are the representative characteristics of the composite electrode microstructure and are used in cell models for the prediction of the overall electrochemical and mechanical behavior. However, mechanical effects have so far only found scarce attention, for instance in determining the effect of porosity change under intercalation or due to external stresses. The contributions from mechanical effects have so far not found consideration in the effective transport quantities.

4. Cell level

Cell models have been proposed and studied extensively in order to predict the overall cycling performance of the whole cell. They are, nevertheless, mostly restricted in the study of electrochemical performance while mechanical contributions are disregarded. Reviews of these models are provided by Thomas et al. [299], Santhanagopalan et al. [300], Landstorfer and Jacob [301], and Jøkar et al. [302]. However, as will be shown in this section, mechanical stresses in electrodes and separator influence the overall electrochemical performance of the battery cell even with liquid electrolyte. Mechanical effects play an even more significant role in batteries with solid electrolyte, which will be discussed in Section 5.

Modeling the complete functioning of a battery cell involves a set of partial differential equations across the porous electrodes, the electrolyte, and the separator. The computational costs to solve these equations in great detail, be it even for one charge and discharge cycle, are unaffordably high. Thus, simplified cell models with different multi-scale techniques are proposed. In this section, we will review these models, putting our focus on the cell models which consider mechanical contributions to the cell performance. Based on the employed homogenization techniques and the levels of detail that the models can resolve, we organize these models into three categories: pseudo-2D cell models, single-particle cell models, and 2D/3D cell models.

4.1. Pseudo 2D cell models

Pseudo-2D (P2D) models consider two length scales concurrently, namely the cell level and the particle level. These models are denoted as “pseudo-2D” models due to the fact that at both length scales a respective 1D problem is solved. At the cell level, the Li-ion transport and the consequent potential variation are assumed to occur only between the electrodes; at the particle level, a spherical particle with spherical symmetric properties is assumed, which reduces the intercalation process to a 1D problem in radial direction. Understandably, these models are also referred to as “one-plus-one models”. The first P2D model, which did not consider mechanical effects, was proposed by Doyle [303] for a Li|PEO₈-LiCF₃SO₃|TiS₂ half cell. Fuller et al. [304] extended this model to consider a full cell in a Li_xC₆|propylene carbonate-LiClO₄|LiMn₂O₄ system. The finite-volume-method-based package Dualfoil [303] was developed for the simulation of the half cell and full cell systems. Despite a wide variety of P2D models considering mechanical stresses, the governing equations at the cell level usually

exhibit the same structure, summarized in Eqs. (18) to (20) in Table 1. Note that, in the model presented in Table 1, mechanical stresses at the cell level are disregarded. They are only considered at the particle level, where the stress-assisted diffusion equation in a single spherical particle (e.g. Eq. (7)) is solved at the anode and the cathode. The pore-wall flux $j_{s,k}$ in Eq. (21) is then critical to bridge the two levels, which is based on Butler–Volmer kinetics, involving physical quantities at both cell level and particle level.

This P2D model has been used by Christensen [305] in combination with their earlier work on single particles [19] in order to study the electro-chemo-mechanical response at high currents. Further coupling with thermal effects in the cell level, applied to the description of a lithium-ion polymer battery pouch cell, was performed by Fu et al. [306]. They concluded that the pressure diffusion and the lattice distortion with large deformation have a significant impact on the electrochemical performance of the battery cell. Suthar et al. [307] proposed an optimization framework to estimate optimal charging profiles. Their results show that the local pore wall flux has a significant difference from the average current density, which highlights the importance to apply P2D model to capture the peak radial and tangential stresses. Later, they extended their model to investigate the effect of porosity, thickness, and tortuosity on the degradation of graphite anode [308]. This study shows that a smaller porosity together with a larger tortuosity can lead to a significant reduction in discharge capacity, where the stresses play an important role in capacity fade mechanisms. Dai et al. [309] extended the P2D model to consider an electrode with blended and mixed LiMn₂O₄ (LMO) and LiNi_{0.8}Co_{0.15}Al_{0.05}O₂ (NCA) particles. They found that stresses generated in the LMO particles are reduced by adding NCA to the cathode, which can improve the cell performance.

Renganathan et al. [310] studied phase transformations within LiCoO₂ particles with an extended P2D model, where a two phases system coupled with mechanics has been modeled at the particle level. Their results indicate that particles can be damaged due to the residual strain caused by phase transformation. In order to consider the influence of phase separation and particle morphology, Bai et al. [311] considered a cell with spheroidal particles that experience phase separation, as shown in Fig. 8. They concluded that stresses can play a major role in modifying the capacity, and that phase separation inside an active particle can lead to a long potential plateau during discharge.

In order to account for external loading at the cell level, Golmon et al. [295] extended the P2D model by adding a RVE for the mechanical bridging between the cell and particle level. The effective elastic tensor was calculated based on Mori-Tanaka's theory, as

Table 1

The governing equations for the P2D model at the cell level and for bridging between the particle and the cell levels. The models for the particle level can be found in detail in Section 2. In the equations, subscripts n, p, and s represent the negative electrode, positive electrode and separator regions, respectively. In each region, there are two phases: a solid particle phase (with subscript s) and a liquid electrolyte phase (with subscript e). At the cell level, one solves for the liquid concentration c_e and the electrostatic potentials ϕ_s and ϕ_e in all three regions. c_k is the lithium concentration inside the particle with the subscript representing the electrodes. Its surface concentration is denoted by a superscript surf and the maximum concentration by the suffix max. D_{eff} and k_{eff} are the effective diffusivity and conductivity in the electrolyte defined in Section 3, and σ_{eff} is the effective conductivity of solid phase. $j_{s,k}$ denotes a scalar flux between a particle and the surrounding electrolyte, governed by a Butler–Volmer equation depending on the overpotential η . Comparing the expression of Eq. (21) and Eq. (12) in Section 2.1, $K_k \sqrt{(c_k^{\text{max}} - c_k^{\text{surf}}) c_k^{\text{surf}}}$ equals to an exchange current i_0 . K represents the reaction rate for (de-)lithiation. Note that in the separator region, $j_s = 0$, thus leading to a vanishing source term in Eqs. (18) to (20).

Region	Governing equations
Cell level (k=n, p,s)	$\epsilon_k \frac{\partial c_k}{\partial t} = \nabla \cdot (D_{\text{eff},k} \nabla c_{e,k}) + a_k (1 - I_+) j_{s,k}$ (18)
	$\nabla \cdot (\sigma_{\text{eff},k} \nabla \phi_{s,k}) - a_k F j_{s,k} = 0$ (19)
	$\nabla \cdot (k_{\text{eff},k} \left[\nabla \phi_{e,k} - \frac{RT}{F} (1 - I_+^0) \nabla \ln c_{e,k} \right]) + a_k F j_{s,k} = 0$ (20)
Level bridging (k=n,p)	$j_{s,k} = K_k \sqrt{(c_k^{\text{max}} - c_k^{\text{surf}}) c_k^{\text{surf}}} c_{e,k} \left[\exp\left(\frac{F \eta_k}{2RT}\right) - \exp\left(-\frac{F \eta_k}{2RT}\right) \right]$ (21)
	$\eta_k = \phi_{s,k} - \phi_{e,k} - U_k(c_k^{\text{surf}})$ (22)

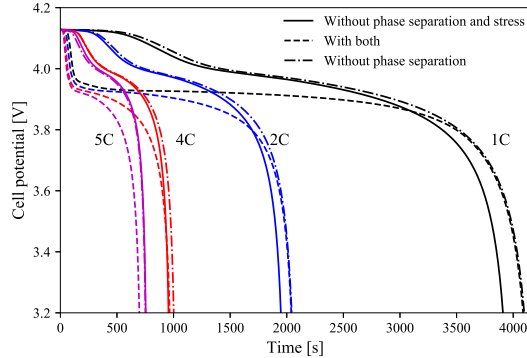


Fig. 8. Evolution of a Li|PEO-LiCF₃SO₃|LiMn₂O₄ cell potential during discharge with models considering different coupling cases in cathode particles at different discharge rate: one model considering both stress-assisted diffusion and phase separation, one considering only stresses and the last one disregarding both. For the modeling, Eqs. (18) to (22) and the mechanically coupled Cahn–Hilliard diffusion model described in Section 2.2.2 are employed. It is shown that stresses in general improve cell capacity, especially at low discharge rates. Phase separation promotes a stable discharge potential for a long time.

discussed in Eq. (17). They applied their work to the study of a Li-foil|LiMn₂O₄ half-cell and the results show good agreements with previous published work as well as the experimental observations. Based on Golmon's work, Xiao et al. [312] studied the stress distribution in polymeric separators in a LiC₆|LiPF₆|Li_{1-x}Mn₂O₄ battery. In their model, instead of an analytical expression, they build a numerical RVE (sub-model) to obtain the stress-strain relation, where different stacks of particles are investigated. They concluded that the local strain at the indented areas was much higher than the nominal strain of the separator, which is dependent upon the particle size and particle packing. Xie and Yuan [313] further incorporated SEI formation in the model and simulated the capacity fading process. Behrou and Maute [314] introduced a damage variable to the active particles to investigate the capacity fade of LIBs due to accumulated damage of the active particles. They have also discussed the influence of particle size polydispersity on the battery performance and they concluded that cathodes with uniform particle size will lead to more significant capacity fade than with non-uniform particles.

4.2. Single-particle cell models

Single-particle cell models (SP models) can be considered as a simplified version of P2D models, where the spatial variation over both electrodes at the cell level is neglected, such that all the active particles share the same distribution of current density on the surface during cycling. Thus, the pore-wall flux $j_{s,k}$ will be computed only once for each electrode, with either the expressions such as Eq. (21), or an analytic expression based on averaged pore-wall area. Please note that, in this review, a “single-particle” model refers to a cell model described in this section, whereas a “single particle” refers to the models discussed in Section 2.1.

Using the volume fraction ($\epsilon_{s,k}$) and the radius of active particles ($R_{s,k}$), the total surface area $A_{s,k}$ and the pore wall flux density $j_{s,k}$ of active particles per unit volume of composite electrode can be expressed as

$$A_{s,k} = \frac{3\epsilon_{s,k}}{R_{s,k}}, \quad j_{s,k} = \frac{J_{app}R_{s,k}}{3\epsilon_{s,k}}, \quad (23)$$

where J_{app} is the applied flux. With the simplified $j_{s,k}$, Eqs. (18) to (20) can be solved independently, thus improving the computational

efficiency. Moreover, since the simulations for single particles occur only once per electrode, all the complex physics identified in Section 2 can be considered for different electrode materials, such as plastification, phase separation, and fracture. This facilitates the investigation of the influence of particle behavior on cell performance.

Purkayastha and McMeeking [315] derived a simplified SP model with two assumptions: firstly, Li⁺ is the only mobile charge carrier in the electrolyte; secondly, the electrodes always operate close to equilibrium. The first assumption yields a linear relationship between the electric field and the current density inside the electrolyte. The second assumption leads to a linear relationship between the current density on the surface of active particles and the overpotential through linearized Butler–Volmer kinetics. The stresses inside the active particles in both electrodes are thereby described similar to the basic model described in Section 2.1, where the stress generation can be mapped in terms of battery performance and design parameters. Their results show that the gradient of stress plays a significant role in lithium diffusion. A low-order SP cell model considering stress-enhanced diffusion was derived by Li et al. [316]. In this model, the concentration of electrolyte is represented by an approximated analytical expression to improve computational efficiency. The mechanical coupled model shows that for medium to high C-rate charge/discharge processes stresses plays an important role. In particular, the stresses can increase diffusivity, resulting in a considerable change in surface concentration and hence in an increased cell performance. Based on this model, Li et al. [317] developed a degradation model which considers SEI formation and crack propagation due to the stresses generated by the volume expansion of the active particle. They concluded that the crack propagation accelerated the SEI layer formation, leading to a significant capacity fade.

4.3. 2D/3D cell models

The last class of battery cell models explicitly models two or three spatial dimensions at the cell level. The first work in this regard has been undertaken by García et al. [44] with an application in a Li_xC|Li_yMn₂O₄ battery cell, where the distributions of the electrochemical and mechanical fields were calculated for porous electrode microstructure. In this model, unlike the P2D and SP models, the porous electrolyte microstructure was explicitly modeled, circumventing the need to employ effective coefficient for Li transport. Their work provided a framework for modeling effects of electrode microstructures that cannot be treated in mean-field models. However, as pointed out already in Section 2.1, their model disregarded mechanical contribution to the overall electrochemical performance of battery cell.

A similar model was proposed by Purkayastha and McMeeking [318], who integrated a 2D two-way coupled spherical particle model into a 2D cell model. In their model, they analyzed the influence among active particles and their influence on the cell performance. They performed a parameter analysis, developing non-dimensional parameters based on particle morphology and material properties. Their results showed that particle distribution as well as electrode material properties play big role in predicting the stress generation within the particle and the cell performance. Nevertheless, these models are still considering spherical particles for electrode active materials. In order to gain the understanding of stress distribution of the real battery cell, Wu et al. [319] developed a microstructurally resolved model of a Li_xC₆|PP|Li_yMn₂O₄ cell. In their model, a conductive binder covering the active particle was also explicitly modeled and their results suggest that a softer binder can provide better interfacial adhesion between the binder and particles.

Ferrese and Newman [320] proposed an alternative model that uses porous-electrode theory with a smeared-out microstructure (model in Table 1) and a second spatial dimension at the cell level. Using this model, they studied the mechanical effect of a stiff separator to a lithium-metal anode and found that a stiff polymer separator can make

the lithium to deform both elastically and plastically which, as a consequence, can flatten the electrode surface considerably.

A fully coupled electro-chemo-mechanical model that considered the interactions at both the particle and the cell level was developed by Wu and Lu [321] in a multiscale setting. The model in Table 1 was thereby employed for the cell level, and Eq. (21) was modified such that $j_{i,k}$ included also stress effects. This model was employed to the study of the impact of small inactive regions within an electrode, demonstrating the importance of electrode homogeneity in order to avert electrode degradation. This degradation also a significant problem for large-format batteries where it was found that the loss of LiMn_2O_4 active material in a LMO|carbon cell is more serious at the electrode edge than in the bulk of the electrode. Dai et al. [322] found that this edge effect is due to the misalignment of the cathode and anode. At a larger scale, Rieger et al. [323] placed 21 P2D cells between two 2D current collector foils in order to explore the electro-chemo-mechanical behavior in a large-format pouch cell. Their results indicate that high stresses in the positive electrode arise over a wide range of discharge processes and are strongly correlated to the current density distribution.

Full 3D models consider the physical behavior variation in three spatial directions, allowing an in-depth investigation of the influence of spatial inhomogeneity on the electrochemical performance of battery cells. In 3D models, electrode microstructures play very important roles in electrochemical and mechanical performance of batteries. The earlier works mainly focused on the electrochemical behavior of the battery [324] and studies have been performed to compare the models with a fully resolved microstructure to P2D models [325]. Stress analyses in LCO and NMC cathodes reconstructed from FIB-SEM scans or from X-ray tomography have been performed by Wu et al. [275,276] and highlight the influence of complex microstructures in the resulting stress levels.

4.4. Concluding remarks

Cell models are very important since their outcomes can be directly compared with experimental measures, which offers optimization criteria for the electrodes and the electrolyte. Current research focuses mainly on the electrochemical behavior, with only a few studies employing mechanically coupled models. This choice is motivated by the fact that liquid electrolyte can well accommodate active electrode particle swelling and shrinkage. Despite accumulated evidence on the importance of mechanical effects on cell performance, even for liquid electrolytes, mechanical effects are still considered to be a secondary factor.

5. All-solid-state batteries

All-solid-state lithium batteries (SSBs) emerged as a promising alternative to currently used LIBs, which feature flammable organic liquid electrolytes [326,327]. Apart from safety gains, solid electrolytes (SE) also enable the use of lithium metal as anode, which significantly increases the volumetric and gravimetric energy density of a cell [327]. Solid electrolytes span wide classes of materials, ranging from organic polymers to inorganic ceramics. Although, in general, they show lower ionic conductivity ($\sim 10^{-4} \text{Scm}^{-1}$) than their liquid counterparts ($\sim 10^{-2} \text{Scm}^{-1}$), some polymers and inorganic ceramic solids, including garnet oxides and sulfides, exhibit an ionic conductivity comparable to liquid electrolytes [328,329]. The ionic conductivity inside the electrolyte is therefore not the bottleneck that prevents successful applications of SEs in LIBs. The challenge is rather to integrate SEs into high-performance batteries. Apart from electrochemical stability [330], mechanical compatibility with electrodes plays also a big role. In batteries with liquid electrolytes, as already shown in previous sections, mechanical stresses mainly arise in active particles during cyclic charge and discharge, and the overall cell performance is thus affected through mechanically modified pore-wall flux. Liquid electrolytes in general

show good compliance to the active particles' deformation and they do not degrade directly due to mechanical stresses. However, when solid electrolytes—ceramic electrolytes in particular—are employed, electrolytes alone can cause mechanical issues. Firstly, the rigid nature of SEs makes their contact area with electrode particles very limited, which results in a large resistance [331]. This contact area can be further reduced due to large swelling and shrinkage of particles, as shown in Fig. 2(f). Surface coating is thus crucial in order to maintain a good contact between electrolyte and electrodes [396]; a proper external pressure is also necessary for mechanical integrity. However, this external pressure should not be too large because ceramic electrolytes are brittle and vulnerable to fracture. Composite-structured electrolytes combining a ceramic scaffold with polymer infill are thus proposed to offer a good ionic conductivity and fracture resistivity at the same time [332]. Theoretical model for deriving optimized designs are nonetheless lacking in the literature.

From the modeling point of view, most mechanically coupled models summarized from previous sections can be directly adapted for SSBs. At the particle level, bulk governing equations depend only on the electrode active materials, thus remaining unchanged. The boundary conditions, especially mechanical constraints, should be modified since solid electrolytes provide stronger mechanical confinements. Homogenization methods at the composite electrode level also remain valid, with liquid electrolyte being replaced by SE with the same volume fraction. However, the modeling of SE is slightly different because mechanical stresses are critical in SEs, which are mostly absent in liquid electrolytes. In this section, we will first introduce models for SEs, and the emphasis will be mainly on the difference from the model for liquid electrolytes. We will then focus on varied proposed models that try to describe the mechanisms of lithium dendritic growth in the electrolyte.

5.1. Mechanistic and degradation modeling of solid electrolyte

Solid electrolytes can, in general, be divided into two groups: organic polymers and inorganic ceramics. Most solid polymeric electrolytes are using high-molecular-weight polymers, such as poly (ethylene oxide) (PEO) and/or poly (propylene oxide) (PPO), as solvents for different Li^+ salts [333]. Ionic conductivity mechanism in polymeric electrolytes involves both Li^+ diffusion and polymer segmental motion [334]. Li^+ transport in ceramic electrolytes, on the other hand, is associated with ionic hopping between the interstitials and vacancies in crystalline structure [335], and anions are usually considered as non-mobile. Bucci et al. [336] started from a model describing species diffusion in a lattice material with large deformation (as shown in active materials) and extended it in order to consider multiple species and electric field. A similar formulation was also employed by Grazioli et al. [337]. Goyal and Monroe [338], on the other hand, started from Newman's concentrated-solution theory for liquid electrolyte and modified the mechanical part of Gibb's free energy from

$$dG_{\text{mech}}^{\text{liquid}} = V dp \quad (24)$$

to

$$dG_{\text{mech}}^{\text{solid}} = V dp - \frac{1}{3} \text{dev} \epsilon: d(\text{dev} \sigma) \quad (25)$$

in order to consider both the volumetric and deviatoric part of stresses in the solid electrolyte. In Eq. (25), $\text{dev} \epsilon$ and $\text{dev} \sigma$ are the deviatoric part of strain and stress of the electrolyte, respectively. Note that the sign difference of Eq. (25) with Eq. (4) in the original paper [338] is due to the fact that in that paper σ is defined as compressive (negative) stress. It should also be pointed out that a more general expression of Gibb's free energy is expressed in terms of a thermodynamic tension τ and its conjugate \mathbf{v} , leading to

$$dG_{\text{mech}} = -\mathbf{v} \cdot d\tau = -\epsilon: d\sigma \quad (26)$$

in a small deformation regime. It is worth noting that, although it is

highly popular to employ the Poisson–Nernst–Planck (PNP) equation to govern ion transport in electrolyte (e.g. Refs. [339,340]), Dreyer et al. [341] pointed out the deficiencies PNP model and derived a thermodynamically consistent formulation for non-compressible liquid electrolyte. Earlier than that, Landstorfer et al. [342] also developed a modified PNP model for ion diffusion in solid electrolyte without considering mechanical stresses. The mechanically coupled model in solid electrolyte beyond PNP equation was then proposed by Braun et al. [343], where the deviatoric contribution of electrolyte is disregarded. This model can naturally account for the space-charge layer, without involving the Gouy–Chapman theory.

Due to the stiff nature of many electrolytes and lithium intercalation-induced large deformation of electrode particles, the composite structures of electrolytes and electrode particles are likely to crack within each phase and delaminate from each other [344,345]. The fracture of the particles has been already discussed in Section 2. As for the SE, it is natural to predict that an SE is less likely to fracture if its compliance is improved. However, Bucci et al. [346] found that compliant sulfide electrolytes are more prone to micro-cracking than brittle ceramic ones. They attributed this to the fact that more compliant SEs allow for larger deformation, and thus result in higher stress concentrations. Using a random walk analysis, they further calculated how the effective conductivity is affected by micro-cracking [347]. In their work, they predicted a linear relationship between the average diffusivity and the mechanical degradation. They also observed an increased heterogeneity with progressive damage, which, in turn, increases stress concentrations. Delamination between the active particles with SEs and current collectors is another big issue that contributes to the mechanical failure [348,349]. Guo et al. [350] studied the delamination between current collector and electrode due to wrinkling of electrode in a layer-structured battery. They found that single-blister buckling is more likely to occur in a battery with liquid electrolyte, and multi-blistering buckling has higher chances to take place in SSBs. At the cell level, Behrou and Maute [351] employed a P2D model, using a modification of the flux in Eq. (18) with a stress-drifting term, and analyzed the damage evolution of the battery due to degradation in the electrode active particles. The model demonstrated that particles with large aspect ratio will operate better in terms of damage-induced capacity fade inside solid state battery.

5.2. Modeling of lithium deposition

Lithium plating usually occurs when lithium metal is used as anode, and unstable lithium deposition—such as formation of lithium dendrites and filaments—can penetrate the separator, giving rise to a short circuit. However, the use of pure Li metal anodes should not be disregarded, as it allows for a significantly increased energy density over traditional LIBs with porous electrodes [327].

One major driving force for the application of SEs is the widely shared belief that the mechanical stresses arising within SEs can suppress dendrite growth. However, accumulated evidences show that lithium dendrites grow regardless of electrolyte materials [352–355]. Even SEs with high elastic moduli—predicted from theoretical modeling—cannot effectively suppress lithium dendrites [17]. A corresponding theory has yet to be proposed. Due to the aforementioned reasons, SSBs well deserve the investigation from mechanical aspects.

The mechanism of lithium dendritic growth is not completely clear. Some models established based on Na systems with β -alumina as the electrolyte can offer insights into instable metal deposition in ceramics [356,357]. The first model on lithium deposition in a polymer electrolyte was proposed by Monroe and Newman, who considered the contribution of bulk and surface stresses to the electrochemical reaction of lithium deposition [20,358,359]. They concluded that surface stress and bulk pressure contributed deposition stability, and that their contribution increased with an enhanced electrolyte shear modulus. Their theory was confirmed by Stone et al. for a battery system with very stiff

polymer electrolytes and good adhesion [360]. Tikekar et al. [361] modified Monroe and Newman's theory to consider a polymer with non-mobile anions. They concluded that, by using a polymer with immobilized anions, stable electrodeposition can be achieved even with moderate shear modulus.

In ceramic electrolytes, however, the Monroe–Newman-based models appear to be not applicable. Ceramic electrolytes in general have very large elastic moduli and in them, Li^+ is the only mobile ion. They are supposed to have better performance against lithium dendritic growth. Nonetheless, Cheng et al. [362] showed that lithium dendrites formation can occur even for an electrolyte whose shear modulus is far above the critical value estimated in the Monroe–Newman model. Further, Porz et al. [17] performed Li-deposition experiments on surfaces of amorphous, single-crystalline, and polycrystalline electrolytes. Based on these experiments, they proposed a model based on the concept that reduced lithium wedges and cracks open a pre-existing flaw despite of the low shear modulus and yield strength of lithium. The critical overpotential is thus expressed as a function of the fracture toughness of SE. Raj and Wolfenstine [363] proposed a model that considers lithium nucleation in the ceramic electrolyte at the grain boundary. The coupling of mechanical stresses and the electrical potential was shown by the electro-chemo-mechanical potential. The excess potential served as the nucleation barrier for dendrite formation. They concluded that the critical current above which lithium nucleates within the electrolyte depends on the ionic conductivity and fracture strength of the electrolyte. It was further proposed by Natsiavas et al. [21] that the electrolyte morphology plays a major role for lithium dendrite formation. To that end, they developed a 3D model to discuss the instability of lithium-electrolyte interface due to lithium bulk and surface transport, lithium deposition, and elastic stresses. They concluded that interfacial roughness played a crucial role in triggering the lithium dendrite growth, and that a pre-stretch will always substantially reduce the roughening of the lithium surface during cycling. Despite all these efforts, it is still debatable which model, if it exists at all, can fully cover the mechanism of lithium dendrite growth.

5.3. Concluding remarks

Mechanical stress is the one of the most important factors in designing solid-state batteries. There are a handful of models that incorporate electro-chemo-mechanical behavior of solid electrolytes. Their applications in describing functioning and failure of these SEs are still deficient. Simulations are needed in order to provide an optimal design of these SEs in terms of volume fraction, structural design, as well as mechanical constraint in order to provide a solid yet fracture-free contact between the electrode and electrolyte. Moreover, the understanding of lithium dendritic growth is still in its infancy. To the authors' knowledge, there is not yet a single theory that can explain the lithium dendritic growth in an SE satisfactorily. To achieve this, a joint work from electrochemical and mechanical aspects is essential.

6. Conclusions

The role of mechanical effects on the deterioration of lithium-ion batteries has in the last two decades experienced considerable attention by the scientific community and the industry alike. Lithium-ion batteries provide a rich field of mechanical phenomena at the microscale alone, comprising, to name only a few, large deformations coupled with nonlinear elasticity, plastification, fracture, anisotropic material behavior, structural instability, and phase separation phenomena. This has motivated a vast amount of experimental and theoretical studies that investigate and try to predict this behavior. The initial simple model assumptions have thereby been successively replaced by more realistic

model parameters. Nonetheless, there remain several open issues regarding the mechanically coupled modeling of Li-ion batteries, in addition to those mentioned for each scale at the end of corresponding sections.

Tremendous progress has been made on modeling the performance of lithium-ion batteries at the different scales involved, be it in the form of the strongly predictive battery cell models such as P2D or SPM, the composite-level modeling of diffusion and stresses, or the description of plasticity and failure of free-standing electrode particles. What is currently lacking is the integration of these disconnected modeling efforts into a true multiscale model, where microscale mechanical effects inform and affect the material and the battery cell performance at the higher scales.

A major factor limiting the veracity of the discussed models lies in the employed material parameters. To an increasing degree, factors such as crystal anisotropy are regarded in the computational studies. The computation of appropriate parameters and their transfer from the atomistic level to a continuum view is, in our view, still undertaken too seldom.

Overcoming these roadblocks to further efficiency increases for lithium-ion batteries requires, to a growing extent, the collaboration of researchers from both electrochemistry and the mechanical community. In order to aid this endeavour, a shared language and understanding is vital. With this review we try to present, to expert and newcomer alike, a comprehensive overview of the modeling efforts that have been made in the last years to describe and understand mechanical phenomena at three different scales of a lithium-ion battery. We envision that the insights on modeling and material/cell behavior gained in these reports are not restricted to lithium-ion batteries but are transferable to other battery chemistries such as Na-ion or Mg-ion batteries and other energy technologies featuring a strong coupling between ionic/electric transport and mechanics, for instance fuel cells or supercapacitors.

Acknowledgment

B.-X. Xu would particularly like to thank the Adolf Messer Foundation for awarding her the Adolf Messer Prize and for the financial support.

References

- [1] J.-M. Tarascon, M. Armand, Issues and challenges facing rechargeable lithium batteries, *Nature* 414 (2001) 359–367.
- [2] G.-A. Nazri, G. Pistoia (Eds.), *Lithium Batteries: Science and Technology*, Springer US, 2003.
- [3] D. Abraham, D.W. Dees, J. Knuth, E. Reynolds, R. Gerald, Y.-E. Hyung, I. Belharouak, M. Stoll, E. Sammann, S. MacLaren, R. Haasch, R. Twisten, M. Sardela, V. Battaglia, E. Cairns, J. Kerr, M. Kerlar, R. Kostecki, J. Lei, L. Norin, Diagnostic Examination of Generation 2 Lithium-ion Cells and Assessment of Performance Degradation Mechanisms, Technical Report ANL-05/21 Argonne National Lab, 2005.
- [4] A. Mukhopadhyay, B.W. Sheldon, Deformation and stress in electrode materials for Li-ion batteries, *Prog. Mater. Sci.* 63 (2014) 58–116.
- [5] M.E. Stourara, P.R. Guduru, V.B. Shenoy, Elastic behavior of crystalline Li-Sn phases with increasing Li concentration, *J. Power Sources* 208 (2012) 165–169.
- [6] Y. Qi, H. Guo, J. Hector, G. Louis, A. Timmons, Threefold increase in the Young's modulus of graphite negative electrode during lithium intercalation, *J. Electrochem. Soc.* 157 (2010) A558–A566.
- [7] C.K. Chan, H. Peng, G. Liu, K. McMillwrath, X.F. Zhang, R.A. Huggins, Y. Cui, High-performance lithium battery anodes using silicon nanowires, *Nat. Nanotechnol.* 3 (2008) 31–35.
- [8] M. Ebner, F. Marone, M. Stapanoni, V. Wood, Visualization and quantification of electrochemical and mechanical degradation in Li ion batteries, *Science* 342 (2013) 716–720.
- [9] L.Y. Beaulieu, K.W. Eberman, R.L. Turner, L.J. Krause, J.R. Dahn, Colossal reversible volume changes in lithium alloys, *Electrochem. Solid State Lett.* 4 (2001) A137–A140.
- [10] S.W. Lee, M.T. McDowell, L.A. Berla, W.D. Nix, Y. Cui, Fracture of crystalline silicon nanopillars during electrochemical lithium insertion, *Proc. Natl. Acad. Sci. U.S.A.* 109 (2012) 4080–4085.
- [11] J.Y. Huang, L. Zhong, C.M. Wang, J.P. Sullivan, W. Xu, L.Q. Zhang, S.X. Mao, N.S. Hudak, X.H. Liu, A. Subramanian, H. Fan, L. Qi, A. Kushima, J. Li, In situ observation of the electrochemical lithiation of a single SnO₂ nanowire electrode, *Science* 330 (2010) 1515.
- [12] L. Bagetto, D. Danilov, P.H.L. Notten, Honeycomb-structured silicon: remarkable morphological changes induced by electrochemical (de)lithiation, *Adv. Mater.* 23 (2011) 1563–1566.
- [13] M.K. Jangid, F.J. Sonia, R. Kali, B. Ananthoju, A. Mukhopadhyay, Insights into the effects of multi-layered graphene as buffer/interlayer for a-Si during lithiation/delithiation, *Carbon* 111 (2017) 602–616.
- [14] R. Koerver, I. Aygün, T. Leichtweiß, C. Dietrich, W. Zhang, J.O. Binder, P. Hartmann, W.G. Zeier, J. Janek, Capacity fade in solid-state batteries: interphase formation and chemomechanical processes in nickel-rich layered oxide cathodes and lithium thiophosphate solid electrolytes, *Chem. Mater.* 29 (2017) 5574–5582.
- [15] H. Wu, G. Chan, J.W. Choi, I. Ryu, Y. Yao, M.T. McDowell, S.W. Lee, A. Jackson, Y. Yang, L. Hu, Y. Cui, Stable cycling of double-walled silicon nanotube battery anodes through solid-electrolyte interphase control, *Nat. Nanotechnol.* 7 (2012) 310–315.
- [16] I. Laresgoiti, S. Käbitz, M. Ecker, D.U. Sauer, Modeling mechanical degradation in lithium ion batteries during cycling: solid electrolyte interphase fracture, *J. Power Sources* 300 (2015) 112–122.
- [17] L. Porz, T. Swamy, B.W. Sheldon, D. Rettenwander, T. Frömling, H.L. Thaman, S. Berendts, R. Uecker, W.C. Carter, Y.-M. Chiang, Mechanism of lithium metal penetration through inorganic solid electrolytes, *Adv. Energy Mater.* 7 (2017) 1701003.
- [18] G. Kermani, E. Sahraei, Review: characterization and modeling of the mechanical properties of lithium-ion batteries, *Energies* 10 (2017) 1730.
- [19] J. Christensen, J. Newman, Stress generation and fracture in lithium insertion materials, *J. Solid State Electrochem.* 10 (2006) 293–319.
- [20] C. Monroe, J. Newman, The effect of interfacial deformation on electrodeposition kinetics, *J. Electrochem. Soc.* 151 (2004) A880–A886.
- [21] P.P. Natsiavas, K. Weinberg, D. Rosato, M. Ortiz, Effect of prestress on the stability of electrode-electrolyte interfaces during charging in lithium batteries, *J. Mech. Phys. Solid.* 95 (2016) 92–111.
- [22] X. Cheng, M. Pecht, In situ stress measurement techniques on Li-ion battery electrodes: a review, *Energies* 10 (2017) 951.
- [23] A.A. Franco, Multiscale modelling and numerical simulation of rechargeable lithium ion batteries: concepts, methods and challenges, *RSC Adv.* 3 (2013) 13027–13058.
- [24] D. Grazioli, M. Magri, A. Salvadori, Computational modeling of Li-ion batteries, *Comput. Mech.* 58 (2016) 889–909.
- [25] Y.F. Gao, M. Cho, M. Zhou, Mechanical reliability of alloy-based electrode materials for rechargeable Li-ion batteries, *J. Mech. Sci. Technol.* 27 (2013) 1205–1224.
- [26] R. Xu, K. Zhao, Electrochemomechanics of electrodes in Li-ion batteries: a review, *J. Electrochem. En. Conv. Stor.* 13 (2016) 030803.
- [27] J. Swallow, W. Woodford, Y. Chen, Q. Lu, J. Kim, D. Chen, Y.-M. Chiang, W. Carter, B. Yildiz, H. Tuller, et al., Chemomechanics of ionically conductive ceramics for electrical energy conversion and storage, *J. Electroceram.* 32 (2014) 3–27.
- [28] M.T. McDowell, S. Xia, T. Zhu, The mechanics of large-volume-change transformations in high-capacity battery materials, *Extreme Mech. Lett.* 9 (2016) 480–494.
- [29] S. Zhang, Chemomechanical modeling of lithiation-induced failure in high-volume-change electrode materials for lithium ion batteries, *npj Comput. Mater.* 3 (2017) 7.
- [30] S. Zhang, K. Zhao, T. Zhu, J. Li, Electrochemomechanical degradation of high-capacity battery electrode materials, *Prog. Mater. Sci.* 89 (2017) 479–521.
- [31] J. Newman, K. Thomas-Alyea, *Electrochemical Systems*, Electrochemical Society Series, John Wiley & Sons, 2004.
- [32] S. Prussin, Generation and distribution of dislocations by solute diffusion, *J. Appl. Phys.* 32 (1961) 1876–1881.
- [33] J.C.-M. Li, Physical chemistry of some microstructural phenomena, *Metall. Trans. A* 9 (1978) 1353–1380.
- [34] F. Larché, J.W. Cahn, A linear theory of thermochemical equilibrium of solids under stress, *Acta Metall.* 21 (1973) 1051–1063.
- [35] F. Larché, J.W. Cahn, A nonlinear theory of thermochemical equilibrium of solids under stress, *Acta Metall.* 26 (1978) 53–60.
- [36] F.C. Larché, The interactions of composition and stress in crystalline solids, *J. Res. Natl. Bur. Stand.* 89 (1984) 467–500.
- [37] I.V. Belova, G.E. Murch, Thermal and diffusion-induced stresses in crystalline solids, *J. Appl. Phys.* 77 (1995) 127–134.
- [38] E.C. Aifantis, On the problem of diffusion in solids, *Acta Mech.* 37 (1980) 265–396.
- [39] I.R.K. Wilson, E.C. Aifantis, On the theory of stress-assisted diffusion, i, *Acta Mech.* 45 (1982) 273–296.
- [40] D.J. Unger, E.C. Aifantis, On the theory of stress-assisted diffusion, ii, *Acta Mech.* 47 (1983) 117–151.
- [41] P.A. Taylor, E.C. Aifantis, On the theory of diffusion in linear viscoelastic media, *Acta Mech.* 44 (1982) 259–298.
- [42] G.B. Stephenson, Deformation during interdiffusion, *Acta Metall.* 36 (1988) 2663–2683.
- [43] S.P. Girrens, F.W. Smith, Constituent diffusion in a deformable thermoelastic solid, *J. Appl. Mech.* 54 (1987) 441–446.
- [44] R.E. García, Y.-M. Chiang, W.C. Carter, P. Limthongkul, C.M. Bishop, Microstructural modeling and design of rechargeable lithium-ion batteries, *J. Electrochem. Soc.* 152 (2005) A255–A263.
- [45] S.-B. Son, S.C. Kim, C.S. Kang, T.A. Yersak, Y.-C. Kim, C.-G. Lee, S.-H. Moon,

- J.S. Cho, J.-T. Moon, K.H. Oh, S.-H. Lee, A highly reversible nano-Si anode enabled by mechanical confinement in an electrochemically activated $\text{Li}_4\text{Ti}_5\text{Ni}_4\text{Si}_7$ matrix, *Adv. Energy Mater.* 2 (2012) 1226–1231.
- [46] F. Hao, D. Fang, Diffusion-induced stresses of spherical core-shell electrodes in lithium-ion batteries: the effects of the shell and surface/interface stress, *J. Electrochem. Soc.* 160 (2013) A595–A600.
- [47] F. Hao, D. Fang, Tailoring diffusion-induced stresses of core-shell nanotube electrodes in lithium-ion batteries, *J. Appl. Phys.* 113 (2013) 013507.
- [48] D. Molina Piper, T.A. Yersak, S.-H. Lee, Effect of compressive stress on electrochemical performance of silicon anodes, *J. Electrochem. Soc.* 160 (2013) A77–A81.
- [49] B.W. Sheldon, S.K. Soni, X. Xiao, Y. Qi, Stress contributions to solution thermodynamics in Li-Si alloys, *Electrochem. Solid State Lett.* 15 (2012) A9–A11.
- [50] M.T. McDowell, S.W. Lee, I. Ryu, H. Wu, W.D. Nix, J.W. Choi, Y. Cui, Novel size and surface oxide effects in silicon nanowires as lithium battery anodes, *Nano Lett.* 11 (2011) 4018–4025.
- [51] T. Ichitsubo, K. Tokuda, S. Yagi, M. Kawamori, T. Kawaguchi, T. Doi, M. Oishi, E. Matsubara, Elastically constrained phase-separation dynamics competing with the charge process in the $\text{LiFePO}_4/\text{FePO}_4$ system, *J. Mater. Chem.* 1 (2013) 2567–2577.
- [52] F. Ning, S. Li, B. Xu, C. Ouyang, Strain tuned Li diffusion in LiCoO_2 material for Li ion batteries: a first principles study, *Solid State Ionics* 263 (2014) 46–48.
- [53] A. Moradabadi, P. Kaghazchi, J. Rohrer, K. Albe, Influence of elastic strain on the thermodynamics and kinetics of lithium vacancy in bulk- LiCoO_2 , *Phys. Rev. Materials* 2 (2018) 015402.
- [54] N. Muralidharan, C.N. Brock, A.P. Cohn, D. Schauben, R.E. Carter, L. Oakes, D.G. Walker, C.L. Pint, Tunable mechanochemistry of lithium battery electrodes, *ACS Nano* 11 (2017) 6243–6251.
- [55] S. Natarajan, Hirshikesh, N. Swaminathan, R.K. Annabattula, Effects of stress-diffusion interactions in an isotropic elastic medium in the presence of geometric discontinuities, *J. Coupled Syst. Multiscale Dyn.* 4 (2016) 230–240.
- [56] X. Zhang, W. Shyy, A.M. Sastry, Numerical simulation of intercalation-induced stress in Li-ion battery electrode particles, *J. Electrochem. Soc.* 154 (2007) A910–A916.
- [57] H.-Y. Amanieu, H.N.M. Thai, S.Y. Luchkin, D. Rosato, D.C. Lupascu, M.-A. Keip, J. Schröder, A.L. Kholkin, Electrochemical strain microscopy time spectroscopy: model and experiment on LiMn_2O_4 , *J. Appl. Phys.* 118 (2015) 055101.
- [58] M.W. Verbrugge, B.J. Koch, Modeling lithium intercalation of single-fiber carbon microelectrodes, *J. Electrochem. Soc.* 143 (1996) 600–608.
- [59] G.G. Botte, R.E. White, Modeling lithium intercalation in a porous carbon electrode, *J. Electrochem. Soc.* 148 (2001) A54–A66.
- [60] M. Papakyriakou, X. Wang, S. Xia, Characterization of stress-diffusion coupling in lithiated germanium by nanoindentation, *Exp. Mech.* 58 (2018) 613–625.
- [61] Y. Li, K. Zhang, B. Zheng, F. Yang, Effect of local velocity on diffusion-induced stress in large-deformation electrodes of lithium-ion batteries, *J. Power Sources* 319 (2016) 168–177.
- [62] I. Ryu, J.W. Choi, Y. Cui, W.D. Nix, Size-dependent fracture of Si nanowire battery anodes, *J. Mech. Phys. Solid.* 59 (2011) 1717–1730.
- [63] P. Stein, B. Xu, 3d Isogeometric Analysis of intercalation-induced stresses in Li-ion battery electrode particles, *Comput. Methods Appl. Mech. Engrg.* 268 (2014) 225–244.
- [64] C. Miehe, S. Mauthe, H. Ulmer, Formulation and numerical exploitation of mixed variational principles for coupled problems of Cahn-Hilliard-type and standard diffusion in elastic solids, *Int. J. Numer. Methods Eng.* 99 (2014) 737–762.
- [65] C.V. Di Leo, E. Rejovitzky, L. Anand, Diffusion–deformation theory for amorphous silicon anodes: the role of plastic deformation on electrochemical performance, *Int. J. Solid Struct.* 67–68 (2015) 283–296.
- [66] A. Krischok, C. Linder, On the enhancement of low-order mixed finite element methods for the large deformation analysis of diffusion in solids, *Int. J. Numer. Methods Eng.* 106 (2016) 278–297.
- [67] A. Bard, L. Faulkner, *Electrochemical Methods: Fundamentals and Applications*, Wiley, 2000.
- [68] Y.T. Cheng, M.W. Verbrugge, Evolution of stress within a spherical insertion electrode particle under potentiostatic and galvanostatic operation, *J. Power Sources* 190 (2009) 453–460.
- [69] B.C. Han, A. Van der Ven, D. Morgan, G. Ceder, Electrochemical modeling of intercalation processes with phase field models, *Electrochim. Acta* 49 (2004) 4691–4699.
- [70] D. Zhang, B.N. Popov, R.E. White, Modeling lithium intercalation of a single spinel particle under potentiodynamic control, *J. Electrochem. Soc.* 147 (2000) 831.
- [71] S. Golmon, K. Maute, S.H. Lee, M.L. Dunn, Stress generation in silicon particles during lithium insertion, *Appl. Phys. Lett.* 97 (2010) 2008–2011.
- [72] E. Bohn, T. Eckl, M. Kamlah, R. McMeeking, A model for lithium diffusion and stress generation in an intercalation storage particle with phase change, *J. Electrochem. Soc.* 160 (2013) A1638–A1652.
- [73] H. Dal, C. Miehe, Computational electro-chemo-mechanics of lithium-ion battery electrodes at finite strains, *Comput. Mech.* 55 (2014) 303–325.
- [74] V. Sethuraman, M. Chon, M. Shimshak, N. Van Winkle, P. Guduru, In situ measurement of biaxial modulus of Si anode for Li-ion batteries, *Electrochem. Commun.* 12 (2010) 1614–1617.
- [75] V.A. Sethuraman, V. Srinivasan, A.F. Bower, P.R. Guduru, In situ measurements of stress-potential coupling in lithiated silicon, *J. Electrochem. Soc.* 157 (2010) A1253–A1261.
- [76] V.A. Sethuraman, M.J. Chon, M. Shimshak, V. Srinivasan, P.R. Guduru, In situ measurements of stress evolution in silicon thin films during electrochemical lithiation and delithiation, *J. Power Sources* 195 (2010) 5062–5066.
- [77] V.A. Sethuraman, A. Nguyen, M.J. Chon, S.P.V. Nadimpalli, H. Wang, D.P. Abraham, A.F. Bower, V.B. Shenoy, P.R. Guduru, Stress evolution in composite silicon electrodes during lithiation/delithiation, *J. Electrochem. Soc.* 160 (2013) A739–A746.
- [78] K. Zhao, W.L. Wang, J. Gregoire, M. Pharr, Z. Suo, J.J. Vlassak, E. Kaxiras, Lithium-assisted plastic deformation of silicon electrodes in lithium-ion batteries: a first-principles theoretical study, *Nano Lett.* 11 (2011) 2962–2967.
- [79] A. Bower, P. Guduru, V. Sethuraman, A finite strain model of stress, diffusion, plastic flow, and electrochemical reactions in a lithium-ion half-cell, *J. Mech. Phys. Solid.* 59 (2011) 804–828.
- [80] A.F. Bower, E. Chason, P.R. Guduru, B.W. Sheldon, A continuum model of deformation, transport and irreversible changes in atomic structure in amorphous lithium–silicon electrodes, *Acta Mater.* 98 (2015) 229–241.
- [81] F.C. Larche, J.W. Cahn, Thermochemical equilibrium of multiphase solids under stress, *Acta Metall.* 26 (1978) 1579–1589.
- [82] Y. Gao, M. Cho, M. Zhou, Stress relaxation through interdiffusion in amorphous lithium alloy electrodes, *J. Mech. Phys. Solid.* 61 (2013) 579–596.
- [83] D.R. Baker, M.W. Verbrugge, A.F. Bower, Thermodynamics, stress, and stefan-maxwell diffusion in solids: application to small-strain materials used in commercial lithium-ion batteries, *J. Solid State Electrochem.* 20 (2016) 163–181.
- [84] A. Salvadori, R. McMeeking, D. Grazioli, M. Magri, A coupled model of transport-reaction-mechanics with trapping. part I – small strain analysis, *J. Mech. Phys. Solid.* 114 (2018) 1–30.
- [85] G. Singh, T.K. Bhandakkar, Analytical investigation of binder's role on the diffusion induced stresses in lithium ion battery through a representative system of spherical isolated electrode particle enclosed by binder, *J. Electrochem. Soc.* 164 (2017) A608–A621.
- [86] L. Anand, A Cahn–Hilliard-type theory for species diffusion coupled with large elastic–plastic deformations, *J. Mech. Phys. Solid.* 60 (2012) 1983–2002.
- [87] K. Zhao, M. Pharr, S. Cai, J.J. Vlassak, Z. Suo, Large plastic deformation in high-capacity lithium-ion batteries caused by charge and discharge, *J. Am. Ceram. Soc.* 94 (2011) s226–s235.
- [88] Z. Cui, F. Gao, J. Qu, A finite deformation stress-dependent chemical potential and its applications to lithium ion batteries, *J. Mech. Phys. Solid.* 60 (2012) 1280–1295.
- [89] G. Bucci, S.P.V. Nadimpalli, V.A. Sethuraman, A.F. Bower, P.R. Guduru, Measurement and modeling of the mechanical and electrochemical response of amorphous Si thin film electrodes during cyclic lithiation, *J. Mech. Phys. Solid.* 62 (2014) 276–294.
- [90] Z. Jia, W.K. Liu, Rate-dependent stress evolution in nanostructured Si anodes upon lithiation, *Appl. Phys. Lett.* 109 (2016) 163903.
- [91] K. Zhao, G.A. Tritsaris, M. Pharr, W.L. Wang, O. Okeke, Z. Suo, J.J. Vlassak, E. Kaxiras, Reactive flow in silicon electrodes assisted by the insertion of lithium, *Nano Lett.* 12 (2012) 4397–4403.
- [92] L. Brassart, Z. Suo, Reactive flow in large-deformation electrodes of lithium-ion batteries, *Int. J. Appl. Mech.* 04 (2012) 1250023.
- [93] L. Brassart, K. Zhao, Z. Suo, Cyclic plasticity and shakedown in high-capacity electrodes of lithium-ion batteries, *Int. J. Solid Struct.* 50 (2013) 1120–1129.
- [94] M. Pharr, Z. Suo, J.J. Vlassak, Variation of stress with charging rate due to strain-rate sensitivity of silicon electrodes of Li-ion batteries, *J. Power Sources* 270 (2014) 569–575.
- [95] S.M. Khosrownejad, W.A. Curtin, Model for charge/discharge-rate-dependent plastic flow in amorphous battery materials, *J. Mech. Phys. Solid.* 94 (2016) 167–180.
- [96] H. Gabisrich, R. Yazami, B. Fultz, A transmission electron microscopy study of cycled LiCoO_2 , *J. Power Sources* 119–121 (2003) 674–679.
- [97] H. Wang, Y.-I. Jang, B. Huang, D.R. Sadoway, Y.-M. Chiang, Electron microscopic characterization of electrochemically cycled LiCoO_2 and $\text{Li}(\text{Al},\text{Co})\text{O}_2$ battery cathodes, *J. Power Sources* 81–82 (1999) 594–598.
- [98] A. Ulvestad, A. Singer, J. Clark, H. Cho, J. Kim, J. Maser, Y. Meng, O. Shpyrko, Topological defect dynamics in operando battery nanoparticles, *Science* 348 (2015) 1344–1347.
- [99] M. Legros, G. Dehm, E. Arzt, T.J. Balk, Observation of giant diffusivity along dislocation cores, *Science* 319 (2008) 1646–1649.
- [100] L. Zhong, X.H. Liu, G.F. Wang, S.X. Mao, J.Y. Huang, Multiple-stripe lithiation mechanism of individual SnO_2 nanowires in a flooding geometry, *Phys. Rev. Lett.* 106 (2011) 248302.
- [101] M. Mao, A. Nie, J. Liu, H. Wang, S.X. Mao, Q. Wang, K. Li, X. Zhang, Atomic resolution observation of conversion-type anode RuO_2 during the first electrochemical lithiation, *Nanotechnology* 26 (2015) 125404.
- [102] A. Nie, L.-Y. Gan, Y. Cheng, H. Asayesh-Ardakani, Q. Li, C. Dong, R. Tao, F. Mashayek, H.-T. Wang, U. Schwingenschlög, R.F. Klie, R.S. Yassar, Atomic-scale observation of lithiation reaction front in nanoscale snO_2 materials, *ACS Nano* 7 (2013) 6203–6211.
- [103] P. Wei, J. Zhou, X. Pang, H. Liu, K. Deng, G. Wang, Y. Wu, B. Chen, Effects of dislocation mechanics on diffusion-induced stresses within a spherical insertion particle electrode, *J. Mater. Chem.* 2 (2013) 1128–1136.
- [104] Y. Estrin, Dislocation theory based constitutive modelling: foundations and applications, *J. Mater. Process. Technol.* 80–81 (1998) 33–39.
- [105] F. Yang, Comments on Effects of dislocation mechanics on diffusion-induced stresses within a spherical insertion particle electrode, *J. Mater. Chem.* 2 (2014) 17183–17184.
- [106] F. Yang, A simple model for diffusion-induced dislocations during the lithiation of crystalline materials, *Theor. Appl. Mech. Lett.* 4 (2014) 051001.
- [107] B. Chen, J. Zhou, J. Zhu, Z. Liu, Diffusion induced stress and the distribution of dislocations in a nanostructured thin film electrode during lithiation, *RSC Adv.* 4

- (2014) 64216–64224.
- [108] J. Zhu, J. Zhou, B. Chen, Z. Liu, T. Liu, Dislocation effect on diffusion-induced stress for lithiation in hollow spherical electrode, *J. Solid State Electrochem.* 20 (2016) 37–46.
- [109] J. Li, Q. Fang, F. Liu, Y. Liu, Analytical modeling of dislocation effect on diffusion induced stress in a cylindrical lithium ion battery electrode, *J. Power Sources* 272 (2014) 121–127.
- [110] B. Chen, J. Zhou, J. Zhu, T. Liu, Z. Liu, Effect of misfit dislocation on Li diffusion and stress in a phase transforming spherical electrode, *J. Electrochem. Soc.* 162 (2015) H493–H500.
- [111] B. Chen, J. Zhou, R. Cai, Analytical model for crack propagation in spherical nano electrodes of lithium-ion batteries, *Electrochim. Acta* 210 (2016) 7–14.
- [112] Z. Liu, J. Zhou, B. Chen, J. Zhu, Interaction between dislocation mechanics on diffusion induced stress and electrochemical reaction in a spherical lithium ion battery electrode, *RSC Adv.* 5 (2015) 74835–74843.
- [113] Y.-T. Cheng, M.W. Verbrugge, The influence of surface mechanics on diffusion induced stresses within spherical nanoparticles, *J. Appl. Phys.* 10 (2008) 083521.
- [114] R. Deshpande, Y.-T. Cheng, M.W. Verbrugge, Modeling diffusion-induced stress in nanowire electrode structures, *J. Power Sources* 195 (2010) 5081–5088.
- [115] J. Li, D. Lu, Q. Fang, Y. Liu, P. Wen, Cooperative surface effect and dislocation effect in lithium ion battery electrode, *Solid State Ionics* 274 (2015) 46–54.
- [116] X. Li, Q. Fang, J. Li, H. Wu, Y. Liu, P. Wen, Diffusion-induced stress and strain energy affected by dislocation mechanisms in a cylindrical nanoanode, *Solid State Ionics* 281 (2015) 21–28.
- [117] Z. Ma, H. Wu, Y. Wang, Y. Pan, C. Lu, An electrochemical-irradiated plasticity model for metallic electrodes in lithium-ion batteries, *Int. J. Plast.* 88 (2017) 188–203.
- [118] Y. Wang, Z. Ma, W. Lei, Y. Zou, C. Lu, Double effect of electrochemical reaction and substrate on hardness in electrodes of lithium-ion batteries, *Acta Mech.* 227 (2016) 2505–2510.
- [119] Z. Ma, Z. Xie, C. Wang, YanAND. Lu, Softening by electrochemical reaction-induced dislocations in lithium-ion batteries, *Scripta Mater.* 127 (2017) 33–36.
- [120] H.-Y.S. Huang, Y.-X. Wang, Dislocation based stress developments in lithium-ion batteries, *J. Electrochem. Soc.* 159 (2012) A815–A821.
- [121] X. Li, Q. Fang, H. Wu, J. Li, Y. Liu, P. Wen, Misfit dislocations induced by lithium-ion diffusion in a thin film anode, *J. Solid State Electrochem.* 21 (2017) 419–427.
- [122] C.J. Wen, R.A. Huggins, Chemical diffusion in intermediate phases in the lithium-silicon system, *J. Solid State Chem.* 37 (1981) 271–278.
- [123] M.J. Chon, V.A. Sethuraman, A. McCormick, V. Srinivasan, P.R. Guduru, Real-time measurement of stress and damage evolution during initial lithiation of crystalline silicon, *Phys. Rev. Lett.* 107 (2011) 045503.
- [124] X.H. Liu, J.Y. Huang, In situ TEM electrochemistry of anode materials in lithium ion batteries, *Energy Environ. Sci.* 4 (2011) 3844–3860.
- [125] X.H. Liu, J.W. Wang, S. Huang, F. Fan, X. Huang, Y. Liu, S. Krylyuk, J. Yoo, S.A. Dayeh, A.V. Davydov, S.X. Mao, S.T. Picraux, S. Zhang, J. Li, T. Zhu, J.Y. Huang, In situ atomic-scale imaging of electrochemical lithiation in silicon, *Nat. Nanotechnol.* 7 (2012) 749–756.
- [126] J. Rohrer, K. Albe, Insights into degradation of Si anodes from first-principle calculations, *J. Phys. Chem. C* 117 (2013) 18796–18803.
- [127] X.H. Liu, F. Fan, H. Yang, S. Zhang, J.Y. Huang, T. Zhu, Self-limiting lithiation in silicon nanowires, *ACS Nano* 7 (2013) 1495–1503.
- [128] J.W. Wang, Y. He, F. Fan, X.H. Liu, S. Xia, Y. Liu, C.T. Harris, H. Li, J.Y. Huang, S.X. Mao, T. Zhu, Two-phase electrochemical lithiation in amorphous silicon, *Nano Lett.* 13 (2013) 709–715.
- [129] M.T. McDowell, S.W. Lee, J.T. Harris, B.A. Korgel, C. Wang, W.D. Nix, Y. Cui, In situ TEM of two-phase lithiation of amorphous silicon nanospheres, *Nano Lett.* 13 (2013) 758–764.
- [130] C. Delmas, M. Maccario, L. Croguennec, F. Le Cras, F. Weill, Lithium deintercalation in LiFePO₄ nanoparticles via a domino-cascade model, *Nat. Mater.* 7 (2008) 665–671.
- [131] A. Van der Ven, J. Bhattacharya, A.A. Belak, Understanding Li diffusion in Li-intercalation compounds, *Acc. Chem. Res.* 46 (2013) 1216–1225.
- [132] S. Huang, F. Fan, J. Li, S. Zhang, T. Zhu, Stress generation during lithiation of high-capacity electrode particles in lithium ion batteries, *Acta Mater.* 61 (2013) 4354–4364.
- [133] H. Yang, W. Liang, X. Guo, C.-M. Wang, S. Zhang, Strong kinetics-stress coupling in lithiation of Si and Ge anodes, *Extreme Mech. Lett.* 2 (2015) 1–6.
- [134] Y. Hu, X. Zhao, Z. Suo, Averting cracks caused by insertion reaction in lithium-ion batteries, *J. Mater. Res.* 25 (2010) 1007–1010.
- [135] Y. Liu, P. Lv, J. Ma, R. Bai, H.L. Duan, Stress fields in hollow core-shell spherical electrodes of lithium ion batteries, *Proc. R. Soc. A* 470 (2014) 20140299.
- [136] X.H. Liu, L. Zhong, S. Huang, S.X. Mao, T. Zhu, J.Y. Huang, Size-dependent fracture of silicon nanoparticles during lithiation, *ACS Nano* 6 (2012) 1522–1531.
- [137] R. Deshpande, Y.-T. Cheng, M.W. Verbrugge, A. Timmons, Diffusion induced stresses and strain energy in a phase-transforming spherical electrode particle, *J. Electrochem. Soc.* 158 (2011) A718–A724.
- [138] M.T. McDowell, I. Ryu, S.W. Lee, C. Wang, W.D. Nix, Y. Cui, Studying the kinetics of crystalline silicon nanoparticle lithiation with in situ transmission electron microscopy, *Adv. Mater.* 24 (2012) 6034–6041.
- [139] A. Vemulapally, R. Kali, A. Bhandakkar, Tanmay K. ANDMukhopadhyay, Transformation plasticity provides insights into concurrent phase transformation and stress relaxation observed during electrochemical Li alloying of Sn thin film, *J. Phys. Chem. C* 122 (2018) 16561–16573.
- [140] A.F. Bower, P.R. Guduru, E. Chason, Analytical solutions for composition and stress in spherical elastic-plastic lithium-ion electrode particles containing a propagating phase boundary, *Int. J. Solid Struct.* 69–70 (2015) 328–342.
- [141] X. Zhang, S.W. Lee, H.-W. Lee, Y. Cui, C. Linder, A reaction-controlled diffusion model for the lithiation of silicon in lithium-ion batteries, *Extreme Mech. Lett.* 4 (2015) 61–75.
- [142] Z. Jia, T. Li, Intrinsic stress mitigation via elastic softening during two-step electrochemical lithiation of amorphous silicon, *J. Mech. Phys. Solid.* 91 (2016) 278–290.
- [143] R. Xu, K. Zhao, Mechanical interactions regulated kinetics and morphology of composite electrodes in Li-ion batteries, *Extreme Mech. Lett.* 8 (2016) 13–21.
- [144] Y. Zhao, P. Stein, B.-X. Xu, Isogeometric analysis of mechanically coupled Cahn–Hilliard phase segregation in hyperelastic electrodes of Li-ion batteries, *Comput. Methods Appl. Mech. Eng.* 297 (2015) 325–347.
- [145] M. Huttin, M. Kamlah, Phase-field modeling of stress generation in electrode particles of lithium ion batteries, *Appl. Phys. Lett.* 101 (2012) 133902.
- [146] E.A. Guggenheim, *Mixtures: the Theory of the Equilibrium Properties of Some Simple Classes of Mixtures Solutions and Alloys*, Clarendon Press, 1952.
- [147] C.V. Di Leo, E. Rejovitzky, L. Anand, A Cahn–Hilliard-type phase-field theory for species diffusion coupled with large elastic deformations: application to phase-separating Li-ion electrode materials, *J. Mech. Phys. Solid.* 70 (2014) 1–29.
- [148] L. Chen, F. Fan, L. Hong, J. Chen, Y.Z. Ji, S.L. Zhang, T. Zhu, L.Q. Chen, A phase-field model coupled with large elasto-plastic deformation: application to lithiated silicon electrodes, *J. Electrochem. Soc.* 161 (2014) F3164–F3172.
- [149] Y. Zhao, B.-X. Xu, P. Stein, D. Gross, Phase-field study of electrochemical reactions at exterior and interior interfaces in Li-ion battery electrode particles, *Comput. Methods Appl. Mech. Eng.* 312 (2016) 428–446.
- [150] D.A. Cogswell, M.Z. Bazant, Coherency strain and the kinetics of phase separation in LiFePO₄ nanoparticles, *ACS Nano* 6 (2012) 2215–2225.
- [151] N. Nadkarni, E. Rejovitzky, D. Fraggedakis, C.V. Di Leo, R.B. Smith, P. Bai, M.Z. Bazant, Interplay of phase boundary anisotropy and electro-autocatalytic surface reactions on the lithium intercalation dynamics in Li₂FePO₄ platelet-like nanoparticles, *Phys. Rev. Materials* 2 (2018) 085406.
- [152] M. Tang, J.F. Belak, M.R. Dorr, Anisotropic phase boundary morphology in nanoscale olivine electrode particles, *J. Phys. Chem. C* 115 (2011) 4922–4926.
- [153] M. Tang, H.-Y. Huang, N. Meethong, Y.-H. Kao, W.C. Carter, Y.-M. Chiang, Model for the particle size, overpotential, and strain dependence of phase transition pathways in storage electrodes: application to nanoscale olivines, *Chem. Mater.* 21 (2009) 1557–1571.
- [154] M. Tang, W.C. Carter, J.F. Belak, Y.-M. Chiang, Modeling the competing phase transition pathways in nanoscale olivine electrodes, *Electrochim. Acta* 56 (2010) 969–976.
- [155] Y.-H. Kao, M. Tang, N. Meethong, J. Bai, W.C. Carter, Y.-M. Chiang, Overpotential-dependent phase transformation pathways in lithium iron phosphate battery electrodes, *Chem. Mater.* 22 (2010) 5845–5855.
- [156] V.B. Shenoy, P. Johari, Y. Qi, Elastic softening of amorphous and crystalline Li-Si phases with increasing Li concentration: a first-principles study, *J. Power Sources* 195 (2010) 6825–6830.
- [157] J.B. Ratchford, B.A. Crawford, J. Wolfenstine, J.L. Allen, C.A. Lundgren, Young's modulus of polycrystalline Li₁₂Si₇ using nanoindentation testing, *J. Power Sources* 211 (2012) 1–3.
- [158] S. Lee, J. Park, A.M. Sastry, W. Lu, Molecular dynamics simulations of SOC-dependent elasticity of Li₂Mn₂O₄ spinels in Li-ion batteries, *J. Electrochem. Soc.* 160 (2013) A968–A972.
- [159] Y. Qi, L.G. Hector, C. James, K.J. Kim, Lithium concentration dependent elastic properties of battery electrode materials from first principles calculations, *J. Electrochem. Soc.* 161 (2014) F3010–F3018.
- [160] R. Deshpande, Y. Qi, Y.-T. Cheng, Effects of concentration-dependent elastic modulus on diffusion-induced stresses for battery applications, *J. Electrochem. Soc.* 157 (2010) A967.
- [161] B. Yang, Y.P. He, J. Irsa, C.A. Lundgren, J.B. Ratchford, Y.P. Zhao, Effects of composition-dependent modulus, finite concentration and boundary constraint on Li-ion diffusion and stresses in a bilayer Cu-coated Si nano-anode, *J. Power Sources* 204 (2012) 168–176.
- [162] Z. Guo, T. Zhang, H. Hu, Y. Song, J. Zhang, Effects of hydrostatic stress and concentration-dependent elastic modulus on diffusion-induced stresses in cylindrical Li-ion batteries, *J. Appl. Mech.* 81 (2013) 031013.
- [163] X.H. Liu, H. Zheng, L. Zhong, S. Huang, K. Karki, L.Q. Zhang, Y. Liu, A. Kushima, W.T. Liang, J.W. Wang, J.-H. Cho, E. Epstein, S.A. Dayeh, S.T. Picraux, T. Zhu, J. Li, J.P. Sullivan, J. Cumings, C. Wang, S.X. Mao, Z.Z. Ye, S. Zhang, J.Y. Huang, Anisotropic swelling and fracture of silicon nanowires during lithiation, *Nano Lett.* 11 (2011) 3312–3318.
- [164] M. Pharr, K. Zhao, X. Wang, Z. Suo, J.J. Vlassak, Kinetics of initial lithiation of crystalline silicon electrodes of lithium-ion batteries, *Nano Lett.* 12 (2012) 5039–5047.
- [165] Q. Zhang, Y. Cui, E. Wang, Anisotropic lithium insertion behavior in silicon nanowires: binding energy, diffusion barrier, and strain effect, *J. Phys. Chem. C* 115 (2011) 9376–9381.
- [166] W. Hong, A kinetic model for anisotropic reactions in amorphous solids, *Extreme Mech. Lett.* 2 (2015) 46–51.
- [167] V.I. Levitas, H. Attariani, Anisotropic compositional expansion in elastoplastic materials and corresponding chemical potential: large-strain formulation and application to amorphous lithiated silicon, *J. Mech. Phys. Solid.* 69 (2014) 84–111.
- [168] H. Yang, S. Huang, X. Huang, F. Fan, W. Liang, X.H. Liu, L.-Q. Chen, J.Y. Huang, J. Li, T. Zhu, S. Zhang, Orientation-dependent interfacial mobility governs the anisotropic swelling in lithiated silicon nanowires, *Nano Lett.* 12 (2012) 1953–1958.
- [169] H. Yang, F. Fan, W. Liang, X. Guo, T. Zhu, S. Zhang, A chemo-mechanical model of lithiation in silicon, *J. Mech. Phys. Solid.* 70 (2014) 349–361.

- [170] Y. An, B.C. Wood, J. Ye, Y.-M. Chiang, Y.M. Wang, M. Tang, H. Jiang, Mitigating mechanical failure of crystalline silicon electrodes for lithium batteries by morphological design, *Phys. Chem. Chem. Phys.* 17 (2015) 17718–17728.
- [171] S. Hu, Y. Li, K.M. Rosso, M.L. Sushko, Mesoscale phase-field modeling of charge transport in nanocomposite electrodes for lithium-ion batteries, *J. Phys. Chem. C* 117 (2013) 28–40.
- [172] S. Han, J. Park, W. Lu, A.M. Sastry, Numerical study of grain boundary effect on Li⁺ effective diffusivity and intercalation-induced stresses in Li-ion battery active materials, *J. Power Sources* 240 (2013) 155–167.
- [173] S.K. Vanimisetti, N. Ramakrishnan, Effect of the electrode particle shape in Li-ion battery on the mechanical degradation during charge-discharge cycling, *Proc. IMechE Part C: J. Mech. Eng. Sci.* 226 (2012) 2192–2213.
- [174] P. Stein, Y. Zhao, B.-X. Xu, Effects of surface tension and electrochemical reactions in Li-ion battery electrode nanoparticles, *J. Power Sources* 332 (2016) 154–169.
- [175] S.J. Harris, R.D. Deshpande, Y. Qi, I. Dutta, Y.-T. Cheng, Mesopores inside electrode particles can change the Li-ion transport mechanism and diffusion-induced stress, *J. Mater. Res.* 25 (2010) 1433–1440.
- [176] Z. Jia, T. Li, Stress-modulated driving force for lithiation reaction in hollow nano-anodes, *J. Power Sources* 275 (2015) 866–876.
- [177] R. Purkayastha, R. McMeeking, Stress due to the intercalation of lithium in cubic-shaped particles: a parameter study, *Meccanica* 51 (2016) 3081–3096.
- [178] B. Sathar, V.R. Subramanian, Lithium intercalation in core-shell materials – theoretical analysis, *J. Electrochem. Soc.* 161 (2014) A682–A692.
- [179] N. Swaminathan, S. Balakrishnan, K. George, Elasticity and size effects on the electrochemical response of a graphite, Li-ion battery electrode particle, *J. Electrochem. Soc.* 163 (2016) A488–A498.
- [180] C. Lim, B. Yan, L. Yin, L. Zhu, Simulation of diffusion-induced stress using reconstructed electrodes particle structures generated by micro/nano-CT, *Electrochim. Acta* 75 (2012) 279–287.
- [181] M. Chung, J. Seo, X. Zhang, A. Sastry, Implementing realistic geometry and measured diffusion coefficients into single particle electrode modeling based on experiments with single LiMn₂O₄ spinel particles, *J. Electrochem. Soc.* 158 (2011) A371–A378.
- [182] V. Malavé, J. Berger, H. Zhu, R.J. Kee, A computational model of the mechanical behavior within reconstructed Li₂CoO₂ Li-ion battery cathode particles, *Electrochim. Acta* 130 (2014) 707–717.
- [183] J. Hun, M. Chung, M. Park, S. Woo, X. Zhang, A. Marie, Generation of realistic particle structures and simulations of internal stress: a numerical/AFM study of LiMn₂O₄ particles, *J. Electrochem. Soc.* 158 (2011) A434–A442.
- [184] Y. Lu, Y. Ni, Effects of particle shape and concurrent plasticity on stress generation during lithiation in particulate Li-ion battery electrodes, *Mech. Mater.* 91 (2015) 372–381.
- [185] M. Okubo, E. Hosono, J. Kim, M. Enomoto, N. Kojima, T. Kudo, H. Zhou, I. Honma, Nanosize effect on high-rate Li-ion intercalation in LiCoO₂ electrode, *J. Am. Chem. Soc.* 129 (2007) 7444–7452.
- [186] P. Poizot, S. Laruelle, S. Grugeon, L. Dupont, J.-M. Tarascon, Nano-sized transition-metal oxides as negative-electrode materials for lithium-ion batteries, *Nature* 407 (2000) 496–499.
- [187] H. Sclar, D. Kovacheva, E. Zhecheva, R. Stoyanova, R. Lavi, G. Kimmel, J. Grinblat, O. Girshevitz, F. Amalraj, O. Haik, E. Zinigrad, B. Markovsky, D. Aurbach, On the performance of LiNi_{1/3}Mn_{1/3}Co_{1/3}O₂ nanoparticles as a cathode material for lithium-ion batteries, *J. Electrochem. Soc.* 156 (2009) A938–A948.
- [188] Y.J. Wei, K. Nikolowski, S.Y. Zhan, H. Ehrenberg, S. Oswald, G. Chen, C.Z. Wang, H. Chen, Electrochemical kinetics and cycling performance of nano Li [Li_{0.25}Co_{0.3}Mn_{0.47}]O₂ cathode material for lithium ion batteries, *Electrochem. Commun.* 11 (2009) 2008–2011.
- [189] A. Van der Ven, M. Wagemaker, Effect of surface energies and nano-particle size distribution on open circuit voltage of Li-electrodes, *Electrochem. Commun.* 11 (2009) 881–884.
- [190] W. Qi, J.G. Shapter, Q. Wu, T. Yin, G. Gao, D. Cui, Nanostructured anode materials for lithium-ion batteries: principle, recent progress and future perspectives, *J. Mater. Chem.* 5 (2017) 19521.
- [191] N. Zhao, L. Fu, L. Yang, T. Zhang, G. Wang, Y. Wu, T. van Ree, Nanostructured anode materials for Li-ion batteries, *Pure Appl. Chem.* 80 (2008) 2283–2295.
- [192] G.A. Horrocks, M.F. Lively, J.M. Velazquez, S. Banerjee, Finite size effects on the structural progression induced by lithiation of V₂O₅: a combined diffraction and Raman spectroscopy study, *J. Mater. Chem.* 1 (2013) 15265–15277.
- [193] J. Wan, A.F. Kaplan, J. Zheng, X. Han, Y. Chen, N.J. Wadlock, N. Faenza, S. Lacey, T. Li, J. Guo, L. Hu, Two dimensional silicon nanowalls for lithium ion batteries, *J. Mater. Chem.* 2 (2014) 6051–6057.
- [194] J.-H. Jeong, K.-H. Kim, D.-W. Jung, K. Kim, S.-M. Lee, E.-S. Oh, High-performance characteristics of silicon inverse opal synthesized by the simple magnesium reduction as anodes for lithium-ion batteries, *J. Power Sources* 300 (2015) 182–189.
- [195] C.J. Chalker, H. An, J. Zavalala, A. Parija, S. Banerjee, J.L. Lutkenhaus, J.D. Beateas, Fabrication and electrochemical performance of structured mesoscale open shell V₂O₅ networks, *Langmuir* 33 (2017) 5975–5981.
- [196] Q. Xiao, M. Gu, H. Yang, B. Li, C. Zhang, Y. Liu, F. Liu, F. Dai, L. Yang, Z. Liu, X. Xiao, G. Liu, P. Zhao, S. Zhang, C. Wang, Y. Lu, M. Cai, Inward lithium-ion breathing of hierarchically porous silicon anodes, *Nat. Commun.* 6 (2015) 8844.
- [197] J. Ye, A.C. Baumgaertel, Y.M. Wang, J. Biener, M.M. Biener, Structural optimization of 3D porous electrodes for high-rate performance lithium ion batteries, *ACS Nano* 9 (2015) 2194–2202.
- [198] X. Xia, C.V. Di Leo, X.W. Gu, J.R. Greer, In situ lithiation-delithiation of mechanically robust Cu-Si core-shell nanolattices in a scanning electron microscope, *ACS Energy Lett* 1 (2016) 492–499.
- [199] J. Wang, H.L. Duan, Z.P. Huang, B.L. Karihaloo, A scaling law for properties of nano-structured materials, *Proc. R. Soc. A* 462 (2006) 1355–1363.
- [200] J. Wang, Z. Huang, H. Duan, S. Yu, X. Feng, G. Wang, W. Zahng, T. Wang, Surface stress effect in mechanics of nanostructured materials, *Acta Mech. Solida Sin.* 24 (2011) 52–82.
- [201] D. Davydov, A. Javili, P. Steinmann, On molecular statics and surface-enhanced continuum modeling of nano-structures, *Comput. Mater. Sci.* 69 (2013) 510–519.
- [202] D. Gross, R. Müller, M. Müller, B.-X. Xu, K. Albe, On the origin of inhomogeneous stress and strain distributions in single-crystalline metallic nanoparticles, *Int. J. Mater. Res.* 102 (2011) 743–747.
- [203] J.W. Gibbs, *The Scientific Papers of J. Willard Gibbs* vol. 1, Longmans Green and Co, 1906.
- [204] R. Shuttleworth, The surface tension of solids, *Proc. Phys. Soc.* 63 (1950) 444–457.
- [205] C. Herring, Surface tension as a motivation for sintering, in: J.M. Ball, D. Kinderlehrer, P. Podio-Guidugli, M. Slemrod (Eds.), *Fundamental Contributions to the Continuum Theory of Evolving Phase Interfaces in Solids*, Springer, Berlin, Heidelberg, 1999, pp. 33–69, <https://doi.org/10.1007/978-3-642-59938-5>.
- [206] M.E. Gurtin, A.I. Murdoch, A continuum theory of elastic material surfaces, *Arch. Ration. Mech. Anal.* 57 (1975) 291–323.
- [207] A.T. McBride, A. Javili, P. Steinmann, S. Bargmann, Geometrically nonlinear continuum thermomechanics with surface energies coupled to diffusion, *J. Mech. Phys. Solid.* 59 (2011) 2116–2133.
- [208] J. Weissmüller, J.W. Cahn, Mean stresses in microstructures due to interface stresses: a generalization of a capillary equation for solids, *Acta Mater.* 45 (1997) 1899–1906.
- [209] F. Hao, X. Gao, D. Fang, Diffusion-induced stresses of electrode nanomaterials in lithium-ion battery: the effects of surface stress, *J. Appl. Phys.* 112 (2012) 103507.
- [210] C.M. DeLuca, K. Maute, M.L. Dunn, Effects of electrode particle morphology on stress generation in silicon during lithium insertion, *J. Power Sources* 196 (2011) 9672–9681.
- [211] J.-L. Zang, Y.-P. Zhao, A diffusion and curvature dependent surface elastic model with application to stress analysis of anode in lithium ion battery, *Int. J. Eng. Sci.* 61 (2012) 156–170.
- [212] Y. Lu, P. Zhang, F. Wang, K. Zhang, X. Zhao, Reaction-diffusion-stress coupling model for Li-ion batteries: the role of surface effects on electrochemical performance, *Electrochim. Acta* 274 (2018) 359–369.
- [213] P. Stein, A. Moradabadi, M. Diehm, B.-X. Xu, K. Albe, The influence of anisotropic surface stresses and bulk stresses on defect thermodynamics in LiCoO₂ nanoparticles, *Acta Mater.* 159 (2018) 225–240.
- [214] T.K. Bhandakkar, H.T. Johnson, Diffusion induced stresses in buckling battery electrodes, *J. Mech. Phys. Solid.* 60 (2012) 1103–1121.
- [215] J. Chakraborty, C.P. Please, A. Goriely, S.J. Chapman, Combining mechanical and chemical effects in the deformation and failure of a cylindrical electrode particle in a Li-ion battery, *Int. J. Solid Struct.* 54 (2015) 66–81.
- [216] K. Zhang, Y. Li, B. Zheng, G. Wu, J. Wu, F. Yang, Large deformation analysis of diffusion-induced buckling of nanowires in lithium-ion batteries, *Int. J. Solid Struct.* 108 (2017) 230–243.
- [217] K. Zhang, Y. Li, J. Wu, B. Zheng, F. Yang, Lithiation-induced buckling of wire-based electrodes in lithium-ion batteries: a phase-field model coupled with large deformation, *Int. J. Solid Struct.* (2018).
- [218] C. Yu, X. Li, T. Ma, J. Rong, R. Zhang, J. Shaffer, Y. An, Q. Liu, B. Wei, H. Jiang, Silicon thin films as anodes for high-performance lithium-ion batteries with effective stress relaxation, *Adv. Energy Mater.* 2 (2011) 68–73.
- [219] X. Wang, W. Zeng, L. Hong, W. Xu, H. Yang, F. Wang, H. Duan, M. Tang, H. Jiang, Stress-driven lithium dendrite growth mechanism and dendrite mitigation by electroplating on soft substrates, *Nature Energy* 3 (2018) 227–235.
- [220] Z. Jia, T. Li, Failure mechanics of a wrinkling thin film anode on a substrate under cyclic charging and discharging, *Extreme Mech. Lett.* 8 (2016) 273–282.
- [221] M.E. Stourmar, X. Xiao, Y. Qi, P. Johari, P. Lu, B.W. Sheldon, H. Gao, V.B. Shenoy, Li segregation induces structure and strength changes at the amorphous Si/Cu interface, *Nano Lett.* 13 (2013) 4759–4768.
- [222] G.R. Hardin, Y. Zhang, C.D. Fincher, M. Pharr, Interfacial fracture of nanowire electrodes of lithium-ion batteries, *JOM* 69 (2017) 1519–1523.
- [223] R. Xu, L.S. de Vasconcelos, J. Shi, J. Li, K. Zhao, Disintegration of mealball electrodes for LiNi_{0.8}Mn_{0.2}Co_{0.2}O₂ cathode materials, *Exp. Mech.* 58 (2018) 549–559.
- [224] R. Xu, K. Zhao, Corrosive fracture of electrodes in Li-ion batteries, *J. Mech. Phys. Solid.* 121 (2018) 258–280.
- [225] Y. Itou, Y. Ukyo, Performance of LiNiCoO₂ materials for advanced lithium-ion batteries, *J. Power Sources* 146 (2005) 39–44.
- [226] D. Wang, X. Wu, Z. Wang, L. Chen, Cracking causing cyclic instability of LiFePO₄ cathode material, *J. Power Sources* 140 (2005) 125–128.
- [227] P. Yan, J. Zheng, M. Gu, J. Xiao, J.-G. Zhang, C.-M. Wang, Intragranular cracking as a critical barrier for high-voltage usage of layer-structured cathode for lithium-ion batteries, *Nat. Commun.* 8 (2017) 14101.
- [228] J. Christensen, J. Newman, A mathematical model of stress generation and fracture in lithium manganese oxide, *J. Electrochem. Soc.* 153 (2006) A1019.
- [229] M. Qu, W.H. Woodford, J.M. Maloney, W.C. Carter, Y.-M. Chiang, K.J. Van Vliet, Nanomechanical quantification of elastic, plastic, and fracture properties of LiCoO₂, *Adv. Energy Mater.* 2 (2012) 940–944.
- [230] J.G. Swallow, W.H. Woodford, F.P. McGrogan, N. Ferralis, Y.-M. Chiang, K.J.V. Vliet, Effect of electrochemical charging on elastoplastic properties and fracture toughness of Li₂CoO₂, *J. Electrochem. Soc.* 161 (2014) F3084–F3090.
- [231] R. Xu, H. Sun, L. S. de Vasconcelos, K. Zhao, Mechanical and structural degradation of LiNi_{0.8}Mn_{0.2}Co_{0.2}O₂ cathode in Li-ion batteries: an experimental study, *J. Electrochem. Soc.* 164 (2017) A3333–A3341.
- [232] R. Grantab, V.B. Shenoy, Pressure-gradient dependent diffusion and crack propagation in lithiated silicon nanowires, *J. Electrochem. Soc.* 159 (2012)

- A584–A591.
- [233] T.K. Bhandakkar, H. Gao, Cohesive modeling of crack nucleation under diffusion induced stresses in a thin strip: implications on the critical size for flaw tolerant battery electrodes, *Int. J. Solid Struct.* 47 (2010) 1424–1434.
- [234] I. Ryu, S.W. Lee, H. Gao, Y. Cui, W.D. Nix, Microscopic model for fracture of crystalline Si nanopillars during lithiation, *J. Power Sources* 255 (2014) 274–282.
- [235] R. Grantab, V.B. Shenoy, Location- and orientation-dependent progressive crack propagation in cylindrical graphite electrode particles, *J. Electrochem. Soc.* 158 (2011) A948–A954.
- [236] S.K. Soni, B.W. Sheldon, X. Xiao, M.W. Verbrugge, A. Dongjoo, H. H. G. Huajian, Stress mitigation during the lithiation of patterned amorphous Si Islands, *J. Electrochem. Soc.* 159 (2011) A38–A43.
- [237] H. Haftbaradaran, S.K. Soni, B.W. Sheldon, X. Xiao, H. Gao, Modified stoney equation for patterned thin film electrodes on substrates in the presence of interfacial sliding, *J. Appl. Mech.* 79 (2012) 031018.
- [238] B. Lu, Y. Song, J. Zhang, Time to delamination onset and critical size of patterned thin film electrodes of lithium ion batteries, *J. Power Sources* 289 (2015) 168–183.
- [239] C. Miehe, H. Dal, A. Raina, A phase field model for chemo-mechanical induced fracture in lithium-ion battery electrode particles, *Int. J. Numer. Methods Eng.* 106 (2015) 683–711.
- [240] B.-X. Xu, Y. Zhao, P. Stein, Phase field modeling of electrochemically induced fracture in Li-ion battery with large deformation and phase segregation, *GAMM-Mitt.* 39 (2016) 92–109.
- [241] M. Klinsmann, D. Rosato, M. Kamlah, R.M. McMeeking, Modeling crack growth during Li insertion in storage particles using a fracture phase field approach, *J. Mech. Phys. Solid.* 92 (2016) 313–344.
- [242] M. Klinsmann, D. Rosato, M. Kamlah, R.M. McMeeking, Modeling crack growth during Li extraction in storage particles using a fracture phase field approach, *J. Electrochem. Soc.* 163 (2016) A102–A118.
- [243] P. Barai, P.P. Mukherjee, Stochastic analysis of diffusion induced damage in lithium-ion battery electrodes, *J. Electrochem. Soc.* 160 (2013) A955–A967.
- [244] P. Barai, P.P. Mukherjee, Mechano-electrochemical stochastics in high-capacity electrodes for energy storage, *J. Electrochem. Soc.* 163 (2016) A1120–A1137.
- [245] W.H. Woodford, W. Craig Carter, Y.-M. Chiang, Design criteria for electrochemical shock resistant battery electrodes, *Energy Environ. Sci.* 5 (2012) 8014–8024.
- [246] B. Wu, W. Lu, Mechanical-electrochemical modeling of agglomerate particles in lithium-ion battery electrodes, *J. Electrochem. Soc.* 163 (2016) A3131–A3139.
- [247] W.H. Woodford, Y.-M. Chiang, W.C. Carter, Electrochemical shock of intercalation electrodes: a fracture mechanics analysis, *J. Electrochem. Soc.* 157 (2010) A1052–A1059.
- [248] G. Sun, T. Sui, B. Song, H. Zheng, L. Lu, A.M. Korsunsky, On the fragmentation of active material secondary particles in lithium ion battery cathodes induced by charge cycling, *Extreme Mech. Lett.* 9 (2016) 449–458.
- [249] M. Gauthier, T.J. Carney, A. Grimaud, L. Giordano, N. Pour, H.-H. Chang, D.P. Fenning, S.F. Lux, O. Paschos, C. Bauer, F. Maglia, S. Lupart, P. Lamp, Y. Shao-Horn, Electrode-electrolyte interface in Li-ion batteries: current understanding and new insights, *J. Phys. Chem. Lett.* 6 (2015) 4653–4672.
- [250] A. Wang, S. Kadam, H. Li, S. Shi, Y. Qi, Review on modeling of the anode solid electrolyte interphase (SEI) for lithium-ion batteries, *npj Comput. Mater.* 4 (2018) 15.
- [251] E. Rejovitzky, C.V. Di Leo, L. Anand, A theory and a simulation capability for the growth of a solid electrolyte interphase layer at an anode particle in a Li-ion battery, *J. Mech. Phys. Solid.* 78 (2015) 210–230.
- [252] P. Guan, L. Liu, X. Lin, Simulation and experiment on solid electrolyte interphase (SEI) morphology evolution and lithium-ion diffusion, *J. Electrochem. Soc.* 162 (2015) A1798–A1808.
- [253] D.A. Freedman, D. Roundy, T.A. Arias, Elastic effects of vacancies in strontium titanate: short and long-range strain fields, elastic dipole tensors, and chemical strain, *Phys. Rev. B* 80 (2009) 064108.
- [254] V. Wenzel, H. Nirschl, D. Nützel, Challenges in lithium-ion-battery slurry preparation and potential of modifying electrode structures by different mixing processes, *Energy Technol.* 3 (2015) 692–698.
- [255] Z. Liu, T.W. Verhallen, D.P. Singh, H. Wang, M. Wagemaker, S. Barnett, Relating the 3D electrode morphology to Li-ion battery performance; a case for liFePO₄, *J. Power Sources* 324 (2016) 358–367.
- [256] D.-W. Chung, P.R. Shearing, N.P. Brandon, S.J. Harris, R.E. García, Particle size polydispersity in Li-ion batteries, *J. Electrochem. Soc.* 161 (2014) A422–A430.
- [257] L. Ji, Z. Guo, Y. Wu, Computational and experimental observation of Li-ion concentration distribution and diffusion-induced stress in porous battery electrodes, *Energy Technol.* 5 (2017) 1702–1711.
- [258] Y. Zhao, L.R. De Jesus, P. Stein, G.A. Horrocks, S. Banerjee, B.-X. Xu, Modeling of phase separation across interconnected electrode particles in lithium-ion batteries, *RSC Adv.* 7 (2017) 41254–41264.
- [259] L.R.D. Jesus, Y. Zhao, G.A. Horrocks, J.L. Andrews, P. Stein, B.-X. Xu, S. Banerjee, Lithiation across interconnected V₂O₅ nanoparticle networks, *J. Mater. Chem.* 5 (2017) 20141–20152.
- [260] Y. Li, F. El Gabaly, T.R. Ferguson, R.B. Smith, N.C. Bartelt, J.D. Sugar, K.R. Fenton, D.A. Cogswell, A.L.D. Kilcoyne, T. Tylliszczak, M.Z. Bazant, W.C. Chueh, Current-induced transition from particle-by-particle to concurrent intercalation in phase-separating battery electrodes, *Nat. Mater.* 13 (2014) 1149–1156.
- [261] Y. Zhao, D. Schilling, B.-X. Xu, Variational boundary conditions based on the Nitsche method for fitted and unfitted isogeometric discretizations of the mechanically coupled Cahn–Hilliard equation, *J. Comp. Physiol.* 340 (2017) 177–199.
- [262] K.E. Aifantis, J.P. Dempsey, Stable crack growth in nanostructured Li-batteries, *J. Power Sources* 143 (2005) 203–211.
- [263] K.E. Aifantis, S.A. Hackney, J.P. Dempsey, Design criteria for nanostructured Li-ion batteries, *J. Power Sources* 165 (2007) 874–879.
- [264] B.J. Dimitrijevic, K.E. Aifantis, K. Hackl, The influence of particle size and spacing on the fragmentation of nanocomposite anodes for Li batteries, *J. Power Sources* 206 (2012) 343–348.
- [265] E.K. Rahani, V.B. Shenoy, Role of plastic deformation of binder on stress evolution during charging and discharging in lithium-ion battery negative electrodes, *J. Electrochem. Soc.* 160 (2013) A1153–A1162.
- [266] R. Xu, L. S. d. Vasconcelos, K. Zhao, Computational analysis of chemomechanical behaviors of composite electrodes in Li-ion batteries, *J. Mater. Res.* 31 (2016) 2715–2727.
- [267] H. Wang, S.P. Nadimpalli, V.B. Shenoy, Inelastic shape changes of silicon particles and stress evolution at binder/particle interface in a composite electrode during lithiation/delithiation cycling, *Extreme Mech. Lett.* 9 (2016) 430–438.
- [268] S. Kim, H.-Y.S. Huang, Mechanical stresses at the cathode-electrolyte interface in lithium-ion batteries, *J. Mater. Res.* 31 (2016) 3506–3512.
- [269] B. Vijayaraghavan, D.R. Ely, Y.-M. Chiang, R. García-García, R.E. García, An analytical method to determine tortuosity in rechargeable battery electrodes, *J. Electrochem. Soc.* 159 (2012) A548–A552.
- [270] D. Westhoff, J. Feinauer, K. Kuchler, T. Mitsch, I. Manke, S. Hein, A. Latz, V. Schmidt, Parametric stochastic 3D model for the microstructure of anodes in lithium-ion power cells, *Comput. Mater. Sci.* 126 (2017) 453–467.
- [271] M. Ebner, D.-W. Chung, R.E. García, V. Wood, Tortuosity anisotropy in lithium-ion battery electrodes, *Adv. Energy Mater.* 4 (2014) 1301278.
- [272] S.A. Roberts, V.E. Brunini, K.N. Long, A.M. Grillet, A framework for three-dimensional mesoscale modeling of anisotropic swelling and mechanical deformation in lithium-ion electrodes, *J. Electrochem. Soc.* 161 (2014) F3052–F3059.
- [273] H. Mendoza, S.A. Roberts, V.E. Brunini, A.M. Grillet, Mechanical and electrochemical response of a LiCoO₂ cathode using reconstructed microstructures, *Electrochim. Acta* 190 (2016) 1–15.
- [274] S. Kim, J. Wee, K. Peters, H.-Y.S. Huang, Multiphysics coupling in lithium-ion batteries with reconstructed porous microstructures, *J. Phys. Chem. C* 122 (2018) 5280–5290.
- [275] L. Wu, X. Xiao, Y. Wen, J. Zhang, Three-dimensional finite element study on stress generation in synchrotron X-ray tomography reconstructed nickel-manganese-cobalt based half cell, *J. Power Sources* 336 (2016) 8–18.
- [276] L. Wu, Y. Wen, J. Zhang, Three-dimensional finite element study on Li diffusion induced stress in FIB-SEM reconstructed LiCoO₂ half cell, *Electrochim. Acta* 222 (2016) 814–820.
- [277] G.-A. Nazri, G. Pistoia, *Lithium Batteries: Science and Technology*, Springer Science & Business Media, 2008.
- [278] D. Andre, M. Meiler, K. Steiner, C. Wimmer, T. Soczka-Guth, D. Sauer, Characterization of high-power lithium-ion batteries by electrochemical impedance spectroscopy. i. experimental investigation, *J. Power Sources* 196 (2011) 5334–5341.
- [279] C. Chen, J. Liu, K. Amine, Symmetric cell approach and impedance spectroscopy of high power lithium-ion batteries, *J. Power Sources* 96 (2001) 321–328.
- [280] J. Park, W. Lu, A.M. Sastry, Numerical simulation of stress evolution in lithium manganese dioxide particles due to coupled phase transition and intercalation, *J. Electrochem. Soc.* 158 (2011) A201.
- [281] J. Newman, W. Tiedemann, Porous-electrode theory with battery applications, *AIChE J.* 21 (1975) 25–41.
- [282] M. Doyle, T.F. Fuller, J. Newman, Modeling of galvanostatic charge and discharge of the lithium/polymer/insertion cell, *J. Electrochem. Soc.* 140 (1993) 1526–1533.
- [283] M. Doyle, J. Newman, A.S. Gozdz, C.N. Schmutz, J.-M. Tarascon, Comparison of modeling predictions with experimental data from plastic lithium ion cells, *J. Electrochem. Soc.* 143 (1996) 1890–1903.
- [284] D. a. G. Bruggeman, Berechnung verschiedener physikalischer Konstanten von heterogenen Substanzen. I. Dielektrizitätskonstanten und Leitfähigkeiten der Mischkörper aus isotropen Substanzen, *Ann. Phys.* 416 (1935) 636–664.
- [285] B. Tjaden, S.J. Cooper, D.J. Brett, D. Kramer, P.R. Shearing, On the origin and application of the Bruggeman correlation for analysing transport phenomena in electrochemical systems, *Curr. Opin. Chem. Eng.* 12 (2016) 44–51.
- [286] P.M. Gomadam, J.W. Weidner, Modeling volume changes in porous electrodes, *J. Electrochem. Soc.* 153 (2006) A179–A186.
- [287] T.R. Garrick, K. Kanneganti, X. Huang, J.W. Weidner, Modeling volume change due to intercalation into porous electrodes, *J. Electrochem. Soc.* 161 (2014) E3297–E3301.
- [288] T.R. Garrick, X. Huang, V. Srinivasan, J.W. Weidner, Modeling volume change in dual insertion electrodes, *J. Electrochem. Soc.* 164 (2017) E3552–E3558.
- [289] T.R. Garrick, K. Higa, S.-L. Wu, Y. Dai, X. Huang, V. Srinivasan, J.W. Weidner, Modeling battery performance due to intercalation driven volume change in porous electrodes, *J. Electrochem. Soc.* 164 (2017) E3592–E3597.
- [290] B. Yan, C. Lim, L. Yin, L. Zhu, Three dimensional simulation of galvanostatic discharge of LiCoO₂ cathode based on X-ray nano-CT images, *J. Electrochem. Soc.* 159 (2012) A1604–A1614.
- [291] A.H. Wiedemann, G.M. Goldin, S.A. Barnett, H. Zhu, R.J. Kee, Effects of three-dimensional cathode microstructure on the performance of lithium-ion battery cathodes, *Electrochim. Acta* 88 (2013) 580–588.
- [292] T. Hutzenlaub, S. Thiele, R. Zengerle, C. Ziegler, Three-dimensional reconstruction of a LiCoO₂ li-ion battery cathode, *Electrochem. Solid State Lett.* 15 (2011) A33–A36.
- [293] M. Ebner, V. Wood, Tool for tortuosity estimation in lithium ion battery porous electrodes, *J. Electrochem. Soc.* 162 (2015) A3064–A3070.

- [294] S. Cooper, A. Bertei, P. Shearing, J. Kilner, N. Brandon, Tafactor, An open-source application for calculating tortuosity factors from tomographic data, *SoftwareX* 5 (2016) 203–210.
- [295] S. Golmon, K. Maute, M.L. Dunn, Numerical modeling of electrochemical–mechanical interactions in lithium polymer batteries, *Comput. Struct.* 87 (2009) 1567–1579.
- [296] T. Mori, K. Tanaka, Average stress in matrix and average elastic energy of materials with misfitting inclusions, *Acta Metall.* 21 (1973) 571–574.
- [297] G. Inoue, K. Ikeshita, M. Iwabu, Y. Sagae, M. Kawase, Simulation of lithium-ion battery with effect of volume expansion of active materials, *ECS Trans* 80 (2017) 275–282.
- [298] A. Awarke, S. Lauer, M. Wittler, S. Pischinger, Quantifying the effects of strains on the conductivity and porosity of LiFePO_4 based Li-ion composite cathodes using a multi-scale approach, *Comput. Mater. Sci.* 50 (2011) 871–879.
- [299] K.E. Thomas, R.M. Darling, J. Newman, Mathematical modeling of lithium batteries, in: W. van Schalkwijk, B. Scrosati (Eds.), *Advances in Lithium-ion Batteries*, Kluwer Academic/Plenum, 2002, pp. 345–392.
- [300] S. Santhanagopalan, Q. Guo, P. Ramadass, R.E. White, Review of models for predicting the cycling performance of lithium ion batteries, *J. Power Sources* 156 (2006) 620–628.
- [301] M. Landstorfer, T. Jacob, Mathematical modeling of intercalation batteries at the cell level and beyond, *Chem. Soc. Rev.* 42 (2013) 3234–3252.
- [302] A. Jökar, B. Rajabloo, M. Désilets, M. Lacroix, Review of simplified pseudo-two-dimensional models of lithium-ion batteries, *J. Power Sources* 327 (2016) 44–55.
- [303] M. Doyle, Modeling of galvanostatic charge and discharge of the lithium/polymer/insertion cell, *J. Electrochem. Soc.* 140 (1993) 1526.
- [304] T.F. Fuller, M. Doyle, J. Newman, Simulation and optimization of the dual lithium ion insertion cell, *J. Electrochem. Soc.* 141 (1994) 1–10.
- [305] J. Christensen, Modeling diffusion-induced stress in Li-ion cells with porous electrodes, *J. Electrochem. Soc.* 157 (2010) A366–A380.
- [306] R. Fu, M. Xiao, S.Y. Choe, Modeling, validation and analysis of mechanical stress generation and dimension changes of a pouch type high power Li-ion battery, *J. Power Sources* 224 (2013) 211–224.
- [307] B. Suthar, P.W.C. Northrop, R.D. Braatz, V.R. Subramanian, Optimal charging profiles with minimal intercalation-induced stresses for lithium-ion batteries using reformulated pseudo 2-dimensional models, *J. Electrochem. Soc.* 161 (2014) F3144–F3155.
- [308] B. Suthar, P.W.C. Northrop, D. Rife, V.R. Subramanian, Effect of porosity, thickness and tortuosity on capacity fade of anode, *J. Electrochem. Soc.* 162 (2015) A1708–A1717.
- [309] Y. Dai, L. Cai, R.E. White, Simulation and analysis of stress in a li-ion battery with a blended LiMn_2O_4 and $\text{LiNi}_{0.8}\text{Co}_{0.15}\text{Al}_{0.05}\text{O}_2$ cathode, *J. Power Sources* 247 (2014) 365–376.
- [310] S. Renganathan, G. Sikha, S. Santhanagopalan, R.E. White, Theoretical analysis of stresses in a lithium ion cell, *J. Electrochem. Soc.* 157 (2010) A155–A163.
- [311] Y. Bai, Y. Zhao, W. Liu, B.-X. Xu, Two-level Modeling of Lithium-ion Batteries, (2019) (submitted for publication).
- [312] X. Xiao, W. Wu, X. Huang, A multi-scale approach for the stress analysis of polymeric separators in a lithium-ion battery, *J. Power Sources* 195 (2010) 7649–7660.
- [313] Y. Xie, C. Yuan, An integrated anode stress model for commercial Li_xC_6 - $\text{Li}_x\text{Mn}_2\text{O}_4$ battery during the cycling operation, *J. Power Sources* 274 (2015) 101–113.
- [314] R. Behrou, K. Maute, Multiscale modeling of non-local damage evolution in lithium-ion batteries, *ECS Trans* 77 (2017) 1163–1177.
- [315] R. Purkayastha, R.M. McMeeking, A linearized model for lithium ion batteries and maps for their performance and failure, *J. Appl. Mech.* 79 (2012) 031021–031021.
- [316] J. Li, N. Lotfi, R.G. Landers, J. Park, A single particle model for lithium-ion batteries with electrolyte and stress-enhanced diffusion physics, *J. Electrochem. Soc.* 164 (2017) A874–A883.
- [317] J. Li, K. Adewuyi, N. Lotfi, R. Landers, J. Park, A single particle model with chemical/mechanical degradation physics for lithium ion battery state of health (soh) estimation, *Appl. Energy* 212 (2018) 1178–1190.
- [318] R.T. Purkayastha, R.M. McMeeking, An integrated 2-D model of a lithium ion battery: the effect of material parameters and morphology on storage particle stress, *Comput. Mech.* 50 (2012) 209–227.
- [319] W. Wu, X. Xiao, M. Wang, X. Huang, A microstructural resolved model for the stress analysis of lithium-ion batteries, *J. Electrochem. Soc.* 161 (2014) A803–A813.
- [320] A. Ferrese, J. Newman, Mechanical deformation of a lithium-metal anode due to a very stiff separator, *J. Electrochem. Soc.* 161 (2014) A1350–A1359.
- [321] B. Wu, W. Lu, A battery model that fully couples mechanics and electrochemistry at both particle and electrode levels by incorporation of particle interaction, *J. Power Sources* 360 (2017) 360–372.
- [322] Y. Dai, L. Cai, R.E. White, Simulation and analysis of inhomogeneous degradation in large format LiMn_2O_4 /carbon cells, *J. Electrochem. Soc.* 161 (2014) E3348–E3356.
- [323] B. Rieger, S.V. Erhard, S. Kosch, M. Venator, A. Rheinfeld, A. Jossen, Multi-dimensional modeling of the influence of cell design on temperature, displacement and stress inhomogeneity in large-format lithium-ion cells, *J. Electrochem. Soc.* 163 (2016) A3099–A3110.
- [324] C.-W. Wang, A.M. Sastry, Mesoscale modeling of a Li-ion polymer cell, *J. Electrochem. Soc.* 154 (2007) A1035–A1047.
- [325] S. Lee, A.M. Sastry, J. Park, Study on microstructures of electrodes in lithium-ion batteries using variational multi-scale enrichment, *J. Power Sources* 315 (2016) 96–110.
- [326] J.F. Oudenhoven, L. Baggetto, P.H. Notten, All-solid-state lithium-ion microbatteries: a review of various three-dimensional concepts, *Adv. Energy Mater.* 1 (2011) 10–33.
- [327] J. Janek, W.G. Zeier, A solid future for battery development, *Energy* 500 (2016) 300.
- [328] R. Agrawal, G. Pandey, Solid polymer electrolytes: materials designing and all-solid-state battery applications: an overview, *J. Phys. D* 41 (2008) 223001.
- [329] J.W. Fergus, Ceramic and polymeric solid electrolytes for lithium-ion batteries, *J. Power Sources* 195 (2010) 4554–4569.
- [330] W.D. Richards, L.J. Miara, Y. Wang, J.C. Kim, G. Ceder, Interface Stability Solid-State Batteries 28 (2016) 266–273.
- [331] Y.-S. Hu, *Batteries: Getting Solid 1 (????) 16042*.
- [332] S. Zekoll, C. Marriner-Edwards, A.K.O. Hekselman, J. Kasemchainan, C. Kuss, D.E.J. Armstrong, D. Cai, R.J. Wallace, F.H. Richter, J.H.J. Thijssen, P.G. Bruce, Hybrid electrolytes with 3d bicontinuous ordered ceramic and polymer microchannels for all-solid-state, *Batteries* 11 (2018) 185–201.
- [333] Y.V. Baskakova, O.V. Yarmolenko, O.N. Efimov, Polymer gel electrolytes for lithium batteries, *Russ. Chem. Rev.* 81 (2012) 367.
- [334] M. Park, X. Zhang, M. Chung, G.B. Less, A.M. Sastry, A review of conduction phenomena in Li-ion batteries, *J. Power Sources* 195 (2010) 7904–7929.
- [335] J.C. Bachman, S. Muy, A. Grimaud, H.-H. Chang, N. Pour, S.F. Lux, O. Paschos, F. Maglia, S. Lupart, P. Lamp, et al., Inorganic solid-state electrolytes for lithium batteries: mechanisms and properties governing ion conduction, *Chem. Rev.* 116 (2015) 140–162.
- [336] G. Bucci, Y.-M. Chiang, W.C. Carter, Formulation of the coupled electrochemical–mechanical boundary-value problem, with applications to transport of multiple charged species, *Acta Mater.* 104 (2016) 33–51.
- [337] D. Grazioli, O. Verners, V. Zadin, D. Brandell, A. Simone, Electrochemical-mechanical modeling of solid polymer electrolytes: impact of mechanical stresses on Li-ion battery performance, *Electrochim. Acta* (2018) in press.
- [338] P. Goyal, C.W. Monroe, New foundations of Newman’s theory for solid electrolytes: thermodynamics and transient balances, *J. Electrochem. Soc.* 164 (2017) E3647–E3660.
- [339] K. Becker-Steinberger, S. Funken, M. Landstorfer, K. Urban, A mathematical model for all solid-state lithium-ion batteries, *ECS Transactions* 25 (2010) 285–296.
- [340] D. Danilov, R. a. H. Niessen, P.H.L. Notten, Modeling all-solid-state Li-ion batteries, *J. Electrochem. Soc.* 158 (2011) A215–A222.
- [341] W. Dreyer, C. Gühllke, R. Müller, Overcoming the shortcomings of the Nernst–Planck model, *Phys. Chem. Chem. Phys.* 15 (2013) 7075–7086.
- [342] M. Landstorfer, S. Funken, T. Jacob, An advanced model framework for solid electrolyte intercalation batteries, *Phys. Chem. Chem. Phys.* 13 (2011) 12817–12825.
- [343] S. Braun, C. Yada, A. Latz, Thermodynamically consistent model for space-charge-layer formation in a solid electrolyte, *J. Phys. Chem. C* 119 (2015) 22281–22288.
- [344] X. Su, T. Zhang, X. Liang, H. Gao, B.W. Sheldon, Employing nanoscale surface morphologies to improve interfacial adhesion between solid electrolytes and Li ion battery cathodes, *Acta Mater.* 98 (2015) 175–181.
- [345] X. Su, K. Guo, T. Ma, P.A. Tamirisa, H. Ye, H. Gao, B.W. Sheldon, Deformation and chemomechanical degradation at solid electrolyte–electrode interfaces, *ACS Energy Lett.* 2 (2017) 1729–1733.
- [346] G. Bucci, T. Swamy, Y.-M. Chiang, W.C. Carter, Modeling of internal mechanical failure of all-solid-state batteries during electrochemical cycling, and implications for battery design, *J. Mater. Chem.* 5 (2017) 19422–19430.
- [347] G. Bucci, T. Swamy, Y.-M. Chiang, W.C. Carter, Random walk analysis of the effect of mechanical degradation on all-solid-state battery power, *J. Electrochem. Soc.* 164 (2017) A2660–A2664.
- [348] G. Bucci, T. Swamy, S. Bishop, B.W. Sheldon, Y.-M. Chiang, W.C. Carter, The effect of stress on battery-electrode capacity, *J. Electrochem. Soc.* 164 (2017) A645–A654.
- [349] G. Bucci, B. Talamini, A. Renuka Balakrishna, Y.-M. Chiang, W.C. Carter, Mechanical instability of electrode–electrolyte interfaces in solid-state batteries, *Phys. Rev. Mater.* 2 (2018) 105407.
- [350] K. Guo, P.A. Tamirisa, B.W. Sheldon, X. Xiao, H. Gao, Pop-up delamination of electrodes in solid-state batteries, *J. Electrochem. Soc.* 165 (2018) A618–A625.
- [351] R. Behrou, K. Maute, Numerical modeling of damage evolution phenomenon in solid-state lithium-ion batteries, *J. Electrochem. Soc.* 164 (2017) A2573–A2589.
- [352] C. Brissot, M. Rosso, J.N. Chazalviel, S. Lascaud, Dendritic growth mechanisms in lithium/polymer cells, *J. Power Sources* 81–82 (1999) 925–929.
- [353] C. Brissot, M. Rosso, J.N. Chazalviel, S. Lascaud, Concentration measurements in lithium/polymer–electrolyte/lithium cells during cycling, *J. Power Sources* 94 (2001) 212–218.
- [354] R.D. Schmidt, J. Sakamoto, In-situ, non-destructive acoustic characterization of solid state electrolyte cells, *J. Power Sources* 324 (2016) 126–133.
- [355] J.-G. Zhang, W. Xu, W.A. Henderson, Characterization and modeling of lithium dendrite growth, *Lithium Metal Anodes and Rechargeable Lithium Metal Batteries, Springer Series in Materials Science, Springer, Cham, 2017, pp. 5–43, https://doi.org/10.1007/978-3-319-44054-5_2*.
- [356] R.D. Armstrong, T. Dickinson, J. Turner, The breakdown of β -alumina ceramic electrolyte, *Electrochim. Acta* 19 (1974) 187–192.
- [357] L.A. Feldman, L.C. De Jonghe, Initiation of mode I degradation in sodium-beta alumina electrolytes, *J. Mater. Sci.* 17 (1982) 517–524.
- [358] C. Monroe, J. Newman, Dendrite growth in lithium/polymer systems: a propagation model for liquid electrolytes under galvanostatic conditions, *J. Electrochem. Soc.* 150 (2003) A1377–A1384.
- [359] C. Monroe, J. Newman, The impact of elastic deformation on deposition kinetics at lithium/polymer interfaces, *J. Electrochem. Soc.* 152 (2005) A396–A404.
- [360] G.M. Stone, S.A. Mullin, A.A. Teran, D.T. Hallinan, A.M. Minor, A. Hexemer,

- N.P. Balsara, Resolution of the modulus versus adhesion dilemma in solid polymer electrolytes for rechargeable lithium metal batteries, *J. Electrochem. Soc.* 159 (2012) A222–A227.
- [361] M.D. Tikekar, L.A. Archer, D.L. Koch, Stabilizing electrodeposition in elastic solid electrolytes containing immobilized anions, *Sci. Adv.* 2 (2016) e1600320.
- [362] E.J. Cheng, A. Sharafi, J. Sakamoto, Intergranular Li metal propagation through polycrystalline $\text{Li}_{6.25}\text{Al}_0.25\text{La}_3\text{Zr}_2\text{O}_{12}$ ceramic electrolyte, *Electrochim. Acta* 223 (2017) 85–91.
- [363] R. Raj, J. Wolfenstine, Current limit diagrams for dendrite formation in solid-state electrolytes for Li-ion batteries, *J. Power Sources* 343 (2017) 119–126.
- [364] Islam, Fisher, Lithium and sodium battery cathode materials: computational insights into voltage, diffusion and nanostructural properties, *Chem. Soc. Rev.* 43 (2014) 185, <https://doi.org/10.1039/c3cs60199d>.
- [365] Haftbaradaran, et al., A surface locking instability for atomic intercalation into a solid electrode, *Appl. Phys. Lett.* 96 (2010) 091909, <https://doi.org/10.1063/1.3330940>.
- [366] Tealdi, et al., Feeling the strain: enhancing ionic transport in olivine phosphate cathodes for Li- and Na-ion batteries through strain effects, *J. Mater. Chem. A* 4 (2018) 6998, <https://doi.org/10.1039/c8ta09418f>.
- [367] Sarkar, Aquino, Changes in electroic reaction rates due to elastic stress and stress-induced surface patterns, *Electrochim. Acta* 111 (2013) 814, <https://doi.org/10.1016/j.electacta.2013.08.085>.
- [368] Ma, et al., Eigenstress model for electrochemistry of solid surfaces, *Scientific reports* 6 (2016) 26897, <https://doi.org/10.1038/srep26897> AND.
- [369] Yang, Generalized > Butler-Volmer relation on a curved electrode surface under the action of stress, *Sci. China-Phys. Mech. Astron.* 59 (11) (2016) 114611, <https://doi.org/10.1007/s11433-016-0198-6>.
- [370] Haftbaradaran, et al., Continuum and atomistic models of strongly coupled diffusion, stress, and solute concentration, *J. Power Sources* 196 (2011) 361, <https://doi.org/10.1016/j.jpowsour.2010.06.080>.
- [371] Li, et al., Effect of local deformation on the coupling between diffusion and stress in lithium-ion battery, *Int. J. Solids Struct.* 87 (2016) 81, <https://doi.org/10.1016/j.ijsolstr.2016.02.029>.
- [372] Wang, et al., Effect of chemical stress on diffusion in a hollow cylinder, *J. Appl. Phys.* 91 (12) (2002) 9584, <https://doi.org/10.1063/1.1477624>.
- [373] Soni, et al., Diffusion Mediated Lithiation Stresses in Si Thin Film Electrodes, *J. Electrochem. Soc.* 159 (9) (2012) A1520, <https://doi.org/10.1149/2.009209jes>.
- [374] Gao, Zhou, Strong dependency of lithium diffusion on mechanical constraints in high-capacity Li-ion battery electrodes, *Acta Mech. Sinica* 28 (4) (2012) 1068, <https://doi.org/10.1007/s10409-012-0141-4>.
- [375] An, Jiang, A finite element simulation on transient large deformation and mass diffusion in electrodes for lithium ion batteries, *Modelling Simul. Mater. Sci. Eng.* 21 (2013) 074007, <https://doi.org/10.1088/0965-0393/21/7/074007>.
- [376] Zhao, et al., Inelastic hosts as electrodes for high-capacity lithium-ion batteries, *J. Appl. Phys.* 109 (2011) 016110, <https://doi.org/10.1063/1.3525990>.
- [377] Walk, et al., Comparison of a phase-field model for intercalation induced stresses in electrode particles of lithium ion batteries for small and finite deformation theory, *Eur. J. Mech. A-Solid* 48 (2014) 74, <https://doi.org/10.1016/j.euromechsol.2014.02.020>.
- [378] Cui et al., "Interface-reaction controlled diffusion in binary solids with applications to lithiation of silicon in lithium-ion batteries", *J. Mech. Phys. Solids* 61:293, 10.1016/j.jmps.2012.11.001 AND.
- [379] Weinberg, et al., A Chemo-Mechanical Model of Diffusion in Reactive Systems, *Entropy* 20 (2018) 140, <https://doi.org/10.3390/e20020140>.
- [380] Li, et al., Fluid-enhanced surface diffusion controls intraparticle phase transformations, *Nat. Mater.* 17 (2018) 915, <https://doi.org/10.1038/s41563-018-0168-4>.
- [381] Nowack, et al., Design and fabrication of microspheres with hierarchical internal structure for tuning battery performance, *Adv. Sci.* 2 (2015) 1500078, <https://doi.org/10.1002/advs.201500078>.
- [382] Cho, et al., Numerical and experimental investigation of (de)lithiation-induced strains in bicontinuous silicon-coated nickel inverse opal anodes, *Acta Mater* 107 (2016) 289, <https://doi.org/10.1016/j.actamat.2016.01.064>.
- [383] Cho, et al., Modeling of stresses and strains during (de)lithiation of Ni₃Sn₂-coated nickel inverse-opal anodes, *ACS Appl. Mater. Interfaces* 9 (18) (2017) 15433, <https://doi.org/10.1021/acsami.7b01640>.
- [384] Malik, et al., Particle size dependence of the ionic diffusivity, *Nano Lett* 10 (2010) 4123, <https://doi.org/10.1021/nl1023595>.
- [385] Gao, Zhou, Strong stress-enhanced diffusion in amorphous lithium alloy nanowire electrodes, *J. Appl. Phys.* 109 (2011) 014310, <https://doi.org/10.1063/1.3530738>.
- [386] Gao, et al., A chemo-mechanics framework for elastic solids with surface stress, *Proc. R. Soc. A* 471 (2015) 20150366, <https://doi.org/10.1098/rspa.2015.0366>.
- [387] Bower, Guduru, A simple finite element model of diffusion, finite deformation, plasticity and fracture in lithium ion insertion electrode materials, *Modelling Simul. Mater. Sci. Eng.* 20 (2012) 045004, <https://doi.org/10.1088/0965-0393/20/4/045004>.
- [388] Chen, et al., Diffusion Induced Damage and Impedance Response in Lithium-Ion Battery Electrodes, *J. Electrochem. Soc.* 161 (14) (2014) A2138, <https://doi.org/10.1149/2.0651414jes>.
- [389] Chen, et al., Scaling Relations for Intercalation Induced Damage in Electrodes, *Electrochim. Acta* 204 (2016) 31, <https://doi.org/10.1016/j.electacta.2016.03.106>.
- [390] Haftbaradaran, et al., Method to deduce the critical size for interfacial delamination of patterned electrode structures and application to lithiation of thin-film silicon islands, *J. Power Sources* 206 (2012) 357, <https://doi.org/10.1016/j.jpowsour.2012.01.097>.
- [391] Zaho, et al., Fracture of electrodes in lithium-ion batteries caused by fast charging, *J. Appl. Phys.* 108 (2010) 073517, <https://doi.org/10.1063/1.3492617>.
- [392] Zhao, et al., Inelastic hosts as electrodes for high-capacity lithium-ion batteries, *J. Appl. Phys.* 109 (2011) 016110, <https://doi.org/10.1063/1.3525990>.
- [393] Zhao, et al., Fracture and debonding in lithium-ion batteries with electrodes of hollow core-shell nanostructures, *J. Power Sources* 218 (6) (2012), <https://doi.org/10.1016/j.jpowsour.2012.06.074>.
- [394] Gao, Zhou, Coupled mechano-diffusional driving forces for fracture in electrode materials, *J. Power Sources* 230 (2013) 176, <https://doi.org/10.1016/j.jpowsour.2012.12.034>.
- [395] Zhang, et al., Constitutive behavior and progressive mechanical failure of electrodes in lithium-ion batteries, *J. Power Sources* 357 (2017) 126, <https://doi.org/10.1016/j.jpowsour.2017.04.103>.
- [396] Hüter, et al., Electrode–electrolyte interface stability in solid state electrolyte systems: influence of coating thickness under varying residual stresses, *AIMS Mater. Sci.* 4 (4) (2017) 867, <https://doi.org/10.3934/mat.2017.4.867>.
- [397] Purkayastha, McMeeking, A parameter study of intercalation of lithium into storage particles in a lithium-ion battery, *Comp. Mater. Sci.* 80 (2) (2013), <https://doi.org/10.1016/j.commat.2012.11.050>.
- [398] Zhang, Kamla, Phase-field modeling of the particle size and average concentration dependent miscibility gap in nanoparticles of $\text{Li}_x\text{Mn}_2\text{O}_4$, Li_xFePO_4 , and Na_xFePO_4 during insertion, *Electrochim. Acta* 298 (2019) 31, <https://doi.org/10.1016/j.electacta.2018.12.007>.

6 Summary and outlook

6.1 Summary

This thesis provides a general framework for modeling the chemo-mechanical interplay in energy materials or polycrystalline materials with GBs or interfaces, as well as their impact on the battery cell performance. Although there has been everlasting interests and efforts on the modeling, the present thesis has its innovations in terms of both the modeling and numerical treatments.

For the modeling part, we have formulated a general thermodynamically consistent framework. The key features are summarized as follows:

- the contribution of the species diffusion, as well as the finite deformation inside the particles to the system, have been considered via the principals of power of the different physical fields, i.e., the concentration of Lithium, the stresses, the chemical potentials, the traction at the GBs (interface), and the Lithium transport across the GBs (interface).
- the dissipation potentials of the system with the consideration of the contribution from both the grains and GBs (interface) have been formulated.
- from the dissipation potentials, we have successfully formulated, not only the general constitutive laws for the stresses and chemical potentials inside the grains but also the constitutive laws for the traction and interface flux at the GBs (interface).
- accordingly, the Lithium transport across the GBs and the traction-separation laws for the GBs cracking are fully coupled, namely, a chemo-mechanical GB model has been presented.
- besides, this flexible and robust thermodynamically consistent model has been successfully incorporated with the battery cell model, namely the two-level framework we presented in the previous chapter. Therefore, the parameter study of the electrode particle, the chemo-mechanical behavior of the particle, and the

complex geometry of the particles, as well as their impact on the cell performance can be easily considered under our framework.

Numerically, the work presented in this thesis offers:

- an efficient two-level framework for the multiphysics coupling in LIB modeling, where we manage to reduce the degrees of freedom (DoFs) of the system and introduce the parallel algorithm to speed up the data transfer between levels as well as the nonlinear solver for the coupled PDEs/ODEs.
- an efficient way to generate a polycrystalline structure for the particles, and also label the interface between each grain.
- an easy to use open-source package for the presented two-level framework. Thus users can easily adjust the material parameters as well as the electrode particle samples (mesh) to optimize the battery design.

From the simulation results, we found:

- the chemical process and the mechanical degradation of NMC particles go hand-in-hand, where the enhanced intergranular chemical inhomogeneity can weaken the GB mechanical strength, while the GB damage can influence or even block the across-grain transport.
- for the particle with the across-GB transport, the damage percentage is much higher than the cases without this transport. Moreover, this model can well reproduce the enhanced chemical inhomogeneity and also the surface layer delamination which are observed in experiments.
- due to the mechanical drifting effect at the higher curvature, the oblate particle has better cell performance than other spheroidal particles.
- for particles with different geometry, the particle's diffusion behavior has a more significant impact than the geometry on the cell performance when the aspect ratio is far from the critical value. Moreover, the mechanically coupled Cahn–Hilliard–type diffusion is much more sensitive to the change of aspect ratio than other types of diffusion dynamics.
- The attainable capacity can be improved by increasing the particle's stiffness, and once the particle is stiff enough, the improvement is limited. Besides, the phase separation can result in longer discharge time.

6.2 Outlook

For future research, further efforts can be made to gain more understanding of LIBs based on our framework:

- the free energies for the electrode materials can be calculated from CALPHAD [134] to investigate a more realistic study. Moreover, the conductivity coefficient of the cell as well as the elastic moduli, the diffusion coefficient of the electrode can be measured by the first principle calculation (DFT) [135] or the molecular dynamics (MD) [136] simulation for the specific materials system
- the chemo-mechanical GB model can be easily extended to model the delamination behavior of the all-solid-state-battery (ASSB), and its impact on the cell performance
- the composite structure of the electrode can be reconstructed from the SEM image to obtain a more realistic 3D mesh for the simulation, which can be extremely useful for the battery design optimization.

Bibliography

- [1] George E Blomgren. “The development and future of lithium ion batteries”. In: *Journal of The Electrochemical Society* 164.1 (2016), A5019.
- [2] Bruno Scrosati and Jürgen Garche. “Lithium batteries: Status, prospects and future”. In: *Journal of power sources* 195.9 (2010), pp. 2419–2430.
- [3] Bill Schweber. “Lithium Batteries: The Pros and Cons”. In: (2015).
- [4] Claus Daniel and Jürgen O Besenhard. *Handbook of battery materials*. John Wiley & Sons, 2012.
- [5] Wei-Jun Zhang. “Lithium insertion/extraction mechanism in alloy anodes for lithium-ion batteries”. In: *Journal of Power Sources* 196.3 (2011), pp. 877–885.
- [6] Gholam-Abbas Nazri and Gianfranco Pistoia. *Lithium batteries: science and technology*. Springer Science & Business Media, 2008.
- [7] Thomas B Reddy. *Linden’s handbook of batteries*. Vol. 4. Mcgraw-hill New York, 2011.
- [8] Uday Kasavajjula, Chunsheng Wang, and A John Appleby. “Nano-and bulk-silicon-based insertion anodes for lithium-ion secondary cells”. In: *Journal of power sources* 163.2 (2007), pp. 1003–1039.
- [9] Dean J Miller et al. “Observation of microstructural evolution in Li battery cathode oxide particles by in situ electron microscopy”. In: *Advanced Energy Materials* 3.8 (2013), pp. 1098–1103.
- [10] F M Gray and M J Smith. “Secondary Batteries - Lithium Rechargeable Systems | Lithium Polymer Batteries”. In: *Encyclopedia of Electrochemical Power Sources*. 2009, pp. 169–176. ISBN: 9780444527455. DOI: 10.1016/B978-044452745-5.00040-X.
- [11] Ying Zhao et al. “A review on modeling of electro-chemo-mechanics in lithium-ion batteries”. In: *Journal of Power Sources* 413 (2019), pp. 259–283.

-
- [12] M Wohlfahrt-Mehrens, C Vogler, and J Garche. "Aging mechanisms of lithium cathode materials". In: *Journal of power sources* 127.1-2 (2004), pp. 58–64.
- [13] Guanhua Sun et al. "On the fragmentation of active material secondary particles in lithium ion battery cathodes induced by charge cycling". In: *Extreme Mechanics Letters* 9 (2016), pp. 449–458.
- [14] Yuichi Itou and Yoshio Ukyo. "Performance of LiNiCoO₂ materials for advanced lithium-ion batteries". In: *Journal of Power Sources* 146.1-2 (2005), pp. 39–44.
- [15] Shoichiro Watanabe et al. "Capacity fade of LiAl_yNi_{1-x-y}Co_xO₂ cathode for lithium-ion batteries during accelerated calendar and cycle life tests (surface analysis of LiAl_yNi_{1-x-y}Co_xO₂ cathode after cycle tests in restricted depth of discharge ranges)". In: *Journal of Power Sources* 258 (2014), pp. 210–217.
- [16] Shoichiro Watanabe, Masahiro Kinoshita, and Kensuke Nakura. "Comparison of the surface changes on cathode during long term storage testing of high energy density cylindrical lithium-ion cells". In: *Journal of Power Sources* 196.16 (2011), pp. 6906–6910.
- [17] Claude Delmas et al. "Lithium deintercalation in LiFePO₄ nanoparticles via a domino-cascademodel". In: *Materials For Sustainable Energy: A Collection of Peer-Reviewed Research and Review Articles from Nature Publishing Group*. World Scientific, 2011, pp. 180–186.
- [18] Hyejung Kim et al. "A new coating method for alleviating surface degradation of LiNi_{0.6}Co_{0.2}Mn_{0.2}O₂ cathode material: nanoscale surface treatment of primary particles". In: *Nano letters* 15.3 (2015), pp. 2111–2119.
- [19] Hyejung Kim et al. "Enhancing Interfacial Bonding between Anisotropically Oriented Grains Using a Glue-Nanofiller for Advanced Li-Ion Battery Cathode". In: *Advanced materials* 28.23 (2016), pp. 4705–4712.
- [20] Kuichen Wu et al. "Effect of precursor and synthesis temperature on the structural and electrochemical properties of Li(Ni_{0.5}Co_{0.2}Mn_{0.3})O₂". In: *Electrochimica Acta* 75 (2012), pp. 393–398. ISSN: 0013-4686. DOI: <https://doi.org/10.1016/j.electacta.2012.05.035>. URL: <http://www.sciencedirect.com/science/article/pii/S0013468612008006>.
- [21] R Xu et al. "Disintegration of meatball electrodes for LiNi_xMn_yCo_zO₂ cathode materials". In: *Experimental Mechanics* 58.4 (2018), pp. 549–559.
- [22] Davide Grazioli, Marco Magri, and Alberto Salvadori. "Computational modeling of Li-ion batteries". In: *Computational Mechanics* 58.6 (2016), pp. 889–909.

-
- [23] Gerardine G Botte, Venkat R Subramanian, and Ralph E White. “Mathematical modeling of secondary lithium batteries”. In: *Electrochimica Acta* 45.15-16 (2000), pp. 2595–2609.
- [24] Alejandro A Franco. “Multiscale modelling and numerical simulation of rechargeable lithium ion batteries: concepts, methods and challenges”. In: *Rsc Advances* 3.32 (2013), pp. 13027–13058.
- [25] Christopher Marc Doyle. “Design and simulation of lithium rechargeable batteries”. In: (1995).
- [26] Marc Doyle, Thomas F. Fuller, and John Newman. “Modeling of Galvanostatic Charge and Discharge of the Lithium/Polymer/Insertion Cell”. en. In: *Journal of The Electrochemical Society* 140.6 (June 1993), pp. 1526–1533. ISSN: 0013-4651, 1945-7111. DOI: 10.1149/1.2221597. URL: <http://jes.ecsdl.org/content/140/6/1526>.
- [27] Marc Doyle and John Newman. “The use of mathematical modeling in the design of lithium/polymer battery systems”. In: *Electrochimica Acta* 40.13 (Oct. 1995), pp. 2191–2196. ISSN: 0013-4686. DOI: 10.1016/0013-4686(95)00162-8. URL: <http://www.sciencedirect.com/science/article/pii/S0013468695001628>.
- [28] John Newman and Karen E Thomas-Alyea. *Electrochemical systems*. John Wiley & Sons, 2012.
- [29] William Valentine Mayneord. John Alfred Valentine Butler, 14 February 1899-16 July 1977. 1979.
- [30] Thomas F Fuller, Marc Doyle, and John Newman. “Simulation and optimization of the dual lithium ion insertion cell”. In: *Journal of the Electrochemical Society* 141.1 (1994), pp. 1–10.
- [31] Jake Christensen. “Modeling diffusion-induced stress in Li-ion cells with porous electrodes”. In: *Journal of the Electrochemical Society* 157.3 (2010), A366–A380.
- [32] Sindhuja Renganathan et al. “Theoretical Analysis of Stresses in a Lithium Ion Cell”. In: *Journal of The Electrochemical Society* 157.2 (2010), A155. DOI: 10.1149/1.3261809. URL: <https://doi.org/10.1149/1.3261809>.
- [33] Stephanie Golmon, Kurt Maute, and Martin L Dunn. “Numerical modeling of electrochemical–mechanical interactions in lithium polymer batteries”. In: *Computers & Structures* 87.23-24 (2009), pp. 1567–1579.

-
- [34] T Mori and K Tanaka. “Average stress in matrix and average elastic energy of materials with misfitting inclusions”. In: *Acta Metallurgica* 21.5 (1973), pp. 571–574. ISSN: 0001-6160. DOI: [https://doi.org/10.1016/0001-6160\(73\)90064-3](https://doi.org/10.1016/0001-6160(73)90064-3). URL: <http://www.sciencedirect.com/science/article/pii/S0001616073900643>.
- [35] Rujian Fu, Meng Xiao, and Song-Yul Choe. “Modeling, validation and analysis of mechanical stress generation and dimension changes of a pouch type high power Li-ion battery”. In: *Journal of Power Sources* 224 (2013), pp. 211–224. ISSN: 0378-7753. DOI: <https://doi.org/10.1016/j.jpowsour.2012.09.096>. URL: <http://www.sciencedirect.com/science/article/pii/S0378775312015285>.
- [36] Linmin Wu et al. “Three-dimensional finite element study on stress generation in synchrotron X-ray tomography reconstructed nickel-manganese-cobalt based half cell”. In: *Journal of Power Sources* 336 (2016), pp. 8–18. ISSN: 0378-7753. DOI: <https://doi.org/10.1016/j.jpowsour.2016.10.052>. URL: <http://www.sciencedirect.com/science/article/pii/S0378775316314458>.
- [37] John Christensen and John Newman. “A mathematical model of stress generation and fracture in lithium manganese oxide”. In: *Journal of The Electrochemical Society* 153.6 (2006), A1019–A1030.
- [38] Xiangchun Zhang, Wei Shyy, and Ann Marie Sastry. “Numerical Simulation of Intercalation-Induced Stress in Li-Ion Battery Electrode Particles”. In: *Journal of The Electrochemical Society* 154.10 (2007), A910. DOI: [10.1149/1.2759840](https://doi.org/10.1149/1.2759840). URL: <https://doi.org/10.1149%2F1.2759840>.
- [39] Peter Stein, Ying Zhao, and Bai-Xiang Xu. “Effects of surface tension and electrochemical reactions in Li-ion battery electrode nanoparticles”. In: *Journal of Power Sources* 332 (2016), pp. 154–169. ISSN: 0378-7753. DOI: <https://doi.org/10.1016/j.jpowsour.2016.09.085>. URL: <http://www.sciencedirect.com/science/article/pii/S0378775316312484>.
- [40] Ying Zhao, Peter Stein, and Bai-Xiang Xu. “Isogeometric analysis of mechanically coupled Cahn–Hilliard phase segregation in hyperelastic electrodes of Li-ion batteries”. In: *Computer Methods in Applied Mechanics and Engineering* 297 (Dec. 2015), pp. 325–347. ISSN: 0045-7825. DOI: [10.1016/j.cma.2015.09.008](https://doi.org/10.1016/j.cma.2015.09.008).

-
- [41] Ying Zhao et al. “Phase-field study of electrochemical reactions at exterior and interior interfaces in Li-ion battery electrode particles”. In: *Computer Methods in Applied Mechanics and Engineering*. Phase Field Approaches to Fracture 312 (Dec. 2016), pp. 428–446. ISSN: 0045-7825. DOI: 10.1016/j.cma.2016.04.033.
- [42] Bin Wu and Wei Lu. “Mechanical-electrochemical modeling of agglomerate particles in lithium-ion battery electrodes”. In: *Journal of The Electrochemical Society* 163.14 (2016), A3131–A3139.
- [43] Yuwei Zhang, Chunwang Zhao, and Zhansheng Guo. “Simulation of crack behavior of secondary particles in Li-ion battery electrodes during lithiation/delithiation cycles”. In: *International Journal of Mechanical Sciences* (2019), p. 4802.
- [44] Rong Xu and Kejie Zhao. “Corrosive fracture of electrodes in Li-ion batteries”. In: *Journal of the Mechanics and Physics of Solids* 121 (2018), pp. 258–280.
- [45] Avtar Singh and Siladitya Pal. “Coupled chemo-mechanical modeling of fracture in polycrystalline cathode for lithium-ion battery”. In: *International Journal of Plasticity* 127 (2020), p. 102636.
- [46] Morton E Gurtin, Eliot Fried, and Lallit Anand. *The mechanics and thermodynamics of continua*. Cambridge University Press, 2010.
- [47] Ted Belytschko et al. *Nonlinear finite elements for continua and structures*. John wiley & sons, 2013.
- [48] Allan F Bower. *Applied mechanics of solids*. CRC press, 2009.
- [49] Howard Anton and Albert Herr. *Calculus with analytic geometry*. Wiley New York, 1988.
- [50] Tom M Apostol. “Mathematical analysis”. In: (1964).
- [51] Adolf Fick. “Ueber diffusion”. In: *Annalen der Physik* 170.1 (1855), pp. 59–86.
- [52] Dr. Adolph Fick. “V. On liquid diffusion”. In: *The London, Edinburgh, and Dublin Philosophical Magazine and Journal of Science* 10.63 (1855), pp. 30–39. DOI: 10.1080/14786445508641925. URL: <https://doi.org/10.1080/14786445508641925>.
- [53] Victor J Katz. “The history of Stokes’ theorem”. In: *Mathematics Magazine* 52.3 (1979), pp. 146–156.

-
- [54] Kenneth Franklin Riley, Michael Paul Hobson, and Stephen John Bence. *Mathematical methods for physics and engineering: a comprehensive guide*. Cambridge university press, 2006.
- [55] Shunsuke Yamakawa et al. “Numerical study of Li diffusion in polycrystalline Li-CoO 2”. In: *Journal of Power Sources* 223 (2013), pp. 199–205. ISSN: 03787753. DOI: 10.1016/j.jpowsour.2012.09.055.
- [56] Sangwoo Han et al. “Numerical study of grain boundary effect on Li+ effective diffusivity and intercalation-induced stresses in Li-ion battery active materials”. In: *Journal of Power Sources* 240 (2013), pp. 155–167. ISSN: 03787753. DOI: 10.1016/j.jpowsour.2013.03.135. URL: <http://dx.doi.org/10.1016/j.jpowsour.2013.03.135>.
- [57] W. Preis and W. Sitte. “Grain boundary diffusion through thin films. Application to permeable surfaces”. In: *Journal of Applied Physics* 79.6 (1996), pp. 2986–2994. ISSN: 00218979. DOI: 10.1063/1.362651.
- [58] Fridtjov Irgens. *Continuum mechanics*. Springer Science & Business Media, 2008.
- [59] Peter Chadwick. *Continuum mechanics: concise theory and problems*. Courier Corporation, 2012.
- [60] Lallit Anand. “A Cahn–Hilliard-type theory for species diffusion coupled with large elastic–plastic deformations”. In: *Journal of the Mechanics and Physics of Solids* 60.12 (2012), pp. 1983–2002.
- [61] Claudio V Di Leo, Elisha Rejovitzky, and Lallit Anand. “A Cahn–Hilliard-type phase-field theory for species diffusion coupled with large elastic deformations: application to phase-separating Li-ion electrode materials”. In: *Journal of the Mechanics and Physics of Solids* 70 (2014), pp. 1–29.
- [62] Kaspar Loeffel and Lallit Anand. “A chemo-thermo-mechanically coupled theory for elastic-viscoplastic deformation, diffusion, and volumetric swelling due to a chemical reaction”. In: *International Journal of Plasticity* 27.9 (2011), pp. 1409–1431. ISSN: 07496419. DOI: 10.1016/j.ijplas.2011.04.001. URL: <http://dx.doi.org/10.1016/j.ijplas.2011.04.001>.
- [63] Claudio V. Di Leo, Elisha Rejovitzky, and Lallit Anand. “Diffusion-deformation theory for amorphous silicon anodes: The role of plastic deformation on electrochemical performance”. In: *International Journal of Solids and Structures* 67-68 (2015), pp. 283–296. ISSN: 00207683. DOI: 10.1016/j.ijsolstr.2015.

04.028. URL: <http://dx.doi.org/10.1016/j.ijsolstr.2015.04.028>.

- [64] Morton E Gurtin. “A gradient theory of single-crystal viscoplasticity that accounts for geometrically necessary dislocations”. In: *Journal of the Mechanics and Physics of Solids* 50.1 (2002), pp. 5–32.
- [65] Max Planck. *Treatise on thermodynamics*. Courier Corporation, 2013.
- [66] Sybren Ruurds De Groot and Sybren Ruurds De Groot. *Thermodynamics of irreversible processes*. Vol. 336. North-Holland Amsterdam, 1951.
- [67] Clifford Truesdell. “The mechanical foundations of elasticity and fluid dynamics”. In: *Journal of Rational Mechanics and Analysis* 1 (1952), pp. 125–300.
- [68] Clifford Truesdell and Richard Toupin. “The classical field theories”. In: *Principles of classical mechanics and field theory/Prinzipien der Klassischen Mechanik und Feldtheorie*. Springer, 1960, pp. 226–858.
- [69] Michel Frémond. “The Clausius-Duhem inequality, an interesting and productive inequality”. In: *Nonsmooth Mechanics and Analysis*. Springer, 2006, pp. 107–118.
- [70] Dmitrii Nikolaevich Zubarev and PJ Shepherd. *Nonequilibrium statistical thermodynamics*. Consultants Bureau New York, 1974.
- [71] Sybren Ruurds De Groot and Peter Mazur. *Non-equilibrium thermodynamics*. Courier Corporation, 2013.
- [72] Bernard D Coleman and Walter Noll. “The thermodynamics of elastic materials with heat conduction and viscosity”. In: *The Foundations of Mechanics and Thermodynamics*. Springer, 1974, pp. 145–156.
- [73] VA Cimmelli, A Sellitto, and V Triani. “A generalized Coleman–Noll procedure for the exploitation of the entropy principle”. In: *Proceedings of the Royal Society A: Mathematical, Physical and Engineering Sciences* 466.2115 (2010), pp. 911–925.
- [74] Gerafl Hütter. “Coleman-Noll Procedure for Classical and Generalized Continuum Theories”. In: *Encyclopedia of Continuum Mechanics* (2020), pp. 316–323.
- [75] Jean Lemaitre and Jean-Louis Chaboche. *Mechanics of solid materials*. Cambridge university press, 1994.

-
- [76] AD Drozdov. “Viscoplastic response of electrode particles in Li-ion batteries driven by insertion of lithium”. In: *International Journal of Solids and Structures* 51.3-4 (2014), pp. 690–705.
- [77] A Salvadori et al. “A coupled model of transport-reaction-mechanics with trapping. Part I—Small strain analysis”. In: *Journal of the Mechanics and Physics of Solids* 114 (2018), pp. 1–30.
- [78] Morton E Gurtin and Peter W Voorhees. “The thermodynamics of evolving interfaces far from equilibrium”. In: *Acta materialia* 44.1 (1996), pp. 235–247.
- [79] Aurélien Villani et al. “A fully coupled diffusional-mechanical formulation: numerical implementation, analytical validation, and effects of plasticity on equilibrium”. In: *Archive of applied mechanics* 84.9-11 (2014), pp. 1647–1664.
- [80] Morton E Gurtin. “Generalized Ginzburg-Landau and Cahn-Hilliard equations based on a microforce balance”. In: (1994).
- [81] Matthew T McDowell et al. “Studying the kinetics of crystalline silicon nanoparticle lithiation with in situ transmission electron microscopy”. In: *Advanced Materials* 24.45 (2012), pp. 6034–6041.
- [82] Martin Ebner et al. “Visualization and quantification of electrochemical and mechanical degradation in Li ion batteries”. In: *Science* 342.6159 (2013), pp. 716–720.
- [83] Jongwoo Lim et al. “Origin and hysteresis of lithium compositional spatiodynamics within battery primary particles”. In: *Science* 353.6299 (2016), pp. 566–571.
- [84] Peng Bai, Daniel A Cogswell, and Martin Z Bazant. “Suppression of phase separation in LiFePO₄ nanoparticles during battery discharge”. In: *Nano letters* 11.11 (2011), pp. 4890–4896.
- [85] A Van der Ven et al. “Phase transformations and volume changes in spinel Li_xMn₂O₄”. In: *Solid State Ionics* 135.1-4 (2000), pp. 21–32.
- [86] Do Kyung Kim et al. “Spinel LiMn₂O₄ nanorods as lithium ion battery cathodes”. In: *Nano letters* 8.11 (2008), pp. 3948–3952.
- [87] Brandon R Long et al. “Effect of cooling rates on phase separation in 0.5 Li₂MnO₃·0.5 LiCoO₂ electrode materials for Li-ion batteries”. In: *Chemistry of Materials* 26.11 (2014), pp. 3565–3572.
- [88] Seung-Taek Myung et al. “Effects of Al doping on the microstructure of LiCoO₂ cathode materials”. In: *Solid State Ionics* 139.1-2 (2001), pp. 47–56.

-
- [89] John W Cahn and John E Hilliard. “Free energy of a nonuniform system. I. Interfacial free energy”. In: *The Journal of chemical physics* 28.2 (1958), pp. 258–267.
- [90] John W Cahn. “On spinodal decomposition”. In: *Acta metallurgica* 9.9 (1961), pp. 795–801.
- [91] Jean-Louis Barrat and Jean-Pierre Hansen. *Basic concepts for simple and complex liquids*. Cambridge University Press, 2003.
- [92] Harold L Friedman. *A course in statistical mechanics*. Prentice-Hall Englewood Cliffs, NJ, 1985.
- [93] Josiah Willard Gibbs. “On the fundamental formula of statistical mechanics, with applications to astronomy and thermodynamics”. In: *Proceedings of the American Association for the Advancement of Science*. 1884, pp. 57–58.
- [94] International Bureau of Weights et al. *The international system of units (SI)*. US Department of Commerce, Technology Administration, National Institute of . . . , 2001.
- [95] Jacques Dutka. “The early history of the factorial function”. In: *Archive for history of exact sciences* (1991), pp. 225–249.
- [96] Lucien Le Cam. “The central limit theorem around 1935”. In: *Statistical science* (1986), pp. 78–91.
- [97] Pierre Perrot. *A to Z of Thermodynamics*. Oxford University Press on Demand, 1998.
- [98] Yang Bai et al. “Two-level modeling of lithium-ion batteries”. In: *Journal of Power Sources* 422 (2019), pp. 92–103.
- [99] Yang Bai et al. “A chemo-mechanical grain boundary model and its application to understand the damage of Li-ion battery materials”. In: *Scripta Materialia* 183 (2020), pp. 45–49.
- [100] William E Gent et al. “Persistent State-of-Charge Heterogeneity in Relaxed, Partially Charged $\text{Li}_{1-x}\text{Ni}_{1/3}\text{Co}_{1/3}\text{Mn}_{1/3}\text{O}_2$ Secondary Particles”. In: *Advanced Materials* 28.31 (2016), pp. 6631–6638.
- [101] N Taguchi et al. “REELS study of a $\text{LiNi}_{1/3}\text{Mn}_{1/3}\text{Co}_{1/3}\text{O}_2$ positive electrode”. In: *Surface and Interface Analysis* 48.11 (2016), pp. 1144–1147.
- [102] Un-Hyuck Kim et al. “Compositionally Graded Cathode Material with Long-Term Cycling Stability for Electric Vehicles Application”. In: *Advanced Energy Materials* 6.22 (2016), p. 1601417.

-
- [103] Ho-Hyun Sun and Arumugam Manthiram. "Impact of microcrack generation and surface degradation on a nickel-rich layered $\text{Li}[\text{Ni}_{0.9}\text{Co}_{0.05}\text{Mn}_{0.05}]\text{O}_2$ cathode for lithium-ion batteries". In: *Chemistry of Materials* 29.19 (2017), pp. 8486–8493.
- [104] Kyoungsoo Park, Glaucio H Paulino, and Jeffery R Roesler. "A unified potential-based cohesive model of mixed-mode fracture". In: *Journal of the Mechanics and Physics of Solids* 57.6 (2009), pp. 891–908.
- [105] Kyoungsoo Park and Glaucio H Paulino. "Computational implementation of the PPR potential-based cohesive model in ABAQUS: Educational perspective". In: *Engineering fracture mechanics* 93 (2012), pp. 239–262.
- [106] Daniel W Spring and Glaucio H Paulino. "A growing library of three-dimensional cohesive elements for use in ABAQUS". In: *Engineering Fracture Mechanics* 126 (2014), pp. 190–216.
- [107] DE Fenton. "Complexes of alkali metal ions with poly (ethylene oxide)". In: *polymer* 14 (1973), p. 589.
- [108] Wei-Tsu Tseng et al. "Novel polymeric surfactants for improving chemical mechanical polishing performance of silicon oxide". In: *Electrochemical and Solid State Letters* 4.5 (2001), G42.
- [109] Jianhui Wang et al. "Superconcentrated electrolytes for a high-voltage lithium-ion battery". In: *Nature communications* 7.1 (2016), pp. 1–9.
- [110] Masashi Kotobuki et al. "Fabrication of all-solid-state lithium battery with lithium metal anode using Al_2O_3 -added $\text{Li}_7\text{La}_3\text{Zr}_2\text{O}_{12}$ solid electrolyte". In: *Journal of Power Sources* 196.18 (2011), pp. 7750–7754.
- [111] Sheng Shui Zhang. "A review on electrolyte additives for lithium-ion batteries". In: *Journal of Power Sources* 162.2 (2006), pp. 1379–1394.
- [112] Feng Zheng et al. "Review on solid electrolytes for all-solid-state lithium-ion batteries". In: *Journal of Power Sources* 389 (2018), pp. 198–213.
- [113] Zhe Li et al. "A review of lithium deposition in lithium-ion and lithium metal secondary batteries". In: *Journal of power sources* 254 (2014), pp. 168–182.
- [114] Nurhaswani Alias and Ahmad Azmin Mohamad. "Advances of aqueous rechargeable lithium-ion battery: A review". In: *Journal of Power Sources* 274 (2015), pp. 237–251.
- [115] Vladimir S Bagotsky. *Fundamentals of electrochemistry*. Vol. 44. John Wiley & Sons, 2005.

-
- [116] Lars Onsager. “Reciprocal relations in irreversible processes. I.” In: *Physical review* 37.4 (1931), p. 405.
- [117] Lars Onsager. “Reciprocal relations in irreversible processes. II.” In: *Physical review* 38.12 (1931), p. 2265.
- [118] Shen J Dillon and Ke Sun. “Microstructural design considerations for Li-ion battery systems”. In: *Current Opinion in Solid State and Materials Science* 16.4 (2012), pp. 153–162.
- [119] F Tariq et al. “Three-dimensional high resolution X-ray imaging and quantification of lithium ion battery mesocarbon microbead anodes”. In: *Journal of Power Sources* 248 (2014), pp. 1014–1020.
- [120] John S Dunning, Douglas N Bennion, and John Newman. “Analysis of porous electrodes with sparingly soluble reactants”. In: *Journal of The Electrochemical Society* 118.8 (1971), p. 1251.
- [121] Olivier Darrigol. *Electrodynamics from ampere to Einstein*. Oxford University Press, 2003.
- [122] Wolfgang KH Panofsky and Melba Phillips. *Classical electricity and magnetism*. Courier Corporation, 2005.
- [123] Tuck C Choy. *Effective medium theory: principles and applications*. Vol. 165. Oxford University Press, 2015.
- [124] John Thomas Stock, Mary Virginia Orna, et al. *Electrochemistry, past and present*. Vol. 390. ACS Publications, 1989.
- [125] Van Z Karaoglanoff. “Über Oxydations-und Reduktionsvorgänge bei der Elektrolyse von Eisensalzlösungen”. In: *Zeitschrift für Elektrochemie und angewandte physikalische Chemie* 12.1 (1906), pp. 5–16.
- [126] Olek C Zienkiewicz, Robert L Taylor, and Jian Z Zhu. *The finite element method: its basis and fundamentals*. Elsevier, 2005.
- [127] Christophe Geuzaine and Jean-François Remacle. “Gmsh: A 3-D finite element mesh generator with built-in pre-and post-processing facilities”. In: *International journal for numerical methods in engineering* 79.11 (2009), pp. 1309–1331.
- [128] Derek Gaston et al. “MOOSE: A parallel computational framework for coupled systems of nonlinear equations”. In: *Nuclear Engineering and Design* 239.10 (2009), pp. 1768–1778.

-
- [129] Cody J. Permann et al. “MOOSE: Enabling massively parallel multiphysics simulation”. In: *SoftwareX* 11 (2020), p. 100430. ISSN: 2352-7110. DOI: <https://doi.org/10.1016/j.softx.2020.100430>. URL: <http://www.sciencedirect.com/science/article/pii/S2352711019302973>.
- [130] B. S. Kirk et al. “libMesh: A C++ Library for Parallel Adaptive Mesh Refinement/Coarsening Simulations”. In: *Engineering with Computers* 22.3–4 (2006). <https://doi.org/10.1007/s00366-006-0049-3>, pp. 237–254.
- [131] Derek R. Gaston et al. “Physics-based multiscale coupling for full core nuclear reactor simulation”. In: *Annals of Nuclear Energy* 84 (2015), pp. 45–54.
- [132] Satish Balay et al. PETSc Web page. <https://www.mcs.anl.gov/petsc>. 2019. URL: <https://www.mcs.anl.gov/petsc>.
- [133] Shirang Abhyankar et al. “PETSc/TS: A Modern Scalable ODE/DAE Solver Library”. In: arXiv preprint arXiv:1806.01437 (2018).
- [134] Hans Lukas, Suzana G Fries, and Bo Sundman. *Computational thermodynamics: the Calphad method*. Cambridge university press, 2007.
- [135] Zi-Kui Liu. “First-principles calculations and CALPHAD modeling of thermodynamics”. In: *Journal of phase equilibria and diffusion* 30.5 (2009), p. 517.
- [136] Steve Plimpton. “Fast parallel algorithms for short-range molecular dynamics”. In: *Journal of computational physics* 117.1 (1995), pp. 1–19.

Publications and Presentations

Publications

- 1) **Y. Bai**, Y. Zhao, W. Liu, and B.-X. Xu, Two-level modeling of lithium-ion batteries, *J. Power Sources* 422, 92-103 (2019).
- 2) **Y. Bai**, K.-J. Zhao, Y. Liu, P. Stein, and B.-X. Xu, A chemo-mechanical grain boundary model and its application to understand the damage of NMC cathode materials, *Scr. Mater.* 183, 45-49 (2020).
- 3) D.A. Santos, J.L. Andrews, **Y. Bai**, P. Stein, Y. Luo, Y. Zhang, M. Pharr, B.-X. Xu, and S. Banerjee, Bending good beats breaking bad: phase separation patterns in individual cathode particles upon lithiation and delithiation, *Mater. Horiz* 7, 3275-3290 (2020).
- 4) B. Lin, **Y. Bai**, B.-X. Xu, Data-driven microstructure sensitivity study of fibrous paper materials, *Mater. Des* 197, 109193, (2021).
- 5) Y. Liu, **Y. Bai**, W. Jaegermann, R. Hausbrand, and B.-X. Xu, Impedance Modeling of Solid-State Electrolytes: Influence of the Contacted Space Charge Layer, *ACS Appl. Mater. Interfaces* 13, 5895-5906 (2021).
- 6) Y. Zhao, P. Stein, **Y. Bai**, M. Al-Siraj, Y. Yang, and B.-X. Xu, A review on modeling of electro-chemo-mechanics in lithium-ion batteries, *J. Power Sources* 413, 259-283 (2019).
- 7) Y. Yang, O. Ragnvaldsen, **Y. Bai**, M. Yi, and B.-X. Xu, 3D non-isothermal phase-field simulation of microstructure evolution during selective laser sintering, *Npj Comput. Mater.* 5(1), 1-12 (2019).

Conferences with Presentations and Posters

- 4th GAMM Workshop on Phase Field Modeling, 2017, RWTH Aachen.
- 88th GAMM Annual Meeting, 2017, Weimar.
- The Society of Engineering Science (SES) Technical Meeting, 2018, Madrid, Spain.
- Materials Science and Engineering conference (MSE), 2018, Darmstadt.
- 8th GACM Colloquium on Computational Mechanics (GACM 2019), 2019, Kassel.